UNIVERSITY OF NAPLES "FEDERICO II"

PhD SCHOOL IN INDUSTRIAL ENGINEERING

DEPARTMENT OF ELECTRICAL ENGINEERING AND INFORMATION TECHNOLOGIES

PhD COURSE IN ELECTRICAL ENGINEERING
XXVI course

PhD Thesis of **Flavio Ciccarelli**

Energy management and control strategies for the use of supercapacitors storage technologies in urban railway traction systems

Tutor: PhD Coordinator

Prof. Diego Iannuzzi   Prof. Claudio Serpico

March 2014

Summary

Outline

In recent years the need to reduce global energy consumption and CO_2 emissions in the environment, has been involved even in the railways sector, aimed at the highly competitive concept of new vehicles / transportation systems. The requirements hoped by the operating companies, particularly as concerns tramway and metro-train systems, are increasingly focused on products with so far advanced features in terms of energy and environmental impact. In order to accomplish this possible scenario, this could be put into effects in technological subsystems and critical components, which are able to fulfill not only functional and performance requirements, but also regarding the new canons of energy saving. On the other hand, the regional and national energetic political strategies impose a continuous effort in the eco-sustainability and energy saving direction both for the vehicles and for the infrastructure management.

In this scenario, the thesis aims to fill the gap in the technical literature and deals with improving the energy efficiency of urban rail transport systems by proposing both design methodologies and effective control strategies for supercapacitor-based energy storage systems, to be installed on-board urban rail vehicles or along the rail track.

Firstly, a deep, rigorous and comprehensive study on the factors which affect energy issues in a DC-electrified urban transit railway system is carried out. Then a widespread overview of the currently available strategies and technologies for recovery and management of braking energy in urban rail is presented, also by providing an assessment of their main advantages and disadvantages alongside a list of the most relevant scientific studies and well established commercial solutions.

Afterwards, some effective control strategies for the optimal energy management of the supercapacitor-based energy storage system have been

studied. Extensive simulations have been performed with the aim of validating the proposed techniques by employing a methodology which is based on tests carried out by means of scale models of the real systems.

A wide range of experimental tests has been developed and carried out on a laboratory-scale simulator for a typical urban service railway vehicle, in order to fully confirm the theoretical performances, validity, and feasibility of the studied controls, and quantify the technical and economic advantages obtained in terms of global energy saving, voltage regulation, power compensation and infrastructure power loss reduction.

The overall goal of this study is to gain an understanding of the methods and approaches for assessing the use of supercapacitor storage systems in urban rail transit oriented to the optimization of the energy saving and the reduction of the vehicle energy consumption, for whatever technological solutions are adopted.

The thesis is structured as follows:

Chapter One − In this chapter, after a brief introduction which lays the framework and the purpose of the research, the goal of the thesis is articulated and the objectives to be attained are presented. The main characteristics of urban rail transport modes and the related terminology are presented, in order to provide the reader with a better understanding of the subject and the relevant parameters.

Chapter Two − This section shows a comprehensive overview of the currently available technologies for recovery and management of braking energy in urban rail and, finally, it identifies the Supercapacitor storage technology as the most suitable that matches the performance requirements of the urban rail traction.

Chapter Three − In this section is presented the novel Lithium-ion Capacitor technology with a proposal of full-frequency high temperature model.

Chapter Four − This chapter presents the mathematical model of the entire urban railway network system, equipped with on-board or stationary Supercapacitor energy storage system. With reference to real data of a sample metro line network, a design methodology is assessed and finally some energy management *control strategies* are developed.

Chapter Five − The chapter outlines the methodology for assessing the achievable performances offered by the implementation of the proposed controls. The execution of wide experimental investigation on a laboratory reduced *scale model* of urban railway network, actually, has proved to be a

powerful tool for testing and validating the energy management control strategies.

Chapter Six – This final chapter presents the performed experimental test campaign conduced on the electromechanical scale model for confirming the validity and the effectiveness of the control techniques suggested on typical traction cycles. Therefore, an overall comparison among the different control strategies tested is carried out, as well as the energy saving improvement is highlighted. Finally, the conclusions and further requirements are drawn.

List of symbols and acronyms

a	Motion resistance 1$^{\text{st}}$ coefficient
b	Motion resistance 2$^{\text{nd}}$ coefficient
c	Motion resistance 3$^{\text{rd}}$ coefficient
C_{LiC}	Lithium ion Capacitor module equivalent capacitance
c_{line}	Per-unit length contact line capacitance
C_{sc}	Equivalent capacitance of supercapacitors
d	Maximum deceleration rate
D_{wh}	Railway vehicle wheel diameter
E_{kin}	Railway vehicle kinetic energy
E_{LiC}	Lithium ion capacitor module stored energy
$E_{LiC,max}$	Lithium ion capacitor module maximum storable energy
E_{line}	Contact line delivered energy
E_{loss}	System energy losses
E_{mech}	Railway vehicle mechanical energy delivered by electrical motors
E_{sc}	Supercapacitor energy stored
$E_{sc,max}$	Supercapacitor maximum storable energy
E_{sub}	Electrical substation delivered energy
$E_{sub}^{(BR)}$	Electrical substation delivered energy in case of dissipative braking
$E_{line}^{(BR)}$	Electrical substation delivered energy in case of dissipative braking
$E_{loss}^{(BR)}$	System energy losses in case of dissipative braking
f_{inv}	Modulation function of the PWM inverter
F_r	Total resistance force
F_t	Total traction effort
$F_{t,max}$	Maximum total traction effort
$F_{t,ref}$	Traction effort reference for field oriented control of the induction motors
i_{inv}	Railway vehicle DC-side inverter current
i_{LiC}	Lithium ion capacitor module actual current
$i_{LiC,\max}$	Lithium ion capacitor module maximum current
$i_{LiC,ref}$	Lithium ion capacitor module reference current
i_{line}	Current supplied by the contact line
$i_{line,ref}$	Reference set-point of the current supplied by the contact line
i_{sc}	Supercapacitor actual current
$i_{sc,\max}$	Maximum current of supercapacitors
$i_{sc,ref}$	Supercapacitor reference current
$i_{sd,ref}$	d-axis reference current for field oriented control of the induction motors
$i_{sd,\upsilon}$	d-axis symmetrical component of stator current of the υ-th motor
$i_{sq,ref}$	q-axis reference current for field oriented control of the induction motors

$i_{sq,\upsilon}$	q-axis symmetrical component of stator current of the υ-th motor
i_{sto}	Actual current of the storage system DC-DC converter
i_{sub}	Electrical substation output current
$i_{t,i}$	*i-th* railway vehicle load current
$i_{t,max}$	Maximum current of the railway vehicle
$J_{t,i}$	*i-th* railway vehicle equivalent rotating inertia
k_i	*i-th* railway vehicle mechanical and electrical losses coefficient
$k_{I,\,\omega}$	Integral constant speed regulator Reg_ω
$k_{I,i}$	Integral constant regulator Reg_i
$k_{I,L}$	Integral constant regulator Reg_L
$k_{I,u}$	Integral constant regulator Reg_u
$k_{I,v}$	Integral constant speed digital filter Reg_v
k_o	Proportional gain of the Luemberger observer
$k_{P,i}$	Proportional constant regulator Reg_i
$k_{P,L}$	Proportional constant regulator Reg_L
$k_{P,u}$	Proportional constant regulator Reg_u
$k_{P,v}$	Proportional constant speed digital filter Reg_v
$k_{P,\omega}$	Proportional constant regulator Reg_ω
k_T	Torque coefficient of the induction motor
L	Total length of an electrical section of the contact line
L'_r	Rotor phase inductance of the induction motor referred to the stator
L_f	Filter inductance of the DC-DC storage converter
l_{line}	Per-unit length contact line inductance
L_m	Self-inductance of induction motor
L_S	Substation transformer leakage inductance
L_s	Stator phase inductance of the induction motor
M	Number of supercapacitor modules connected in parallel
m_{sc}	Supercapacitor mass
$m_{t,e}$	*i-th* railway vehicle equivalent mass
$m_{t,i}$	*i-th* railway vehicle mass
N	Number of supercapacitor modules connected in series
p	Number of the pole pair of the induction motor
P_{inv}	Power drawn by the traction inverter
P_{LiC}	Power output of Lithium ion capacitor module
$P_{LiC,ref}$	Lithium ion capacitor unit reference power
P_{sc}	Power output of supercapacitors
$\tilde{P}_{sc,feed}$	Feed forward term of the supercapacitor reference power
$\tilde{P}_{sc}$	Compensating term of the supercapacitor reference power
$P_{sc,max}$	Maximum power of supercapacitors
$P_{sc,ref}$	Supercapacitor reference power
P_{sub}	Output power of the electrical substation
R'_r	Rotor phase resistance of the induction motor referred to the stator

r_{BR}	Braking rheostat resistance
r_{LiC}	Lithium ion capacitor module equivalent series resistance
r_{line}	Per-unit length contact line resistance
$R_{line,i}$	Equivalent variable line resistance of *i-th* rail track
R_0	Total value of the contact line resistance
R_s	Stator phase resistance of the induction motor
r_{sc}	equivalent resistance of supercapacitors
$\delta \hat{r}_{sc}$	Estimated variation of equivalent resistance of supercapacitors
r_{sub}	Electrical substation internal resistance
$T_{m,\nu}$	torque of ν-th induction motor
$T_{m,i}$	*i-th* railway vehicle equivalent motor torque
u_{LiC}	Lithium ion capacitor module internal voltage
$u_{LiC,ref}$	Lithium ion capacitor module reference internal voltage
$\hat{u}_{LiC}$	Lithium ion capacitor module estimated internal voltage
u_{sc}	Supercapacitor internal voltage
$u_{sc,ref}$	Supercapacitor reference internal voltage
$\hat{u}_{sc}$	Supercapacitor estimated internal voltage
v_{dc}	Railway vehicle DC-link inverter voltage
v_{LiC}	Lithium ion capacitor module terminal voltage
$V_{LiC,max}$	Maximum voltage of Lithium ion capacitor module
$V_{LiC,min}$	Minimum voltage of Lithium ion capacitor module
V_{line}	Voltage of the contact line
V_{line}	Reference value of the voltage of the contact line
$V_{m,max}$	maximum voltage of a single supercapacitor module
v_{sc}	Supercapacitor terminal voltage
$V_{sc,max}$	maximum voltage of supercapacitors
V_{sto}	Actual voltage of the storage system DC-DC converter
V_{sub}	Equivalent output voltage of electrical substation
$V_{sub,0}$	No-load voltage of electrical substation
$V_{t,i}$	*i-th* railway vehicle voltage at the pantograph
$v_{t,i}$	*i-th* railway vehicle speed
$v_{t,i,ref}$	*i-th* railway vehicle reference speed
$v_{t,max}$	Maximum speed of the railway vehicle
$\dot{v}_{t,max}$	Maximum acceleration rate
$\dot{\hat{v}}_{t,i}$	*i-th* railway vehicle estimated acceleration
$\hat{\omega}_{m,i}$	*i-th* railway vehicle estimated motor angular speed
$\dot{\hat{\omega}}_{m,i}$	*i-th* railway vehicle estimated motor angular acceleration
$x_{t,i}$	*i-th* railway vehicle reference abscissa along the track
y	Output of the current regulator of the DC-DC converter
α	Supercapacitor energy density

β	Regenerative braking energy share coefficient
η_{dcdc}	Rated efficiency of DC-DC converter
η_{em}	Rated efficiency of electrical motor
η_{inv}	Rated efficiency of traction inverter
η_{mech}	Rated mechanical efficiency
η_{sc}	Rated efficiency of supercapacitors
$\phi_{r,ref}$	Rotor flux reference for field oriented control of the motors
ρ	Reference command signal of the DC-DC converter
τ	Railway vehicle gearbox ratio
$\omega_{m,i}$	*i-th* railway vehicle actual motor angular speed
$\omega_{t,i}$	*i-th* railway vehicle wheel angular speed
BES	Battery Energy Storage
DAQ	Data Acquisiton
DSP	Digital Signal Processor
EDLC	Electric Double Layer Capacitor
EIS	Electrochemical Impedance Spectroscopy
EPR	Equivalent Parallel Resistance
ESR	Equivalent Series Resistance
ESS	Energy Storage System
FES	Flywheel Energy Storage
FOC	Field Oriented Control
LCSC	Line Current State Control
LiC	Lithium-Ion Capacitor
LRT	Light Rail Transit
LVTC	Line Voltage Tracker Control
MC	Motion Control
SC	Supercapacitor
SMES	Superconducting Magnetic Energy Storage
STC	Speed Tracker Control

List of figures

List of tables

Chapter 1

Review of Rail Urban Transit, Sustainable Transportation, and Energy Efficiency

Transport is responsible for about a quarter of Europe's greenhouse gas emissions, with 12.7% of the overall emissions generated by civil aviation, 13.5% by maritime transport, 0.6% by rail, 1.7% by inland navigation, and 70.8% by road transport [1].

The intrinsic advantage that rail has, of being able to source low-carbon electricity, means that journeys such as London to Brussels by train produce only around 10% of the emissions per passenger of a plane journey on the same route. In the European Commission's 2011 *Transport White Paper*, it has been set a target of reducing Green House Gas emissions from transport by at least 60 % by 2050 compared to 1990 levels. As a mode of transport with average specific emissions at least 3–4 times lower than road or air transport, the important role that rail transport can play in reaching the 2050 target is obvious, especially through a significant modal shift in the transportation of goods from road to rail [1].

Rail is also a vital part of public transportation, which consumes 3.7 times less energy per passenger transported in Europe than private car. The advantage of rail is its very low consumption of urban space and land.

All major European cities benefit from *urban rail networks*, which are the backbone of their urban transport systems, along with bus services feeding into these. These rail networks are composed of a combination of suburban and regional conventional rail lines, and metro, tram, and light rail networks. Generally, *public transport services* are coordinated with integrated ticketing and passenger information systems. These ensure the seamless and optimized use of the urban transport system.

Public transport in urban areas represents 21% of motorized mobility and is responsible for roughly 10% of transport-related greenhouse gas emissions, being already able to help cities to better manage their transport energy consumption and pollution. Today, between 40% and 50% of public transport is already powered by electricity. Public transport has thus already been a major and robust e-mobility provider for decades and is capable of further decreasing its carbon footprint [1].

Rail transport in urban areas is already running nearly exclusively on electricity. In the last ten years, passenger rail transport decreased its specific energy consumption by 22% [1].

Increasing public transit ridership, and even more so for urban rail systems, is becoming a priority for cities all over the world today. Urban rail transit ridership not only provides a funding mechanism to amplify the supply of such transit, but also creates an inherent social mark that travels throughout society. **Metro** and **light rail** systems have therefore been recognized as an essential instrument for setting up a new urban development and sustainable mobility paradigm.

Clearly, in these contexts, the *smart use* of resources through the efficient management of energy, both on-board and throughout the whole system, is a key point. As a result, more attention has been paid to issues related to the rationalization of electric consumption and energy savings through improving the *energy efficiency* of the entire urban electrified transportation system. In fact, the increase in power requested by rolling stock and the number of vehicles operating on urban rail tracks involves hard-working operating conditions for the existing electrical supply networks, with consequent overall increases in power losses and significant line voltage drops. Because the *energy efficiency* in an electrified transportation system is properly quantified by the total losses of its subsystems (electrical substations, overhead contact lines, electrical traction drives, etc...), there is an obvious need for new technical developments that both allow the subsystems to be exploited as efficiently as possible and permit an optimal energy management strategy for the power flows between the vehicles and the supply network. This is especially true when considering the fact that the energy consumption in electric railway systems is quite significant and represents an significant percentage of the overall operation costs.

As a consequence, new concepts concerning the use of the *regenerated braking energy* of vehicles have become increasingly important over the last few years.

Currently, in the scientific and industrial world, there is a strong belief that the use of *storage systems* might be a viable technical solution to compensate for the difference between the power available and the power required by loads, contributing decisively to improvements in system performance and the rationalization of consumption through an increase in *energy recuperation*.

From the electrified rail transport viewpoint, the use of *supercapacitor* technologies for storage devices, which may be onboard, located at substations, or distributed along the rail track, seems to be a powerful solution for effectively providing contemporaneous energy saving, energy efficiency, pantograph voltage stabilization, and peak regularization. More specifically, storage devices, suitably controlled by modern fast power converters, may play a fundamental role in facing the challenge of global energy savings, because they constitute some of the most promising alternatives to guarantee better performances in terms of power quality and reliability. These benefits have persuaded designers and energy distributors to upgrade actual electrical systems, because the capital costs show much reduced *payback* periods.

The benefits related to the adoption and operation of a supercapacitor-based storage system are, however, subject to the synergistic action of the individual devices and their complementary use. More specifically, the power flows in the system (to and from each device) must be carefully planned and controlled in accordance with a comprehensive management strategy and effective control architectures. The common goal required by the resulting control algorithms is to adjust the control action to respond adequately to multiple constraints and critical conditions (low state of charge, over-voltage, over-current) with a predetermined priority order.

Because of product-design confidentiality, any publications and advertisements for the energy storage products available from the companies operating in this transportation sector present mainly the advantages and only a few drawbacks. They do not mention in detail how to design, control, and connect the devices, or which power electronics interface is used to control the power flows with the electrified railway line. On the other hand, many of the articles recently published in the literature by independent research teams, who do not deal directly with the manufacturers, have considered issues that concern both the design and control strategies of energy storage devices for urban railway applications. Although the latter offer a wide range of technology solutions and types of controls, some of which are used in prototype installations, they do not

address in a complete, comprehensive, and organic way the topic of integrating the storage system with the main network that it supports. Above all, however, not all of the controls have been verified and validated by a careful series of experimental tests.

The objective of this thesis, as already mentioned in the outline, is to meet this need of analysis, by carrying out proposals of suitable control strategies for proper energy management of energy flows among the involved subsystems.
In this first introductory chapter, the goal of the research is articulated, by presenting and briefly describing the main characteristics of urban rail transport modes and the related terminology, in order to provide the reader with a better understanding of the subject and the relevant parameters.

1.1 Public Railway Transportation

Using railways as a means of transportation is a very old idea. When they began, railways were mainly utilized in central European mines, with different means of traction being applied. They did not come into general use until the invention of the steam engine. Since the 18th century, railway development has accelerated, until now, in the 21st century, it has become the most efficient means of transport for medium distances, thanks to the remarkable development of high speed service.
Railways have been playing a significant social role in ground-based mass public transportation. In spite of the discussion regarding its social role in the era of motorization in the latter half of the 20th century, electric railway systems are again growing in importance as a result of recent arguments on *energy saving* and environmentally friendly sustainability. In fact, globalization, climate change, and population growth require new and optimized transport systems.
A substantial advantage of electric railways compared to other modes of transportation is the use of electric energy, which allows the utilization of a variety of primary energy sources. This is also the reason for the recent intensive technical development of electric traction in the automobile industries, including hybrid and fuel-cell-based electric vehicle technologies. The increase in the ratio of electric traction to mechanical/petroleum traction is expected to contribute to a reduction in the carbon dioxide emissions due to transportation, and a consequent sustainable growth in mobility, as shown in Figure 1.1 .
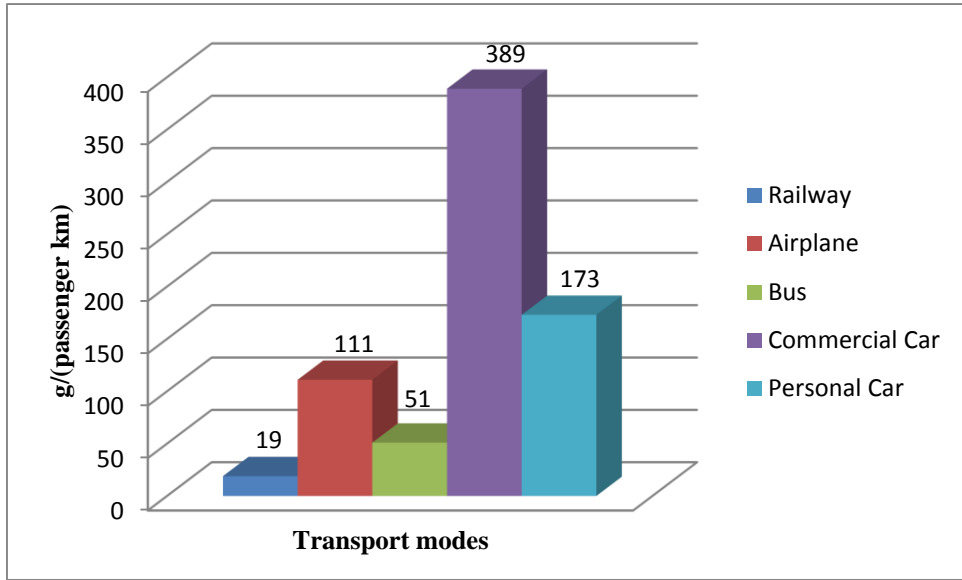
Figure 1.1 - CO$_2$ emissions of different modes of transport [18]

From this perspective, the prospects offered by public transport become crucial. *Public transportation* is, and should be, at the "heart" of any city today. For decades, people around the world have enjoyed public transportation's ability to offer reliable and timely transportation to various destinations in urban areas. Without it, cities such as Rome, New York, Tokyo, Beijing, and Amsterdam could not operate. A common misconception of public transit is the increased amount of time it takes to arrive at a specific destination compared to driving your own vehicle. When done right, public transit has the ability to be faster and timelier. Public transit has an inherent capability to transport more passengers in a shorter amount of time because of the travel demand of the system. This in turn can alleviate many traffic-induced problems (environmental impacts, congestion, photochemical smog, etc.). The problem that most cities run into today involves the ability to increase their public transit ridership levels. Focusing on a large segment of the public transit market, urban rail symbolizes the heart of any major public transport system, while buses, and even bicycles, can become the "veins" of the system due to their greater flexibility.

Cities all over the world are faced with the heavy capital costs of public infrastructure and are looking for answers about how to either pay for such service provisions, or find better alternatives. Governments around the world understand that policies and measures are needed, but at what level and to what extent?. While more automobile owners are commuting to work every year, the

24

increasing urban rail transit ridership as a means of decreasing highway congestion creates less strain on the environment, and enables a mechanism for cities to allocate funds toward increasing the urban public transportation infrastructure.

1.2 Definition and Classification of Public Transportation

As commonly defined, *transport* is the movement of people and goods from one place to another [2]. Evolving from human walking to high-speed rail, transportation (supply component), both the modes and infrastructure, has changed the way that society (demand component) reacts to movement. This innovation in technology creates flow patterns that shape the way society moves from point A to point B. As a result, overuse by people and the combination of mode and infrastructure create congestion. *Cascetta* suggested a basic model to describe how transport interacts with and affects specific trends as a basis for transport flows (Figure 1.2) [2]:

- **Demand** for transportation stems from the size of a city's population and the market environment, which affect the extent and volume of the stakeholders. People's choice of transit mode is a critical concern.
- **Transport** can include various modal choices to achieve the desired demand on the system. It is the system as a whole that moves freight and people by air, land, and sea.
- **Infrastructure** includes all the transport networks (roads, railways, canals, airways, etc.) and terminal nodes (seaports, railway stations, airports, etc.).
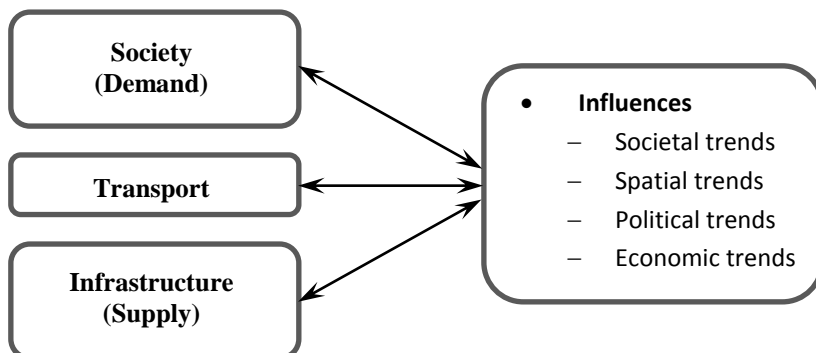
Figure 1.2 - Transport influence model [2].

"*Public transportation* (also called *transit*, *public transit*, or *mass transit*) is transportation by a conveyance that provides regular and continuing general or special transportation to the public, but not including school buses, charter or sightseeing services" [3]. Later, public urban rail transit will be presented in detail.

The various railway infrastructures, UNI-8379 (see Table 1.1) [4], differ depending on parameters such as the minimum frequency, average and maximum speeds, distance, and overall travel speed:

Railway: transport system for people and/or goods, even over long distances and for high traffic volumes, bound and guided along its own path, with circulation controlled by signals;

Urban or suburban rail service: transportation system that uses the routes of urban and suburban railway lines as a metropolitan tramway system for urban basins; the service extends a maximum of 50 *km* from the urban center;

Regional railway service: transportation system that uses urban and peri-urban railway lines with rhythmic services with a regional extension. To reduce travel times, often the stops classified as "urban" are not made, and so-called "gate stations" are used for exchanges with suburban rail systems and other vectors of local public transport. This service extends up to 150 *km* from the urban center;

Metro system: transport system for people with high flow and frequency rates consisting of driven and towed convoys in a constrained path, with circulation controlled by signals and completely independent from any other type of traffic;

Light metro: transport system for people with average flow rate and frequency, with driven and towed convoys in a constrained path, with movement controlled by signals and completely independent from any other type of traffic. Vehicles and trains have less capacity than traditional metro;

Tramway: transport system for people and/or goods in urban areas and/or metropolitan areas (suburban tramways), consisting of driven and towed convoys in constrained paths, generally on ordinary roads and therefore subject to the highway code, with circulation on sight;

Light Rail – Fast Tramway (LRT): tram system that allows higher revenue

Transportation System	Freq. min. (min)	Freq. max. (min)	Freq. avg. (min)	Distance stop/station (m)	Revenue Speed (km/h)	Carrying capacity min. (phpd)	Carrying capacity max. (phpd)	Carrying capacity avg. (phpd)	Convoy capacity (seats)	Convoy length (m)
Regional Rail serv.	22,5	30,0	15,0	1500 ÷ 4000	50 ÷ 85	3000	6000	4000	1500	200
Suburban Rail serv.	10,0	15,0	5,0	700 ÷ 2000	35 ÷ 50	6000	18000	9000	1500	200
Metro	4,0	5,0	3,0	600 ÷ 1000	25 ÷ 30	14400	24000	18000	1200	150
Light Metro	3,0	5,0	1,0	500 ÷ 800	25 ÷ 30	4800	24000	8000	400	80
Fast Tramway	4,0	5,0	3,0	350 ÷ 500	20 ÷ 25	2000	3600	2700	180	60
Tramway	7,5	10,0	5,0	200 ÷ 350	15 ÷ 20	1000	2200	1400	180	40

phpd: passengers per hour and per direction

Table 1.1 - Key features of urban transport systems

speeds and higher flow rates through measures to reduce interference with pedestrian and vehicular traffic. They are improperly called light metro systems: as seen before, a metro is light when using convoys with smaller capacities, but always remains in the metro system infrastructure.

The next paragraphs cover some background information about the metro and LRT systems, pointing out the main differences between them, so that the projects used for the purpose of this study may be applied to these systems.

1.2.1 Metro Systems

As briefly stated before, a *metro* can be defined a mass transit system with high capacity and frequency, consisting of driven motor vehicles and/or towed vehicles circulating on rail, or with other binding guides or completely separated from any other type of traffic, with the operation regulated by signals [4].

The *International Union of Public Transport* (UITP) defines a metro as "a tracked, electrically driven local means of transport, which has an integral, continuous track bed of its own (large underground or elevated sections)" [5]. Metros are totally independent from other traffic, road or pedestrian. They are consequently designed in tunnels, viaducts, or on the surface level, but with physical separation (see Figure 1.3). *Metropolitan railways* are the optimal public transport mode for a high-capacity line or network service. Some systems run on rubber-tires but are based on the same control-command principles as steel-wheel systems. In different parts of the world, metro systems are also known as the *Underground*, *Subway*, *Urban* or *Rapid Transit*, or *Tube*; the term metro best generalizes the various names used for the same type of transit system. In other words, a metro system is a fully segregated system. UITP notes that this results in a high degree of freedom for the choice of vehicle width and length, and thus a large carrying capacity (above 30,000 passengers per hour per direction–pphpd). The intervals between stations would typically be more than 1 km, and because the alignment does not have to follow existing streets, curve radii and section gradient can be more generously dimensioned and permit an overall higher commercial speed [6]. This large carrying capacity indicates the main difference between the metro and LRT systems. Therefore, UITP states that metro systems require heavier investments than LRT, and can be implemented only in large cities where the demand justifies the capital cost.

Figure 1.3 - View from metro system

In this work, the term *metro* is used wherever necessary, since the topic under examination for the research purposes could include systems consisting of elevated, at grade, and underground sections.

The volume of passengers that a metro train can carry is often quite high. Broadly classifying the public transportation systems for a large city as the bus transit system and rapid transit system (referring to the metro), it could be stated that the public transportation system stands on the metro system, where any disruption in the metro system might lead to the fall of the overall structure.

1.2.2   Light Rail Transit

Light rail transit (LRT) is a particular class of urban and suburban passenger railway that utilizes equipment and infrastructure that are typically less massive than that used for metro systems and heavy rail. As such, the main difference between LRT and metro systems is the mass of the utilized equipment and infrastructure. When a heavier mass of equipment and infrastructure is used, the cost of the system is higher, where one can broadly compare the costs of metro and LRT systems.

UITP defines LRT as a tracked, electrically driven local means of transport, which can be developed step by step from a modern tramway to a means of transport running in tunnels or above ground level [7]. Every development stage can be a final stage in itself. It should, however, permit further development to the next higher stage.

LRT systems are thus flexible and expandable. It is not absolutely necessary to have an independent bed track over the whole route; however, the highest degree of segregation from private traffic should be aimed for [6].

Figure 1.4 - View of light rail system

In this aspect, one of the differences between metro and LRT systems can be stated to be the concept of segregation. As previously mentioned, metro systems are fully segregated systems. In other words, metro systems operate fully independent from other traffic. However, LRT systems cannot be classified in this way. They are usually semi-segregated systems, although, as noted in the above statement, a highest degree of segregation from private traffic should be aimed in their development.

The term light rail is derived from the British English term *light railway long* used to distinguish tram operations from steam railway lines, as well as from its usually lighter infrastructure (see Figure 1.4).

LRT systems are almost universally operated by electricity delivered through overhead lines (see Figure 1.5). However, third rail systems have been coming into practice, where the trains use a standard third rail for electrical power.

Regarding the number of passengers carried within a comparable time period or per vehicle, the main difference between the LRT and metro systems is the passenger carrying capacity, where systems designed with less passenger capacity are considered to be "lighter." The speed of the vehicles may be another aspect in the classification of such systems. LRT systems can handle steeper inclines than heavy rail, and curves sharp enough to fit within street intersections (though this is hardly true for all light rail lines). They are typically built in urban areas, providing frequent service with small, light trains or single cars.

Figure 1.5 - Overhead contact wires to power light rail system

1.2.3   Tram Systems

A *tram* (also known as a *tramcar*, *streetcar*, *trolley*, or *trolley car*) is a rail vehicle that runs on tracks along public urban streets (called street running), and also sometimes on separate rights of way (see Figure 1.6). Trams powered by electricity, which were the most common type historically, were once called electric street railways. Trams also included horse-car railways, which were widely used in urban areas before electrification reached the world [8].

The length of an articulated tram vehicle reaches up to 30 m, and the capacity can reach more than 250 seats.

Advantages: low operating costs due to the low energy consumption (low rolling resistance), the absence of polluting emissions, medium-high capacity, possibility of working on both public streets and separate rights of way, and considerably lower investment costs than those of a metro system.

Disadvantages: The line feeding area has a strong negative impact from the visual point of view on the urban environment, and the tracks are "bound " to the rails.

The most common vehicle has 4–6 axes, a typical length of 13–21 m, a width of 2.3–2.8 m, a capacity of 150–250 passengers with 20%–40% of the seats, and a maximum speed of 60 km/h.

Figure 1.6 - View of tram system

In general, the guide is unidirectional, but bi-directional vehicles have recently come into operation in different cities. In addition, the latest research has focused on improving access to vehicles through the implementation of low loaders or raised docks, along with improving the overall appearance of the system through the use of information systems, the employment of intermodal nodes, services, and equipment at stops.

The electrical energy is always supplied by an overhead contact line and captured by a sliding pantograph on the top of the vehicle; the supply voltage is around 600 V DC. In certain cases, to improve performance and completely eliminate the visual impact of the airlines, the power has been taken from a so-called ground-level power supply, also known as surface current collection, which is a modern method of third-rail electrical pick-up for street trams, whose voltage is 750 V DC.

The main problems for these routes include the curvature limits of the track, and difficulties overcoming slopes due to the low adhesion values that result from iron-iron contact. Trams are often used as a form of local transit, making frequent stops. Thus, the most meaningful comparison of their advantages and disadvantages is with other forms of local transit, primarily local buses.

The most difficult distinction to draw is between LRT and streetcar or tram systems. There is a significant amount of overlap between the technologies, and it is common to classify streetcars/trams as a subtype of LRT, rather than as a distinct type of transportation. Two general versions are noted:

- The traditional type, where the tracks and trains run along the streets and share space with road traffic. Stops tend to be very frequent, but little

effort is made to set up special stations. Because space is shared, the tracks are usually visually fairly good.

- A more modern variation, where the trains tend to run along their own right of way and are often separated from road traffic. Stops are generally less frequent, and the vehicles are often boarded from a platform. Tracks are highly visible, and in some cases significant effort is expended to keep traffic away through the use of special signaling and even grade crossings with gate arms.

1.3   Sustainable Transportation

Today, there is an ever increasing emphasis on the environmental impacts of all public projects and decisions. Through the enhanced knowledge acquired by humans about the reactionary changes and degradation of planet earth that we continually see, sustainability continues to be of utmost importance.

Sustainability can be described using the common definition of the *Brundtland Reports* of 1987 as "development that meets the needs of the present without compromising the ability of future generations to meet their own needs." Based on this definition, *Munasinghe* created one of the most well known and adopted sustainable development icons: the "*Sustainable Development Triangle*" [9], with the perspective of what the earth may sustain in the future. A subsequent model from *Ralph P. Hall*, as shown in Figure 1.7 was created to depict what society can do to accomplish these tasks (conceptual factors). Here, sustainable development is conceptually broken down into three constituent parts: environmental protection, economic sustainability, and social justice [10].

Sustainable development's core theory is based on the knowledge of the need to increase the wellbeing of society, while at the same time decreasing the resource requirements to do so. The concern can be formulated from the degradation of the environment through the impacts of the production and consumption produced by the needs of the people. Ultimately, the sustainable development approach is the only approach that humans can take for future generations. Without it, the earth will be depleted of all its natural resources, and synthetic materials will be the only substances left. According to *Grin*, these choices involve a system of boundaries in time (25–50 years), space (micro- and macro-levels), and domain (social, economic, and environment) [11].
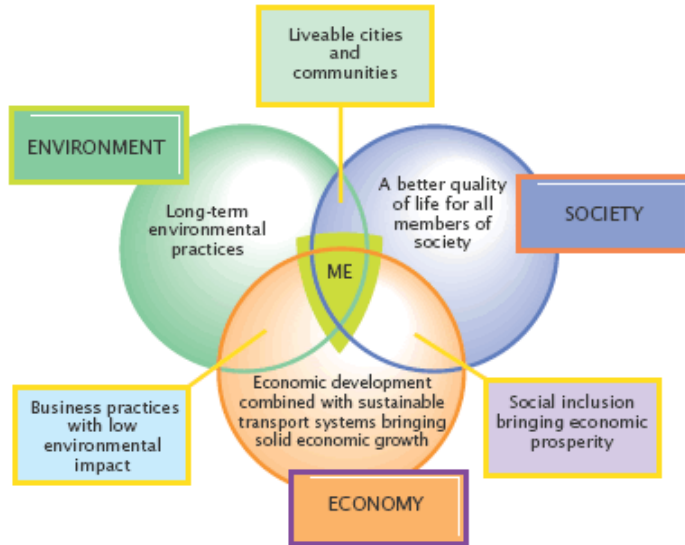
Figure 1.7 - Concept of sustainable development [10]

Sustainability continually plays a vital role in the implementation of rail transport. As countries look toward the future for sustainable transportation, electrified rail systems have provided a mode that does and will continue to use renewable energy. Studies have shown that rail is inherently more efficient than road transport, and coupled with renewable energy, it can provide a lasting source of mobility for future generations, while at the same time decreasing emission quantities.

There are, however, difficulties with the implementation of policies toward sustainable transit. As society increases, the demand on government follows. Basically, a balance between society and government to create and invest in sustainable transportation will prove to be the proper alignment. With this noted, governments need to start taking a conceded approach toward policies and measures that increase ridership through sustainable advances in transportation, with the help of society's participation.

Finally, after the analysis of this long introduction, it is clear that urban rail systems play a key role in the sustainable development of metropolitan areas for many reasons, but mainly because of their relatively low ratio between energy consumption and transport capacity. Nonetheless, in order to retain their environmental advantages over other transportation modes in an environment characterized by growing capacity demands and energy costs, significant improvements in energy efficiency must be achieved.

34

1.4 Energy Efficiency in Railway Systems

Energy efficiency is an issue of growing relevance for the competitive position of railway companies. The reputation of railways as the transport mode with the least environmental impact could dwindle in the future, with negative consequences both for railways' market share and for its standing in policy making. In addition, deregulation and privatization processes have increased the pressure on railway operators to be cost-effective and competitive within their networks.

There is a widespread consensus among experts that the energy saving potential in railways is large. Most rail operators have launched initiatives to exploit this potential in one field or another. Systematic approaches are rare, and the knowledge transfer of technologies for energy efficiency and the measures to be taken are often limited.

There is general agreement that there is considerable saving potential in railways, both in the short and long terms. Whereas technological improvements to rail vehicles will be rather incremental and require a long time for diffusion, there are many promising short- and medium-term saving strategies aimed at optimized control and the use of present technologies or operational improvements. Many of these require only minor investments in new technologies and often rely on "soft" factors such as training programs. The enhanced use of energy efficient driving strategies and regenerative braking are among the most promising measures. From a long-term perspective, the introduction of innovative traction technologies, integration of energy efficiency targets into vehicle strategies, and optimization of railways as systems will yield considerable further progress toward energy-efficient (and cost-effective) railway operations.

The creation of suitable framework conditions turns out to be as important as progress in research. This includes procurement strategies, along with well-defined financial interfaces between the functional divisions of railway companies. The payback and profitability strongly depend on scale effects reached within or outside railway markets, as well as on the future development of energy prices.

1.4.1 Energy Consumption of Trains

The energy demand of a rail vehicle can be split into four main categories, which are associated with the same losses:

➢ **Mechanical losses**: Mechanical power at the wheels is needed to overcome the different types of resistance confronted by the train (running resistance, inertia, and grade resistance).

➢ **Traction equipment losses**: The mechanical power is provided by traction equipment, with a certain consequent amount of heat loss.

➢ **Auxiliary services losses**: These include auxiliaries such as motor ventilation and compressed air production. Moreover, an appreciable share of the overall energy consumption is needed for passenger comfort (heating, lighting, toilets, etc.).

➢ **Supply line losses**: In the case of electric traction, part of the energy never reaches the vehicles, but is lost on the way from the electrical substation to the pantograph.

Figure 1.8 represents the energy flows in the most general situation for a DC-electrified railway system, typical of an urban rail system, where trains regenerate energy during braking (so-called regenerative or dynamic braking). This energy is fed back into the system and used again by other trains or by the braking trains themselves for their own auxiliary equipment consumption. The blue arrow "*Inertia and grade resistance*" is split into three arrows, one for the energy coming from the regenerative braking, one for the heat losses in the inverse traction chain, and one for the share of the energy that for technical or operational reasons could not be recuperated. If trains are not equipped with regenerative braking, the green-arrow energy feedback will not take place. All of the energy consumed by the trains will be delivered by the electrical substation rectifiers, and all of the energy used to overcome inertia and grade resistance will be converted into heat in the braking resistor and mechanical brakes. In Figure 1.8 the situation is shown for a train with regenerative braking.
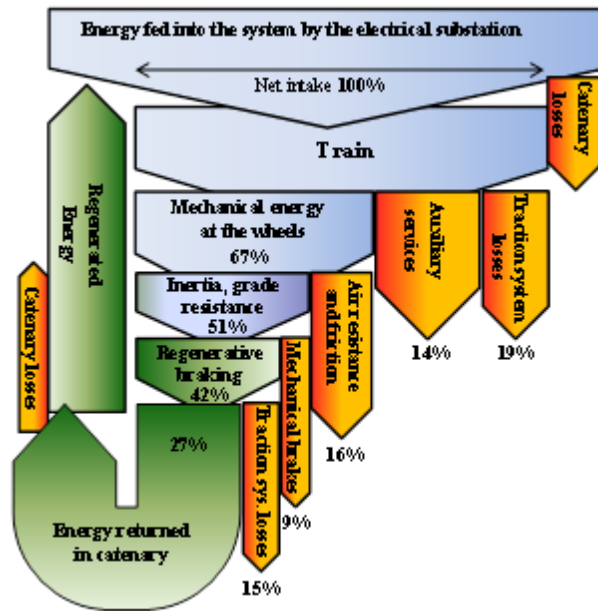
Figure 1.8 - Sankey diagram of energy flows for typical urban rail vehicle with regenerative braking

1.4.2 Mechanical Losses

Mechanical power at the wheels is needed to overcome the different types of resistance confronted by the vehicle (running resistance, inertia, and grade resistance).

Because the inertia and grade resistance are both proportional to the vehicle mass and are non-dissipative, their effects are in most cases treated as one. Hence, the energy invested in acceleration and uphill driving is not dissipated into heat but rather stored as kinetic and potential energy and can therefore be recovered to a large degree by regenerative braking (as far as electric or diesel-electric traction is concerned). The relative share of the total energy demand taken by inertia and grade effects is largely determined by the train mass, track topography, and number of stops.

As regards the motion power losses, these are mainly explained by the *Davis equation* (1.1), which includes numerous dissipative effects, different frictional forces of the wheel-track system, and air drag [12]:

$$P_{loss\_run} = \left(a + bv_t + cv_t^2\right)v_t \tag{1.1}$$

where the coefficients depend on the train design, and v_t represents the train speed. The coefficient a is mainly derived from the mechanical resistance (friction), whereas bv_t and cv_t^2 are derived from the air drag. These coefficients are usually given by train manufacturers and are not general constants but depend on the train (mass, length, etc.) and track characteristics (wheel-track adhesion, etc.).

The quadratic term is dominant in most cases. Its coefficient c can be expressed as follows:

$$c = \frac{1}{2}\rho_{air}A_f C_D \qquad (1.2)$$

where $A_f C_D$ is defined as the *air drag area*. It can be divided into two parts. One part is independent of the train length and depends mainly on the shape and size of the front and rear ends of the train. The other part increases approximately linearly with the train length.

The relative importance of the running resistance for the energy demand of train operation is strongly dependent on the speed pattern of the service. In a high-speed operation, where the average speeds are high and the typical distances between stations are long, the running resistance is the dominant quantity. This is almost exclusively because of the air drag. The track friction is generally small. It mainly depends on the train weight and, to a certain degree, on the curving radii of the track. In heavy freight trains, the wheel-track friction plays an important role in energy consumption.

1.4.3   Traction Equipment Losses

The mechanical energy required at the wheels is provided by *traction equipment*, which is fed electric energy from the catenary or uses diesel fuel. The induced conversion chains from the catenary or fuel tank to the wheel give rise to an additional energy consumption in the form of heat loss in the involved components and in auxiliaries such as fan equipment. For the sake of simplicity, reference is made only to the electric traction.

The energy is taken from the catenary to supply a complex conversion chain that eventually feeds the traction motors. Each of the involved components has a certain amount of heat loss. In order to prevent the equipment from overheating, auxiliary cooling devices are needed.

Modern electric rail vehicles are driven by AC induction motors, which are supplied by 3-phase variable voltage and variable frequency traction inverters. The supply systems differ in the way the DC current feeding these inverters is produced. The inverters are supplied by the catenary in the case of DC systems, by a transformer and rectifier in the case of AC power supply, and by an internal combustion engine with a generator in the case of diesel-electric traction. The efficiencies of rail vehicles' traction chains also differ between DC and AC supplied systems. State-of-the-art AC locomotives with 16.7-Hz, 15-kV systems typically have an overall efficiency of around 85% at maximum load. In 50-Hz and DC systems, the value is somewhat higher. The traction efficiency from the catenary to wheel and the efficiency of the inverse chain during braking are roughly the same.

As mentioned before, urban rail electrified systems usually employ DC-electrified catenary lines. This involves the use of several DC electrical substations placed along the tracks connecting the feeding lines to the main supply. This type of substation only allow power flows from the utility network to the railway system. This could be enough when trains in the system are designed only to draw power from the lines. Nowadays, many train models are equipped with *regenerative braking*. This kind of rolling stock is able to convert kinetic energy back into electrical energy during braking.

Generally, the electric traction equipment collects *commutatio*n and *conduction losses* in the vehicle converters and motors, both when energy is flowing from the electrical to the mechanical side and during regenerative braking. The first terms of the losses are quite independent from the motor current, and consequently from the delivered torque; while the latter depend on the traction drive current and tractive effort. There are several ways of modeling these losses, but considering the range of possible operating points of the traction motors, an accurate estimation of the traction power chain losses is proposed as follows [13]:

$$P_{loss\_tract} = \left| V_t I_{t,max} \frac{F_t(v_t)}{F_{t,max}(v_t)} \frac{1}{k} - F_t(v_t)v_t \right| \tag{1.3}$$

where V_t represents the voltage at the train pantograph; $I_{t,max}$ is the train current consumption for the maximum traction effort $F_{t,max}$; $F_t/F_{t,max}$ is the ratio between the actual traction effort and the maximum effort; and k represents a penalty factor, which assumes values between 0.55 and 1 as far as urban rail vehicles are

concerned. This term is representative of the efficiency of the traction chain, and its value could be evaluated by considering the current consumption curves given by motor manufacturers.

1.4.4 Auxiliary Services Losses

In general, this includes the *auxiliary energy* needed for the ventilation of traction motors and the traction converter cooling, but also includes the operation of the brake system for the vehicle (e.g., compressed air). As far as passenger vehicles are concerned, there is an additional energy demand to ensure passenger comfort, such as heating, lighting, and coach ventilation. This energy, which typically accounts for about 20% of the total energy consumption of a train, is supplied by the primary energy source used for traction (catenary or diesel) and delivered along the train by the auxiliary bus supply distribution.

1.4.5 Supply line losses

The energy needed to power a railway electrified system is produced and transmitted across a wide area. *Losses* in the electric supply system include conversion losses in substations, as well as losses in the supply lines and catenary. This situation highly depends on the characteristics of the individual supply system. Generally, losses decrease with higher voltages. DC systems with their rather low voltages have the biggest losses in the catenary.

Mainly, supply line losses consist of *Joule losses* in conductors, which are proportional to the impedance of the conductors and the square of the currents. In a DC electrical system with nodes from *1* to *N*, the power losses in the conductors may be calculated as follows [13]:

$$P_{loss\_line} = \sum_{i=1}^{N-1}\sum_{j=1}^{N}\left(V_i - V_j\right)^2\left(-\mathbf{G}_{ij}\right) \qquad (1.4)$$

where V_i is the voltage in a given node, and $\mathbf{G}_{ij}$ represents the element *i, j* in the nodal conductance matrix (equivalent to the nodal admittance matrix in an AC system), which defines the electrical conductance between nodes.

In this category of losses, it is appropriate to include those that occur on the *braking rheostat* when regenerative braking is not provided or cannot be performed (e.g., the system is not receptive).

1.4.6 Some Consideration about Energy Consumption

In Figure 1.8, it is clear that the inputs are represented by the energy delivered by substations (E_{sub}) and the regenerated energy (E_{reg}), defined as energy flowing from motors to the electrical side of the system from braking. The output is the energy consumed by the vehicles, which is decomposed into mechanical energy for traction, auxiliary equipment energy (E_{mech} and E_{aux}), the energy wasted in rheostats when the system is not receptive to regenerated energy (E_{BR}), and energy losses in line conductors (E_{sub}-E_{line}). Because the power must be balanced at every instant in the system, the energy relations may be defined as follows:

$$E_{sub} + E_{reg} = E_{mech} + E_{aux} + E_{line} + E_{BR} \tag{1.5}$$

In the following, a general relationship for the net energy intake for traction is reported.

If χ denotes the energy efficiency of the traction conversion chain of a vehicle (E_{mech}/E_{sub}), i.e., the percentage of the energy taken from the catenary that is actually converted into mechanical energy at the wheels, and β is the share coefficient of recoverable energy in braking, the net energy intake for traction (E_{mech}) during a given journey can be defined as follows:

$$E_{net,tract} = \frac{1}{\chi}\left(E_{kin+pot} + E_{run} + E_{aux}\right) - \chi\beta E_{kin+pot} \tag{1.6}$$

where $E_{kin+pot}$ the sum of inertia and grade energy required at the wheels, E_{run} is the energy required at the wheels to overcome the running resistance (mechanical friction + air drag), and E_{aux} is the energy needed for auxiliary service functions[1]. As mentioned earlier, the non-dissipative part ($E_{kin+pot}$) of this intake can be recovered by regenerative braking. Because the "backward" efficiency of the conversion chain is assumed to be χ as well, and the dynamic brake is only partly applied ($\beta < 1$), we get a recovered energy of $\chi\beta \, E_{kin+pot}$.

The principal strategies for saving energy can be derived from the aforementioned relationship. Each of the output quantities in Eq. (1.6) could be influenced to reduce the overall energy consumption:

➢ Reducing the **vehicle's mass** reduces $E_{kin+pot}$;

---

[1]This is based on the assumption that the efficiency of the conversion chain for comfort energy is the same as for traction. This is only approximately true, because the train bus supply is taken from the DC link, and so no DC/AC inverter and motor losses occur.

> ➢ Optimizing the vehicle's **aerodynamics** and **track friction** reduces E_{mech};

> ➢ Reducing the **conversion losses** in the driven car or EMU increases its energetic efficiency χ;

> ➢ Making **auxiliary functions** more efficient reduces E_{aux};

> ➢ Improving the vehicle's capacity to use **regenerative braking** or the catenary **receptivity** increases β.

These are the basic efficiency strategies that will be briefly discussed in the next section.

1.5   Energy Efficiency Strategies

Rolling stock has been continuously subject to design improvements. Hence, the trend for modern electric trains is to become increasingly efficient, but qualitative improvements in their performance cannot be easily and immediately achieved. Comprehensive studies on the different factors affecting the efficiency of rolling stock and some techniques to improve their efficiency are presented in [13–20]. This, together with a wide literature review on the topic of energy efficiency in urban metro transit systems reveal the following facts [21–51].

Weight is a crucial factor for the energy demand of a train, particularly in an urban rail operation, where phases with changes in motion are prevalent. In addition, the lower weight of the train itself permits a higher passenger load at a given axle load. New materials and lighter traction components still offer some potential in this field (aluminum and carbon-fiber materials can be used as car-body technologies) [21–22]. Apart from this component-based approach, the approach of system-based lightweight design aims at a weight-optimized solution for the whole system. This includes concepts such as articulated trains with Jacob-type bogies, as well as more innovative approaches such as curve-steered single-axle bogies or novel suspension technologies based on mechatronics [23–24].

In high-frequency passenger trains, **air resistance** is a key driver for energy consumption. The problem of producing aerodynamic designs for passenger trains has been addressed and these have been optimized for many years, getting

to the point that the potential for energy savings is practically exhausted [25]. Some details such as the design of the pantograph or the bogie coverage can still be optimized [26]. Covering trucks with smooth fairings is the most promising measure to reduce the air resistance of high-speed trains. In freight transport, there is a huge (theoretical) reduction potential to be exploited by covering open freight wagons and the introduction of a car order that is aerodynamically favorable in train formation.

By improving the **use of space** in the vehicles, more seats can be installed in a passenger train with only slight increases in the mass of train and air resistance. The result is a significant reduction in the energy consumption per seat. Both double-decked and wide-body train designs offer a quantum leap in overall energy efficiency. However, the compatibility with the infrastructure and the gauge requirements of interoperability pose strong limitations, especially on wide-body design. The replacement of locomotive-hauled trains with electrical multiple units (EMU) is the most promising common means to increase the number of seats per convoy length [27].

Regarding the **reduction of conversion chain losses** in electrical traction equipment, in recent years it has reached a technological level that is not far from the theoretical limits. An important milestone in this development was the replacement of the conventional SCR (silicon controlled rectifier) thyristor circuit technology with GTO (gate turn-off thyristor) converters and later IGBT (insulated gate bipolar transistor) technology, in order to provide better control algorithms, as well as simple paralleling of converter modules with consequent significant reductions in the weight, volume, and overall number of power semiconductor devices [28–29]. In future years, the promising silicon carbide (SiC) technology will push the limits of switching devices in three directions: higher blocking voltage, higher operating temperature, and higher switching speed [30].

However, at the present's state of the art, the **electric traction** components (AC asynchronous traction motors with IGBT inverters) are very reliable and mature and offer little potential for further energetic optimization. However, substantial short-term improvements can be realized by optimizing the control of these components and their interaction, e.g., by using an innovative modular multilevel converter (MMC), which is one of the emerging inverter topologies for high- or medium-voltage, transformer-less power conversion [31], and by

employing topologies with medium frequency transformers [32]. From the long-term perspective, quantum leaps in energy efficiency could be achieved by the next generation of traction components such as wheel-mounted drives (direct drives) employing permanent magnet synchronous motors [33] or transformers based on superconducting material [34].

If non-electric trains are considered, more prospects to optimize them from an energy point of view are incoming. Currently, several research efforts are being put into **hybridization**, optimal energy management in diesel-fuel powered trains, etc. [35–36]. Long-term options for replacing diesel traction range from natural gas engines to fuel cells [37].

Another relevant topic in relation to the energy efficiency of railway systems is **energy efficient driving** (or eco-driving). This covers a wide range of measures and approaches ranging from instructional and training programs for an "unaided" energy efficient driving style to sophisticated electronic driving advice systems. Studies in this field try to determine the speed and power profiles (driving strategy) that yield the minimum energy consumption for a given trip time. As a result, optimization problems evaluate the best driving strategies for a set of trip times, whereas modern **traffic flow management** based on telematics could offer a huge theoretical saving potential by smoothening speed profiles and avoiding stop-and-go driving in bottlenecks [38–42].

The energy consumption of **auxiliary services** represents a substantial part of the energy demand of passenger trains. The current degree of optimization of these systems is arguably much lower than that of the traction components, and the theoretical saving potential is accordingly high. Promising measures include the revision of temperature target values, intelligent adaptive control tools for air-conditioning, and a generalized use of waste heat from traction components [43–45].

Nowadays, one of the most effective techniques to improve the energy efficiency of modern urban rail vehicles is absolutely the enhancement of **energy recuperation** during dynamic braking. The actual recuperation rates are strongly influenced by the supply system and traffic density. While in most AC networks, the main barriers are non-technological, DC networks can be technologically upgraded to enhance recovery rates. The introduction of

regenerative braking represents a qualitative reduction in the energy consumption, both in AC and DC railway systems. In fact, modern rail vehicles have the ability to regenerate the braking energy into electrical energy. In that case, the electric motor can be configured to recover the mechanical energy produced by the vehicle's kinetic energy and then works as a generator producing electricity. In these vehicles, while a small portion of this kinetic energy can be reused to power the vehicle's auxiliaries, the remaining energy can be sent back into the network. Hence, it is recovered only if a vehicle is accelerating nearby (see Figure 1.9). In this case, the accelerating vehicle takes advantage of this energy transfer. If this is not the case, the network voltage increases as a result of the excess energy, and this extra energy has to be dissipated in braking resistors.

Given that numerous and frequent stops are a significant characteristic of urban rail operation, the recuperation of braking energy offers great potential to reduce the energy consumption of urban rail systems [46–90]. The importance and central role of this last topic will be further developed in the present work. The next section provides a comprehensive overview of the currently available strategies and technologies for the recovery and management of braking energy in urban rail transportation.

It should also be stated that important goals for energy efficient train operation should also come from **management and organization**. Procurement departments can provide additional incentives for manufacturers to produce energy efficient stock. Training programs and incentive systems may be set up to raise the awareness and motivation of personnel in relation to energy efficiency.

1.6   Enhancement in Use of Regenerative Braking Energy

Thanks to the current technologies, **regenerative braking** appears to be a very promising solution to reduce the energy consumption of electrified urban transport networks, as schematically depicted in Figure 1.9.

Generally speaking, the use of electric braking, also commonly known as dynamic braking, makes it possible to limit the use of friction braking systems during normal operation, which, by their nature, involve considerable costs for maintenance and the replacement of parts subject to wear.
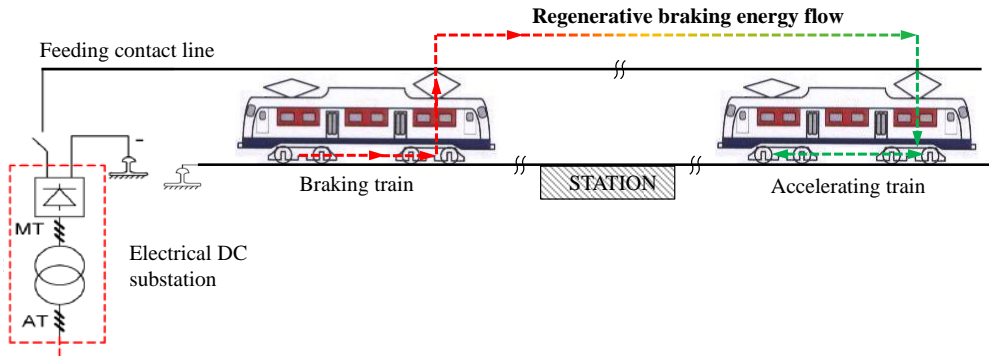
Figure 1.9 – Schematic representation of regenerative energy exchange in urban rail. (modified from [14])

This provides a technically advantageous way to solve the problem of braking when travelling downhill or making small reductions in speed, without any generation of dust, smell, heat, or noise. The use of electric motors in braking, as already mentioned, is also particularly favorable in both urban and suburban lines, which are characterized by the shortness of their individual path sections and high deceleration rates.

Usually in regenerative braking, the recovered energy is primarily used to supply the auxiliary and comfort functions of the vehicle itself.

However, in DC electrified rail networks, which are the most commonly used urban rail systems, the regenerated energy is not always accepted by the system if substations work in one power quadrant, and is hence wasted. This is because the system is, as is commonly said, "unreceptive." In fact, the network *receptivity* can be defined as the ratio of the total energy returned back to the line over the potential energy that could be regenerated in the braking process.

Several studies have shown that the application of regenerative braking in urban rail systems could potentially reduce their net energy consumption by 10%–42%, depending on the characteristics of the system (note that track gradients have a notable influence on the amount of energy that can be recovered) [13–14, 16, 20, 46–51]. Even though these studies have pointed out that this major part of the consumed energy could be fed back to the catenary, measurements show an actual recuperation of only 19%. Indeed, the effective ability of the power supply network to receive the recovered energy cannot be given for certain, mainly because of the significant randomness of the relevant parameters: the amount of recovered energy depends on the service frequency, train power

profile, electric network configuration, rolling stock, line voltage, track profile, length of feed sections, and train auxiliary power consumption.

By bearing in mind that the potential energy recovery strongly depends on the track profile (track gradients in particular) and frequency of the stops, and consequently it is fixed for every single system, an immediate operational method to improve the line receptivity is to increase the number of trains accelerating and braking simultaneously. Note that this assumes that the energy is provided to another vehicle in the vicinity, in the same electrical supply section, which only occurs if this vehicle is accelerating. Because there are limits to the increase in the frequency of circulating vehicles, related essentially to their headways, this situation is infrequent and often the remaining braking energy is dissipated by the braking (or ballast) rheostat or by mechanical braking.

Some techniques have been proposed to **maximize the use of the regenerated energy** and consequently minimize the use of on-board braking resistors. These improve the receptivity by making the energy interchange between vehicles easier (e.g., demanding energy at the same time that the braking energy occurs), by returning the regenerated energy to the utility supply grid, or by storing it in appropriate dedicated locations for later release.

The first approach, as said before, is related to the system operation and is based on **traffic control**, both at the individual vehicle level (e.g., train performance control in terms of speed and acceleration profiles and energy-efficient driving strategies) and at the fleet level (optimized scheduled timetables, coordination of individual cinematic profiles), along with on-line centralized traffic regulation [52–56].

The second option consists of equipping the traction substations with DC/AC inverters (**inverting**, **reversible,** or **active substations**), in order to pump back the regenerated energy into the primary supply network [57–62]. A reversible substation may either use thyristor-based rectifiers or active front ends, which have the additional feature of grid harmonics suppression. The greatest advantage of this option is that the primary AC network is naturally receptive and, as a result, all the regenerated energy may be potentially recovered. Conversely, the main drawback of this approach is related to the large cost of new equipment and the strong impact on the layout of existing substations. In

addition, the economic benefits of inverting substations strongly depend on the possibility to sell the energy to the public network operators and the price set by them, as well as restrictive power quality requirements.

As regards the latter approach, the use of **energy storage systems** (ESS) have been conceived as the main tool to improve energy efficiency in urban railway systems. The installation of energy storage devices both on-board the vehicle and at the traction substation or along the track, makes the supply network system perform better by combining the requirements of energy saving and comfort. Storage technologies and control schemes for ESS are constantly being improved under the influence of hybrid and pure electrical vehicles, which is leading to new possibilities for the railway sector. Moreover, the fast and outstanding development of power electronic converters has definitely enabled ESS to become an optimal alternative for the re-use of the regenerated braking energy in urban rail systems. In fact, nowadays, ESS are able to guarantee higher values of specific energy, higher values of specific power, longer life cycles, reduced environmental impact and costs, and better dynamic performances.
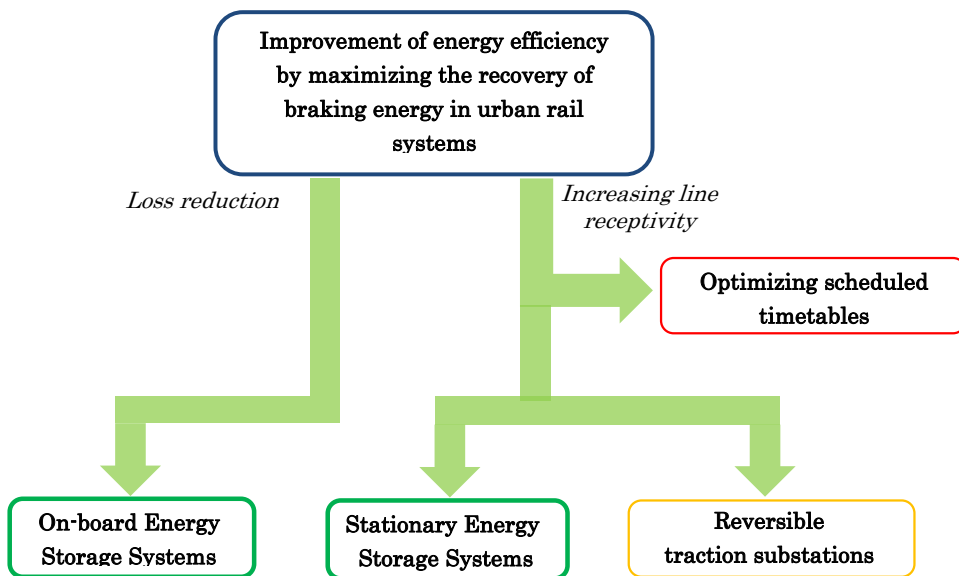
Figure 1.10 – Summary diagram of strategies for maximizing regenerative braking energy

48
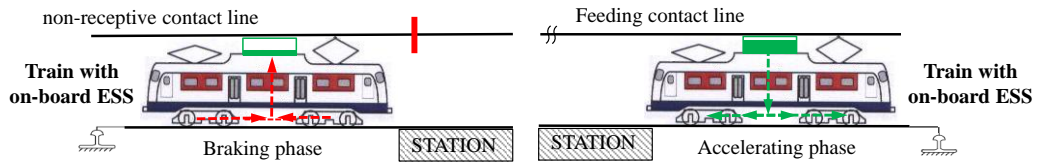
Figure 1.11 – Schematic operation of on-board ESS for urban rail vehicles (modified from [14])

The benefits, whatever the technological solutions adopted, are not only reductions in the total energy consumption, power peak, and demand, but voltage regulation, energy and power compensation, and the possibility for light railway vehicles to be independent of an external power supply. Some locations on the rail path cannot be electrified for aesthetic reasons, such as a city center, square, or tracks passing historical buildings, or where it is difficult to install overhead wires, such as on bridges, underground sections, and in tunnels. Finally, it is necessary to mention the decrease in the heat production in an underground environment associated with less intervention of the braking rheostat, which involves minor thermal loads in tunnels and stations.

The summary diagram shown in Figure 1.10, gives an immediate idea of the strategies already described.

As already mentioned, regarding the ESS implementation, two options are possible:

a) **Mobile** ESS (or so called **on-board** ESS), which consists of onboard ESS usually located on the vehicle roof. Every system works independently, and the recovered energy is directly sent to the storage system placed on the vehicle. When the vehicle accelerates, energy is used in priority from the ESS to propel the vehicle [63–74]. This principle is illustrated in Figure 1.11 ;

b) **Stationary** ESS (or also **wayside** ESS), consisting of one or several ESS placed at the feeding substation or along the tracks. These devices recover the excess energy when no other vehicle is receptive [75–90]. The principle is shown in Figure 1.12.

In order to prevent radical changes in the electrified railway line, the recovery of the electrical energy by means of storage devices is an extremely effective solution.
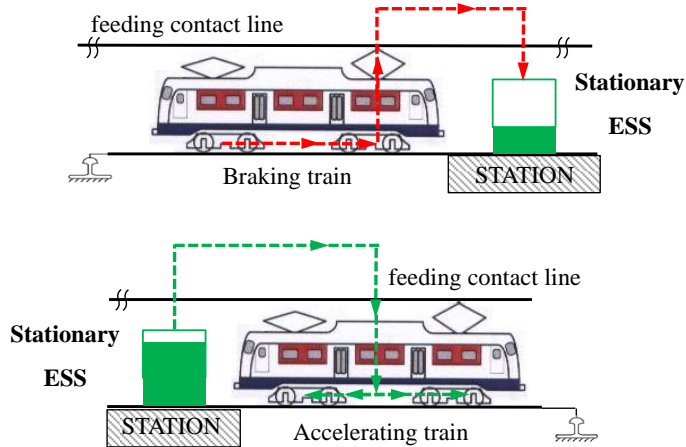
Figure 1.12 - Schematic operation of stationary ESS for urban rail applications (modified from [14])

To this end, several storage technologies have been developed over the last few years, namely **advanced electrochemical batteries**, **flywheels,** and **supercapacitors**. All of these devices have different performances and life-cycle costs. In urban railway applications, the power density and number of charge–discharge cycles are the most sought after requirements. Despite their high energy-density value, batteries have the problem of a limited number of load cycles. Therefore, flywheels and supercapacitors (SC) seem to be the most appropriate for this scope, because they have typical power densities of over 5 kW/kg, more than 10^6 cycles, and are easy to adapt to different voltages to configure in series or parallel stacks. At the present state of the art, both the implementations in the public transportation sector coming from the rolling stocks suppliers and the operators, and the interest of researchers, is highlighted by the many papers in the relevant literature on stationary and on-board applications to urban railway networks. These mainly discuss their intrinsic capability to save regenerative energy with a consequent increase in the energy saving of the systems. Neither the power supply nor the rolling stock requires substantial modifications in the first solution, but the energy management has to be extended at the network level, and lower efficiencies should be expected due to the energy travelling along the contact line.

The on-board solution overcomes these inconveniences but requires a redesign of the carriages to accommodate the storage device. In this case, only an SC can

be successfully used because of the practical limitation of flywheels in movable applications.

In any case, because it is a recent technology, in spite of the above-mentioned advantages of regenerative braking, the recovered energy is for the most part intended to be dissipated on the braking rheostats, and only a small portion of it is used to supply the auxiliary systems of vehicles or returned to the feeder line. A lack of experience in this area could cause operators and local authorities to miss an opportunity to invest in energy storage systems as a measure to increase the energy efficiency of urban rail.

In order to investigate the fast and outstanding development of ESS for both on-board and stationary applications and emphasize their potential benefits, the next chapter introduces and compares the storage technologies suitable for urban railway applications, pointing out the most recent advances in the area. A comprehensive overview of both on-board and stationary installations will be described with a discussion of their advantages and drawbacks. Finally, the SC storage technology will be identified as the most suitable option for ESS in urban rail transportation in general.

1.7   Chapter 1 references

[1] ERRAC, The European Rail Research Advisory Council Rail route 2050: The Sustainable Backbone of the Single European Transport Area. Available on-line: http://www.errac.org/wp-content/uploads/2013/11/D9-SRRA-RAILROUTE2050.pdf, (accessed 2014).

[2] Cascetta, E. Modelli per i sistemi di trasporto. Teoria e applicazioni. *UTET Università*, 2006.

[3] APTA, Resource Library: Fact Book Glossary, (Online). Available: http://www.apta.com/resources/statistics/Pages/glossary.aspx, (accessed 2013).

[4] UNI 8379. Sistemi di trasporto a guida vincolata (ferrovia, metropolitana, metropolitana leggera, tranvia veloce e tranvia) - Termini e definizioni. 2000.

[5] UITP, International Association of Public Transport. Metro. http://www.uitp.org/Public-Transport/metro/index.cfm, (accessed 2013).

[6] ERRAC, The European Rail Research Advisory Council. Light Rail and Metro Systems in Europe – Current market, perspectives and research implication, Brussels,

April 2004. Available: http://www.vialibre-ffe.com/PDF/errac%20metro%20y%20fcligero%2004.pdf, (accessed 2013).

[7] UITP, International Association of Public Transport. Light Rail. http://www.uitp.org/Public-Transport/ light-rail/index.cfm, (accessed 2013).

[8] Post, R. C. Urban Mass Transit: The Life Story of a Technology. *Greenwood Publishing Group*, 2007.

[9] Munasinghe, M. Environmental Economics and Sustainable Development, *World Bank, Washington D.C.*, 1997.

[10] UITP, International Association of Public Transport. Sustainable development. http://www.uitp.org/Public-Transport/sustainabledevelopment/, (accessed 2013).

[11] Grin, J.; Rotmans, I.; Schot, J. Transitions to Sustainable Development: New Directions in the Study of Long Term Transformative Change. *Routledge*, 2009.

[12] Perticaroli, F. Electric Systems for Transportation. (in Italian), *Casa Editrice Ambrosiana*, Milan, Italy, 2001.

[13] López-López T.J.; Pecharromán R.R.; Fernández-Cardador A.; Cucala A.P. Assessment of energy-saving techniques in direct-current-electrified mass transit systems. *Transportation Research Part C: Emerging Technologies*, vol. 38, Jan. 2014, pp. 85-100.

[14] González-Gil, A.; Palacin, R., Batty, P. Sustainable urban rail systems: Strategies and technologies for optimal management of regenerative braking energy. *Energy Conversion and Management*, vol. 75, 2013, pp. 374-388.

[15] Nolte, R. Evaluation of Energy Efficiency Technologies for Rolling Stock and Train Operation of Railways. *Institut fur Zukunftsstudien und Technologiebewertung IZT*, Berlin, Mar. 2003.

[16] Gunselmann W. Technologies for increased energy efficiency in railway systems. *Proc. 11th Eur. Conf. Power Electron. and Appl. EPE2005*, Dresden, Germany, 11-14 Sept. 2005.

[17] Ogasa M. Energy saving and environmental measures in railway technologies: Example with hybrid electric railway vehicles. *IEEJ Trans. Electrical and Electronic Engineering*, vol. 3 (1), Jan. 2008, pp. 15-20.

[18] Koseki, T. Technologies for saving energy in railway operation: general discussion on energy issues concerning railway technology. *IEEJ Trans. Electrical and Electronic Engineering*, vol. 5 (3), May 2010, pp. 285–290.

[19] Kondo K. Recent energy saving technologies on railway traction systems. *IEEJ Trans. Electrical and Electronic Engineering*. Vol. 5 (3), May 2010, pp. 298-303.

[20] Falvo, M.C.; Lamedica, R.; Bartoni, R.; Maranzano, G. Energy management in metro-transit systems: an innovative proposal toward an integrated and sustainable urban

mobility system including plug-in electric vehicles. *Electric Power Systems Research,* vol. 81 (12), Dec. 2011, pp. 2127–2138.

[21] Seo, S.I.; Kim, J.S.; Cho, S.H. Development of a hybrid composite bodyshell for tilting trains. *Proc. Inst. Mech. Eng. Pt. F: J Rail Rapid Transit,* vol. 222 (1), 2008, pp. 1-13.

[22] Kim, J.S.; Lee, S.J.; Shin, K.B. Manufacturing and structural safety evaluation of a composite train car body. *Composite Structures*, vol. 78 (4), June 2007, pp. 468-476.

[23] Xue, X.; Ingleton, S.; Roberts J.; Robinson, M. Qualitative comparison of the characteristics of articulated and non-articulated trains and their effects on impact. *Proc. Inst. Mech. Eng. Pt. F: J Rail Rapid Transit*, vol. 225 (1), Jan. 2011, pp. 24-37.

[24] Goodall, R.M.; Kortüm, W. Mechatronic developments for railway vehicles of the future. *Control Eng. Pract.*, vol. 10 (8), Aug. 2002, pp. 887-898.

[25] Tabares, A. F.; Gómez, N.; Nieto, C.; Giraldo, M. Critical Sources of Aerodynamic Resistance in a Medium Distance Urban Train: a CFD approach. *Revista Científica Guillermo de Ockham*, vol. 11 (1), June 2013, pp. 111-124.

[26] Ikeda, M.; Mitsumoji, T.; Sueki, T.; Takaishi, T. Aerodynamic noise reduction in pantographs by shape-smoothing of the panhead and its support and by use of porous material in surface coverings. *Quarterly Report of RTRI (Railway Technical Research Institute)*, vol. 51 (4), 2010, pp.220-226.

[27] Andersson, E.; Kottenhoff, K.; Nelldal, B. Extra Wide-body Passenger Trains in Sweden – background and introduction. *Proc. of the World Congress of Railway Research WCRR 2001*, Cologne, Germany, 2001.

[28] Hillmansen, S. Sustainable traction drives. *IET seminar digest*, 2009, pp. 255-265.

[29] Eckel, H.; Bakran, M.M.; Krafft, E.U.; Nagel, A. A new family of modular IGBT converters for traction applications. *Proc. 11ᵗʰ Eur. Conf. Power Electron. and Appl. EPE 2005*, Dresden, Germany, 11-14 Sept. 2005.

[30] Ladoux, P.; Mermet, M.; Casarin, J.; Fabre, J. Outlook for SiC devices in traction converters. *Proc. 2ⁿᵈ Int. Conf. Electrical Systems for Aircraft, Railway and Ship Propulsion ESARS 2012*, Bologna, Italy, 18-20 Oct. 2012.

[31] Coppola, M; Del Pizzo, A.; Iannuzzi, D. A power traction converter based on modular multilevel architecture integrated with energy storage devices. *Proc. 2ⁿᵈ Int. Conf. Electrical Systems for Aircraft, Railway and Ship Propulsion ESARS 2012*, Bologna, Italy, 18-20 Oct. 2012.

[32] Hoffmann, H.; Piepenbreier, B. High voltage IGBTs and medium frequency transformer in DC-DC converters for railway applications. *Proc. 20ᵗʰ Int. Symp. Power Electronics Electrical Drives Automation and Motion SPEEDAM 2010*, Pisa, Italy, 14-16 June 2010, pp. 744-749.

[33] Frenzke, T.; Piepenbreier, B. Position-sensorless control of direct drive permanent magnet synchronous motors for railway traction. *35th Annual Power Electronics Specialists Conf. 2004. PESC 2004*, vol. 2, Aachen, Germany, 20-25 June 2004, pp. 1372-1377.

[34] Hata, H.; Kamijo, H.; Nagashima, K.; Ikeda, K. Development of superconducting transformer for railway traction. *Proc. Int. Conf. Electrical Systems for Aircraft, Railway and Ship Propulsion ESARS 2010*, Bologna, Italy, 19-21 Oct. 2010.

[35] Hillmansen, S.; Roberts, C. Energy storage devices in hybrid railway vehicles: a kinematic analysis. *Proc. Inst. Mech. Eng. Pt. F: J Rail Rapid Transit*, vol. 221 (1), 2007, pp. 135–143.

[36] Ogawa, K.; Yamamoto, T.; Hasegawa, H.; Furuya, T. Development of the fuel-cell/battery hybrid railway vehicle. *Proc. 5th IEEE Vehicle Power Propulsion Conf. VPPC 2009*, Dearborn, MI, USA, 7-10 Sept. 2009, pp. 1730–1735.

[37] Destraz, B.; Barrade, P.; Rufer, A. Power assistance for diesel-electric locomotives with supercapacitive energy storage. *Proc. IEEE 35th Annual Power Electronics Specialists Conf. PESC 2004*, vol. 1, Aachen, Germany, 20-25 June 2004, pp. 677-682.

[38] Bocharnikov, Y.V.; Tobias, A.M.; Roberts, C.; Hillmansen, S.; Goodman, C.J. Optimal driving strategy for traction energy saving on DC suburban railways. *IET Electric Power Applications*, vol. 1 (5), Sept. 2007, pp. 675–682.

[39] Dominguez, M.; Fernandez, A.; Cucala, A.P.; Lukaszewicz, P. Optimal design of metro automatic train operation speed profiles for reducing energy consumption. *Proc. Inst. Mech. Eng. Pt. F: J Rail Rapid Transit*, vol. 225 (5), Sept. 2011, pp. 463–473.

[40] Sicre, C.; Cucala, P.; Fernández-Cardador, A.; Jiménez, J.A.; Ribera, I.; Serrano, A. A method to optimise train energy consumption combining manual energy efficient driving and scheduling. *WIT Trans. Built Environment,* vol. 114, Sept. 2010, pp. 549–560.

[41] Lin, W.M.; Sheu, J. Optimization of train regulation and energy usage of metro lines using an adaptive-optimal-control algorithm. *IEEE Trans. Automation Science & Engineering*, vol. 8 (4), Oct. 2011, pp.855–864.

[42] Miyatake, M.; Ko, H. Optimization of train speed profile for minimum energy consumption. *IEEJ Trans.Electrical and Electronic Engineering*, vol. 5 (3), May 2010, pp. 263–269.

[43] Kokken, K. The reduction of energy consumption in EMU-trains of NS. *World Congress on Railway Research*, Edinburgh, 2003.

[44] Amri, H.; Hofstädter, R.N.; Kozek, M. Energy efficient design and simulation of a demand controlled heating and ventilation unit in a metro vehicle. *IEEE forum on integrated and sustainable transportation systems FISTS 2011*, Vienna, Austria, 29 June -1 July 2011, pp. 7-12.

[45] Beusen, B.; Degraeuwe, B., Debeuf, P. Energy savings in light rail through the optimization of heating and ventilation. *Transportation Research Part D: Transport and Environment*, Vol. 23, August 2013, pp. 50-54.

[46] Adinolfi, A., Lamedica, R.; Modesto, C.; Prudenzi, A.; Vimercati S. Experimental assessment of energy saving due to trains regenerative braking in an electrified subway line. *IEEE Trans. Power Delivery*, vol. 13 (4), Oct. 1998, pp. 1536-1542.

[47] Bae, C.; Jang, D.; Kim, Y.; Chang, S.; Mok, J. Calculation of regenerative energy in DC 1500V electric railway substations. *Proc. 7th Int. Conf. Power Electronics ICPE 2007*, Daegu, South Korea, 22-26 Oct. 2007, pp. 801-805.

[48] Foiadelli, F.; Roscia, M., Zaninelli, D. Optimization of storage devices for regenerative braking energy in subway systems. *Proc. IEEE Power Engineering Society General Meeting PES 2006*, Montreal, QC, Canada, 18-22 June 2006.

[49] Lee, C.K., Kim, D.H.; Jun, W.S. Study on the energy saving running technology and its CO_2 reduction effect of railway vehicle. *Proc. 9th World Congress on Railway Research WCRR 2011*, Lille, France, 22-26 May 2011.

[50] Ticket to Kyoto. Overview of braking energy recovery technologies in the public transport field. WP2B Deliv. 1, March 2011 http://www.tickettokyoto.eu/sites/default/files/download/file/T2K_WP2B_deliverable1_20110520.pdf, (accessed November 2012).

[51] Borrelli, A.; Ciccarelli, F.; Fusco, L. The new electric trains of the Circumvesuviana srl. *Ingegneria Ferroviaria*, vol. 66 (2), Feb. 2011, pp.141-163.

[52] Albrecht, T. Reducing power peaks and energy consumption in rail transit systems by simultaneous train running time control. *Proc. 9th Int. Conf. Computers in Railways IX COMPRAIL IX*, vol.15, Dresden, Germany, 17-19 May 2004, pp. 885–894.

[53] Chen, J.F., Lin, R.L.; Liu, Y.C. Optimization of an MRT train schedule – reducing maximum traction power by using genetic algorithms. *IEEE Trans. Power Syst.*, vol. 20 (3), Aug. 2005, pp. 1366–1372.

[54] Nasri, A.; Fekri Moghadam, M.; Mokhtari, H. Timetable optimization for maximum usage of regenerative energy of braking in electrical railway systems. *Proc. 21st Int. Symp. Power Electron., Elect. Drives, Automation and Motion SPEEDAM 2012,* Pisa, Italy, 14-16 June 2010, pp. 1218-1221.

[55] Peña-Alcaraz, M.; Fernández, A.; Cucala, A.P.; Ramos, A.; Pecharromán, R.R. Optimal underground timetable design based on power flow for maximizing the use of regenerative-braking energy. *Proc. Inst. Mech. Eng. Pt. F: J Rail Rapid Transit,* vol. 226 (4), July 2012, pp. 397-408.

[56] Yang, X.; Ning, B., Li, X.; Tang, T.; Song, X.A. Subway timetable optimization model for maximizing the utilization of recovery energy. *Proc. Joint Rail Conference JRC 2013*, Knoxville, TN, USA, 15-18 April 2013.

[57] Ortega, J.M., Ibaiondo, H. Kinetic energy recovery on railway systems with feedback to the grid. *Proc. 14th Int. Conf. Power Electronics and Motion Control EPE-PEMC 2010*, Ohrid, Macedonia, 6-8 Sept. 2010, pp. T9-94-T9-97.

[58] Gelman, V. Braking energy recuperation. *IEEE Vehicular Technology Magazine*, vol. 4 (3), Sept. 2009, pp. 82-89.

[59] Mellitt, B., Mouneimne, Z.S., Goodman, C.J. Simulation study of DC transit systems with inverting substations. *IEE Proc. B Electric Power Applications*, vol. 131 (2), Mar. 1984, pp.38-50.

[60] Yii-Shen, T.; Ruay-Nan, W.; Nanming, C. Electric network solutions of DC transit systems with inverting substations, *IEEE Trans. Vehicular Technology,* vol. 47 (4), Nov 1998, pp.1405-1412.

[61] Cornic, D. Efficient recovery of braking energy through a reversible dc substation. *Proc. Int. Conf. Electrical Systems for Aircraft, Railway and Ship Propulsion ESARS 2010* , Bologna, Italy, 19-21 Oct. 2010.

[62] Takagi, R. Energy saving techniques for the power feeding network of electric railways. *IEEJ Trans. Electrical and Electronic Engineering*, vol. 5 (3), May 2010, pp. 312-316.

[63] Steiner, M.; Scholten, J. Energy storage on board of railway vehicles. *Proc. 11th Eur. Conf. Power Electron. and Applicat. EPE 2005*, Dresden, Germany, 11-14 Sept. 2005.

[64] Steiner, M., Klohr, M.; Pagiela, S. Energy storage system with ultracaps on board of railway vehicles. *Proc. 12th Eur. Conf. Power Electron. and Applicat. EPE 2007*, Aalborg, Denmark, 2-5 Sept. 2007.

[65] Barrero, R.; Tackoen, X.; Van Mierlo, J. Energy saving in public transport: enhanced energy storage systems for improved on-board light rail vehicle efficiency, *IEEE Vehicular Tech. Magazine*, vol. 3 (3), Sept. 2008, pp. 26-36.

[66] Allègre, A.L., Bouscayrol, A.; Delarue, P.; Barrade, P.; Chattot, E.; El-Fassi, S. Energy storage system with supercapacitor for an innovative subway, *IEEE Trans. Ind. Electron.*, vol. 57 (12), Dec. 2010, pp. 4001-4012.

[67] Iannuzzi D. Improvement of the energy recovery of traction electrical drives using supercapacitors. *Proc. 13th Int. Power Electronics and Motion Control Conference EPE-PEMC 2008*, Poznan, Poland, 1-3 Sept.r 2008, pp. 1469-1474.

[68] Iannuzzi, D., Tricoli, P. Metro trains equipped onboard with supercapacitors: a control technique for energy saving. *Proc. 20th Int. Symp. Power Electron., Elect. Drives, Automation and Motion SPEEDAM 2010*, Pisa, Italy, June 14-16, 2010, pp. 750-756.

[69] Iannuzzi, D.; Tricoli, P. Optimal control strategy of onboard supercapacitor storage system for light railway vehicles. *Proc. IEEE Int. Symp. Industrial Electronics ISIE 2010*, Bari, Italy, 4-7 July 2010, pp.280-285.

[70] Iannuzzi, D.; Tricoli, P. Supercapacitor state of charge control based on changeover finite state controller for metro-train applications. *Proc. 3rd Int. Conf. on Clean Electrical Power ICCEP 2011*, Ischia, Italy, 14-16 June 2011, pp. 550-556.

[71] Iannuzzi, D.; Tricoli, P. Speed-based State of Charge Tracking Control for Metro-Trains with Onboard Supercapacitors. *IEEE Trans. on Power Electronics*, vol. 27 (4), Apr. 2012, pp. 2129-2140.

[72] Ciccarelli, F.; Iannuzzi, D.; Tricoli, P. Speed-based supercapacitor state of charge tracker for light railway vehicles. *Proc. 14th Eur. Conf. Power Electronics and Applications EPE 2011*, Birmingham, UK, Aug. 30 – Sept. 1, 2011.

[73] Ciccarelli, F., Iannuzzi, D.; Tricoli, P. Control of metro-trains equipped with onboard supercapacitors for energy saving and reduction of power peak demand. *Transportation Research Part C: Emerging Technologies*, vol. 24, Oct. 2012, pp. 36-49.

[74] Iannuzzi, D.; Pagano, E.; Tricoli, P.. The use of energy storage systems for supporting the voltage needs of urban and suburban railway contact lines. *Energies*, vol. 6 (4), Apr. 2013, pp. 1802-1820.

[75] Rufer, A.; Hotellier, D.; Barrade, P. A Supercapacitor-based energy storage substation for voltage compensation in weak transportation networks. *IEEE Trans. Power Delivery*, vol. 19 (2), Feb. 2004, pp. 629-636.

[76] Brenna, M.; Foiadelli, F.; Tironi, E.; Zaninelli, D. Ultracapacitors application for energy saving in subway transportation systems. *Proc. Int. Conf. Clean Electrical Power ICCEP 2007*, Capri, Italy, 21-23 May 2007, pp. 69-73.

[77] Morita, G.; Konisihi, T.; Hase, S.; Nakamichi, Y.; Nara, H.; Uemura, T. Verification tests of electric double layer capacitors for static energy storage system in DC electrified railway. *Proc. 19th Int. Symp. Power Electron. Elect. Drives, Automation and Motion SPEEDAM 2008*, Ischia, Italy, 11-13 June 2008, pp. 1017-1022.

[78] Barrero, R.; Tackoen, X.; Van Mierlo, J. Improving energy efficiency in public transport: stationary supercapacitor based energy storage systems for a metro-network. *Proc. Vehicle Power Propulsion Conf. VPPC 2008*, Harbin, China, 3-5 Sept. 2008.

[79] López-López, A.J.; Pecharromán, R.R., García-Matos, J.A.; Fernández-Cardador, A.; Cucala, A.P. Optimal deployment of energy storage systems in a dc-electrified railway system. *WIT transactions on the built environment*, vol. 127, 2012, pp. 603-614.

[80] Ciccarelli, F.; Iannuzzi, D.; Lauria, D.; Supercapacitors-based energy storage for urban mass transit systems. *Proc. 14th Eur. Conf. Power Electronics and Applications EPE 2011*, Birmingham, UK, 30 Aug. – 1 Sept. 2011.

[81] Iannuzzi, D.; Pighetti, P.; Tricoli, P. A study on stationary supercapacitor sets for voltage droops compensation of streetcar feeder lines. *Proc. Int. Conf. Electrical Systems for Aircraft, Railway and Ship Propulsion ESARS 2010*, Bologna, Italy, 19-21 Oct. 2010.

[82] D'Avanzo, S.; Iannuzzi, D.; Murolo, F.; Rizzo, R.; Tricoli, P. A sample application of supercapacitor storage systems for suburban transit. *Proc. Int. Conf. Electrical Systems for Aircraft, Railway and Ship Propulsion ESARS 2010*, Bologna, Italy, October 19-21, 2010.

[83] Ciccarelli, F.; Iannuzzi, D.; Lauria, D. Stationary ultracapacitors storage device for improving energy saving and voltage profile of light transportation networks. *Transportation Research Part C: Emerging Technologies*, vol. 21 (1), Jan. 2012, pp. 321-337.

[84] Battistelli, L.; Ciccarelli, F.; Lauria, D.; Proto, D. Optimal design of DC electrified railway Stationary Storage System. *Proc. 2nd Int. Conf. Clean Electrical Power ICCEP 2009*, Capri, Italy, June 9-11, 2009, pp. 739-745.

[85] Iannuzzi, D.; Lauria, D.; Tricoli, P. Optimal Design of Stationary Supercapacitors Storage Devices for Light Electrical Transportation Systems. *Journal of Optimization and Engineering*, vol. 13 (4), Dec. 2012, pp. 689-704.

[86] Battistelli, L.; Fantauzzi, M.; Iannuzzi, D.; Lauria, D. Energy management of electrified mass transit systems with Energy Storage devices. *Proc. 21st Int. Symp. Power Electron., Elect. Drives, Automation and Motion SPEEDAM 2012*, Sorrento, Italy, 20-22 June 2012, pp. 1172-1177.

[87] Battistelli, L.; Fantauzzi, M.; Iannuzzi, D.; Lauria, D. Generalized approach to design supercapacitor-based storage devices integrated into urban mass transit systems. *Proc. 3rd Int. Conf. on Clean Electrical Power ICCEP 2011*, Ischia, Italy, 14-16 June 2011, pp. 530-534.

[88] Ciccarelli, F.; Iannuzzi, D. A Novel energy management control of wayside Li-Ion capacitors-based energy storage for urban mass transit systems. *Proc. 21st Int. Symp. Power Electron., Elect. Drives, Automation and Motion SPEEDAM 2012*, Sorrento, Italy, 20-22 June 2012, pp. 773-779.

[89] Ciccarelli, F.; Clemente, G.; Iannuzzi, D.; Lauria, D. An analytical solution for optimal design of stationary lithium-ion capacitor storage device in light electrical transportation networks. *International Review of Electrical Engineering*, vol. 8 (3), June 2013, pp. 989-999.

[90] Ciccarelli, F.; Del Pizzo, A.; Iannuzzi, D. Improvement of energy efficiency in light railway vehicles based on power management control of wayside lithium-ion capacitor storage. *IEEE Trans. Power Electronics*, vol. 29 (1), Jan. 2014, pp. 275-286.

Chapter 2

Energy Storage Systems for urban railway traction systems

2.1 Energy Storage technologies

Electrical energy in a power system cannot be stored electrically, rather it can be stored by converting itself as primary source and then storing it electromagnetically, electrochemically, kinetically, or as potential energy. *Energy Storage Systems* (ESS) are a tool of great interest, as they can play a vital role in improving the flexibility and efficiency of energy systems and the availability of different energy sources. The possibility to use the storage systems in most parts of the energy chain has enabled many disciplines of science and technology and involved a number of methods, materials and systems able to make more efficient, cost-effective and environmentally acceptable the process of energy accumulation.

There are many technologies available today to store electrical energy. The term "*storage*" leads immediately to the batteries also called electrochemical accumulators, which have pioneered these systems. They are in fact the first components that were used to store electrical energy, but are not the only ones, since it can be easily converted into other forms for storing it, and re-use it to perform useful operation at a later time. ESS in commercial use today can be broadly categorized as mechanical, electrical, chemical, biological and thermal. In particular *electrical energy storage* refers to a process of converting electrical energy from a power network into a form that can be stored for converting back to electrical energy when needed [1,2]. The need for electrical ESS can occur in the following cases:

- it is necessary to supply power electrical loads when the primary power source (mains) is unavailable due to faults or maintenance (backup power);

- requirement of the immediate availability of energy on-board vehicles with electric propulsion, even partial;

- there is compelling need for early availability of additional power which cannot be supplied by an existing infrastructure;

- energy is available in a useful and advantageous form but cannot be used instantly as there is no demand.
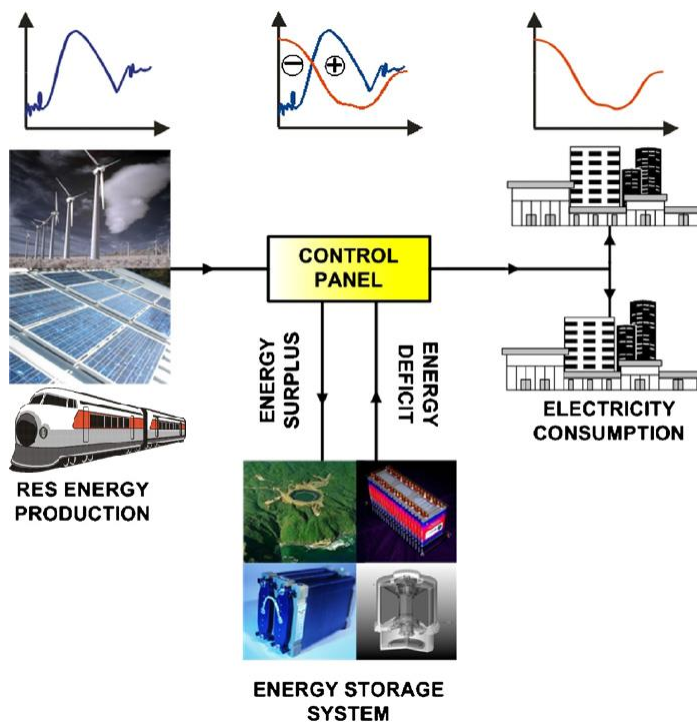
Figure 2.1- Typical configuration of an ESS

Three major parameters define an electrical ESS:

- **Energy storage capacity**, which is determined by the size and energy density of the storage technology.
- **Power rating**, which is directly related to the maximum current that can be transmitted between the main supply and the storage device.

- **Load cycles**, or how many charging/discharging cycles can the storage system handle over its lifetime.

Electrical energy storage has numerous applications including portable devices, transport vehicles and stationary energy resources [3-5]. In fact, electric utilities have long been interested in energy storage technology because of its potential to support the operation of electric power grids. Historically, one of the most important grid storage functions has been in storing off-peak electricity during periods of low demand and releasing it during periods of high demand, enabling the decreased use of high-cost peaking generation. Similarly, this function has been extended to include support for renewable electricity generation, given their typical variable production, in order to reduce sudden power peak absorption. More recently, utilities have also been considering how energy storage can provide a partial alternative to the development of the power grid itself by helping utilities optimize the use of grid infrastructure already in place and thereby avoid the installation of new power lines (so called *smart-grids*). Other key storage functions include technical services called "ancillary services" needed to provide electric power transmission service to a customer. Since substantially ESS allows energy production to be de-coupled from its supply, self-generated or purchased, they can provide remarkable benefits that can be synthesized, by adopting a common terminology nowadays, in a *load-leveling* and a *peak-shaving* actions. Once again these terms emphasize the use of ESS to equalize the supply of power delivered by the primary source (load leveling) or by ensuring that they provide the power peaks (peak shaving).
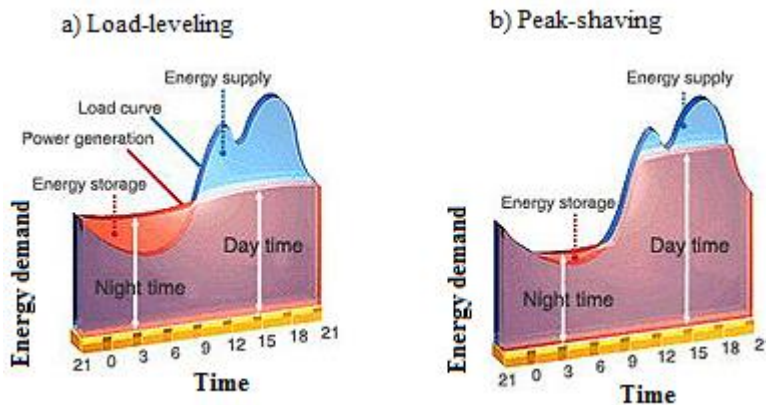
Figure 2.2 - Schematic picture of load-leveling action a) and peak-shaving action b)

The term *load-leveling* refers to the irregular distribution of the loads on a power grid at various times of day. An ESS could carry out an optimization between generation and supply with load or demand, which, potentially might postpone the need for a grid upgrade. An example of the effects of load leveling is in Figure 2.2 a).

With reference to the user, the expression *peak-shaving* refers to the non-uniformity of the power demand from the main grid. An ESS, appropriately programmed, may furnish a flattening action of short-term peak loads in order to optimize power. It is shown for example in Figure 2.2 b).

By resuming how deeply treated in the previous chapter, as far as urban rail transportation is concerned, the low supply voltage levels of tramways and metro systems, together with other relevant factors such the high power density of traction vehicles (< 1 MW per traction-unit), the wide extension of the urban/suburban rail DC distribution network (lines with lengths up to 20-30 km) and the typical operating conditions of the circulating vehicles (repeated starts, high acceleration and braking frequencies) next to the traffic conditions, have obviously accentuated the problems related to the reduction of the overall performance of the electrical transport system, i.e. the issue of voltage drops along the line. In fact, the peak power demands during the continuous and repeated start up phases of one or more trains result in an increase of the line current and consequently an increase of the voltage drops . This turn into a rise of losses due to joule effect on the feeding line (reduction of the maximum delivered power) and in the electric traction drive of the rail vehicle.

This phenomenon is particularly critical near network areas with higher traffic density (most vehicles are at the same time accelerating or starting) and at singular feeding points, as far away from the supply substation. Under some critical operating conditions of the rail supply network it is possible that the line voltage is reduced by up to 50 % of the voltage at the beginning of the line.

In conclusion, the increase in power and energy required to meet the growing needs, leads to the emergence of the two aforementioned supporting actions.

Once again the previously treated concept of the enhancement of regenerative braking energy, is invoked and it is emphasized that ESS can be regarded as a valid solution to improve efficiency and reliability in urban rail systems, with additional mitigation of other problems typically associated to urban rail such as voltage drops or pronounced consumption power peaks.

Given the wide range of storage technologies, and because their use is specific to any power applications, it is essential to have an idea of the assessed performance of available storage devices, as well as the energy requirements that characterize the urban railway application, regardless of whether they are used for mobile or stationary applications. In order to fulfill this clarification, the next paragraph introduces and compares the storage technologies suitable for urban railway applications, pointing out the most recent advances in this field. Afterwards, a technical comparative analysis between the identified technologies is carried out.

Typically, both in literature and in technical applications, the term electrical ESS is intended to be the set of three main components that perform many functions (see Figure 2.3): the energy storage *device* itself, a *power electronic converter* to guarantee a proper operation of the input and output electrical energy flows, and a *control unit* which is able to promptly and efficiently manage the charge and discharge processes. In particular power converter have to allow a bidirectional energy flow and to adapt the main electrical variables to the working conditions of the energy storage device (voltage, current and/or frequency) acting as an adaptive interface even for the main supply system.
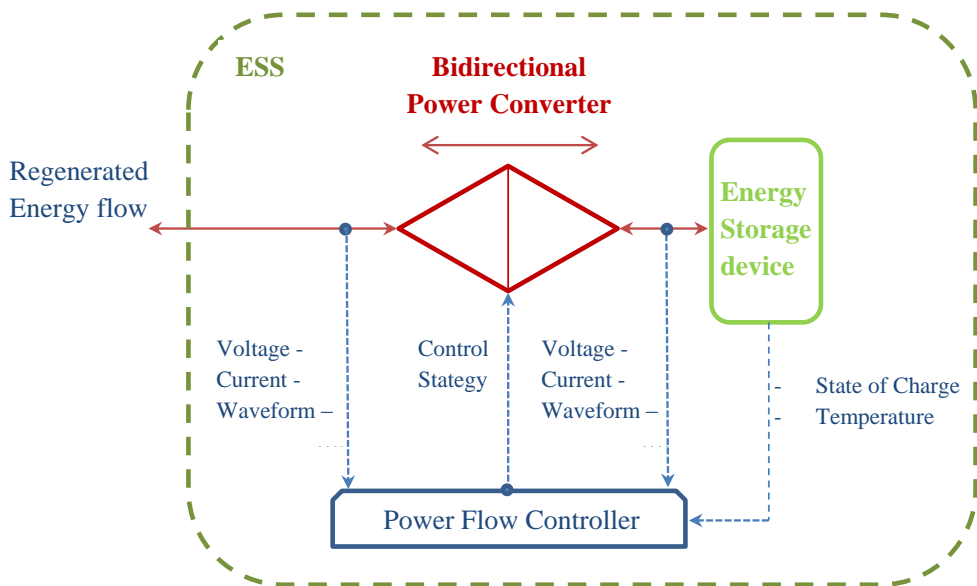
Figure 2.3 – Typical components of ESS in urban rail application (modified from [14])
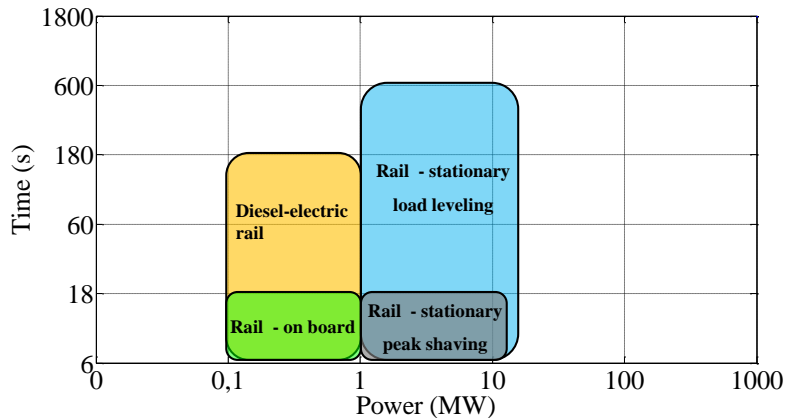
Figure 2.4 – ESS Power magnitude and duration requirements for various transport applications [4]

As previously said, the selection of the energy storage technology depends on the specific characteristics of each application. In addition, for setting up and implementing control laws for energy management of urban railway vehicles it is necessary a basic knowledge of the different storage device families.

In the case of electrified transport employment, the power consumption is very uneven, and benefits can be obtained from electric energy storage to smooth out the vehicle power demand, regardless of the installation criterion, serving as **peak-shaving units** or as **demand-flattening units** [4].

As shown in Figure 2.4, power and duration constraints greatly affect the energy storage requirements.

Therefore, regarding urban rail applications, as a rule it can be asserted that the most investigated requirements for urban rail applications can be summarized in the following:

- time ranges from seconds to minutes;
- high power peaks of charge and discharge, typically between 0.1 and 10 MW
- large number of load cycles, typically between 100,000 and 300,000 per year;
- intermediate energy capacities, reduced weight and volume,

Hence, portability, scalability and energy and power density are definitely key performance criteria.

It is necessary to do an accurate analysis to understand which type of device have the better characteristic for a determinate application. The next sections

discuss and give a brief description of the most relevant technologies for urban rail applications.

2.1.1   Electrochemical Batteries

Batteries are the most known energy storage device. Their operating principle stays in collecting and delivering energy by means of reversible electrochemical reactions, that occur between two different materials (electrodes) immersed in an electrolyte solution. These phenomena occur within the elementary cells, which are the basic units that form a battery. Depending on the basic chemistry used, the batteries can provide a wide range of operational characteristics. A short description of the most common and promising battery configurations available for energy storage in urban rail systems is given below.

a. **Lead-acid batteries**. Among this technology, rechargeable lead-acid batteries are the oldest and certainly the most used. Even their constitution is well established: in the charged state, the electrodes are made of metallic lead and lead oxide, while a dilute solution of sulfuric acid behaves as electrolyte (see Figure 2.5). Instead, in the state of discharge both electrodes are transformed into lead sulfate and the electrolyte becomes primarily water. These are characterized by relatively low cost, high reliability and efficiency, a quite limited lifetime, low energy density and relatively high power density compared to other batteries, and finally a low self-discharge rate, see Table 2.3. However, affecting factors to their disadvantage are the limited performance at low temperature, the fact that they cannot be fully discharged and their negative influence on the environment, because of the lead processing.
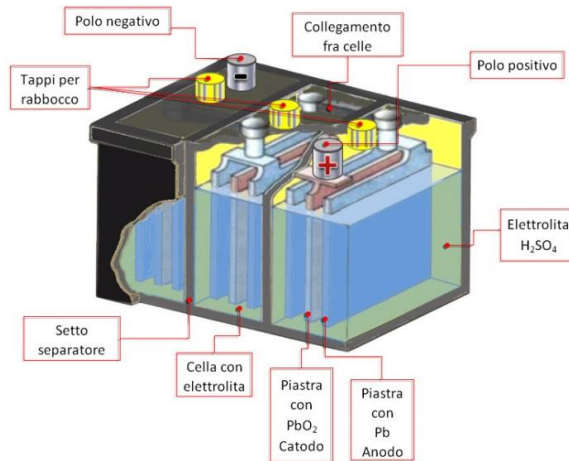
Figure 2.5 – Schematic view of a lead-acid battery pack

Lead–acid batteries are mainly used in cost sensitive applications where restrictions as low energy density or short cycle life do not represent an issue. Concerning railway systems, they can be employed mainly in back up applications [6]. Some recent research studies focus on increasing the energy and power density by replacing lead with lighter materials such as carbon, which might allow for their use in the traction equipment [7,8].

b. **Nichel-based batteries**. In this category are included Nichel-Cadmium (NiCd) and Nichel-Metal Hydrate (NiMH) battery types, which employ nickel hydroxide as a positive electrode and an alkaline solution as electrolyte, whereas for the negative electrode, the NiCd type uses cadmium hydroxide (see Figure 2.6) and the NiMH ones has a metal alloy capable of absorbing and desorbing hydrogen. With respect to lead-acid, NiCd batteries have a higher energy and power density, as well as the higher lifetime and robust reliability, see Table 2.3.
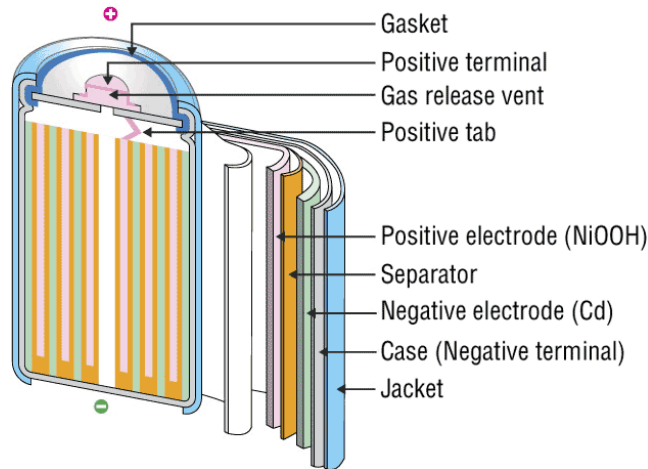
Figure 2.6 – Schematic view of a Ni-Cd battery cell

In contrast, their cost is much higher and have a lower efficiency together with worse rates of self-discharge. In railway applications, NiCd batteries have been primarily used as a backup for auxiliary systems [9]. As well as the traction Operation is concerned, they have been replaced by NiMH batteries, that offer greater energy and power density, longer life, reduced memory effect and, moreover, avoid the use of a toxic heavy metals such as cadmium. The efficiency of NiMH batteries is not particularly high, but their main disadvantage is the high self-discharge rate, which could be improved by the introduction of new separators [10].

c. **Lithium-based batteries**. Based on the migration of lithium ions between the electrodes through the electrolyte (made of lithium salts), lithium-ion (Li-ion, see Figure 2.7) and lithium-polymer (Li-poly) represent the major families of cells [11]. In this latter, the electrolyte is held in a solid polymer composite instead of an organic solvent. Major advantages of this technology stay in their comparatively high energy and power densities, good efficiency, low self-discharge rate, elevated number of cycles, no memory effect and fewer maintenance. On the other hand, a battery management system (BMS) is strongly required in order to keep working temperatures, voltages and SoC within a safe and efficient range of operation [12,13].

$$LiCoO_2 + C_6 \underset{\text{Discharge}}{\overset{\text{charge}}{\rightleftharpoons}} Li_{1-x}CoO_2 + Li_xC_6$$
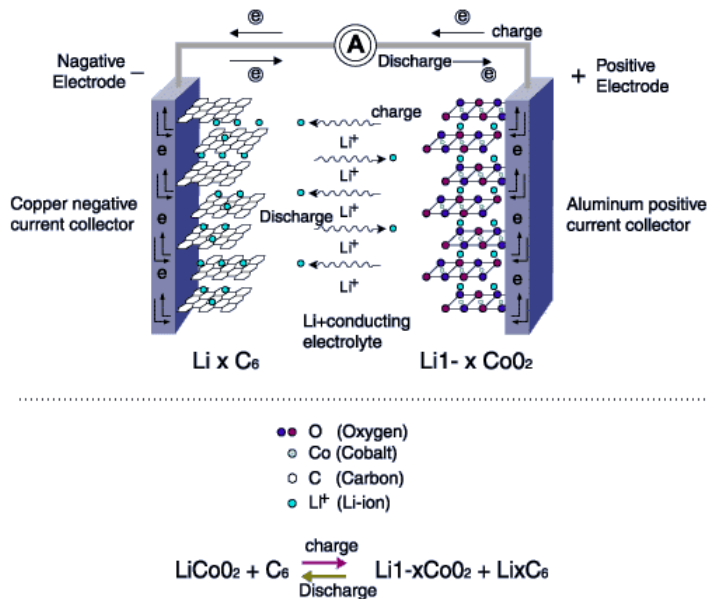
Figure 2.7 – Schematic principle of a Li-ion battery

This, together with the reasonable request for special packaging, involves a high total cost, which therefore turns out to be the main cause of their low diffusion [2]. In this sense, the technology Li-poly, even though it has a lower temperature range of operation, offers potentially to reduce the manufacture cost of manufacture and wider adaptability to packaging shapes. Furthermore, they are lighter and present lower risk of flammability than Li-ion batteries. Current research on lithium-based batteries is focused on finding new electrochemical combinations and nanostructures that improve their energy and power densities, durability, cost and safety [14–16].

d. **Sodium-based batteries**. Sodium-beta batteries use molten (liquid) sodium for the anode, with sodium ions transporting the electric charge. The two main types of sodium-beta batteries are distinguished by the type of cathode they use. The sodium-sulfur (Na-S) type employs a liquid sulfur cathode (see Figure 2.8), while the sodium-nickel chloride (typically called the ZEBRA cell) type employs a solid metal chloride cathode. Both types include a beta-alumina solid electrolyte material separating the cathode and anode. This ceramic material offers ionic conductivity similar to that of typical aqueous electrolytes, but only at

68

high temperature. Consequently, sodium-beta batteries ordinarily must operate at temperatures around 300°C. The impermeability of the solid electrolyte to liquid electrodes and its minimal electrical conductivity eliminates self-discharge and allows high efficiency.
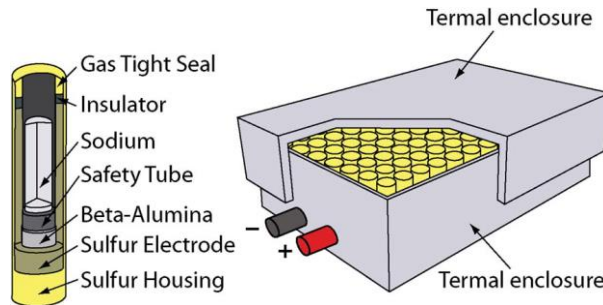
Figure 2.8 – Schematic view oa a NaS battery pack

Technical challenges associated with sodium-beta battery chemistry generally stem from the high temperature requirements. To maintain a 300°C operating point the battery must have insulation and active heating. Na-S batteries are manufactured commercially for a variety of grid services ranging from short term rapid discharge services to long-term energy management services. The problem of high operation temperature is an intrinsic disadvantage of the sodium-based batteries that may limit their use to large-scale stationary systems like power quality and peak shaving applications [17].

e. **Other emerging batteries**. It is worth mentioning Metal–Air batteries and Redox Flow Storage systems. Metal–Air technology (see Figure 2.9) offers high energy densities (up to 3000 Wh/kg) at reasonable costs. Therefore they represent a favorable option for a wide range of applications, from portable electronics to electric vehicles. However, intensive research is still needed in terms of cathode materials and electrolyte systems to improve their low efficiency [18,19]. Conversely, Redox technologies, for instance Vanadium Redox batteries (VRB), have important advantages such as no self-discharge, no degradation for deep discharge and long lifecycle. Nevertheless, they still require high investment costs and need further technical development, especially to increase their energy capacity [20].
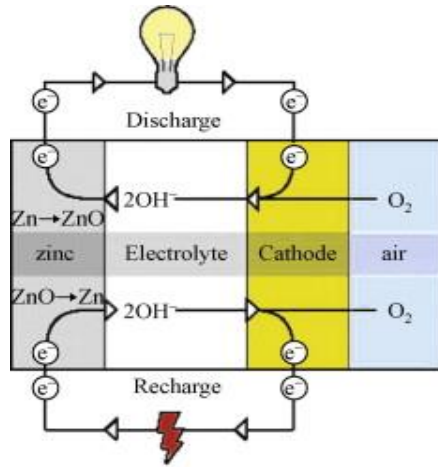
Figure 2.9 - Schematic principle of a Metal-Air battery

2.1.2 Flywheels

Flywheels store rotational kinetic energy in the form of a spinning cylinder or disc, then use this kinetic energy to regenerate electricity at a later time.
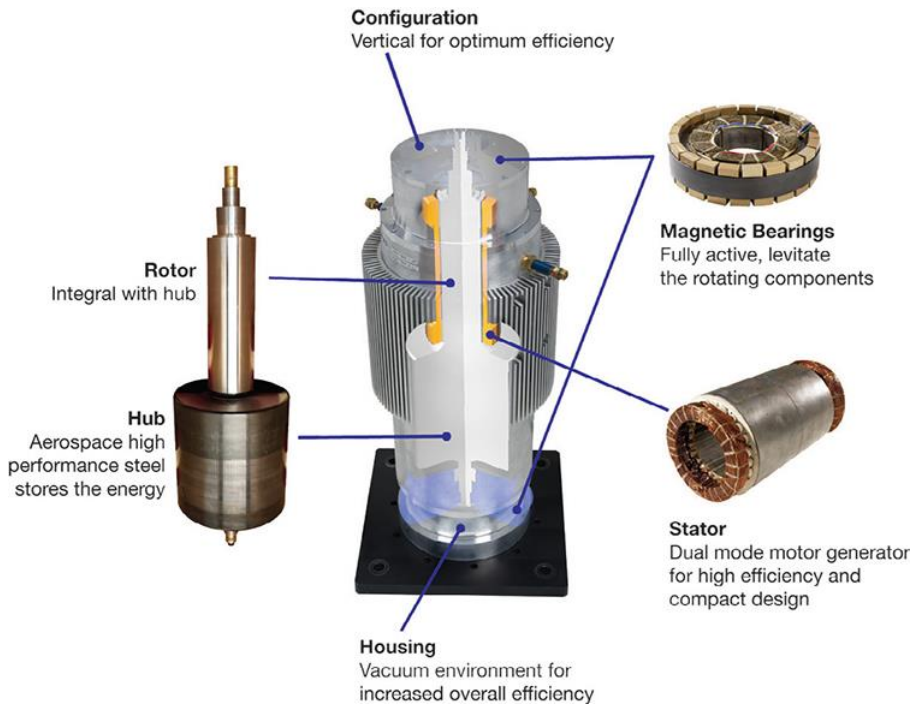
Figure 2.10 – Schematic view of a FES

The amount of energy stored in a flywheel depends directly on the dimensions of the flywheel and its mass, and on the square of its rotational speed at which it spins. Consequently, its SoC can be easily measured as a function of angular speed.

Flywheels typically use an electric motor to spin a cylindrical rotor at very high speed, and therefore, consist of the spinning rotor(s), bearings, a motor/generator, power electronics, and a containment enclosure (see Figure 2.10). The bearings connecting the rotor to the non-rotating platform are of two types: mechanical bearings, which physically connect the rotor to the housing, or magnetic bearings, which levitate the rotor inside the housing to reduce friction losses [21]. In order to increase the rotational speed, at the expense of an acceptable reduction in inertia, the use of light composite materials is promising, thanks to their higher tensile strength. The motor/generator converts electrical energy to rotational kinetic energy to "spin up" the flywheel, and then regenerates electrical energy at a later time from the spinning rotor. The containment enclosure is the non-rotating platform in which the rotor spins, designed to contain rotor debris in the case of catastrophic rotor failure. The enclosure may also hold a vacuum to reduce air drag on the rotor and standby energy losses. Even for these vacuum systems, novel alternatives such as using a helium–air mixture gas have been proposed in the literature to reduce the air blast loss [22].

FES can be designed for a broad range of applications with different power and energy requirements. In fact, FES have long lifetimes (lasting decades with little or no maintenance; full-cycle lifetimes quoted for flywheels range from in excess of 10^5, up to 10^7, cycles of use), high energy density (100–130 Wh/kg) and large maximum power output. The energy efficiency of flywheels can be as high as 90 %. It is evident that they allow a fast charge/discharge process for a potentially infinite number of cycles. Considering also that their temperature range of operation is very wide and by making use of low-environmental-impact materials, these resulting advantageous features make FES a very suitable option for different applications such as transportation or power quality applications [23-25].

Unfortunately, the presence of a flywheel involves some significant problems. Firstly, the increase of the mass and the diameter is not viable beyond a certain point in mobile installation, where a further drawback is also given by the gyroscopic effect, which produces a force perpendicular due to the change in

orientation of the rotation axis. This contributes to the increase in self-discharge rates. Another important aspect is safety in case of an accident with rupture of the casing protection, so they have a potential risk of explosive shattering even when overloads may occur. In order to prevent sudden releases of energy due to the case explosion, modern fiber reinforced composite rotors could be employed [26]. By summarizing, the drawbacks tend to inhibit their extensive use in railway applications, particularly if the potential danger is regarded as a major safety issue in public transport applications.

2.1.3   Supercapacitors

Electrochemical double layer capacitors (EDLC), also commonly known as *Ultracapacitors* (UC) or *Supercapacitors* (SC), store energy via electrostatic field. The energy is stored by charge transfer at the boundary between electrode and electrolyte. According to [27], it is constituted of two electrodes, a separator and an electrolyte. The electrodes are made-up of activated carbon particles strongly packed, which provides a high surface area responsible for energy density acting as polarizable electrodes. The two electrodes are separated by a membrane, which allows the mobility of charged ions and forbids electronic contact (see Figure 2.11). The amount of stored energy is a function of electrodes surface area, the size of the ions, and the level of the electrolyte decomposition voltage.
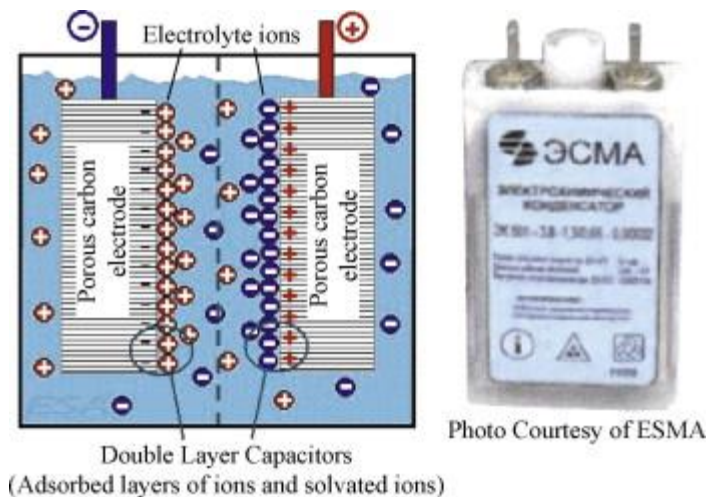
Figure 2.11 – Principle and schematic view of a SC cell

72

Due to this technology, this devices exhibit relatively low energy densities (6 Wh/kg) but high power densities (6 kW/kg), with discharge times ranging from ten of seconds to minutes, high efficiency (around 95 %), larger current charge and/or discharge capacity, long lifecycle (up to 10^6 cycles) and low heating losses. Other advantages of SC include long life with little degradation, which makes the device environmentally friendly, good reversibility, improved safety (use of non-corrosive electrolytes and low material toxicity) and simple charge methods. Conversely, disadvantages include significant self-discharge, low maximum voltage (series connections are needed to obtain higher voltages and voltage balancing may be required), rapid voltage drop and spark hazard when shorted. The resulting characteristic suggests their utilization for supplying power peaks, for energy recovery, and for compensating quickly voltage variations.

Current SC recent research primarily targets reducing material and device cost and increasing energy density without sacrificing power and life. Specific areas of research and development focuses on increasing their energy capacity by developing advanced carbon materials. Although carbon electrodes have the potential to cost less in the future, Nanotube and graphene structures are also under investigation as possible SC electrode materials [28,29], with estimates enhancement of energy density to 60 Wh/kg and power densities of 100 kW/kg. Furthermore, recent studies have been conducted on a hybrid type of capacitor, the lithium-ion capacitors (LiC). In this type, activated carbon is used as cathode. The anode of the LiC consists of carbon material which is pre-doped with lithium ion. This pre-doping process lead to increased operating voltages as well as higher energy and power densities [30,31].

Characteristics of SC make them a very suitable option for energy storage in both railway and power applications. Due to their rapid response they may be effectively used for supplying power peak demands and for voltage regularization purposes.

2.1.4   Superconducting magnetic storage

Superconducting magnetic energy storage (SMES) devices store energy in the form of a magnetic field. By applying a DC current to a coil, a magnetic field is created, storing magnetic energy (see Figure 2.12). When the DC potential is removed, the energy is released. Using superconducting wires allows SMES

units to achieve very high efficiencies. Superconducting materials are characterized by the temperature required to achieve superconductivity: low-temperature or high-temperature. Low-temperature superconductors, which require expensive liquid helium, have been used in most SMES demonstrations. Recent SMES research and development have focused on developing high-temperature SMES devices,

which could use less costly liquid nitrogen and therefore, could have lower overall system costs that the low-temperature SMES devices demonstrated to date.

The main advantages of SMES systems are their great energy storage efficiency and very fast responses, see Table 2.3. Additionally, they can be almost completely discharged and present a very high cycle life. Their major drawbacks are, by contrast, the high investment and operational costs due mainly to the cooling system.

There have been several SMES demonstration projects for quick-response and very short-term capacity applications, primarily for electric grid power quality and network stability applications [32,33]. However, their features make them potentially suitable for railway applications as well, especially for the case of stationary storage [34,35].
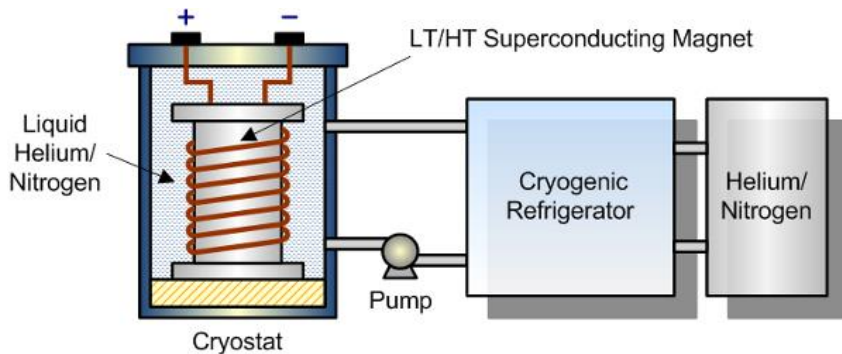
Figure 2.12 – Schematic view of a SMES

2.2   Comparison for urban railway application

2.2.1   Characteristics of the urban railway "load"

As well known, the typical *driving cycle* of railway vehicle presents motoring, cruises and braking phases. These driving cycle to four different motion states of operation: acceleration, cruising at constant speed (and/or coasting, or free running), braking and standstill.

In case of electrified railway system, the energy in the accelerating phase has to be taken from the main the distribution network. This energy is partially stored as kinetic energy in the vehicle's total translating mass.

During the constant speed phase, the power supplied from the supply is reduced and no further kinetic energy is stored. This phase is long and dominant in long distance trains and very short and negligible in urban and regional vehicles.

In the electrical braking phase, with no regeneration, the electric motors act as generator and the braking energy is dissipated on the *braking rheostats* and this is accompanied by high losses due to the high braking power. It has to be outlined that the vehicle kinetic energy can also be dissipated by the mechanical brake without considering its energy supply and, however these must be used always under a certain speed (< 10 km/h), due to replace the ineffectiveness of the electric braking at very low speed. In all cases, the energy supply is inconsistently loaded and a large proportion of the vehicle's kinetic energy is wasted.

The installation of an ESS allows that the energy requested during the acceleration is supplied partially by the ESS, which discharges, and partially by the feeding contact line; as regards the braking, the ESS is recharged up to their initial state of charge by the energy coming from the contact line and the regenerative electrical traction drive. The ESS management system should be designed in such a way that the main energy supply never needs to deliver the full accelerating power (an important condition to downsize energy supply). When driving at maximum speed the storage device should be completely discharged.

Figure 2.13 shows the typical driving cycle, highlighting the speed, the motor torque and the mechanical power, with the storage device action.
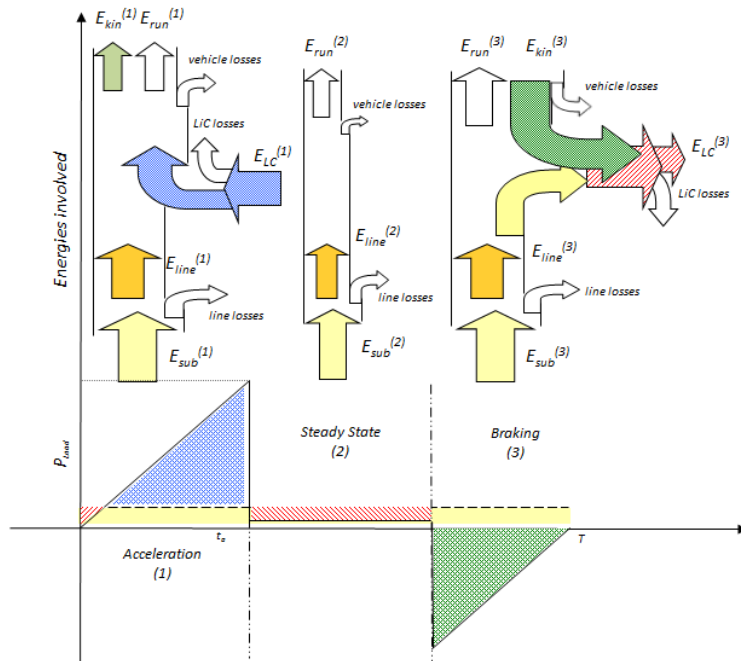
Figure 2.13 - Driving Cycle and Storage Cycle for a typical railway application

It is obvious that it would be advantageous to store the kinetic vehicle energy in the braking phase and to reuse it during the next acceleration phase for vehicles with frequent starts and stops.

The *size* of the energy storage system required on a vehicle is determined by the mass and top speed and by the acceleration and braking rates. These parameters define the amount of energy to be stored and the required power performance of ESS.

The *braking energy* and *power* determine the *braking time*, which corresponds directly to the requested charging time of the ESS.

The driving and storage cycles, show the storage device changed at its max power for a long time during the charging phase. Consequently the power capability of the energy storage system, including the related power electronic converter, has to be increased, depending on the required charging/discharge power range.

The choice of the best ESS device for rail application heavily depends on the individual vehicle and service type. The following Table 2.1 shows the main characteristics to be looked at in an individual rail application context and the corresponding ESS parameters.

Characteristics of rail application context		Corresponding parameter of energy storage device
Braking time	⟵⟶	*Charging time / power density*
Braking energy	⟵⟶	*Energy density*
Drive cycles in lifetime	⟵⟶	*Product life / reliability*

Table 2.1 – Some relevant characteristics for matching railways and ESS requirements

However, apart from these basic requirements, it is necessary to consider economic impact for investments in the new storage technology device in rail application.

Firstly, the storage device introduction uses remarkable *volume* for the considerable energy involved and consequently possible vehicle weight increment . An accurate analysis in order to find a compromise between volume, weight, costs and technical features.

Secondly, it is essential to know the *performance characteristics* of both the rail vehicles and the service type, for the final technical choice and the correct application in use of the ESS. For example, the intrinsic characteristics for long distance vehicles, as *High Speed Trains* (HST) and *Inter City Express* (ICE), are very different compared with regional train vehicles or even urban rail vehicles. There are plenty of technical factors that potentially define the storage device choice. Table 2.2 gives these relevant characteristics for some trains.

Data such as total mass, top speed, maximum tractive effort and braking effort lead to directly related data as storable kinetic energy of vehicle at the maximum speed and the braking time, derived from kinetic energy and braking power. More specifically, the braking time of heavy rail vehicle is in the order of one minute, whereas the corresponding one of LRV results ten seconds.

Finally, the *economical impact* for investment for this new technology is more profitable for vehicle with low operating speed, high acceleration / deceleration rates, deep brake cycles and short average route. It is worth to observe the braking power compared to the maximum tractive effort for each class of vehicle and the drive cycles with respect to lifetime.

Characteristics of vehicle and service	Regional Multiple Unit	Suburban EMU	Metro / Light Rail Vehicles
Total convoy mass	250 Ton	160 Ton	100 / 39 Ton
Top speed	160 km/h	100 km/h	80 / 70 km/h
Traction drive power	4000 kW	1200 kW	600 / 300 kW
Maximum tractive effort	250 kN	180 kN	150 / 60 kN
Braking power	4800 kW	3000 kW	1200 / 900 kW
Maximum braking effort	270 kN	200 kN	160 / 100 kN
Storable kinetic energy	70 kWh	16 kWh	8 / 2 kWh
Braking time	50 s	15 s	12 / 9 s
Drive cycles per year	40000	100000	300000
Drive cycles in lifetime (10^6)	0.8	2	6

Table 2.2 - Relevant characteristics of some railway vehicles related to their operation [36]

From the Table 2.2 it is possible to fully understand how the use of energy storage device could be more remunerative for urban rail application than in regional or high speed rail vehicles.

2.2.2 Comparative analysis among ESS in urban rail transport

In order to compare and assess the suitability of the above discussed technologies for ESS in urban rail applications, one of the first criteria to be considered is energy and power performance.

Energy and *power density* are definitely crucial parameters to be taken into account in the choice of storage technologies for railway applications, especially as far as the on-board ESS is concerned. The Table 2.3 shows that the BES have the greatest energy capacity per weight (20÷200 Wh/kg) and volume unit (20÷200 Wh/kg) than the FES (5÷100 Wh/kg), SC (1÷6 Wh/kg) or also SMES systems (0.5÷5 Wh/kg). More specifically, among electrochemical batteries, the lithium-based technologies offer the widest range of energy density (50÷200 Wh/kg), followed by the sodium-based type (100÷250 Wh/kg).

ESS technology	Energy and Power density			Typical Efficiency	Discharge time
	(Wh/kg)	(kW/kg)	(kWh/m^3)	(%)	(s)
Lead-acid Batteries	$20 \div 50$	$0.025 \div 0.3$	$50 \div 80$	$70 \div 90$	$1 \div 3600$
NiCd Batteries	$30 \div 75$	$0.05 \div 0.3$	$60 \div 150$	$60 \div 80$	$1 \div 3600$
NiMH Batteries	$60 \div 80$	$0.2 \div 0.25$	$100 \div 150$	$65 \div 70$	$1 \div 3600$
Li-ion Batteries	$75 \div 200$	$0.1 \div 0.35$	$150 \div 500$	$90 \div 95$	$1 \div 3600$
Li-poly Batteries	$100 \div 200$	$0.15 \div 0.35$	$150 \div 200$	$90 \div 95$	$1 \div 3600$
NaS Batteries	$120 \div 240$	$0.12 \div 0.23$	$110 \div 250$	$70 \div 90$	$1 \div 3600$
ZEBRA Batteries	$100 \div 200$	$0.15 \div 0.2$	$120 \div 180$	$85 \div 90$	$1 \div 3600$
Flywheel	$5 \div 100$	$1 \div 5$	$20 \div 80$	$90 \div 95$	$0.1 \div 60$
EDLC	$1 \div 6$	$0.5 \div 5$	$1 \div 14$	$90 \div 95$	$0.1 \div 60$
Li-ion Capacitors	$10 \div 15$	$0.5 \div 5$	$15 \div 30$	$90 \div 97$	$0.1 \div 10^3$
SMES	$0.5 \div 5$	$0.5 \div 2$	$0.2 \div 2.5$	$95 \div 98$	$0.1 \div 1$
ESS technology	Self-discharge (daily % of rated capacity) (%)	Lifetime (number of cycles) (-)	Capital cost (per energy) (€/kWh)	Capital cost (per power) (€/kW)	Environ-mental impact
Lead-acid Batteries	$0.05 \div 0.3$	$200 \div 2000$	$35 \div 300$	$220 \div 440$	negative
NiCd Batteries	$0.2 \div 0.6$	$1500 \div 3000$	$300 \div 1800$	$350 \div 1000$	negative
NiMH Batteries	$1 \div 2$	$1500 \div 3000$	$300 \div 1800$	$350 \div 1000$	negative
Li-ion Batteries	$0.1 \div 0.3$	$10^3 \div 10^5$	$350 \div 1850$	$900 \div 3000$	small
Li-poly Batteries	0.15	$600 \div 1500$	$650 \div 1000$	$900 \div 3000$	small
NaS Batteries	20	$2000 \div 3000$	$220 \div 370$	$750 \div 2200$	negative
ZEBRA Batteries	15	>2500	$75 \div 150$	$100 \div 200$	negative
Flywheel	100	$<10^7$	$750 \div 3700$	$190 \div 260$	almost none
EDLC	$20 \div 40$	$<10^6$	$200 \div 1400$	$90 \div 200$	moderate
Li-ion Capacitors	$0.1 \div 0.2$	$<10^6$	$5000 \div 10000$	n.a.	moderate
SMES	$10 \div 15$	$>10^5$	$750 \div 7500$	$180 \div 200$	negative

Table 2.3 – Comparison of technical characteristics of ESS for urban rail application [2,4,5]

However, lithium-based batteries have greater compactness (energy per volume unit between $100 \div 500$ kWh/m^3), which makes them potentially more suitable for on-board ESS. On the other hand, the typical power density of batteries $(0.03 \div 0.3$ kW/kg)is considerably lower than flywheels ($1 \div 2$ kW/kg), SC ($0.5 \div 6$

kW/kg) or SMES systems (0.5÷2 kW/kg). FES and SC have the highest power density, but these last have a little higher energy density and compactness.

Concerning the *discharge time*, electrochemical batteries are clearly restricted in comparison with FES, SC and SMES, which are capable of very fast dynamic behavior, so this becomes a critical parameter for peak shaving and voltage stabilization tasks. SMES systems offer the shortest discharge times (< 1 s) as they are the unique technology to store energy directly into electric current.

A common feature of the aforementioned storage devices is that they may offer the highest *charge/discharge efficiencies*, with average values around 90% or higher. This leads to an useful maximization of the total stored energy that can be effectively. Furthermore, as regard the *self-discharge* rates, batteries present much lower values than other technologies (except for sodium-based batteries). In any case, since urban rail applications involve short storage periods (minutes), high self-discharge ratios do not imply serious issues.

When reference is made to urban rail applications, where the number of charge‑discharge cycles is substantially higher than for other cases, also *durability* (or *cyclability*) of the ESS is also an important parameter to take into account as it is directly related to the final costs of the system. By keeping in mind Table 2.3 it is stated that batteries present considerably shorter life cycles than SC, flywheels and SMES systems, which can last for several hundred thousand cycles. Notwithstanding, it is worth mentioning that modern Li-ion batteries may offer up to 10^4 cycles.

Lastly, Table 2.3 shows the typical *costs* per stored energy unit and per rated storage power unit, without considering operation, maintenance and replacement costs. BES, in particular lead‑acid ones, offer the best capital costs per kWh of stored energy. Conversely, when costs per rated power are considered, batteries are considerably more expensive than the other ESS. This in evident even when the cost per cycle life is considered, and in general, batteries are the most costly options with respect to their cycle life. This is in part related to the fact that the lead-acid batteries are the most mature option given their great long-dated back experience. Next to them, NiCd, NiMH, NaS-based and Li-based can also be considered as a fully established storage technology and already commercially available. Regarding the SMES systems, they have proven to be technically available but not yet largely commercialized.
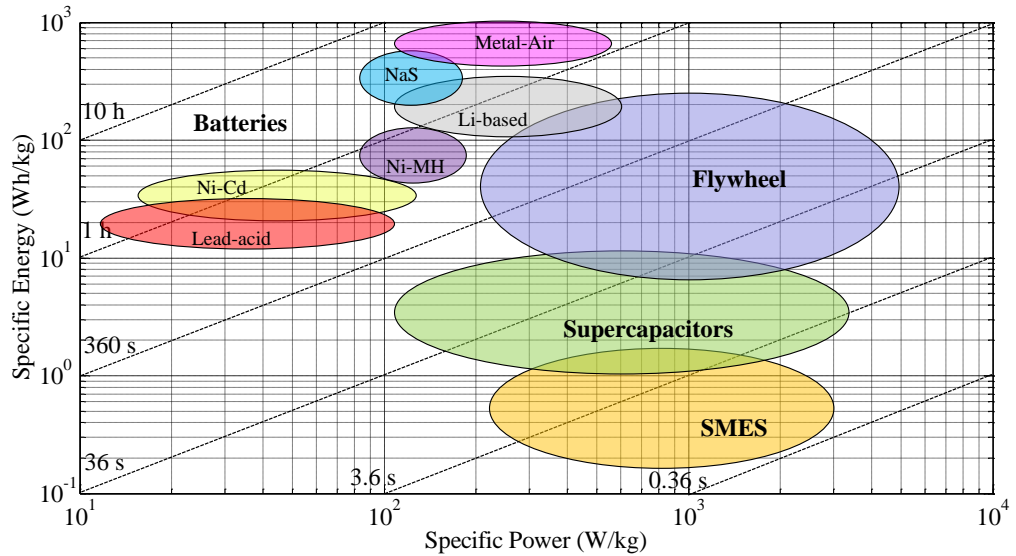
Figure 2.14 - Ragone plot showing the characteristics of different energy storage technologies deployed at electrified railways

Despite significant improvements in recent years, FES and SC are based on well-known technologies and therefore can be considered suitable and mature technologies to support electrified railways and they are becoming more and more important for the actual diffusion of ESS in urban electrified railways.

The characteristics of storage devices can be easily visualized and compared on the Ragone plot, shown in Figure 2.14. The *Ragone diagram* plotting specific energy and specific power (meaning energy and power normalized to the device mass), is a convenient means to compare different storage technologies and assess their suitability for different applications. For each storage technology, this plot shows the typical ranges of power and energy densities on a log-log scale. The 10^{-2} hour slope lines are related to the characteristic discharge time of the energy storage devices.

By keeping in mind the performance characteristics of both the rail vehicles and the rail service, previously highlighted in sec. 2.2.2, an immediate conclusion is reached by matching the above presented *Ragone* plot diagram with the typical braking times of different railway vehicles service, as depicted in the Figure 2.15.
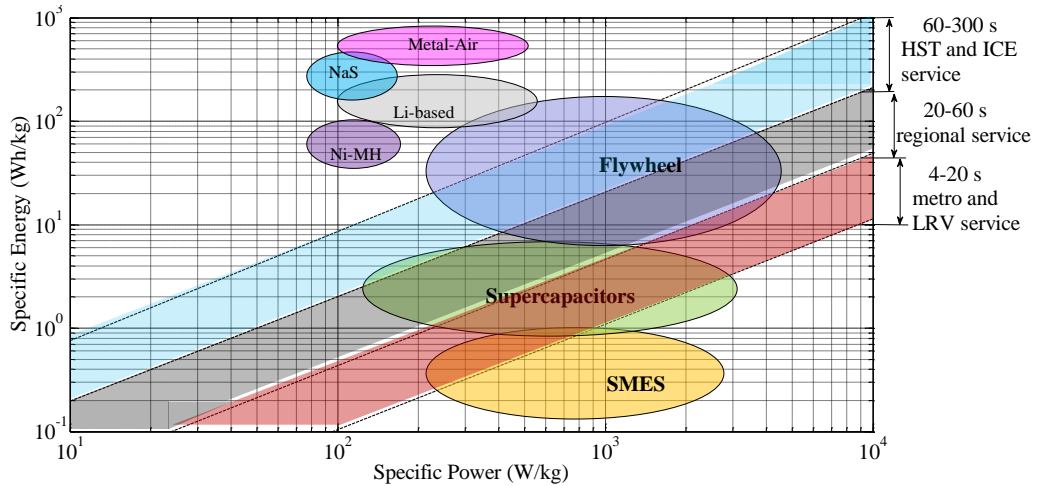
Figure 2.15 - Ragone diagram and charging times (corresponding to braking times of different trains) [36,37]

To conclude, it can be summarized that:

Batteries have very high energy densities but low power densities leading to very high charging times. Lithium-ion and Lithium polymer batteries have sufficient power densities but do not meet the lifespan requirements. Batteries are therefore presently not the first choice for energy storage in urban railway application.

Flywheels have both high power and high energy densities and are therefore ideally fitted to most situations, especially regional trains.

Supercapacitors, which have made considerable development progress in recent years are beginning to become attractive for railway applications especially metro and light rail urban vehicles.

Superconducting magnetic energy storage is of the extreme low-energy high-power type and seems therefore not an attractive option for braking energy storage.

Finally, if there is the need to delve into a further level of detail regarding the ESS application in urban traction, as fully described in Chapter 1, with reference to the two modes of installation, the following conclusions can be drawn.

Surely **SC** currently represent the *best option* for regenerative energy storage **on-board** of urban rail vehicles, thanks to their *fast response*, *high power density* and relatively *low costs*, even though are not able to provide acceptable autonomous operation to vehicles, because of the low energy capacity hinders

their use in applications. This gap can be filled by the use of Li-ion based batteries, especially if higher power densities and reduced costs are achieved in the near future as expected.

Interestingly, an *hybrid combination* of storage devices appears to be a very promising option for urban on-board ESS. The idea behind this hybrid device is the integration of both SC and batteries to get at the same time high power and energy densities. The device has apparently better performances than the previous energy storage devices, especially for energy saving and catenary free operation. The hybrid energy storage device is capable of recharging energy from regenerative braking and also from a dedicated quick charging unit at the substations. On the other hand FES and SMES systems may not be regarded as suitable options for mobile systems due to safety and operability issues (see section 2.1).

As concerns **stationary ESS**, given their less weight and volume restrictions than mobile systems, the range of suitable storage technologies is wider in this case. SC present excellent characteristics to be used in power peak-shaving and voltage stabilization targets, but as for on-board applications, the reduced energy capacity could limit their use depending on the specific requirements of each system. In this sense, FES can provide similar power capacities but with slightly higher energy densities. The safety concerns related to FES are obviously less restrictive in wayside applications as they can be freely installed in dedicated space. SMES systems appear to be a very suitable alternative for stationary ESSs due to their fast response, but their elevated costs, their high complexity and the associated electromagnetic fields may hinder an extensive application. Among BES, sodium-based technology might represent a good solution due to the relatively high power capacities and the reduced capital costs per unit of energy and cycle. Expected advances in Li-ion and Ni-MH might make them promising alternatives as well.

In any case, it is opinion of the researchers that the comparison efficiency of these two types of energy storage devices installations should consider the cost of energy storage devices and their infrastructure parts, maintenance costs, energy costs and the years of payback. Therefore, an economic assessment is one of the factors that must be taken into account to optimize the cost. The best installation method for energy storage is dependent on the agreement of the authority and the purpose of the energy storage devices.

2.3 Characteristics of on-board ESS installation in urban rail

On-board ESS can significantly contribute to energy savings in urban transit systems. Every system works independently and the recovered energy is directly sent to the storage system placed on the vehicle, usually located on its roof. When the vehicle accelerates, energy is used in priority from the ESS to supply the vehicle (see Figure 1.11).

Since the ESS is placed directly on the vehicle, the following potential benefits can be expected:

- ➢ **Power peaks shaving action** during acceleration of vehicles, which leads to reduced energy costs and higher efficiency due to reduced overhead line resistive losses.

- ➢ **Voltage stabilization** by limitation of voltage drops in the system supply network, which might possibly allow for a higher traffic density without further modification in the existing supply infrastructure.

- ➢ Possibility of **catenary-free operation** of vehicles on certain sections of the railroad (urbanistic integration) or in depot operations.

- ➢ Potential **down-sizing** of the onboard braking resistors.

- ➢ **Simpler management** of the recovered energy since the control is independent of traffic conditions and it can be **easily integrated** with the main traction drive control.

On the contrary, **retrofitting** of old vehicles (space availability and weight constraints), **placement** of one ESS per vehicle (increase in the costs), standstill of the vehicle for implementation, maintenance and repair are the main drawbacks. In fact, for an on-board energy storage device, the vehicle would require enough free space for accommodating the box of energy storage and the vehicle would have to carry approximately 2% **more mass,** [38] which leads to an increase in the traction energy consumption by 1‑2% [39,40]. Therefore, the installation of on-board ESS is remarkably considered when designing new vehicles.

The **tuning analysis** is necessary to obtain an optimal design of on board ESS, for avoiding unuseful increase both in mass and in volume of the system (in case

of oversizing), or cases of energy wasting (as concerns undersizing). The sizing method for on-board ESS depends strongly on the task for which it has to be designed, and it will be slightly different among them.

When aiming at improving the energy savings, an assessed criterion for is that the ESS have to receipt the maximum amount of braking energy that can be recovered in a sudden braking, assuming that no energy can be returned to the main network [41]. This procedure can be made more accurate if *variable speeds* and *occupancy rates* are taken into account, also considering *weights* and *costs* to determine the *optimal storage size* [42,43].

If the task attempt at reducing the voltage drops at the feeding line [44], or supporting the AC and DC auxiliary electrical power supply (air-conditioning, lighting, compressed-air production, et al.) [45], it requires to take into account the operational characteristics of the whole line, e.g. distance between substations and trains timetables [43,46]. Some approaches based on *optimization techniques* have also been employed in order to achieve better overall sizing of the storage unit contemporaneously guaranteeing minimization of line voltage drops [47].

Lastly, in the case the main target of the ESS is to allow autonomous operations in *catenary-free* mode [48,49], the system has to be sized in order to supply both the traction drive and vehicle auxiliary systems. Even in this case, it is common optimize the driving style so as to reduce the size of the on-board ESS [43,50].

As regards the *control* of on-board ESS, several parameters such as vehicle speed and mass, SoC, requested traction power and line voltage must be properly taken into account. In any case, control systems have to guarantee that ESS are charged enough to power the vehicle during accelerations and that they keep discharged when braking or during a charging phase from the main supply, so to re-accept the highest amount of regenerative energy.

2.4 State of the art and commercial solution for on-board ESS application

In the following, an *extended review* of the most relevant studies published so far on regenerative energy storage on board vehicles in urban rail is presented.

It easy to see that the great majority of works focus on the application of SC technology. This remarks and put in evidence that **supercapacitors** have been considered as the most suitable option for **on-board applications** for the reasons before extensively described.

SC have good performances in terms of power density, charge and discharge time, long life time cycles, reduced maintenance cost, lower internal resistance and they are widely used for storing regenerative braking energy in public transportation.

There are many *researches* and *applications* which have studied the performance of the **SC** from verification testing to practical use in passenger service. Among the *academic articles*, most discuss the *design* and *sizing* for energy consumption reduction, also supported by real data recorded in measurement campaign conducted in some operating urban lines. *Barrero et al.* discuss the design and energy consumption reduction leading to energy savings of 18÷33 % in one Brussel tram line and 18.6÷35.8 % in one Brussel metro line [51,52]; an assessment of energy consumption reduction has been done by *Dominguez et al.* with resulting 24 % saving in the Metro de Madrid [39]; the same analysis has been carried out by *Chimera et al.* in Blackpool tramway with an overall energy saving of 30.6 % [53] or up to an extra 8 % by adopting a novel converter topology and depending on passenger loading [54]; *Sekijima et al.* have verified the benefits of the an SC ESS on CJRC's metro trains running between Nagoya and Jinryo on the Chuo line (Japan), showing that the ESS unit is able to store 8% of regenerating energy from the motor, which was equal to 1.6 % of energy for acceleration [55]; lastly, *Destraz et al.* confirm an increase in global energy efficiency of the system by a factor between 19.4 and 25.6 % in Mannheim tramway [56].

Some other papers assess *sizing* and *control* of on-board SC ESS for both *energy consumption* and peak-power reduction and *voltage stabilization*, many times confirmed by experimental laboratory validation. *Iannuzzi and Tricoli* have suggested a sizing methodology and a state control for power peak reduction

with method validation by means of simulation and laboratory tests, finalizing power peak demand reduced up to 50 %, with consequent reduction of line drop voltage up to 1 % and 30 % recovering energy on board [57,58]. The same authors proposed a control for maximum energy recovery with theoretical analysis and numerical simulation referring to the Rome metro line B: theoretical energy saving up to 38 % could be achieved [59]; *Ciccarelli et al.* confirmed the validity of this proposed control by means of experimental tests on a laboratory prototype, reaching 12 % energy saving with 22.5 % current peak reduction and a maximum line voltage drop of 5 % respect to the supply rated value [60].

Other approaches based on *optimization theory* are proposed in order to reach both an optimal size of the on-board storage devices and an optimal charge/discharge control. *Miyatake and Matsuda* present the optimal train operation with EDLC minimizing energy consumption up to 5.67 % [61], whereas *Iannuzzi and Tricoli* . use constrained and multi-objective optimization problem for the determination and implementation of the real time control strategy [47]. Finally, as regards the development for *catenary-free operation*, *Mir et al.* present experimental results obtained from a full scale tramway for obtaining 12 s of autonomous mode operation [62], and *Allegre et al.* have verified the control in autonomous mode on a reduced-scale subsystem [48].

Concerning the use of *on-board* **flywheels** in urban rail, *Henning et al.* report on the construction of a prototype by CCM for hybrid light rail vehicles (Ultra Low Emission Vehicle – Transport Advanced Propulsion 2 project), whose numerical simulations remark a comparison between the fuel consumption of the hybrid driven vehicle and the diesel electric driven tram train showing a reduction of more than 40 % [63]; *Daoud et al.* verify experimentally in lab a DC bus control for a FES system underlining a maximum over/under voltage overshoot of 2 % during braking/overloading operation [64]. On the other hand, *Glickenstein* states that a recent agreement between Alstom Transport and Williams group, will lead to the installation of hybrid power flywheels aboard of Alstom's Citadis trams, which will be able to offer potential fuel savings of 15% [65].

Due to their low power density and short lifecycle, the use of **batteries** as *on-board ESS* has not been extensively discussed in the relevant literature so far. However, recent studies have revealed promising results for the application of

lithium-based batteries on board. *Ogasa*, reports the activities of the Railway Technical Research Institute in Japan which has developed and successfully tested a hybrid electric light rail prototype incorporating a Li-ion battery to achieve up to 30 % of energy saving in one light rail line in [50]. On the other hand, among the applications for lithium-based batteries on trams for catenary-free running, *Jeong et al*. present several simulations that have assessed the performance of the new low-floor Light Rail Vehicle with Li-poly batteries on board without any real operation results [66].

Commercially speaking, in urban rail applications the *major companies* dedicated to the railway business have developed their own solutions. Even in this sector, most of the manufacturers have opted for the **SC technology** in their proposals, presenting a range of different products to enhance the efficiency of electrified railways. Every company has carried out the research and development by verifying tests on the real vehicle to confirm the performance of their product.

Bombardier Transportation developed a SC-based system for recovering braking energy in LRVs, metro trains and diesel multiple units: the *MITRAC Energy Saver*. This product is based on the series connection of high performance EDLC, which can quickly charge and discharge high power from train braking and acceleration. The schematic of MITRAC energy saver is shown in Figure 2.16 [67].

Firstly, MITRAC Energy Saver was installed aboard a prototype of a light rail vehicle for public transport by the German operator Rhein-Neckar-Verkehr Gmbh in Mannheim, from Sept. 2003 to 2008. *Steiner et al.* state that the measured performance showed by MITRAC energy saver could reduce the consumption of the traction energy by 30% and line current peak and voltage drop by 50% [38,46]. This feature is of interest for weak power lines where the current must be limited to avoid unacceptable voltage drops. In addition, in the areas of historical buildings, city center squares, tunnels or even transient faults in the grid where catenary free running is required, the additional aboard MITRAC Energy Saver energy storage device can support this requirement and this has been verified as before said: 1 kWh, 300 kW, 477 kg MITRAC Energy Saver was installed aboard the prototype LRV in Mannheim; this vehicle could run without external power source at a speed of 26 km/h and for a distance of 500 m.
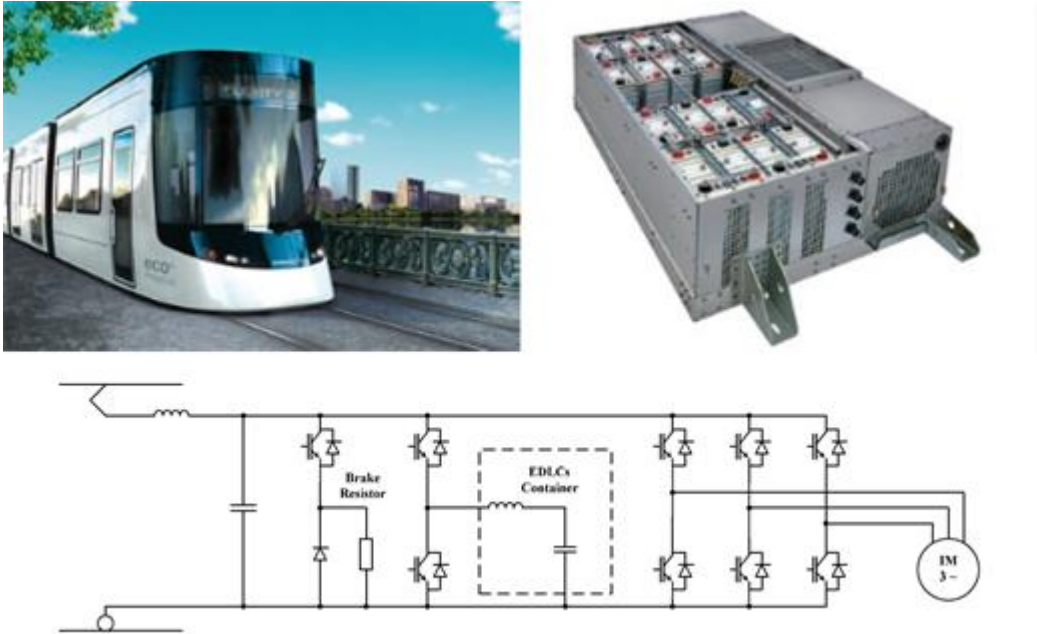
Figure 2.16 - The MITRAC concept on BOMBARDIER FLEXITY 2 light rail vehicle platform, and its electrical schematic [67]

The storage device was recharged quickly by an overhead bus-bar feeder at the substations. The feeder is capable of charging 3 kWh within 20 seconds with a maximum current of 1 kA. On the other hand, the main disadvantages of MITRAC Energy Saver present are the higher train mass, increased by approximately 2%, and the further space required to install on-board the device.

For competition, *Siemens* has developed the *Sitras MES* system for braking energy storage in electric and diesel rail vehicles (see Figure 2.17).

Siemens remarks that the mobile energy storage unit can be integrated in new rail vehicles directly (integrated concept see Figure 2.18) or can be installed at existing rail vehicles additionally (independent concept see Figure 2.19), thus allowing energy saving up to 30 % of the supplied energy and scalability of the energy content for different rail vehicles [68].

Figure 2.17 – Modular design of the SITRAS MES [68]
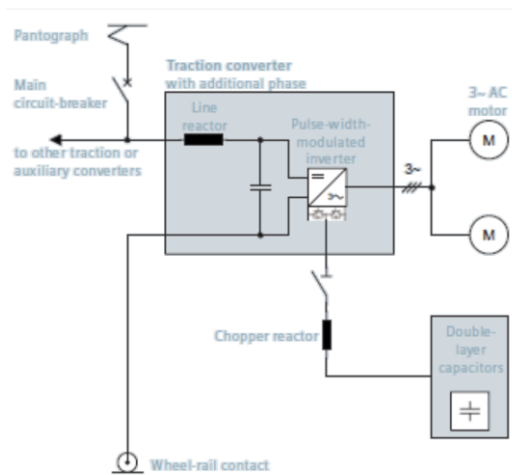
Figure 2.18 – The SITRAS MES Integrated concept [68]
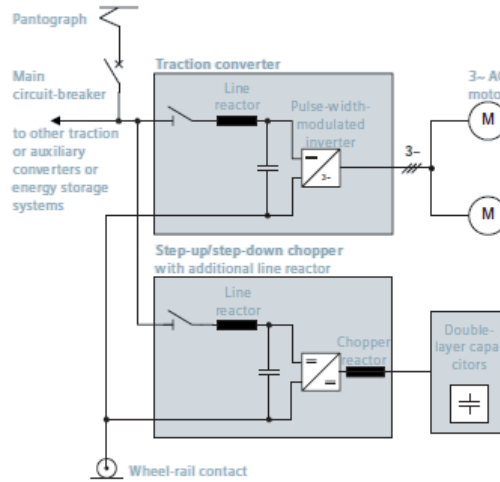
Figure 2.19 - The SITRAS MES Independent concept [68]

According to the manufacturer, a 0.85 kWh, 2x144 kW, 820 kg system has been used to retrofit Innsbruck tramway (Austria) in 2011.

Another EDLC-based ESS available on the market is the *ACR* (Rapid Charge Accumulator) *evoDRIVE* system developed by *CAF* in Spain. This system has been successfully tested on a CAF Urbos-2 vehicle in Seville, Saragozza and Granada and is currently available as a standard option in the new Urbos-3 trams (see Figure 2.20). *CAF* confirms approximately 20 % in energy savings and up to 100 m in a catenary-free area [69].

Figure 2.20 – CAF evoDRIVE solution [69]
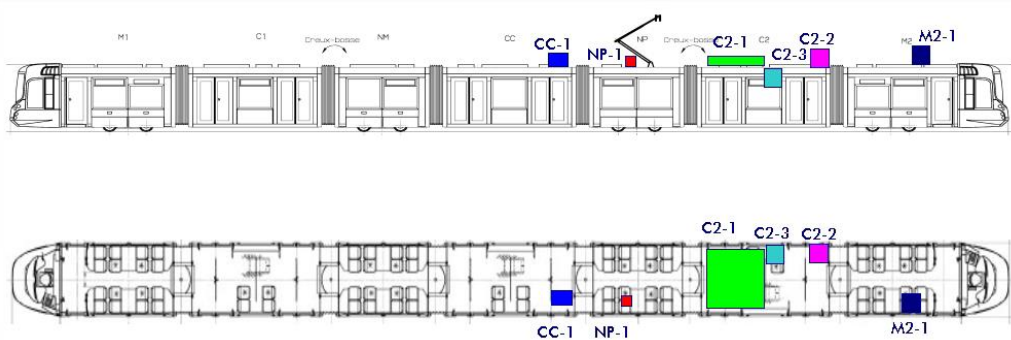
Figure 2.21 – STEEM box and its installation on roof of RATP Citadis [70]

Lastly, *Alstom* has developed the *STEEM* (Maximized Energy Efficiency Tramway System) aiming at increasing the energy efficiency in tramway systems while allowing catenary-free operation. This solution was tested on a RTPA tramway (Paris) in regular operation (see Figure 2.21).

Moskowitz and Cohuau assert that for the test results in the spring with a milder climate, a 1.6 kWh STEEM unit can reduce the average daily energy consumption by 13%, with a minimum and maximum of 10% and 18% respectively, allowing also up to 300 m of autonomy in catenary-free mode [70]. The measure of energy consumption however depended on the driving style, elevation of the land and traffic restrictions. The EDLC modules were quickly charged at the arrival station and then discharged to support the tram acceleration without another supply. The automatic control of this operation was based on the GPS localization. Unfortunately, no results of commercial application have been reported yet.

For applications where relatively long distances of catenary-free operation are required, **battery-based** solutions have been preferred by manufacturers. In this regard, the Japanese manufacturer *Kawasaki* has installed more than 200 Ah capacity, 200 kg, Nickel-metal hydride batteries on a prototype vehicle called
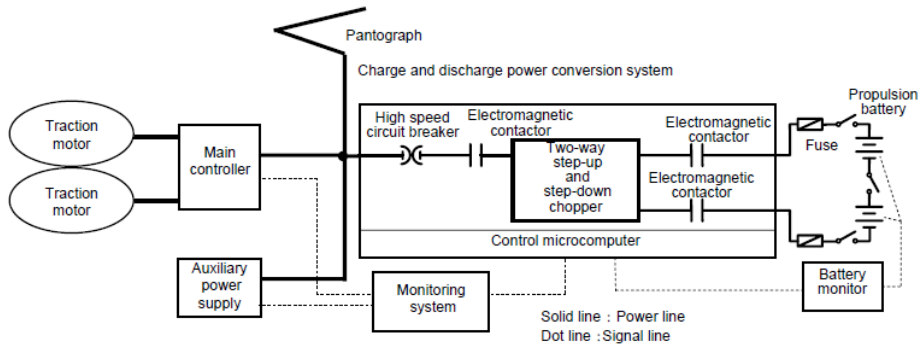
Figure 2.22 – Circuit configuration for ESS on SWIMO [71]

"*SWIMO*" (*Smooth Win MOver*) by Sapporo Municipal Transport and Kawasaki Heavy Industry (see Figure 2.22), whereas *Kinki Shayro* installed Li-ion batteries on the prototype LFX-300 in Charlotte (USA). As concerns the first one, *Akiyama et al.* tested the travel distance at non-electrified line and this resulted more than 10 km with charging times from 3 to 5 minutes [71]; the second one is able to run for up to 8 km on battery power [72]. In both cases, the batteries are able to absorb the regenerative braking energy, but they are mainly recharged through the feeder line during stops.

In turn, the *Citadis* tramway, with a 576 V, 80 kWh NiMH battery developed by *Saft*, was chosen to operate for the first time in Nice, France, by *Alstom* transportation, enabling a catenary-free operation in two non-electrified sections of about 500 m in the historical city center (see Figure 2.23). This tram had a maximum speed of 30 km/h and was able to run catenary free over a length of 1 km [73].

A different approach for urban rail vehicle has been proposed by *Siemens*, which has developed a *hybrid ESS* known as *Sitras HES*, which consists of a nickel metal hydride battery, provided by Saft, and a Sitras MES module based on EDLC [74]. The idea behind this hybrid device is the integration of the two different storage devices to get at the same time high power and energy densities, reaching better performances (see Figure 2.24).

The *Sitras HES*, having energy capacity between 1 and 2 kWh, can be charged quickly and then release the energy stored to the traction motors for the acceleration. On the other hand, a 18 kWh traction battery with high energy density is used to supply the tram for long distances between stations and power to air conditioning and heating required.
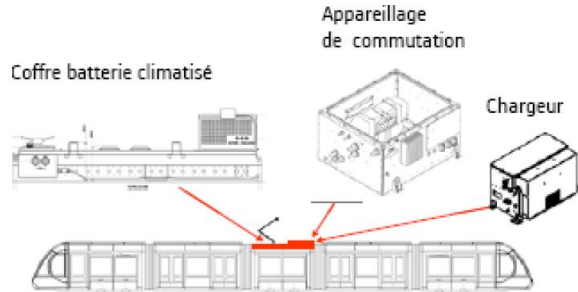
Figure 2.23 – Integration layout of the NiMH battery on the Citadis tramway [73]

The hybrid energy storage device is capable of recharging energy from regenerative braking and also from a dedicated quick charging unit at the substations. This has been tested in passenger operation installed on the roof of a redesigned tram belonging to the Portuguese company Metro Transports do Sul S.A. (MTS), called "Combino plus MTS", which serviced passengers in Lisbon. *Meinert* confirms that an energy saving of 10.8 % in revenue operation and an use without contact line up to 2.5 km is realized by the Sitras HES [37].

Even the Spanish *CAF* proposes a similar solution, called *freeDRIVE*, which is an on-board ESS based on supercapacitors and Li-ion batteries, for the catenary-free operating mode. This hybrid technology incorporates all the energy advantages of the evoDRIVE whilst making it possible to eliminate the overhead power line along the sections. Its key characteristics are approximately 30% energy savings, up to 1400 m in catenary-free operation and ultra-fast charging process, taking just 20 seconds. [69]. This system is compatible with all tram types, both on new installations or on already existing infrastructures.
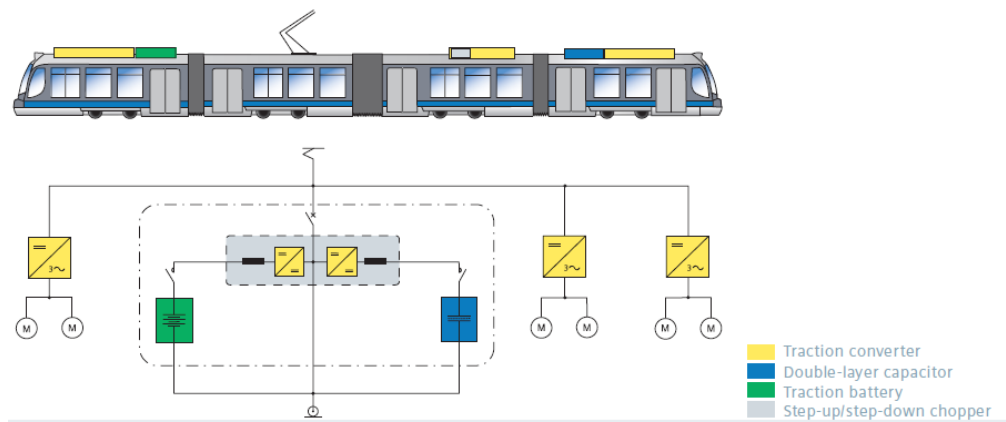
Figure 2.24 – The Siemens SITRAS HES concept [74]

2.5   Characteristics of Stationary ESS installation in urban rail

Stationary, or **wayside** or **trackside**, ESS consists of one or several ESS placed along the rail tracks (see Figure 1.12). This configuration is able to store the surplus braking energy that cannot be directly supplied to other non-receptive vehicles and feed the energy back into the overhead contact lines for subsequent accelerations as far as the same electrical supply section is involved. This contribute to the **quick** and *efficient energy recovery* associated with the reduction of the power delivery rate by *power peaks shaving* and a global improvement of the *power quality* for the whole electrified urban mass transportation system [75]. At the present state of the art, moreover, stationary storage devices seem to be the more suitable solution for *reducing voltage drops* without strong modifications on the main elements of the electrified line, as for example the repowering of electrical substations and the increase of the cross-sectional area of overhead contact wires [44]. Lastly, their implementation and maintenance do not affect operations.

Wayside ESS are usually installed in *existing electrical substations* or in specific places where the contact line voltage variations are more significant, for instance near to *passenger stations*, where it might occur in practice the maximum accelerations and brakings of at most two vehicles circulating in the same feeding line section [76].

This solution can be used by all vehicles operating on the line, and permits different advantages as voltage stabilization by mitigating voltage sags typically associated with end of lines [77], reduction of the peak power demand by averaging loads over a period of time, reduction of the number of traction substations or possibility to include vehicles without upgrading the electrical network. The main drawbacks are related to *fine-tuned analysis* for *sizing* the systems and for choosing the right location, less efficient system due to *overhead line losses* increasing with the distance of the vehicle, if undersized some energy may still be lost in the braking resistors, place availability in the substations or along the line, and no opportunity for individual catenary-free operations.

For the design issue, it is also very important to take into account the variability of the traffic conditions [52] and the service frequency, leading to a fine-tuned

analysis that is required to achieve a compromise solution that optimizes both the size and the optimal position of stationary ESS [78].

The charge and discharge processes require a proper controller that generally operates as a function of the line voltage on the line: when an overvoltage takes place as a result of any braking process, the ESS operate in charging mode by using the excess of regenerated energy on the line; conversely, when a voltage drop is detected, the ESS supply the stored energy in order to keep the threshold value on the network.

2.6   State of the art and commercial solution for stationary ESS application

As in the case of on-board ESSs, it is interesting to note that SC has been the preferred technology for stationary systems so far. Most of the studies dealing with the application of this technology focus on the development of methodologies to obtain *optimized* ESS *designs* and *siting* for urban rail.

In this regard, some *optimization procedures* based on a nonlinear programming technique have been developed. *Ciccarelli et al.* propose an optimization procedure for choosing in the planning stage the fundamental characteristics of a stationary storage device validating the procedure by means of a case simulation [79,80]; *Iannuzzi et al*. show that the optimal design of a stationary ESS can be regarded as a classical isoperimetric problem, whose solution is very attractive in order to determine also the optimal allocation of the storage device: this complex procedure has been validated by simulating it on a tramway system [78]. In order to investigate the need of examining the probabilistic nature of the interest variables, *Lauria et al.* take into account the stochastic nature of the design variables for the aforementioned sizing methods, validating the methodology by means of a case simulation [81], whilst again *Ciccarelli et al.* suggest a multiobjective optimization approach verifying the procedure by means of simulation on a light rail system and laboratory tests [82,83]. Alternatively, another probabilistic method to size wayside ESSs in metro lines has been presented by *Foiadelli et al.* in [84] by referring the application on the metro line in Milan.

All these papers, however, also emphasize the improvements in terms of *energy saving* and above all as regards the *line voltage stabilization*. In particular,

Barrero et al. propose a power flow controller to handle the energy flow in function of the state of charge and evaluate the influence of ESS size and positioning along the line with reference to a simulation in one Brussel metro line. Savings between 11 % (at peak time) and 26 % (at night and weekends) can be achieved depending on the scenario [85]. Interestingly, *Rufer et al.* an ESS based system to reinforce a weak railway network in the city of Lausanne (Switzerland) resulting in a maximum voltage drop compensation of 8.3 % [77]. Other papers discuss deeply the **energy consumption reduction** and the *cost benefits* also by making reference to simulation and prototype installation on real lines. *Teymourfar et al.* propose a simpler algorithm based on predicting the maximum instantaneous regenerative energy and simulate its application on a stationary ESS on the line 3 of Tehran metro network: the results remark a daily energy saving of 25 % and a return of the total investment after 10 months [86]; *Lee et al.* test a ESS on the Seoul Metro line 7, also providing an optimized sizing, pointing out an operation costs reduction of 28 % [87]; *Killer et al.* discuss a fundamental design and the simulation of a EDLC stationary ESS placed along the track in the Metro of Medellin in Colombia and observed between 2.5÷19 % of the consumed energy to be storable, with high and low train density respectively, and payback period of 3÷4 years [88]; *Kwon et al.* verify their proposed control for ESS installation in the Daedong substation of the Daejeon Metropolitan Rapid Transit Co. (Korea) to compensate voltage drop and saving energy. The test results shows that the ESS can save about the 23 % of the energy with a reduction of the DC line voltage fluctuation up to the 3 % of the no load rated voltage [89]; *Okui et al.* put in evidence the installation of two ECDL ESS by Seibu Railway Co. at Agono and Shumaru substations (Japan), which are able to deliver back to the train 77 % of the recovered energy [90]; *Morita et al.* validate two prototypes of wayside ESS in Osaka (600 V in Gokurakuji station and 750 V in Osakako station) showing 7 % and 8.3 % of maximum voltage drop in 750 V and 600 V lines respectively [91]; Finally, it is worth mentioning the work of *Konishi et al.* that compared charge–discharge characteristics of EDLCs and lithium batteries by means of tests carried out at DC 75 V and decided for the ECDL technology to develop an ESS for voltage stabilization purposes [92]. The tests performed at 400 V (laboratory level) revealed very promising results for railway applications.

As for the use of **flywheels** in *wayside ESS*, in 1984 *Turner* showed a technical and economic evaluation between lead-acid batteries and flywheel for using as stationary ESS in Canadian utilities: an application of 10 MVA, 5 MWh, assuming an operating life of 20 years, gives a discount rate of 8 % [93]. *Okui et al.* state that in 1988, flywheels with rated energy and power of 25 kWh and 2,000 kW respectively, were installed in the Keihin Electric Express Railway at the Zushi post in Japan: the report showed that flywheels could save up to 12% of total energy [90]. *Richardson* reports on the performance results on the London underground of a flywheel ESS developed by the company Urenco, which provides a very fast response to changes in power demand and is able to switch between full power motoring and generating modes within 5 ms [23], whereas for the same metro, *Radcliffe et al.* verify a 300 kW testing flywheel, stating that by using at least 1 MW stationary ESS it is possible to reduce the power consumption by 26% per year of and a capital investment recoverable within 5 years [94]. Lastly, *Wheeler* discusses the application of 3×200 kW flywheel units installed on the Lyon metro for regulating the 3rd rail voltage between 850 V and 860 V during train braking. As a result, the track receptivity of the Lyon metro network was increased and the use of mechanical brakes and their maintenance costs were also reduced [95]. More recently, the cooperation among three institutes of railways in Spain, the ADIF Railways infrastructure manger, CEDEX Studies and the CIEMAT Centre, designed, developed and tested a stationary FES system. As *Iglesias et al.* state, within a first project, called "ACE2", they had prototyped a flywheel able to store 200 MJ of energy and able to transfer a power of 350 kW [96]; *Garcia Tabares et al.* prove a limited size of the prototype of 150 kW and 50 MJ, respectively in a 3 kV DC network with no train interactions, though trials under real traffic conditions are expected to be performed in Madrid commuter lines. As concerns a second project called "SA2VE" the flywheels store 3.2 MJ of energy and are able to transfer 5.6 MW of power within 9.5 minutes having therefore an extremely high capacity of smoothing the electric substation power peaks [97].

Ultimately, very few papers face on **BES** system for *wayside* applications [75,90,98]. Among these, it is worthy to remark that *Ogura et al.* describe the NiMH *Gigacell* Battery Power System (see Figure 2.0.25) developed by Kawasaki and present the experimental results of tests conducted at the New York City Transit network that have demonstrated the capability of the system

to capture and manage regenerated braking energy (see Figure 2.26). The battery pack was 670 V, 600 Ah, 400 kWh.

By continuing the discussion on batteries, in addition to the abovementioned Gigacell BPS system, other two solution based on Li-ion technology are commercialized: the *Intensium Max* system, developed by *Saft*, and *B-CHOP* system, developed by *Hitachi*. The first one system, with its 1.5 MW peak power charge/discharge power and 420 kWh storage capability, is currently being tested in the Philadelphia public transport network, as part of an innovative project launched by SEPTA in partnership with *Viridity Energy*, which aims at recovering the full regenerated energy capability of the line and energy return to the main grid [99]. The power control and conversion capabilities in that stationary ESS are provided by the *Envistore* system, originally developed by *Envitech Energy Inc.* to work with SC [100].

Figure 2.0.25 – The Gigacell BPS [98]
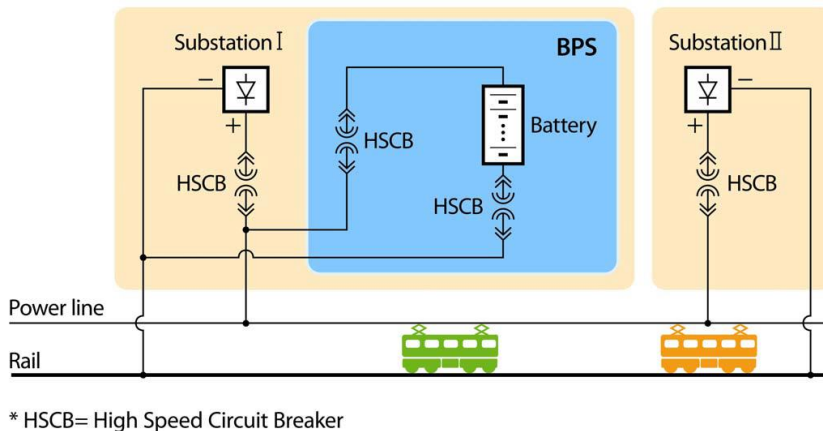
Figure 2.26 – An example of BPS System Diagram [98]

Certainly most of the *manufacturers* develop their **stationary ESS** by adopting the **SC technology**. The most used and commercialized so far appear to be the *Sitras SES* (Static Energy Storage) system marketed by *Siemens*. Its schematic is shown in Figure 2.27 [102].

Maher claims that a 2,5 kWh, 0,7 MW *Sitras SES* could save nearly 30% of energy, reduce the peak power required from the network by 50 %t and regulate the voltage, which improved the reliability of the rapid transit systems and tramways. Another advantage gained by *Sitras SES* is to help the power supply system to avoid short periods of electrical failure [103].
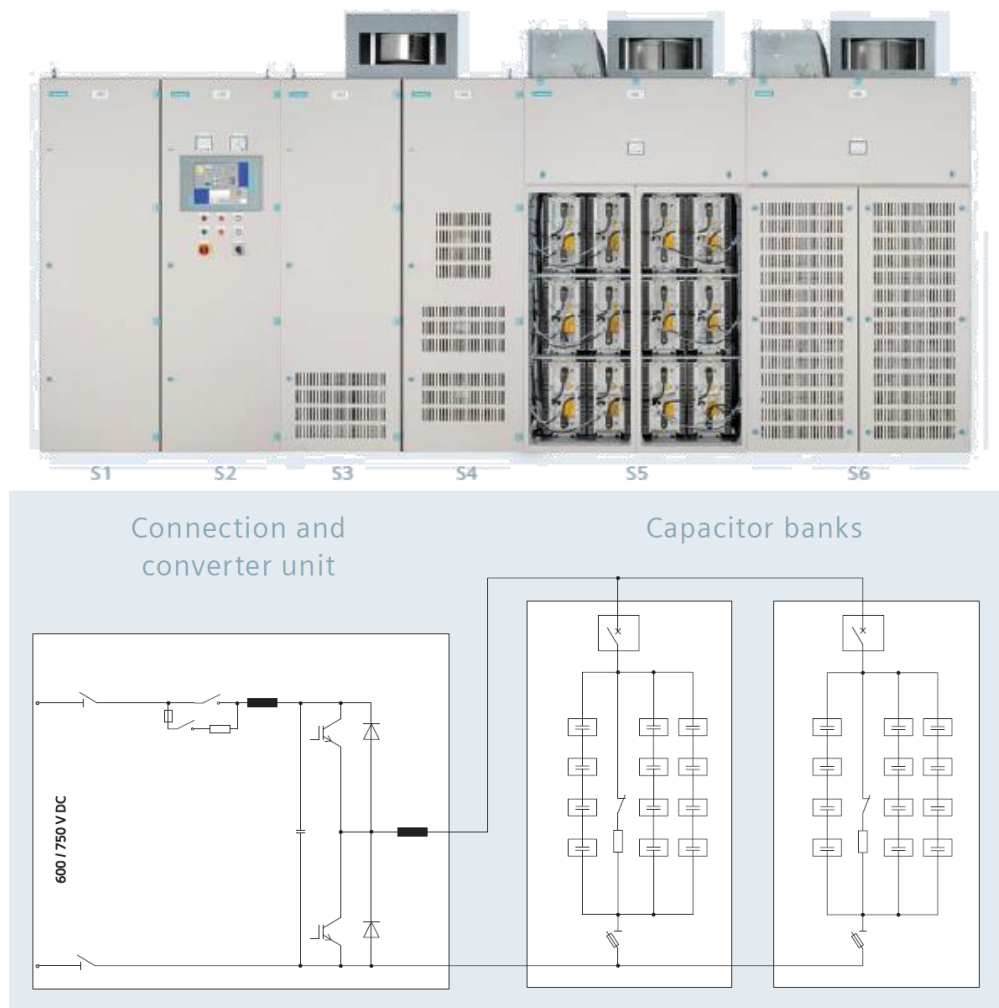
Figure 2.27 – Overview and block diagram of the Sitras SES [102]
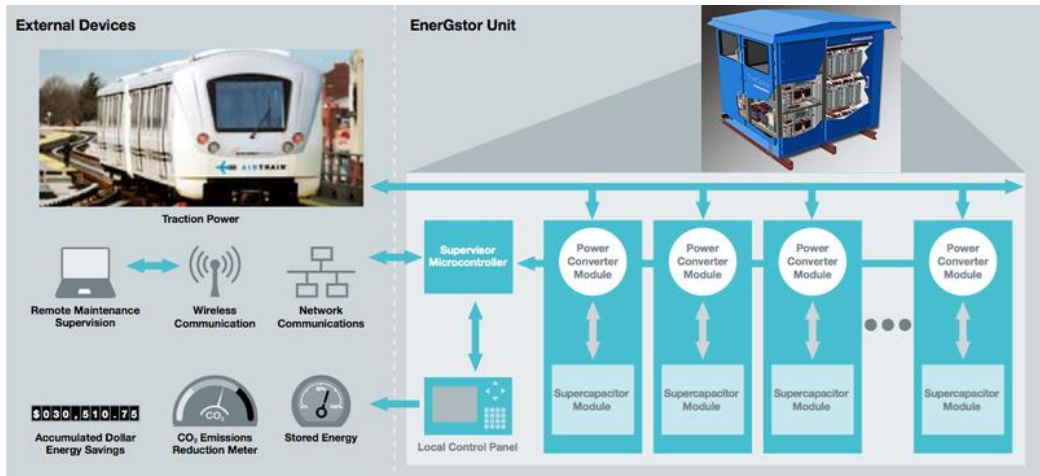
Figure 2.28 – Integration of the EnerGstor unit [104]

There are many applications of the *Sitras SES* in urban public transportation, including *Kölner Verkehrsbetriebe AG* in Cologne, Germany in 2001, Madrid, Spain since 2003 and Portland, Oregon, USA, operating since 2002, Bejing metro, China, in service since 2007 and Toronto rail transit, in service since 2011.

As a competition, *Bombardier* has developed its own system based on supercapacitors, the *EnerGstor* (see Figure 2.28). The system design is scalable, with an energy capacity ranging from 0.25 to 5.0 kWh or more of electrical energy generated by a rail vehicle's braking energy recuperation system and it is capable of offering a 20 to 30% reduction in grid power consumption.

EnerGstor technology can be monitored and controlled locally or remotely through the internet [104]. 1 kWh Energstor prototype unit has been designed, assembled and tested at Kingston (Ontario) by Bombardier (see Figure 2.28).

Adeneo, a member of *Adetel Group*, has developed the *NeoGreen Power* (Ground Regenerative Electricity for Economic Network Power) system (see Figure 2.29). The system offers a storage modularity by autonomous storage branches: the autonomy of every branch allows the system to remain operational in case of one branch faulty [105]. This system is currently being tested in line T2 of the public transport network of Lyon (TCL), where 2 kWh bay has been in operation with very promising energy consumption reduction up to 40 %.
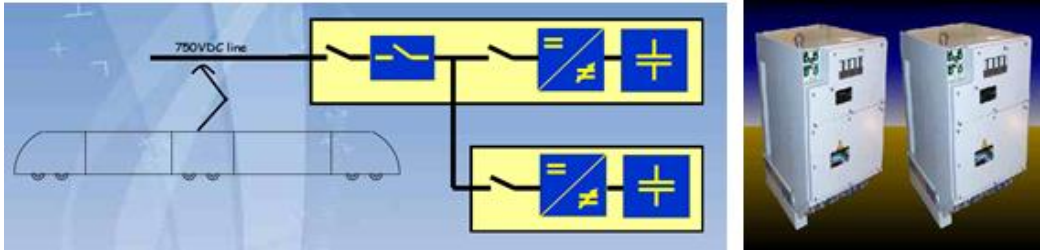
Figure 2.29 – The NeoGreen system [105]

In turn, *National Korean railway research agency* (KRRI) has been trialling the use of SC wayside ESS to store braking energy on the Seoul and New York metro networks. KRRI has contracted *Woojin Industrial Systems* to manage the pilot project in Korea in 2008. A 583 V, 10.5 MJ equipment has been tested at a facility in Gyeongsan (see Figure 2.30). Initial tests suggest that the use of this stationary system could reduce overall energy consumption by 23,4% and would help stabilizing the voltage with a recover of the cost of installing the equipment within 4 years [106].
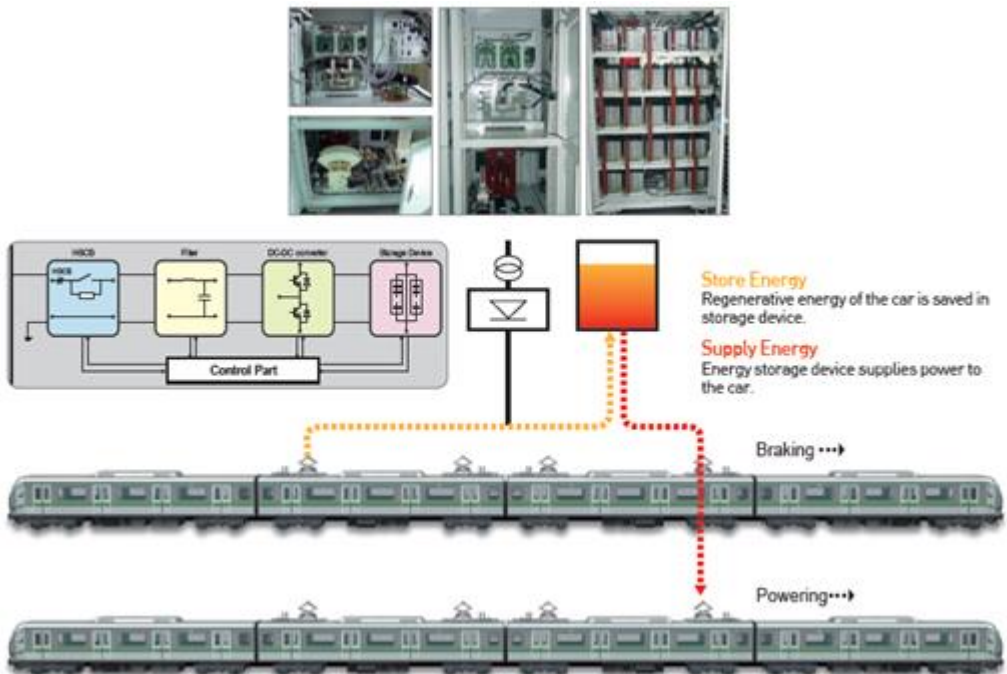
Figure 2.30 – Woojin stationary ESS installed in Gyeongsan LRT [106]

Other EDLC-based systems commercially available are *Capapost,* developed by *Meiden* (see Figure 2.31), and the previously mentioned *Envistor* system (see

102
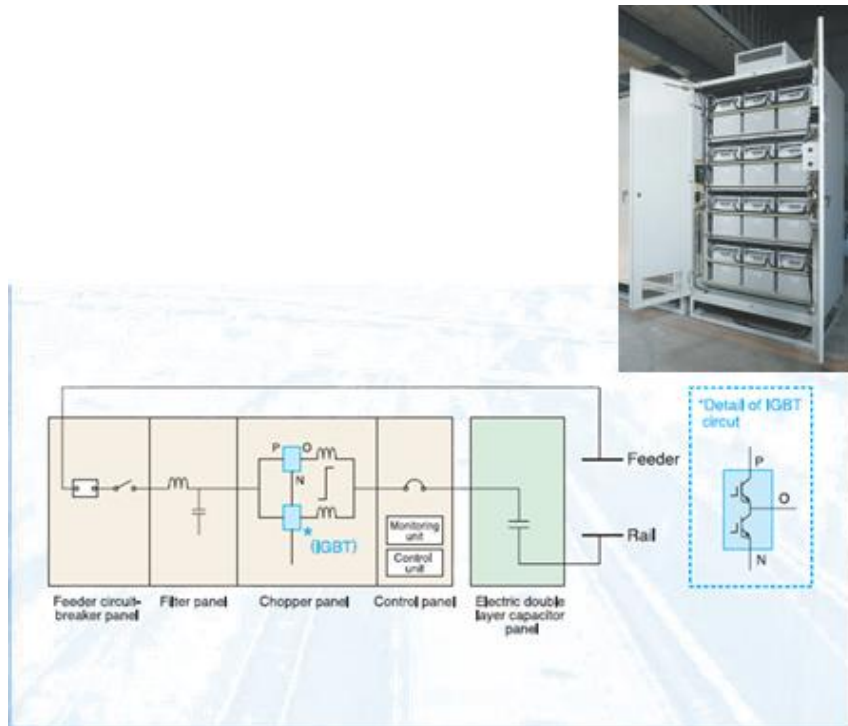
Figure 2.31 – Composition of CAPAPOST regenerative power storage system [107]

Figure 2.32), marketed by *Envitech Energy*, a member of the ABB Group, with great scalability from 2.8 to 45 MJ of storable energy. These systems have been reported to be installed in Hong Kong and Warsaw metro systems, respectively [107].
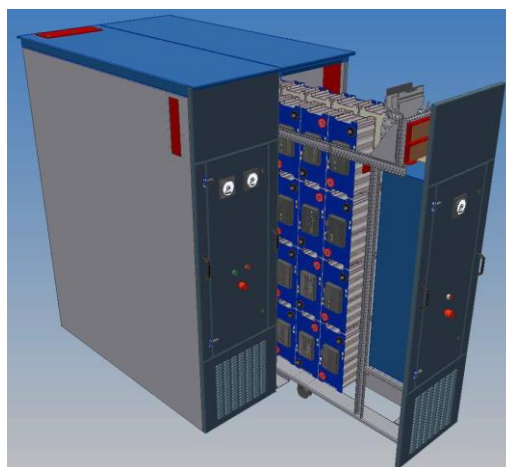
Figure 2.32 – ENVISTORE product view [108]

Finally, as mentioned earlier, an alternative to SC technology proposed by manufacturers, can be **stationary ESS** using **flywheels**.

For instance, The German company *Piller* has developed the *Powerbridge* storage system consisting in kinetic energy storage unit and the interface between the unit and the contact wire (see Figure 2.33)[109]. The system has been installed in Hannover in 2004 with maximum power 1 MW and usable energy content approximately 5 kWh; the French city of Rennes installed a 1 MW flywheel system in Sept. 2010 on their VAL automatic metro network. The 5 kWh available energy system is located in the middle of the metro line and the average efficiency is around 80% except when there are fewer trains where efficiency goes up to 90 %.
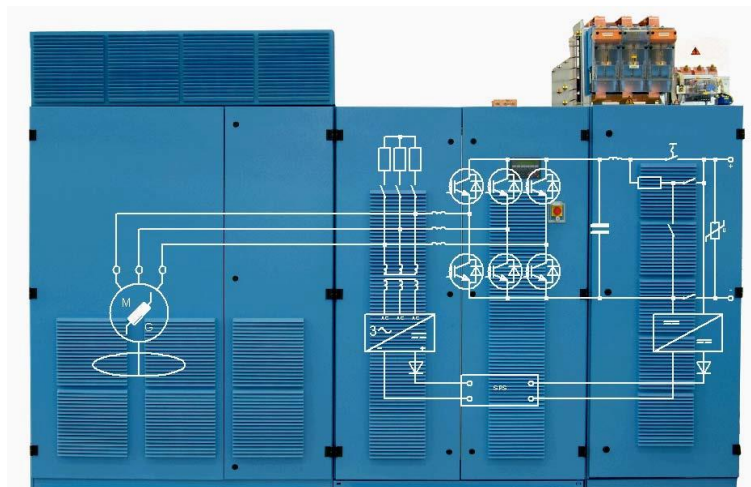
Figure 2.33 – Piller Powerbridge flywheel stationary ESS [109]

Kinetic Traction Systems (KTS) (formerly PENTADYNE) has developed carbon fibre flywheels (*GTR system*) with 200 kW high cycling system featuring a high speed composite rotor running on frictionless bearings requiring no maintenance and an available energy of 1.5 kWh (see Figure 2.34). It is worth remembering that the GTR system, has been originally developed by Urenco Power Technologies, but KTS holds exclusive license to manufacture the technology [110].

Figure 2.34 – The integrated GTR 200 flywheel stationary ESS [110]

Lastly, the *Regen* system has been mainly used for braking energy storage in cranes, but the manufacturer offers a version specifically designed for railway Applications (see Figure 2.35). *Vycon* installs a wayside ESS at Los Angeles metro network, which captures the regenerated energy at cycles as low as once per minute and can scale up in power capacity with parallel systems [111].
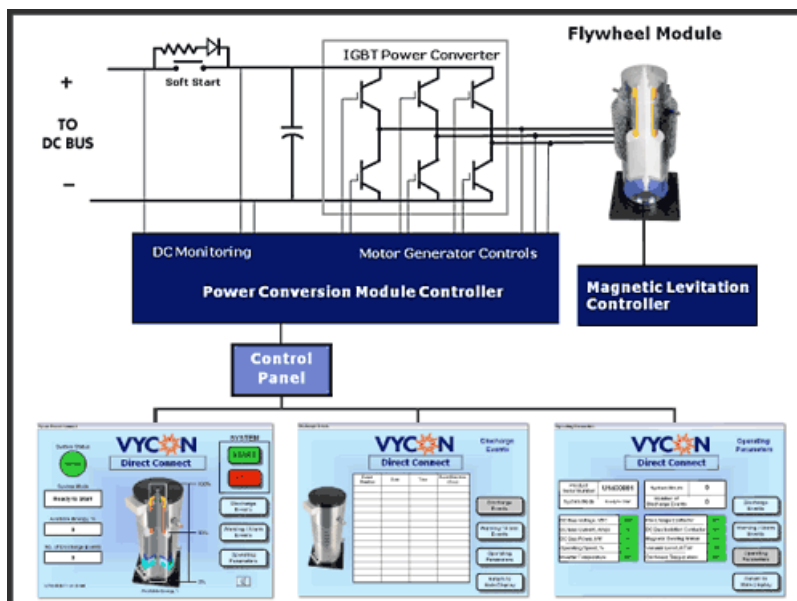
Figure 2.35 – VYCON's REGEN flywheel ESS [111]

2.7   Chapter 2 references

[1] Ibrahim, H.; Ilinca, A.; Perron, J. Energy storage systems-characteristics and comparisons. *Renewable and Sustainable Energy Reviews, vol.* 12 (5), June 2008, pp. 1221-1250.

[2] Chen, H.; Cong, T. N.; Yang, W.; Tan, C.; Li, Y.; Ding, Y. Progress in electrical energy storage system: A critical review. *Progress in Natural Science,* vol. 19 (3), Mar. 2009, pp. 291-312.

[3] Ribeiro, P. F.; Johnson, B. K.; Crow, M. L.; Arsoy, A.; Liu, Y. Energy storage systems for advances power applications. *Proceedings of the IEEE,* vol. 89 (12), 2001, pp. 1744-1756.

[4] Vazquez, S.; Lukic, S. M.; Galvan, E.; Franquelo, L. G.; Carrasco, J. M. Energy storage systems for transport and grid applications. *IEEE Transactions on Industrial Electronics,* vol. 57 (12), Dec. 2010, pp. 3881-3895.

[5] González-Gil, A.; Palacin, R., Batty, P. Sustainable urban rail systems: Strategies and technologies for optimal management of regenerative braking energy. *Energy Conversion and Management*, vol. 75, 2013, pp. 374-388.

[6] Gomez-Parra, M.; Gonzalez-Fernandez, F. J.; Muñoz-Condes, P.; San Andrés, M. A. G.; Sancho, C.; Carpio, J.; Guirado, R. Implementation of a new predictive maintenance methodology for batteries. application to railway operations. *Proc. 5th IEEE Vehicle Power and Propulsion Conference VPPC 2009,* Dearborn, MI; United States, 7-10 Sept. 2009, pp. 1236-1243.

[7] Czerwiński, A.; Obrębowski, S.; Rogulski, Z. New high-energy lead-acid battery with reticulated vitreous carbon as a carrier and current collector. *Journal of Power Sources,* vol. 198, Jan. 2012, pp. 378-382.

[8] Kirchev, A.; Kircheva, N.; Perrin, M. Carbon honeycomb grids for advanced lead-acid batteries. part I: Proof of concept. *Journal of Power Sources,* vol. 196 (20), Oct. 2011, pp. 8773-8788.

[9] Green, A. A nickel cadmium battery for new generation telecommunication applications using major technical improvements from electric vehicle battery developments. *Proc. 17th International Telecommunications Energy Conf. INTELEC 1995.,* The Hague, Holland, 29 Oct-1 Nov 1995, pp.766-771.

[10] Kritzer, P. Separators for nickel metal hydride and nickel cadmium batteries designed to reduce self-discharge rates. *Journal of Power Sources,* vol. 137 (2), Oct. 2004, pp. 317-321

[11] Nazri, G.A.; Pistoia, G. Lithium batteries: ccience and Technology. *Springer*; Berlin, 2009.

[12] Zhang, J.; Lee, J. A review on prognostics and health monitoring of li-ion battery. *Journal of Power Sources,* vol. 196 (15), aug. 2011, pp. 6007-6014.

[13] Rao, Z.; Wang, S. A review of power battery thermal energy management. *Renewable and Sustainable Energy Reviews,* vol. 15 (9), Dec. 2011, pp. 4554-4571.

[14] Mukherjee, R.; Krishnan, R.; Lu, T.; Koratkar, N. Nanostructured electrodes for high-power lithium ion batteries. *Nano Energy,* vol. *1* (4), July 2012, pp. 518-533.

[15] Brutti, S.; Hassoun, J.; Scrosati, B.; Lin, C.; Wu, H.; Hsieh, H. A high power sn-C/C-LiFePO 4 lithium ion battery. *Journal of Power Sources,* vol. 217, Nov. 2012, pp. 72-76.

[16] Kushnir, D.; Sandén, B. A. Multi-level energy analysis of emerging technologies: A case study in new materials for lithium ion batteries. *Journal of Cleaner Production,* vol. 19 (13), Sept. 2011, pp. 1405-1416.

[17] Ellis, B. L.; Nazar, L. F. Sodium and sodium-ion energy storage batteries. *Current Opinion in Solid State and Materials Science,* vol. 16 (4), Aug. 2012, pp. 168-177.

[18] Kraytsberg, A.; Ein-Eli, Y. Review on li-air batteries - opportunities, limitations and perspective. *Journal of Power Sources,* vol. 196 (3), Feb. 2011, pp. 886-893.

[19] Capsoni, D.; Bini, M.; Ferrari, S.; Quartarone, E.; Mustarelli, P. Recent advances in the development of li-air batteries. *Journal of Power Sources,* vol 220, Dec. 2012, pp. 253-263.

[20] Joerissen, L.; Garche, J.; Fabjan, C.; Tomazic, G. Possible use of vanadium redox-flow batteries for energy storage in small grids and stand-alone photovoltaic systems. *Journal of Power Sources,* vol. 127 (1-2), Mar. 2004, pp. 98-104.

[21] Abrahamsson, J.; Bernhoff, H. Magnetic bearings in kinetic energy storage systems for vehicular applications. *Journal of Electrical Systems,* vol. 7 (2), June 2011, pp. 225-236.

[22] Suzuki, Y.; Koyanagi, A.; Kobayashi, M.; Shimada, R. Novel applications of the flywheel energy storage system. *Energy,* vol. 30 (11-12 sp. iss.), Aug. 2005, pp. 2128-2143.

[23] Richardson, M. B.. Flywheel energy storage system for traction applications. *Proc. Int, Conf. on Power Electronics, Machines and Drives, PEMD 2002,* (Conf. Publ. No. 487), Bath, UK, 4-7 June 2002, pp. 275,279.

[24] Liu, H.; Jiang, J. Flywheel energy storage-an upswing technology for energy sustainability. *Energy and Buildings,* vol. 39 (5), May 2007, pp. 599-604.

[25] Flynn, M. M.; McMullen, P.; Solis, O. Saving energy using flywheels. *IEEE Industry Applications Magazine,* vol. 14 (6), Nov. 2008, pp. 69-76.

[26] Thompson, R. C.; Kramer, J.; Hayes, R. J. Response of an urban bus flywheel battery to a rapid loss-of-vacuum event. *Journal of Advanced Materials,* vol. 37 (3), July 2005, pp. 42-50.

[27] Miller, J. M. Ultracapacitor Applications. Iet Power and Energy Series, *The Institution of Engineering and Technology* , London, UK, 2011.

[28] Vondrák, J.; Sedlaříková, M.; Dvořák, P. Review on electrodes with extended surface area for supercapacitors. Proc. *ECS Transactions,* vol. 40 (1), 2012, pp. 75-84.

[29] Wang, G.; Zhang, L.; Zhang, J. A review of electrode materials for electrochemical supercapacitors. *Chemical Society Reviews,* vol 41 (2), Jan. 2012, pp. 797-828.

[30] Marumo, C.; Ando, N.; Taguchi, M. Design and performance of lithium-ion capacitors. *Proc. 3rd Eur. Symp. on Supercapacitors and Applications ESSCAP 2008*, Rome, Italy, November 6-7, 2008.

[31] Lambert, S.M.; Pickert, V.; Holden, J.; He, X.; Li, W. Comparison of supercapacitor and lithium-ion capacitor technologies for power electronics applications. *Proc. 5th IET Int. Conf. on Power Electron., Machines and Drives PEMD 2010*, Brighton, UK, April 19-21, 2010.

[32] Hsu, C.; Lee, W. Superconducting magnetic energy storage for power system applications. *IEEE Transactions on Industry Applications,* vol. 29(5), Sept. 1993, pp. 990-996.

[33] Sutanto, D., Cheng, K. W. E. Superconducting magnetic energy storage systems for power system applications. *Proc. 2009 Int. Conf. on Applied Superconductivity and Electromagnetic Devices, ASEMD 2009,* Chengdu, China; 25-27 Sept. 2009, pp. 377-380.

[34] Suzuki, S.; Baba, J.; Shutoh, K.; Masada, E. Effective application of superconducting magnetic energy storage (SMES) to load leveling for high speed transportation system. *IEEE Trans. on Applied Superconductivity,* vol. 14 (2), June 2004, pp.713,716.

[35] Ise, T.; Kita, M.; Taguchi, A. A hybrid energy storage with a SMES and secondary battery. *IEEE Trans. on Applied Superconductivity,* vol. 15 (2 part II), June 2005, pp. 1915-1918.

[36] Hentschel, F.; K. Müller; M. Steiner. Energy Storage on Urban Railway Vehicles. *Proc. UIC Energy Efficiency Conf.*, Paris, May 2000.

[37] Meinert, M.; Rechenberg, K.; Hein, G.; Schmieder, A. Energy Efficient Solutions for the Complete Railway System. *Proc.8th World Congress on Railway Research*, Seoul, Korea, 18-22 May 2008.

[38] Steiner, M., Klohr, M.; Pagiela, S. Energy storage system with ultracaps on board of railway vehicles. *Proc. 12th Eur. Conf. Power Electron. and Applicat. EPE 2007*, Aalborg, Denmark, 2-5 Sept. 2007.

[39] Dominguez, M.; Cucala, A.P.; Fernandez, A.; Pecharroman, R.R., Blanquer, J. Energy efficiency on train control – design of metro ATO driving and impact of energy accumulation devices. *Proc. 9th World Congress on Railway Research WCRR 2011*, Lille, France, 22-26 May 2011.

[40] Meinert, M. New mobile energy storage system for rolling stock. *Proc. 13th Eur. Conf. Power Electron. and Applicat. EPE 2009*, Barlecona, Spain, 8-10 Sept. 2009.

[41] Ciccarelli, F.; Iannuzzi, D.; Tricoli, P. Speed-based supercapacitor state of charge tracker for light railway vehicles. *Proc. 14th Eur. Conf. Power Electronics and Applications EPE 2011*, Birmingham, UK, Aug. 30 – Sept. 1, 2011.

[42] Barrero R.; Tackoen X.; Van Mierlo, J. Analysis and configuration of supercapacitor based energy storage system on-board light rail vehicles. *Proc. 13th Int. Power Electron. and Motion Control Conf. EPE-PEMC 2008*, Poznan, Poland, 1-3 Sept. 2008, pp. 1512-1517.

[43] Szenasy, I. New energy management of capacitive energy storage in metro railcar by simulation. *Proc. 5th Vehicle Power and Propulsion Conf. VPPC 2009*, Dearborn, Michigan, USA, 7-10 Sep. 2008, pp. 181-187.

[44] Iannuzzi, D.; Pagano, E.; Tricoli, P.. The use of energy storage systems for supporting the voltage needs of urban and suburban railway contact lines. *Energies*, vol. 6 (4), Apr. 2013, pp. 1802-1820.

[45] Xiao-li, C., Jian, Y.; Yu, F. Model and simulation of a super-capacitor braking energy recovery system for urban railway vehicles. *Proc. WASE Int. Conf. on Information Eng. ICIE 2010*, Beidaihe, China, 14-15 Aug. 2010, pp. 295-300.

[46] Steiner, M.; Scholten, J. Energy storage on board of railway vehicles. *Proc. 11th Eur. Conf. Power Electron. and Applicat. EPE 2005*, Dresden, Germany, 11-14 Sept. 2005.

[47] Iannuzzi, D.; Tricoli, P. Optimal control strategy of onboard supercapacitor storage system for light railway vehicles. *Proc. IEEE Int. Symp. Industrial Electronics ISIE 2010*, Bari, Italy, 4-7 July 2010, pp.280-285.

[48] Allègre, A.L., Bouscayrol, A.; Delarue, P.; Barrade, P.; Chattot, E.; El-Fassi, S. Energy storage system with supercapacitor for an innovative subway, *IEEE Trans. Ind. Electron.*, vol. 57 (12), Dec. 2010, pp. 4001-4012.

[49] Ishino, K.; Sakamoto, K.; Miyatake, M. Energy-saving operating strategy of a catenary free light rail transit. *Proc. 15th Int. Conf. on Electrical Machines and Systems ICEMS 2010,* Sapporo, Japan, 21-24 Oct. 2012.

[50] Ogasa, M. Application of energy storage technologies for electric railway vehicles-examples with hybrid electric railway vehicles. *IEEJ Trans. on Electrical and Electronic Engineering,* vol. 5 (3), May 2010, pp. 304-311.

[51] Barrero, R.; Tackoen, X.; Van Mierlo, J. Energy saving in public transport: enhanced energy storage systems for improved on-board light rail vehicle efficiency, *IEEE Vehicular Tech. Magazine*, vol. 3 (3), Sept. 2008, pp. 26-36.

[52] Barrero, R.; Tackoen, X.; Van Mierlo, J. Stationary or onboard energy storage systems for energy consumption reduction in a metro network. *Proc. Inst. Mech. Eng. Pt. F: J Rail Rapid Transit*, vol. 224 (3), Jan. 2010, pp. 207–225.

[53] Chymera, M.; Renfrew, A.; Barnes, M. Analyzing the potential of energy storage on electrified transit systems. Proc. 8th World Congress of Railway Research WCRR 2008, Seoul, South Korea, 18-22 May 2008.

[54] Chymera, M.; Renfrew, A. C.; Barnes, M.; Holden, J. Simplified power converter for integrated traction energy storage. *IEEE Trans.on Vehicular Technology,* vol. 60 (4), May 2011, pp. 1374-1383.

[55] Sekijima, Y.; Inui, M.; Monden, Y.; Aoyama, I. Development of an energy storage system for DC electric rolling stock by applying electric double layer capacitors. *Japanese Railway Engineering,* vol. 156, 2005, pp. 35-41.

[56] Destraz, B.; Barrade, P.; Rufer, A.; Klohr, M. Study and simulation of the energy balance of an urban transportation network. *Proc. 12th Eur. Conf. Power Electron. and Applicat. EPE 2007*, Aalborg, Denmark, 2-5 Sept. 2007.

[57] Iannuzzi, D., Tricoli, P. Metro trains equipped onboard with supercapacitors: a control technique for energy saving. *Proc. 20th Int. Symp. Power Electron., Elect. Drives, Automation and Motion SPEEDAM 2010*, Pisa, Italy, June 14-16, 2010, pp. 750-756.

[58] Iannuzzi, D.; Tricoli, P. Supercapacitor state of charge control based on changeover finite state controller for metro-train applications. *Proc. 3rd Int. Conf. on Clean Electrical Power ICCEP 2011*, Ischia, Italy, 14-16 June 2011, pp. 550-556.

[59] Iannuzzi, D.; Tricoli, P. Speed-based State of Charge Tracking Control for Metro-Trains with Onboard Supercapacitors. *IEEE Trans. on Power Electronics*, vol. 27 (4), Apr. 2012, pp. 2129-2140.

[60] Ciccarelli, F., Iannuzzi, D.; Tricoli, P. Control of metro-trains equipped with onboard supercapacitors for energy saving and reduction of power peak demand. *Transportation Research Part C: Emerging Technologies*, vol. 24, Oct. 2012, pp. 36-49.

[61] Miyatake, M.; Matsuda, K. Energy saving speed and charge/discharge control of a railway vehicle with on-board energy storage by means of an optimization model. *IEEJ Trans. on Electrical and Electronic Engineering,* vol. 4 (6), Nov. 2009, pp. 771-778.

[62] Mir, L.; Etxeberria-Otadui, I.; De Arenaza, I. P.; Sarasola, I.; Nieva, T. A supercapacitor based light rail vehicle: System design and operations modes. *Proc. IEEE Energy Conversion Congress and Exposition ECCE 2009,* San Jose, CA, USA, 20-24 Sept. 2009, pp. 1632-1639.

[63] Henning, U.; Thoolen, F.; Lamperth, M.; Berndt, J.; Lohner, A.; Janig, N. Ultra low emission traction drive system for hybrid light rail vehicles. *Proc. 18th Int. Symp. Power Electron., Elect. Drives, Automation and Motion SPEEDAM 2006,* Taormina, Italy, 23-26 May 2006, pp. 1068-1072.

[64] Daoud, Mohamed I.; Abdel-Khalik, A.S.; Elserougi, A.; Ahmed, S.; Massoud, A.M. DC bus control of an advanced flywheel energy storage kinetic traction system for electrified railway industry. *Proc. 39th Annual Conf. of the IEEE Industrial Electronics Society IECON 2013*, Vienna, Austria, 10-13 Nov. 2013, pp. 6596-6601.

[65] Glickenstein, H. Contactless payment debuts on london's buses, new and improved railways around the world. *IEEE Vehicular Technology Magazine,* vol. 8 (2), 2013, pp. 19-25.

[66] Jeong, W., Kon, S.B.; Park D.; Jung, W.S. Efficient energy management for onboard battery-driven light railway vehicle. *Proc. 9th World Congress on Railway Research WCRR 2011*, Lille, France, 22-26 May 2011

[67] Bombardier. MITRAC Energy Saver. Available on-line: http://www.bombardier.com/content/dam/Websites/bombardiercom/supporting-documents/ BT/Bombardier-Transport-ECO4-MITRAC_Energy_Saver-EN.pdf (accessed 2013).

[68] Siemens. SITRAS MES. Available on-line: http://w3.siemens.com/smartgrid/ global/en/products-systems-solutions/rail-electrification/dc-traction-power-supply/Documents /MES_PI_102_76.pdf (accessed 2013).

[69] CAF Power and Automation. ACR evoDRIVE. Available on-line: http://www.caf.es/en/ecocaf/nuevas-soluciones/tranvia-acr.php (accessed 2013).

[70] Moskowitz, J.; Cohuau, J. STEEM: ALSTOM and RATP experience of supercapacitors in tramway operation. *Proc. 2010 IEEE Vehicle Power and Propulsion Conference VPPC 2010,* Lille, France, 1-3 Sept. 2010.

[71] Akiyama,S.; Tsutsumi, K.; Matsuki, S. The development of low floor battery-driven LRV "SWIMO". *Proc. 8th World Congress of Railway Research WCRR 2008*, Seoul, South Korea, 18-22 May 2008.

[72] Railway Gazette. Lithium-ion batteries on LFX-300. Available on-line: http://www.railwaygazette.com/news/single-view/view/hybrid-streetcar-unveiled-in-charlotte.html (accessed 2013).

[73] Rufer, A. Energy storage for railway systems, energy recovery and vehicle autonomy in Europe. *Proc. Int. Power Electronics Conference - ECCE Asia IPEC 2010*, Sapporo, Japan, 21-24 June 2010.

[74] Siemens. SITRAS HES. Available on-line: http://w3.siemens.com/smartgrid/ global/en/products-systems-solutions/rail-electrification/dc-traction-power-supply/ Documents/HES_PI_102_76.pdf (accessed 2013).

[75] Konishi, T.; Morimoto, H.; Aihara, T.; Tsutakawa, M. Fixed energy storage technology applied for DC electrified railway. *IEEJ Trans. on Electrical and Electronic Engineering*, vol. 5 (3), May 2010, pp. 270–277.

[76] Brenna, M.; Foiadelli, F.; Zaninelli, D.; Roscia, M. Prospective for Energy Saving by Means of Ultracapacitors in Electric Systems for Transportation. *Proc. Int. Conf. and Exhib. on Ecological Vehicles and Renewable Energies EVER 2009,* Monaco, 26-29 Mar. 2009.

[77] Rufer, A.; Hotellier, D.; Barrade, P. A Supercapacitor-based energy storage substation for voltage compensation in weak transportation networks. *IEEE Trans. Power Delivery*, vol. 19 (2), Feb. 2004, pp. 629-636.

[78] Iannuzzi, D.; Lauria, D.; Tricoli, P. Optimal Design of Stationary Supercapacitors Storage Devices for Light Electrical Transportation Systems. *Journal of Optimization and Engineering*, vol. 13 (4), Dec. 2012, pp. 689-704.

[79] Battistelli, L.; Ciccarelli, F.; Lauria, D.; Proto, D. Optimal design of DC electrified railway Stationary Storage System. *Proc. 2nd Int. Conf. Clean Electrical Power ICCEP 2009*, Capri, Italy, June 9-11, 2009, pp. 739-745.

[80] Ciccarelli, F.; Iannuzzi, D.; Lauria, D.; Supercapacitors-based energy storage for urban mass transit systems. *Proc. 14th Eur. Conf. Power Electronics and Applications EPE 2011*, Birmingham, UK, 30 Aug. – 1 Sept. 2011.

[81] Battistelli, L.; Fantauzzi, M.; Iannuzzi, D.; Lauria, D. Generalized approach to design supercapacitor-based storage devices integrated into urban mass transit systems. *Proc. 3rd Int. Conf. on Clean Electrical Power ICCEP 2011*, Ischia, Italy, 14-16 June 2011, pp. 530-534.

[82] Ciccarelli, F.; Iannuzzi, D.; Lauria, D. Stationary ultracapacitors storage device for improving energy saving and voltage profile of light transportation networks. *Transportation Research Part C: Emerging Technologies*, vol. 21 (1), Jan. 2012, pp. 321-337.

[83] Ciccarelli, F.; Clemente, G.; Iannuzzi, D.; Lauria, D. An analytical solution for optimal design of stationary lithium-ion capacitor storage device in light electrical transportation networks. *International Review of Electrical Engineering*, vol. 8 (3), June 2013, pp. 989-999.

[84] Foiadelli, F.; Roscia, M.; Zaninelli, D. Optimization of storage devices for regenerative braking energy in subway systems. Proc. *IEEE Power Engineering Society General Meeting PES 2006*, Montreal, QC, Canada, 18-22 June 2006.

[85] Barrero, R.; Tackoen, X.; Van Mierlo, J. Improving energy efficiency in public transport: stationary supercapacitor based energy storage systems for a metro-network. *Proc. Vehicle Power Propulsion Conf. VPPC 2008*, Harbin, China, September 3-5, 2008.

[86] Teymourfar, R.; Asaei, B.; Iman-Eini, H.; Nejati Fard, R. Stationary super-capacitor energy storage system to save regenerative braking energy in a metro line. *Energy Conversion and Management*, vol. 56, April 2012, pp. 206-214.

[87] Lee, H.; Song, J.; Lee, H.; Lee, C.; Jang, G,; Kim, G. Capacity optimization of thesupercapacitor energy storages on DC railway system using a railway powerflow algorithm. *Int J Innov Comput Inform. Control*, vol. 7 (5BMay 2011, pp. 2739–2753.

[88] Killer, A.; Armstorfer, A.; Díez, A. E.; Biechl, H. Ultracapacitor assisted regenerative braking in metropolitan railway systems. *Proc. 2012 IEEE Colombian Intelligent Transportation Systems Symposium CITSS 2012*, Bogota, Colombia, 30-31 Aug. 2012.

[89] Kwon, K.; Lee, E.; Choi, J.; Baek, S. Efficiency improvement of ESS for DC transit system. *Proc. IEEE 7th Int. Power Electronics and Motion Control Conference - ECCE Asia, IPEMC 2012,* vol. 4, Harbin; China; 2-5 June 2012, pp. 2641-2646.

[90] Okui, A.; Hase, S.; Shigeeda, H.; Konishi, T.; Yoshi, T. Application of energy storage system for railway transportation in Japan. *Proc. Int. Conf. Power Electronics Conference IPEC 2010*, Sapporo, Japan, 21–24 June 2010, pp. 3117–3123.

[91] Morita, G.; Konisihi, T.; Hase, S.; Nakamichi, Y.; Nara, H.; Uemura, T. Verification tests of electric double layer capacitors for static energy storage system in DC electrified railway. *Proc. 19th Int. Symp. Power Electron. Elect. Drives, Automation and Motion SPEEDAM 2008*, Ischia, Italy, 11-13 June 2008, pp. 1017-1022.

[92] Konishi, T.; Hase, S.; Nakamichi, Y. Energy storage system for DC electrified railway using EDLC. *Quarterly Report of RTRI (Railway Technical Research Institute) (Japan),* vol 45 (2), May 2004, pp. 53-58.

[93] Turner, A. B. A Study of Wayside Energy Storage Systems (WESS) for Railway Electrification. *IEEE Trans. on Industry Applications,* vol. IA-20 (3), May 1984, pp. 484-492.

[94] Radcliffe, P.; Wallace, J.S.; Shu, L.H. Stationary applications of energy storage technologies for transit systems. *Proc. Conf. IEEE Electric Power and Energy Conference EPEC 2010*, Halifax, NS, Canada, 25–27 Aug. 2010.

[95] Wheeler, P. Voltage regulation application of a kinetic energy storage system. Proc. 2nd Int. Conf. Power Electronics, Machines and Drives PEMD 2004, Edinburg, UK, 31 Mar.-2 Apr. 2004, pp. 605–608.

[96] Iglesias, I.J.; Martinez, J.C.; Tobajas, C.; Lafoz, M.; Tabares, L.G.; Coauthors, C.V. A kinetic energy storage system for railways applications. *Proc. 8th World Congress of Railway Research WCRR 2008*, Seoul, South Korea, 18-22 May 2008.

[97] Garcia-Tabares, L.; Iglesias, J.; Lafoz, M.; Martinez J. C.; Vazquez, C.; Tobajas, C.; Gomez-Alors, A.; Echeandia, A.; Lucas, J.; Zuazo, C.; Carrasco, J. M.; Vázquez, S.. Development and Testing of a 200 MJ/350 kW Kinetic Energy Storage System for

Railways Applications. *Proc. 9th World Congress on Railway Research WCRR 2011*, Lille, France, 22-26 May 2011.

[98] Ogura, K.; Nishimura, K.; Matsumura, T.; Tonda, C.; Yoshiyama, E.; Andriani, M.; . . . Gianfrancesco, N. Test results of a high capacity wayside energy storage system using ni-MH batteries for DC electric railway at New York city transit. *Proc. IEEE Green Technologies Conf., Green 2011*, Baton Rouge, LA, USA, 14-15 April 2011.

[99] Saft Batteries. Intensium Max 20P. Available on-line: http://www.saftbatteries .com/sites/default/files/21855-2-0213_CS_Septa_Protected.pdf (Accessed 2013).

[100] Envitech Energy Inc. . Envistore. Available on-line: http://www.envitech.com/PDF/ENVISTORE.pdf (Accessed 2013).

[101] Shimada, M.; Oishi, R.; Araki, D.; & Nakamura, Y. Energy storage system for effective use of regenerative energy in electrified railways. Hitachi Review, vol. 59 (1), April 2010, pp. 33-38.

[102] Siemens. SITRAS SES. Available on-line: http://w3.siemens.com /smartgrid/global/en/products-systems-solutions/rail-electrification/dc-traction-power-supply/Documents/SES_PI_131_76.pdf (accessed 2013).

[103] Maher, B. Ultracapacitors provide cost and energy savings for public transportation applications. *Battery Power Products & Technology magazine*, vol. 10 (6), Nov./Dec. 2006, pp. 1–2.

[104] Bombardier. EnerGstor Wayside Energy Storage. Available on-line: http://www.bombardier.com/content/dam/Websites/bombardiercom/supporting-documents/BT/Bombardier-Transportation-ECO4-EnerGstor-EN.pdf (accessed 2013).

[105] Adetel Group. NeoGreen Power System. Available on-line: http://www.adetelgroup.com/library/fiches-produits/4-NEO_GREEN_POWER.pdf (accessed 2013).

[106] Woojin Industrial Systems Co. Ltd. Energy Storage System for Railway Systems. Available on-line: http://www.wjis.co.kr/Energy%20Storge%20System_04.pdf (accessed 2013).

[107] Meiden. CAPAPOST Regenerative Power Storage System. Available on-line: http://www.meidensha.co.jp/catalog/en/ba/ba77-3023b.pdf (accessed 2013).

[108] Envitech Energy Inc.. ENVISTORE. Available on-line: http://www.general-files.pw/download/gs4d70dd9ch32i0/ENVITECH-ENERGY-APTA-Rail-Conference-Vancouver-ENVISTORE-Presentation.pdf.html (accessed 2013).

[109] Piller Power Systems. Piller POWERBRIDGE. Available on-line: http://www.balmex.hu/termekeink/pdf/Railway.pdf (accessed 2013).

[110]Kinetic Traction System . GTR System. Available on-line: http://www.railway-technology.com/contractors/electrification/kinetic-traction-systems/kinetic-traction-systems2 .html (Accessed 2013).

[111]Vycon Energy . REGEN System. Available on-line: http://www.vyconenergy.com/pages/subpages/pr/pr_121114.htm (Accessed 2013).

Chapter 3

Supercapacitor storage technology

3.1 Supercapacitor overview

Supercapacitors (SC), formerly **electric double-layer capacitor** (EDLC), is the generic term for a family of electrochemical capacitors. SC, sometimes also called **Ultracapacitors**, do not have a conventional solid dielectric as occurs in a well-known electrolytic capacitor, so in its construction and operation they differ markedly from these last ones. They have a specific capacitance of the order of F/g or F/cm^3, so very high when compared with the most common electrostatic capacitors, whose capacitances are in order of magnitude of pico, milli-farads per mass and volume units.

The principle of a SC is based on a phenomenon first observed by *H. Helmholtz* [1-3]. In short, if an electrode is immersed in an electrolyte, in the vicinity of the interface between the electrode and electrolyte occurs a separation of charges. Since at least two electrodes are required for connection to an external circuit, it is obvious that definitely two of the above interfaces are required.

More precisely, on electrode surface it may appear an excess (or shortage on the other electrode) of electrons, which is balanced by electrolyte ions in order to have global neutrality. The distance between electrode surface and the center of the ions (in other terms the charge separation distance), that form a *layer* in the immediate vicinity of the electrode is equivalent to the dielectric thickness of a classic capacitor. Therefore at each of the formed interfaces something equivalent to the capacitor appears, and the resulting device is equivalent to a series connection of two capacitors, which is shown in Figure 3.1.
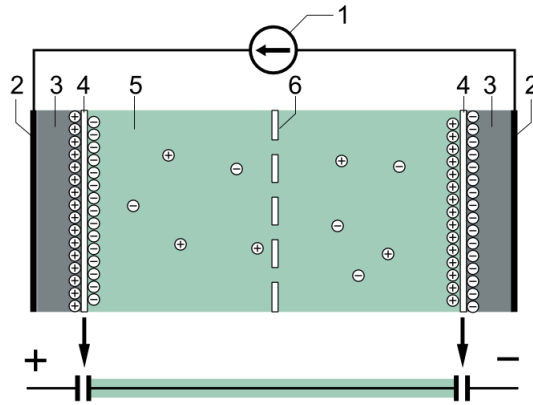
Figure 3.1 – EDLC elementary cell: 1. Charger; 2. Current collectors; 3. Polarized electrodes; 4. Helmholtz Electric Double Layer; 5. Electrolyte solution having positive and negative ions; 6. Separator [8]

Hence, the name **Double Layer Capacitor** derive from these two layers, where the energy is stored due to the presence of a significant electrostatic field. The separator avoid any direct contact between the electrodes with an evident short circuit effect.

Typical EDLC is constructed, as shown in the Figure 3.1, out of two metal plates, current collectors, on which electrode material is deposited, stacked together and separated with a membrane which serves as an electric isolator between two electrodes, but must allow for electrolyte ions to pass through. Compared to electrochemical batteries, the relevant difference is that in EDLC no electrochemical reactions or phase change occur or they may be strongly reduced.
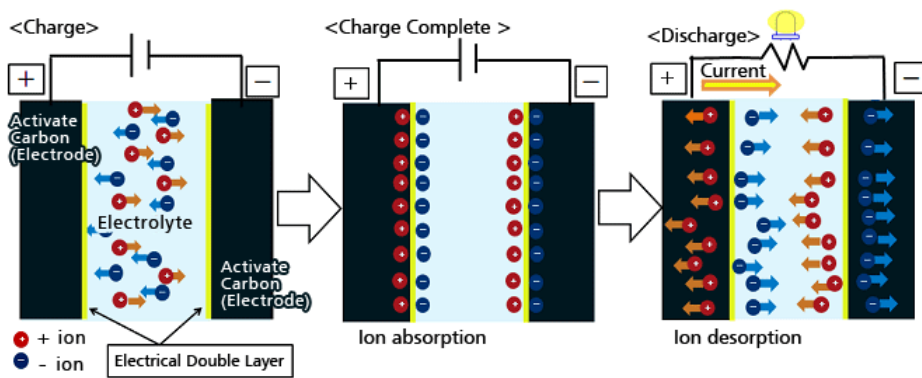
Figure 3.2 - Structure and function of an ideal double-layer capacitor [8]

All the energy is stored by using the reversible absorption of the ions of the electrolyte into active materials that are electrochemically stable and have high accessible specific surface areas, making it possible to have very frequent charge/discharge cycles.

The *Helmholtz* double layer differential capacitance can be expressed as :

$$C_h = \varepsilon_0 \varepsilon_r \frac{S}{d}$$
(3.1)

where $\varepsilon_o \varepsilon_r$ represent the dielectric constant, S is the electrode surface and d is the distance between the electrodes (or the charges) and identifies the double layer thickness.

Besides, *Gouy* and *Chapman* proposed a mathematical formulation of the charge storage, by means of a Poisson equation and Boltzmann distribution, leading to define the double layer differential capacitance as:

$$C_{g-c} = z \sqrt{\frac{2qn_o \varepsilon}{u_t}} \, cosh \frac{z\psi_o}{2u_t}$$
(3.2)

where ε is the absolute dielectric constant, z is the valence of the ions, n_o is the number of ions per cubic meter, ψ_o is the applied potential drop, q is the elementary charge and u_t is the thermodynamic potential, so defined:

$$u_t = \frac{kT}{q}$$
(3.3)

with T the temperature (in Kelvin degree) and k the Boltzmann constant.

Finally, *Stern* enhanced and integrated the two previously theories, also considering the size of the ions in the solution:

$$\frac{1}{C_s} = \frac{1}{C_h} + \frac{1}{C_{g-c}}$$
(3.4)

His theory divides the double layer in two zones: a first area in which, according to Helmholtz theory, the potential distribution is linear, and a second one where the charge distribution is a double diffusion layer.

Apart from this "double-layer" capacitance, the inner storage ability of a supercapacitor is determined also by the **pseudocapacitance** principle, that arises from reversible Faradaic reactions occurring at the electrode. The charge transfer that takes places in these reactions is voltage dependent, so a capacitive phenomenon occurs, achieved by redox reactions electro sorption or

intercalation on the surface of the electrode by specifically adsorbed ions that results in a reversible faradaic charge-transfer on the electrode. Pseudocapacitance can increase the capacitance value by as much as an order of magnitude over that of the double-layer by itself.

From all these electrochemical models, several evolutions have been developed which also take into account the resistive contributions of the electrodes and electrolyte, with consequent investigation of more electrical models obtained from series of resistors and voltage-dependent non-linear capacitor branches.

However, the thickness of the double layer depends on the concentration of the electrolyte and the size of the ions. Typically, for concentrated electrolytes thicknesses of the order of $2 \div 10$ Angstrom are observed [4].

Instead, the electrodes are designed so as to constitute a high surface area, in such a way as to maximize the surface of the double layer itself. Their material is mainly **activated carbon** which is a very porous material and lead to high effective surface area up to over 2000 m^2/g and even 3000 m^2/g. Similarly, carbon aerogels and carbon nanotubes are used for EDLC construction for the same reason. These two construction details result in devices with a specific capacitance on the order of 250 F/kg [5-6].

By summarizing, Double-layer capacitance offers good charge storage capabilities thanks to possessing high surface-area materials as electrodes, and the fact that charge separation occurs at atomic dimensions. Pseudocapacitance that arises from redox or ion sorption reactions further improves the achievable capacitance.

In any case, the dynamic behaviors of supercapacitors are remarkably related to the ion *mobility* of the electrolyte employed and to the *porosity* effects of the porous electrodes.

In order to classify them, the electrode material and electrolyte type are briefly discussed in the following and lastly, a general classification based on the design of the electrodes is explained [8].

3.1.1   Classification according to electrodes material

The choice of materials used in the manufacture of electrodes plays a vital role in determining the properties of SC. The process of charges accumulation in the double layer is a surface process and consequently the characteristics of the electrodes greatly affect the performance of the cell.

Carbon is the most widely used material for the electrodes, but metal oxides and conductive polymers .are also used. Regarding the type of carbon there are two main types of activated carbon: the first ones include powder and fabrics; the other feature *nanostructured* types as *graphene*, *airgel*, *xerogel* and *nanotubes*. The activated carbon electrodes have low costs associated with high surface areas (2500 m^2/g); those nanostructured, in particular nanotubes, offer a porosity even higher that lead to having pore sizes up to 2 nm against a greater expense.

The use of *metal oxides*, however, shows a good behavior from the specific capacitance enhancement, but are observed side-effects related to the presence of many redox reactions localized in the metal oxide thus causing a non-linear behavior with respect to the one of a pure double layer . The compounds most used are oxides of Ruthenium (RuO_2) , Iridium (IrO_2) and other noble metals. These materials have excellent electrical conductivity and an effective area of up to 100 m^2/g.

The *polymer* electrodes, finally, offer the same advantages of inorganic nature SC at the lowest prices . The principle is based on the exploitation of polymers capable of developing redox reactions having fast kinetics. Such polymers are obtained by electrochemical oxidation starting from the respective monomers. They present considerable advantages, including a low production cost, if compared with the oxides of *Ruthenium*, and a high specific capacity. Moreover, these material have the peculiarity to be doped, as it occurs in the semiconductors, in a way to control their conductivity. [7]

3.1.2   Classification based on the electrolyte type

The choice of the *electrolyte* for an EDLC is important as the choice of material used for the electrode . The maximum voltage that can be reached by the cell depends on the decomposition potential of the electrolyte and therefore the energy density is conditioned by the electrolyte itself. The power density is dependent on the equivalent series resistance, which in turn is closely linked to the conductivity of the electrolyte. The ease with which the charges are accumulated on the carbon surface depends on the accessibility of the ions to the carbon pores itself; there is the need to optimize the size of the pores in function of the size of the electrolyte ions.

There are three different types of electrolyte :

Organic: is the most used in commercial devices due to its high potential for dissociation; normal operating voltages are typically of $2.5 \div 3.0$ V for a single cell, and with particular procedures of electrolyte purification some manufacturers reach voltage values higher to about 3.5 V. Currently, *tetraethylammonium tetrafluoroborate* (TEATFB) in *acetonitrile* (CH_3CN) is indicated as the best system of organic electrolyte for use in supercapacitors (and therefore, actually, the most common), reaching values of conductance up to 60 mS/cm. By contrast, despite these good properties, however, there is the high toxicity of acetonitrile, so in the future the preference for this will have to focus on alternative solvents, such as *propylene carbonate* ($C_4H_6O_3$).

Aqueous: it allows to obtain a greater specific capacitance and a lower equivalent series resistance; on the other side they limit the cell potential to lower values, in some cases up to 1 V. The most aqueous electrolytes used are sulfuric acid (H_2SO_4) and potassium hydroxide (KOH), which are able to offer relatively high conductivity values of about 100 to 1000 mS/cm.

Solid: when polymers are combined with appropriate salts, show a high ionic conductivity. More specifically, polymeric type provides less corrosion, less release of hazardous substances, thinner configurations and more compact packaging. The *solid polymer* electrolyte is currently best known as *Nafion* membrane to achieve high ion-conductive. The disadvantage that always accompany it is the cost. This polymer is also used within the fuel cells where its use is linked to some operating problems if used at high temperatures.

Finally, *separators* have to physically separate the two electrodes to prevent a short circuit by direct contact. It can be very thin (a few hundredths of a millimeter) and must be very porous to the conducting ions to minimize equivalent series resistance. Furthermore, separators must be chemically inert to protect the electrolyte stability and conductivity. Inexpensive components use open capacitor papers. More sophisticated designs use nonwoven porous polymeric films like *polyacrylonitrile* or *Kapton*, woven glass fibers or porous woven ceramic fibres.

3.1.3   Classification based on the electrodes design

Supercapacitor is the generic term for the family of electrochemical capacitors. They store, as described above, its electric energy with the two different storage

principles, the static double-layer capacitance and electrochemical pseudocapacitance. The distribution of the amounts of both capacitances per capacitor depends on the material and structure of the electrodes. Based on this the supercapacitor family are divided into three types:

Symmetric types - or properly called "Double-layer capacitors", with activated carbon electrodes or similar with much higher electrostatic double-layer capacitance than electrochemical pseudocapacitance. Symmetric means that both electrodes in a carbon-carbon configuration are fabricated identically, and in fact they are. However, once charged the impurities contained in the activated carbon as residual ash reach with the electrolyte giving each electrode a potential set. A symmetric type is made from high purity aluminum positive termination materials and an aluminum alloy negative termination material. The electrode current collectors are also made of aluminum that is etched for better contact to the activated carbon electrode film.

Asymmetric types - they are Pseudocapacitors, with transition metal oxide or conducting polymer electrodes with a high amount of electrochemical pseudocapacitance. This asymmetric type is ideally a battery-like, non-polarizable electrode, such as a metal oxide, that is paired with ad EDLC electrode, such as the carbon electrode. In particular, the coupling of an activated carbon negative electrode with a conducting polymer positive electrode has received a great deal of attention.

Hybrid capacitors – like asymmetric capacitors, they couple two different electrodes, but hybrid types are unique in coupling a supercapacitor electrode with a battery electrode. This specific configuration reflects the need for higher energy supercapacitors and higher power batteries, combining the energy characteristics of batteries with the power, cycle life, and recharging times of supercapacitors. Research has focused primarily on using nickel hydroxide, lead dioxide, and LTO ($Li_4Ti_5O_{12}$) as one electrode and activated carbon as the other. This suggests that these hybrids may be able to bridge the gap between supercapacitors and batteries. Despite the promising results, the general consensus is that more research will be necessary to determine the full potential of hybrids capacitors in particular the so-called **lithium-ion capacitors**.

The topic introduced in this section are expanded in the next paragraphs, covering the modeling of symmetric supercapacitors and detailed discussion of the novel hybrid lithium-ion capacitors.

3.1.4 Construction and assembly details

Generally, the most common SC are the symmetric types which are constructed by assembling the individual cells in two different configurations: monopolar and bipolar. The *monopolar* devices have very high capacitance values, due to very large surface areas, they are assembled in parallel by winding identical layers of metallic collector, porous electrode and separator, the maximum voltage of the overall device thus assembled is equal to that of a single cell.

The *bipolar* devices instead allow higher voltages, at the cost of reduced capacity and increase endurance. Are assembled by stacking single cells in series; their insulation is very important, since it is necessary to prevent contact of the electrolyte between the various cells.

In any case, the electrodes are bound to aluminum "sheets" wrapped, which owns the metal terminals of the cell. The SC construction is subsequently *rolled* (see Figure 3.3) or *folded* (or *laminated*) (see Figure 3.4) into a cylindrical or rectangular shape and can be stacked in an aluminum can or an adaptable rectangular housing.
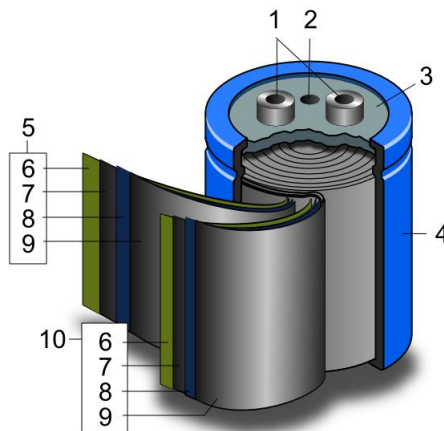
Figure 3.3 - Schematic construction of a wound SC: 1. Terminals, 2. Safety vent, 3. Sealing disc, 4. Aluminum can, 5. Positive pole, 6. Separator, 7. Carbon electrode, 8. Collector, 9. Carbon electrode, 10. Negative pole [8]
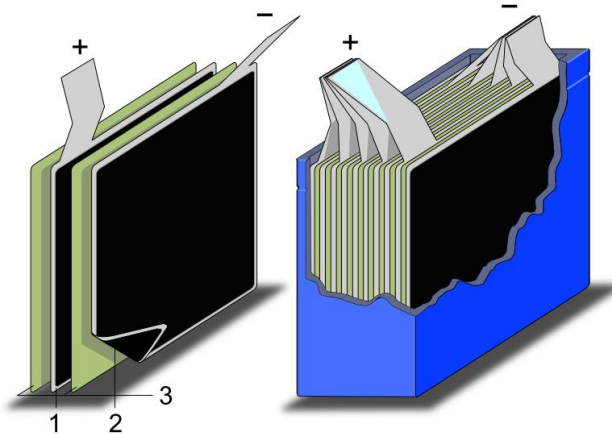
Figure 3.4 - Schematic construction of a SC with stacked electrodes: 1. Positive electrode, 2. Negative electrode, 3. Separator [8]

One of the most used method of assembly of the electrodes consists in the continuous preparation of a *metal strip*, on which is deposited a mixture of activated carbon and extruded polymers loaded, and then is superimposed on the separator (see Figure 3.5).
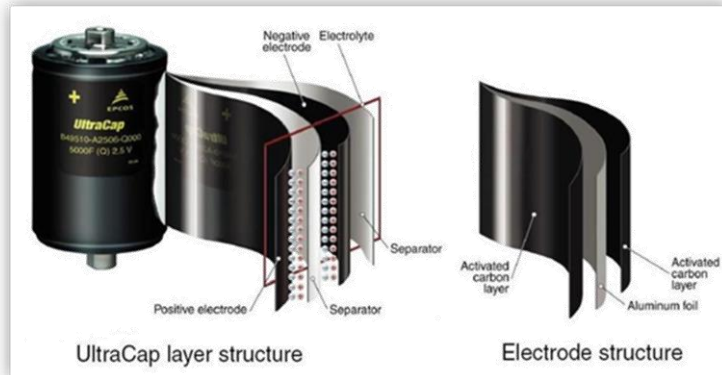
Figure 3.5 – Example of a EPCOS 5000 F SC cell wounded in a metal strip

The tape is then cut, suitably rolled up or folded, impregnated with electrolyte and finally encapsulated. The advantages of this technique of continuous production stays in high productivity, low cost, good homogeneity of the extruded material, ease possibility to fabricate devices of various sizes and shapes (cylinders, parallelepipeds or extremely thin rectangles), limitation of the internal resistance (by controlling appropriately the strip tension). Finally, the housing is hermetically closed to ensure the insulation between the terminals

124

and reducing the spread of the electrolyte to the outside.over the specified life time.

By way of example, Figure 3.6 and Table 3.1 [9]. Shows the shape and the parameters that characterize a Maxwell BCAP350F SC cell. These parameters are determined from information contained in the manufacturer's datasheet, as well as by constant current charging test.

Figure 3.6 – Example of a MAXWELL 350 F SC cell [9]

Rated Capacitance₁	350 F
Internal Resistance in DC	3.2 mΩ
Internal Resistance at 1 kHz	1.6 mΩ
Rated Voltage	2.5 V
Absolute Maximum Voltage	2.85 V
Absolute Maximum Current	170 A
Leakage Current at 25°C, maximum	0.3 mA
Minimum Operating Temperature (Cell case)	-40 °C
Maximum Operating Temperature (Cell case)	65 °C
Capacitance Change (% decrease from minimum initial value)	20%
ESR Change (% increase from maximum initial value)	100%
Usable Specific Power	4.6 W/kg
Specific Energy	5.9 Wh/kg
Storable Energy	0.35 Wh
Projected DC Life at 25 °C	10 years
Projected Cycle Life at 25 °C	$5 \cdot 10^5$ cycles
Mass, typical	60 g

Table 3.1 – Main characteristics of the MAXWELL BCAP350F SC cell [9]

Several applications require voltage levels much higher than that which can be achieved by a single SC cell. It is therefore often necessary to properly connect

many cells together order to accomplish the required performance. The resulting voltage is then simply the product of individual cell voltage and the number N of *series* cells. Each SC in a series connection will contribute its ESR to the total resistance of the *module*, and if power requirements need limits on the allowed ESR, then *parallel* connections of cells may also have to be used. For a SC bank with M parallel strings each consisting of N SC connected in series, the total equivalent resistance will be given by:

$$R_{sc} = R_{sc,cell} \frac{N}{M} \tag{3.5}$$

$R_{sc,cell}$ is the ESR of an individual cell. Larger numbers of parallel strings will therefore lead to reduced module resistance.

Requirements on equivalent capacitance C_{sc} are determined by energy requirements, with the well-known squared relation between energy and capacitance. The total capacitance of the module is then evaluated as:

$$C_{sc} = C_{sc,cell} \frac{M}{N} \tag{3.6}$$

In most applications, SC are furnished already assembled in modules consisting of individual cells connected in series and parallel to increase both the working voltage and the overall capacitance; the whole is encapsulated to obtain mechanical robustness and good insulation degree from moisture and dust, and completed by systems for **balancing** the voltage on individual cells. In particular, these latter are necessary because as the number of cells connected in series, the energy that can be stored in safe conditions is drastically reduced: the use of voltage equalization aims to limit overvoltages between the cells or reverse voltages caused by the tolerances of the cells themselves and/or by leakage currents. Uniform voltage distributions may be obtained by means of active or passive devices. In the simplest case, the balances are made by precision resistors connected in parallel to each cell (passive balancing see Figure 3.7): this solution is preferred for applications in which the SC current rate through the SC is maintained at low levels.
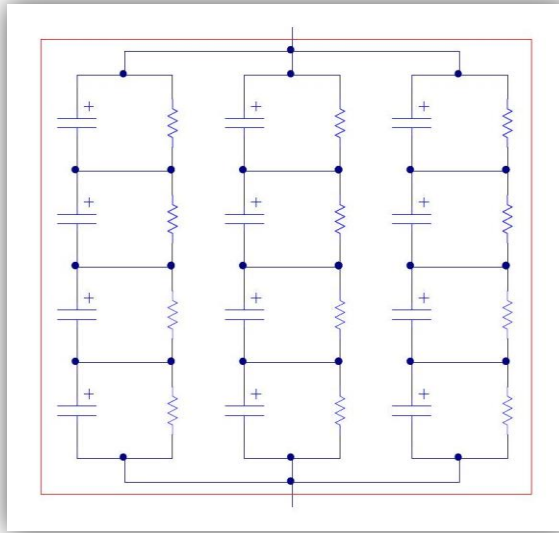
Figure 3.7 – Series and parallel cell connections with passive balancing system

Conversely, the use of **active** electronic devices (active balancing, see Figure 3.8) is carried out, when the SC current may assume high peaks for short time intervals. In this case the balancing is achieved by the individual control circuits connected in parallel to each cell, where each of them has essentially a comparator equipped internally of a precise reference voltage: if the value of the voltage across the SC cell exceeds the threshold, this is temporarily closed on a resistive load until the consequent discharge leads the voltage below the threshold.

Commercially there are modules suitable for transport or industrial applications, with working voltages from few volts to more than 300 V and with capacitances
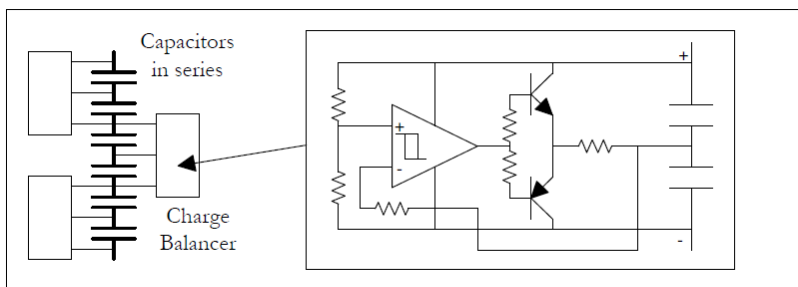
Figure 3.8 – Active SC cell balancing system from MAXWELL technologies [10]

Figure 3.9 - Example of a MAXWELL 63 F SC module [11]

of few hundreds or even thousands of farads.

In Figure 3.9 is shown a MAXWELL BMOD0063P125 SC module for transport application with a capacitance of 63 F, 125 V DC working voltage, and active cell balancing [11].

Rated Capacitance	63 F
Maximum Capacitance, initial	76 F
Maximum ESR DC, initial	18 mΩ
Rated Voltage	125 V
Absolute Maximum Voltage15	136 V
Maximum Continuous Current ($\Delta T = 15$ °C)	140 A
Maximum Continuous Current ($\Delta T = 40$ °C)	240 A
Maximum Peak Current, 1 second (non repetitive)	1800 A
Leakage Current at 25 °C, maximum	10 mA
Maximum Series Voltage	1500 V
Capacitance of individual cells	3000 F
Number of cells	48
Minimum Operating Temperature (Ambient)	-40 °C
Maximum Operating Temperature (Ambient)	65 °C
Specific Power	1.7 W/kg
Specific Energy	2.3 Wh/kg
Storable Energy	140 Wh
Projected DC Life at 25 °C	10 years
Projected Cycle Life at 25 °C	10^6 cycles
Mass, typical	58 kg

Table 3.2 - Main characteristics of the MAXWELL BMOD0063P125 SC module [11]
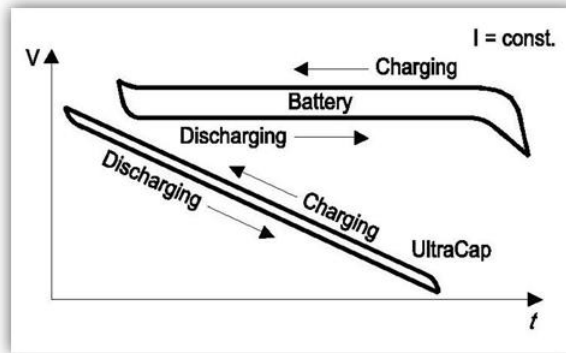
Figure 3.10 - Comparison of the discharge characteristics of a common battery and a SC

For these arrangement, the storage and release energy process is highly reversible and its efficiency is not influenced by the number of charge and discharge cycles: for the this reason they are very tolerant towards the charging method adopted and therefore not predefined cycle profiles can be even used as long as the voltage across the element never exceeds the rated one; the only precaution is due to the low internal resistance value, which requires the use current limitation.

One of the factors to be taken into account in any device for energy storage is the ease with which its charge status can be monitored. The characteristics of the SC show a simple relationship between the level of terminal voltage and charge state (see Figure 3.10).

The reason for this is mainly due to the fact that the energy is stored in the electrostatic field. Therefore, the voltage measured at the terminals of a SC directly indicates the **SoC** (which is not as in the case of batteries).

From the previous Figure 3.10, it is noticed that electrochemical batteries offer a discharge voltage performance fairly constant throughout the spectrum of usable energy, whereas the SC voltage has a linear and decreasing behavior from the maximum value up to 0 V. This results in the fact that the SC is unable to provide all the charge and it implies that in the voltage range not usable remains a rate of energy which is not extracted. Even if the stored energy proportional to the product of the capacitance for the square of the voltage, in the discharging phase, due to the current limitation, the delivered power decreases. This lead to use only a part of the voltage range from 0 to $V_{sc,max}$. A usual value of the operating voltage range is $0.5V_{sc,max} \div V_{sc,max}$ which is also

129

Manufacturer	Type	Cell voltage (rated) [V]	Capacitance (rated) [F]	ESR at Cmax [mΩ]	$\tau = R \cdot C$ [s]	Specific Energy [Wh/kg]	Specific Power [W/kg]	Max specific Power [W/kg]	Mass [kg]	Volume [dm³]
Maxwell	Activated Carbon	2.7	2885	0.38	1.08	4.20	994	8836	0.550	0.414
Maxwell	Activated Carbon	2.7	605	0.90	0.55	2.35	1139	9597	0.200	0.211
Skeleton Technologies	Activated Carbon	2.8	1600	1.30	2.10	5.80	800	7140	0.220	0.130
Yunasko	Hybrid	2.7	55	4.00	0.22	5.50	5695	50625	0.009	N/A
Yunasko	Hybrid	2.7	450	1.30	0.58	5.89	2766	24595	0.057	0.045
Yunasko	Hybrid	2.7	510	0.90	0.46	5.00	2919	25962	0.078	0.055
Ness	Activated Carbon	2.7	1800	0.55	1.00	3.60	975	8674	0.380	0.277
Ness	Activated Carbon	2.7	3640	0.30	1.10	4.20	928	8010	0.650	0.514
Ness	Activated Carbon	2.7	3160	0.40	1.26	4.40	982	8728	0.522	0.379
Asahi Glass	Propilene	2.7	1375	2.50	3.40	4.90	390	3471	0.210	0.151
Panasonic	Propilene	2.5	1200	1.00	1.20	2.30	514	4596	0.340	0.245
EPCOS	Activated Carbon	2.7	3400	0.45	1.50	4.30	760	6750	0.600	0.480
LS Cable	Activated Carbon	2.8	3200	0.25	0.80	3.70	1400	12400	0.630	0.470
Batscap	Activated Carbon	2.7	2680	0.20	0.54	4.20	2050	18225	0.500	0.572
Power Sys.	Activated Carbon - propilene	2.7	1350	1.50	2.00	4.90	650	5785	0.210	0.151
Power Sys.	Graphite propilene	3.3	1800	3.00	5.40	8.00	486	4320	0.210	0.150
Power Sys.	Graphite propilene	3.3	1500	1.70	2.50	6.00	776	6903	0.230	0.150
JSR Micro	Hybrid	3.8	1000	4.00	4.00	11.20	900	7987	0.113	0.073
JSR Micro	Hybrid	4.8	2000	1.90	3.80	12.10	1038	9223	0.206	0.132

Table 3.3 - Electrical parameter of supercapacitor series of different manufacturers [8]

denoted as discharge voltage ratio. With this choice, the usable energy is 75% of that potentially given by a complete SC discharge and usually the datasheet of the manufacturer of useful energy calculated with the following formula:

$$E_{sc,max} = \frac{3}{8} C_{sc} V_{sc,max}^2$$ (3.7)

By finalizing, the following Table 3.3 shows differences among capacitors of various manufacturers in capacitance range, cell voltage, internal resistance (ESR, DC or AC value) and volumetric and gravimetric energy density [8

3.2 EDLC modeling

With reference to the time now, commercial supercapacitors still have three drawback aspects that arise from the intrinsic characteristics of the design of the double layer and that are *low operating voltages*, *non-uniform* rated parameters and *non-linear* characteristics. Furthermore, parameters and SC behavior depend on temperature, state of charge, charge and discharge rate and frequency and other variables. Different models have been developed from the above physical approaches [3]-[6]-[12]. Some of them are complicated according to their ability to properly model the double layer behavior. On the contrary, other of these models, despite their lack in accuracy, are characterized by a simple parameter identification procedure.

3.2.1   Simple RC series/parallel model

The simplest of all is the classical equivalent circuit with the lumped *ideal capacitance*, *equivalent parallel resistance* (EPR) and *equivalent series resistance* (ESR). Figure 3.11 shows the classical equivalent circuit with the three parameters. Determination of these parameters provides a first approximation of an SC cell.
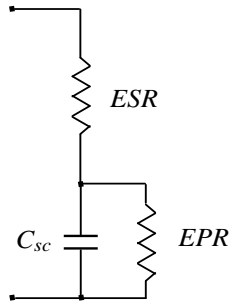
Figure 3.11 – Simple equivalent SC circuit

The ESR models the internal device resistance and empirical verifications by *Sypker and Nelms,* showed that this parameter has not significantly dependent on the terminal voltage nor the charge rates, but is affected mainly from the temperature [13].

The EPR represents the current leakage and influences the long-term energy storage, taking into account the self-discharge. In multiple series connections of SC the EPR influences the cell voltage distribution due to the resistor divider effect. Using empirical methods, *Sypker and Nelms* [12] showed that the EPR is related to the voltage decay ratio by:

$$EPR = \frac{-t}{ln\left(\frac{V_f}{V_0}\right)C_{sc}}$$

(3.8)

where V_0 is the initial voltage, V_f is the final voltage and C_{sc} is taken as the rated capacitance.

Through experimental measurements, it was shown that the EPR effects could be neglected for transient discharge calculations. However, the EPR value is important when cell balancing of series connected SC is considered, as before described.

This model is very easy to use given the ease parameter identification procedure, but it could be inadequate when the dynamic has to be considered, since the dynamic behavior of the SC is non-linear.
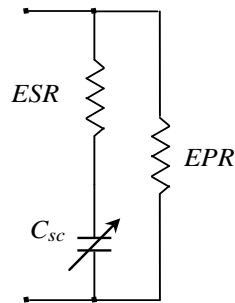
Figure 3.12 – Improved simple equivalent circuit for SC

A first evolution of this model is the *non-linear capacitance model* shown in Figure 3.12, which takes into account the non-linear behavior of the equivalent capacitance of the device according to the polarization voltage, by means of a non-linear capacitance with the applied voltage. Although this is easy enough to use, due to its lack of additional elements to represent the redistribution phenomena and the high dynamic during charge/discharge, it is unable to characterize long-term behavior [14].

To be precise, in such models should always be inserted a *series inductance*, which is very small (of the order of tens of nH) and its contribution is not negligible only at very high frequencies. In all models the inductance is used to ensure the proper compliance of the model with the physical reality even at high frequencies and for this reason is often omitted, since its contribution in the range of frequencies of the common industrial applications involves a negligible error.

3.2.2   Parallel branched model

Describing a more detailed terminal representation model, *Zubieta and Bonert* proposed and investigated a three RC branch network with one branch having a voltage dependent capacitance [15]. Each branch of the circuit shown in Figure 3.13 has a different associated time constant. This model has the following characteristics:

- the structure of the model, related to the physical structure of the device is simple in order to be easily implemented in engineering applications;
- the model describes correctly the behavior of the device in the low-frequency dynamics between a few mHz and a hundred of mHz.

- it is possible to determine the parameters of the model through measures conducted to the SC terminals.

The *first branch* represented by the elements R_i, C_{i0} and the term C_{i1} function of the voltage V_{ci}, represents the "*immediate*" behavior of the device in the time interval of seconds in response to an action of charging or discharging . The *second branch*, represented by the elements R_d and C_d, dominates the "*delayed effect*" behavior at the terminals in the range of minutes and, finally, the *third branch* comprising the elements R_l and C_l characterizes the "*long-term*" behavior for times greater than 10 minutes.

The leakage resistance R_{leak}, in parallel to the branches above described, allows to model the self-discharge phenomenon.

The model just introduced pays particular attention to SC physical whose characteristic has been taken into account by introducing a nonlinear capacitance only in the first branch.

Particular care should be taken in defining the equivalent variable capacitance. The definition of capacitance in the case of linear devices is the following:

$$C = \frac{Q}{V}$$
(3.9)

Where Q is the storage charge and V the terminal voltage.

In the case of the constant capacitance, the ratio indicated in (3.3) is the same also in the case in which one refers to an increase of charge ΔQ as a result of an increase in voltage ΔV.
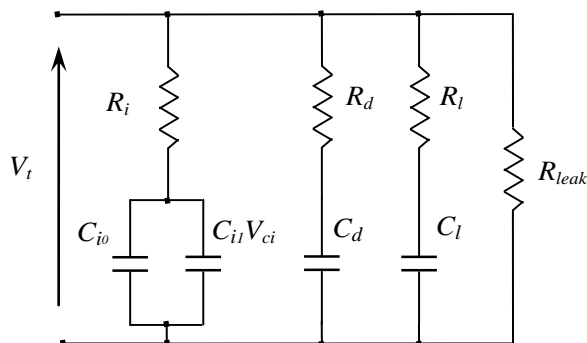
Figure 3.13 – Parallel SC model

134

This, however, is not true in the case of nonlinear capacitance. In order to describe the variation of the charge at a given voltage is necessary to define the differential capacitance as:

$$C_{diff}(V) = \frac{dQ}{dV}\bigg|_{V'}$$

(3.10)

In the range of voltage values applicable to a SC, as indicated by *Zubieta and Bonert*, the *differential capacitance* is modeled as the sum of a constant capacitance C_{i0} and the capacitance $C_{i1} \cdot V$ whose value varies linearly with the voltage applied to the terminals of the same SC:

$$i(t) = C_{diff}(V)\frac{dV}{dt} = (C_0 + 2 \cdot C_1 V)\frac{dV}{dt}$$

(3.11)

Conversely, this model requires precise and accurate measurements in order to identify the several branches parameters, based on constant current charging tests.

3.2.3   Transmission line model

This model even follows a physical approach to model the behavior of SC and takes into account the characteristics of the device in its entirety by modeling the behavior between the anode-membrane and cathode-membrane, whereas the properties are space varying in a non-uniform way. The model consists of a complex *network* of RC circuits in which the capacitances are non-linear [16]-[17]. The resistances depend on many variables such as the resistivity of the electrolyte and the electrodes; the RC circuits depend instead by the size of the pores and the collector connection and are not all equal among them due to the non-uniformity of the electrolyte. The resulting model is represented in Figure 3.14. The complexity of the model implies a difficult adaptability of the same to real applications, even for the considerable troubles inherent in the determination of the different parameters.
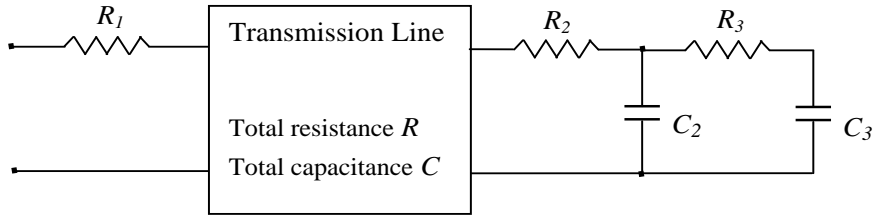
Figure 3.14 – Transmission line model of SC

By applying the theory of transmission lines, the equivalent impedance of the circuit is derived:

$$Z_{eq}(t) = \frac{1}{C}\sqrt{\frac{\tau}{\pi t}}\left[1 + 2\sum_{n=1}^{\infty} e^{\left(-n^2\frac{\tau}{t}\right)}\right]$$

(3.12)

where: C is the capacitance of the line ($C = cl$, with c equal to the capacitance per unit length l); R is the total resistance of the line ($R = rl$, with r equal to the resistance per unit length l); τ is time constant equal to the product RC.

3.2.4   Series model based on SC frequency analysis

This model characterizes the SC characteristics by measures conducted on its external terminals through the *electrochemical impedance spectroscopy* (EIS) method, commonly used to measure the frequency response of electrochemical battery cells.

In order to carry out correct measures the current source must not contain DC components in such a way as to ensure that the measurement is carried out at constant voltage. In fact the cell is fed with a constant DC voltage (*polarization voltage*) which is superimposed by a sinusoidal voltage variable frequency . The relationship between the amplitude of the sine wave voltage and the amplitude of the absorbed current by the cell provides the cell impedance at a given frequency.

136
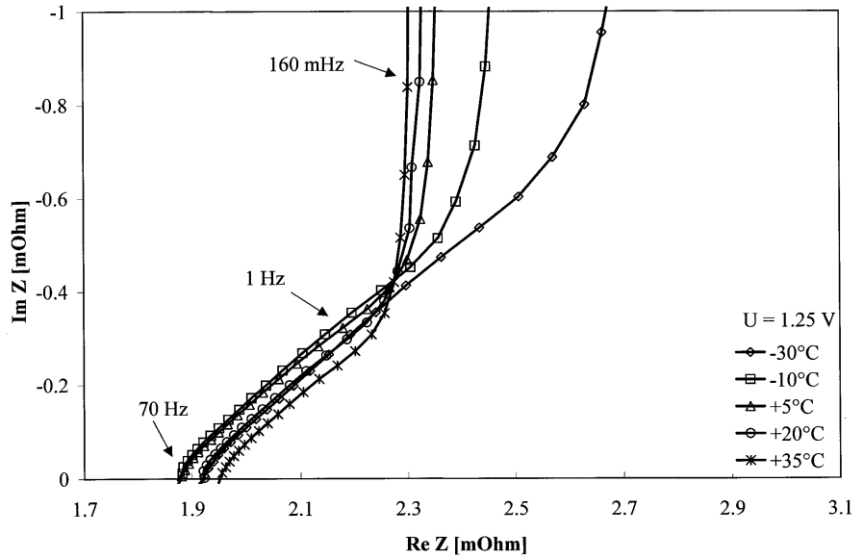
Figure 3.15 – Impedance spectrum on the complex plane of aMontanaComponents SA, 1400 F 2.5 V supercapacitor cell [18]

In Figure 3.15 is shown in the complex plane the impedance spectrum typical of a SC at different temperatures and at polarization voltage of 1.25 V. The frequency range is between 120 mHz and 70 Hz, since, this is the typical range of frequencies of most power applications.

The results show that at high frequencies the behavior of the SC is almost entirely resistive, in fact , the graph intercepts the real axis at a value of about 1.9 mΩ; this feature in the model is represented by a series resistance R_i. For intermediate frequencies, the graph shows a quite unitary slope with respect to the real axis and this can be justified by the porous structure of the electrodes. At low frequencies the graph shows an almost exclusively vertical behavior, typical of an ideal capacitor.

In order to model the impedance spectrum are required N RC circuits which require the computation of $2N$ parameters . These parameters have a strong dependence from each other, resulting quite difficult to determine more than five or six independent parameters in a fast and efficient way. A possible solution , given by *Buller et al.*, is shown in Figure 3.16 where the SC is represented by the series resistance R_i , inductance L and the complex impedance Z_p, which allows to model the device behavior both in the range of intermediate frequencies and close to the ideal capacitor for very low frequencies [18].

137
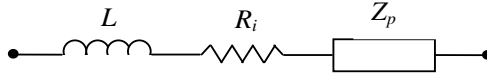
Figure 3.16 – Equivalent SC circuit for frequency analysis [18]

The impedance Z_p takes into account the porosity of the electrodes. Due to the porosity, the real part of the impedance increases with decreasing frequency and the maximum capacitance value is available only in steady-state conditions. The mathematical expression of Z_p as a function of pulsation ω, i.e. $Z_p(j\omega)$ is shown below in (3.13).

$$Z_p\left(j\omega\right) = \frac{\tau\, coth\left(\sqrt{j\omega\tau}\right)}{C\sqrt{j\omega\tau}} \tag{3.13}$$

The expression shows only two independent parameters, C and τ; thus including also the parameters L and R_i, the model is represented by only four independent parameters that have to be extracted from the spectrum measurement. In order to obtain a model that is suitable for a feasible simulation program there is the need to transform the frequency domain to the time domain. From mathematical analysis the inverse transform of the expression in (3.13) is:

$$G\left(j\omega\right) = \frac{k_1}{\sqrt{j\omega}}\, coth\left(\frac{k_1}{k_2}\sqrt{j\omega}\right) \tag{3.14}$$

in which k_1 and k_2 are constant. In the time domain it results:

$$g\left(t\right) = \frac{k_1^2}{k_2} + \frac{2k_1^2}{k_2}\sum_{n=1}^{\infty} e^{\left(-\frac{n^2\pi^2 k_1^2}{k_2^2}\right)t} \tag{3.15}$$

By comparing the coefficients of eqs. (3.13), (3.14), (3.15), it is immediate to have:

$$k_1 = \frac{\sqrt{\tau}}{C} \quad \text{and} \quad k_2 = \frac{\tau}{C} \tag{3.16}$$

and therefore:

$$g\left(t\right) = \frac{1}{C} + \frac{2}{C}\sum_{n=1}^{\infty} e^{\left(-\frac{n^2\pi^2}{\tau}\right)t} \tag{3.17}$$

138

By keeping in mind the transfer function and its inverse transform of a simple RC parallel circuit (with $\tau=RC$), after mathematically analyzing the expression (3.15) is deduced as this can be regarded as the sum of n RC exp functions, which from a circuital point of view is reflected in the series of n RC parallel circuit branches. In particular:

$$\begin{cases} \text{for } n = 0 \implies g(t) = \dfrac{1}{C} \implies C_0 = C \text{ and } R_0 = R \\ \text{for } n \neq 0 \implies g(t) = \dfrac{2}{C}\sum_{n=1}^{\infty} e^{\left(-\frac{n^2\pi^2}{\tau}\right)t} \implies C_n = \dfrac{C}{2} \text{ and } R_n = \dfrac{2\tau}{n^2\pi^2 C} \end{cases} \quad (3.18)$$

The circuital model is depicted in Figure 3.17 Figure 3.17 - SC circuital model represented by 4 parameters L, R_i, C and τ [18]
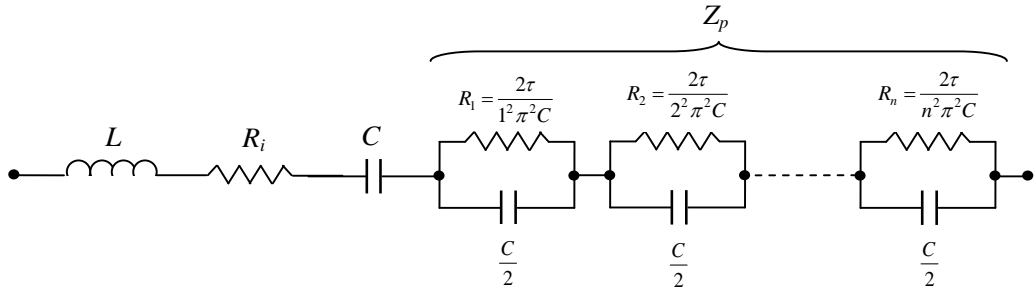
Figure 3.17 - SC circuital model represented by 4 parameters L, R_i, C and τ [18]

For a correct modeling of the SC behavior in industrial applications, it is sufficient to represent the impedance Z_p with a number between five and ten RC circuits. It has to be also emphasized that all the parameters R_n and C_n of the RC circuit branches are mathematically determined starting by the only two parameters C and τ. The limit of this model stays in its inability to represent both the charge redistribution phenomena and the self-discharge and the need to perform a device frequency analysis in order to identify the parameters of the model itself.

3.2.5   Complete full-frequency range model

The *complete model* of SC, proposed by *Musolino et al.*, which is able to correctly represent its full dynamics, is shown in Figure 3.18 [19]. This model consists of three parallel branches: the first is characterized by the same impedance of the series model reported in (3.13); the second is constituted by a series of parallel RC branches able to represent the charge recombination
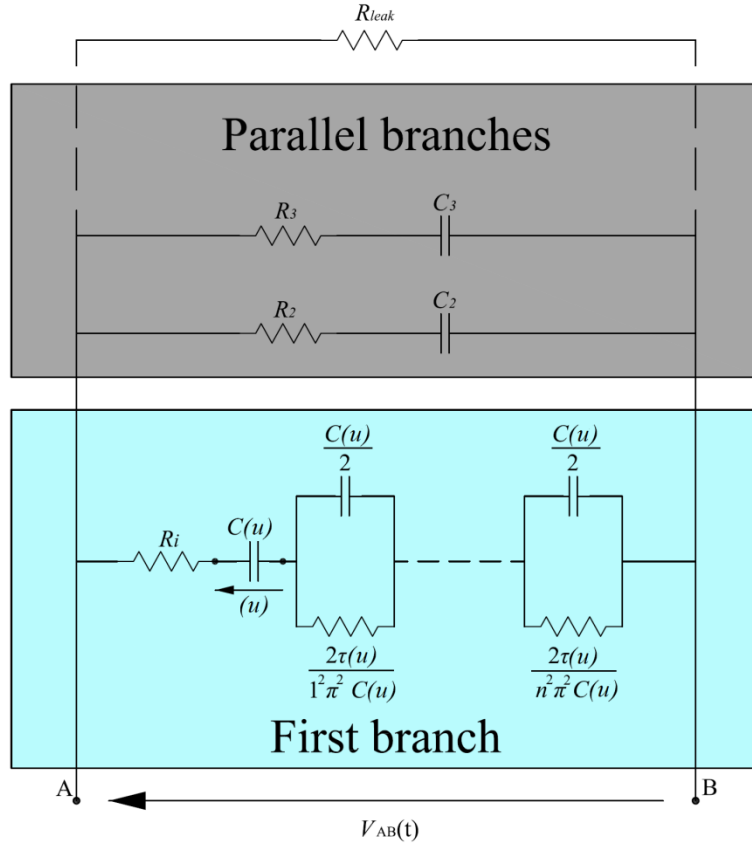
Figure 3.18 – Complete model of a SC [19]

phenomenon following a fast charge or discharge and, lastly, the final resistance R_{leak} that allows to model the self-discharge phenomenon. This model is very accurate for correctly simulate the dynamic behavior of the device in the charge and discharge including time intervals between a few tens of milliseconds and several weeks.

The impedance of the **first branch**, as shown in (3.13) is characterized by the parameters C and τ which are both linear function of the voltage applied to the terminals of the device. More specifically:

$$C(u) = C_0 + k_c u$$
$$\tau(u) = \tau_0 + k_\tau u$$

(3.19)

Furthermore, by specifying the (3.17) for steady state condition, it can be obtained:

$$\lim_{\omega \to 0} \Re\{Z_p\} = \lim_{\omega \to 0} \Re\{R_p\} = R_i + \sum_{n=1}^{\infty} \frac{2\tau(u)}{n^2 \pi^2 C(u)} = R_i + \frac{\tau(u)}{3C(u)} = R_{dc}$$

$$\lim_{\omega \to 0} \Im\{\omega Z_p\} = -\frac{1}{C(u)}$$

(3.20)

where R_p is the real part of the complex impedance Z_p.

The capacitance value for each voltage u value can be determined through a charge constant current test, in particular it is possible to use the same procedure indicated in [18]. The resistance R_p cannot be measured correctly through the constant current test, since at low frequencies (a few tens of mHz) the resistive contribution of the parallel branches cannot be neglected. In accordance to how usually reported in the manufacturers datasheet, working at frequencies equals to the inverse of the discharge time T_{dc} , to which the reported capacitance values are referred, the charge redistribution phenomenon can be neglected. This means that apart from the first one, the contribution of the different parallel branches is negligible, and a resistance measurement conducted in this frequencies range provides an estimation of the resistance R_{dc}. At high frequencies, when the SC behaves like a resistor, the resistance measurement at the terminals of the device provides an estimation of the parameter R_i (this parameter is also usually given in the manufacturers datasheets). From (3.19), by bearing in mind the parameters R_{dc} and R_i is possible to determine the parameter $\tau(u)$ as:

$$\tau(u) \approx 3C(u)(R_{dc} - R_i)$$

(3.21)

By repeating the constant current test for several polarization voltage values, it is possible to estimate the parameter k_c in (3.19) which takes into account the capacitance variation with the applied voltage.

As concerns the *parallel branches identification*, firstly their number have be chosen as compromise between the degree of accuracy to represent the redistribution phenomenon and the complexity of the model. If the time constants of the parallel branches are chosen sufficiently different from each other, it is possible to divide the discharge time in *n+1* intervals. In each interval *n*, only the branches from *1* to *n-1* are involved in the redistribution process. Instead, all other branches are evaluated in a stationary condition and are not affected by the redistribution because they are characterized by time constants

higher. Finally, in the interval $n+1$ all the energy is dissipated on the self-discharge resistance R_{leak}.

In order to make the simplified procedure of parameter identification of the parallel arms, the different time intervals have to be chosen in such a way in each transient n only the branches from 1 to n are affected by a redistribution while all the others are still in the steady state condition. In particular, the intervals can be chosen equally spaced on a logarithmic scale as:

$$
\begin{aligned}
&I_1 : \tau_0 < t < M\tau_0 = \tau_1 \\
&I_2 : \tau_1 < t < M\tau_1 = \tau_2 \\
&... \\
&I_n : \tau_{n-1} < t < M\tau_{n-1} = \tau_n
\end{aligned}
\tag{3.22}
$$

where τ_0 is the time needed for exhausting the redistribution transient from the first branch to the second. This has to be chosen equal to five times the time constant of the first branch, and this value is generally between a few seconds and tens of seconds at most. In order to ensure that the parallel arms transient is terminated before it is involved in the next branch, in (3.22) it is necessary that the time constant of the n branch is at least five times the time constant of the $n-1$ branch; this means that M is at least greater than five. From (3.22), given T_w that is the time window typical of the redistribution phenomenon, the parameter M can be evaluated as:

$$
M = \sqrt[n-1]{\frac{T_w}{\tau_0}}
\tag{3.23}
$$

During the time that occurs the redistribution phenomena, the circuit model can be schematized as in Figure 3.19. At time $t = 0$, the capacitance C_I is discharged on the capacitance C_{II}; the sum of the resistances of the two branches is denoted with R_{eq}.
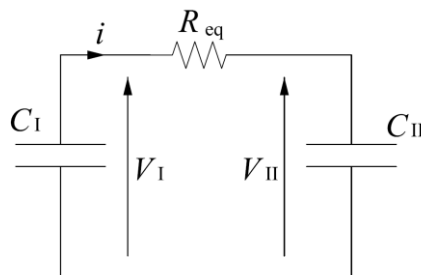
Figure 3.19 – Equivalent circuit for two parallel branches [19]

142

Since the capacitance of the first branch is a function of the voltage during the first transient, by indicating with V_0 and V_f the initial and final voltages measured at the terminals, it can be written:

$$C_{II} = \frac{V_0 - V_f}{V_f} C_I + k_c \frac{V_0^2 - V_f^2}{2 V_f}$$ (3.23)

where k_c is different from zero only during the analysis of the first redistribution transient.

On the basis of the charge conservation principle, all the parallel branches capacitance can be determined in an iterative way and are independent from the resistance. From the knowledge of the capacitance and the different time constants on the basis of (3.21) and (3.22) it is possible to determine the different resistances as:

$$C_\rho = k_c \frac{V_{\tau_{\rho-1}}^2 - V_{\tau_\rho}^2}{2 V_{\tau_\rho}} + \frac{V_{\tau_{\rho-1}} - V_{\tau_\rho}}{V_{\tau_\rho}} \sum_{j=1}^{\rho-1} C_j$$

$$R_\rho = \frac{\tau_\rho}{C_\rho}$$ (3.24)

$$R_{leak} = \frac{\tau_n}{\frac{1}{n-1} \sum_{j=1}^{n-1} C_j}$$

By summarizing, this complete model of SC that is capable of representing the full dynamic of the device, is based on the frequency response of the device itself and is characterized by a simplified parameter identification procedure.

3.2.6   SC model suitable for transport application

Concerning the use of SC as ESS in transport application, by keeping in mind the characteristics dynamic of urban railway traction application (tens of seconds) previously investigated in section 2.2, SC module can be represented by a simplified first order equivalent circuit derived by considering only the **short term** (or **main**) branch of the aforementioned complete model [20]. More specifically, only the first parallel branch has to be taken into account leading to a simples series circuit, as briefly reported in Figure 3.20.
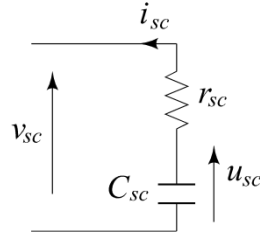
Figure 3.20 – First order equivalent SC devices for railway application

This circuit model exhibits an equivalent series resistance r_{sc} which is constant and independent from the frequency; the equivalent capacitance C_{sc} is modelled by a constant term C_0 [F] (which theoretically is the SC capacitance at v_{sc}=0) and a term linearly variable with the internal voltage across the SC, $C_1 u_{sc}$, where C_1 [F/V] is a constant:

$$C(u_{sc}) = C_0 + C_1 u_{sc} \tag{3.24}$$

If it is desired to specify a single equivalent constant capacitance for a SC, this is only possible for one selected voltage, preferably the rated voltage. Hence, the total **design value** of the SC capacitance has to be evaluated just at its maximum working voltage $V_{sc,max}$ and it is therefore given by $C_{sc}=C_0+C_1$. The previous relationship can be considered as linear when the SC is used between its nominal voltage and the half of this voltage, hence, in this range, the SC provides 75% of the stored energy.

The relationship between the current and the voltage at the terminals of the SC unit finally becomes:

$$\begin{cases} v_{sc} = u_{sc} - r_{sc}\, i_{sc} \\ i_{sc} = -\left(C_0 + 2C_1 u_{sc}\right)\dfrac{du_{sc}}{dt} \end{cases} \tag{3.25}$$

The term $C_0+2C_1 u_{sc}$ is defined as the differential SC capacitance (3.11) and usually C_1 is bounded between 10÷25 % of C_0 for most commercial SC [21]-[22].

Finally, for sake of continuity, in par. 3.4.6 is reported a simple parameter identification according to eq. (3.25) of a SC module by EPCOS.

3.3 Lithium-Ion Capacitor technology

By bearing in mind the application of ESS presented in the Chapter 2 and the features highlighted in the last paragraphs, SC despite of their low energy density present a good advantage over the other two energy storage devices, due their high power density which makes them especially suitable for buffering short term mismatches between power available and power required with consequent significant improvement of both dynamic performance and energy efficiency of the power system in which they are employed to buffer. This makes them especially qualified for usage as *braking energy storage*. However one drawback for ESS application is their low maximum operating voltage, together with the relatively high leakage current which prevents them from holding their stored energy for a long time. This voltage is usually less than 2.5 ÷ 2.85 V, and it might not be exceeded in order to prevent electrolyte oxidation apart from that carbon is not a good insulator; thus they have to be stacked to supply higher voltages.

The intent to improve the existing technology beside the trend of increasing maximum cell voltage maintenance has led to the development of a novel hybrid type of SC that has its intrinsic benefits, but with less leakage current, and with energy density comparable to batteries and power density that is higher to either batteries or standard EDLC too [23-26]. These are the **Lithium-ion Capacitor** (LiC).

3.3.1 Principles of the LiC

The Lithium-ion capacitor introduced here belongs to the class of advanced hybrid capacitor devices which combine the *intercalation* mechanism of Lithium batteries with the cathode of a conventional EDLC. The LiC approach is in fact to first *pre-dope* the negative electrode with lithium so that a ready source of Li+ ions is available, and to construct an opposing electrode (cathode) of *activated carbon* to act as a standard EDLC.
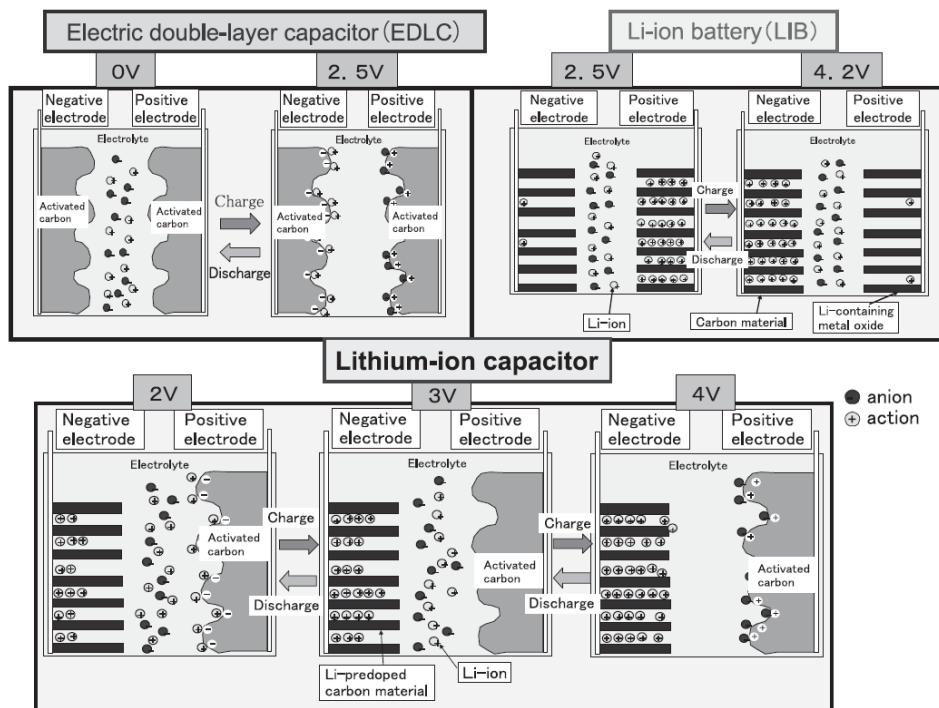
Figure 3.21 - Operating principle of LiC [24]

As depicted in Figure 3.21, the negative electrode (anode) is typically made with graphitic carbon material similar to Lithium batteries, which is pre-doped with the lithium ions. The electrolyte used in an LIC is a lithium-ion salt solution which can be combine with other organic components. The Li foil is set close to the assembled electrodes which are supported by porous current collectors and is connected with porous current collector of anode. On charging, Lithium intercalates into the negative electrode, leaving the anions to be physically adsorbed into the positive electrode active carbon surface. On discharge, lithium de-intercalates into solution and neutralizes anions, maintaining charge neutrality of the electrolyte. By summarizing, the positive electrode adopts the same physical adsorption mechanism as for the EDLC and the negative electrode is accompanied by the chemical reaction involving lithium-ion pre-dope/discharge just as for the negative electrode material of lithium batteries.

The effect of Lithium pre-doping on charge/discharge behavior are briefly shown in Figure 3.22, where it can be seen that pre-doping process makes the anode potential as low as, e.g. 0.25 V (vs. Li/Li+) and it is then lowered again

146
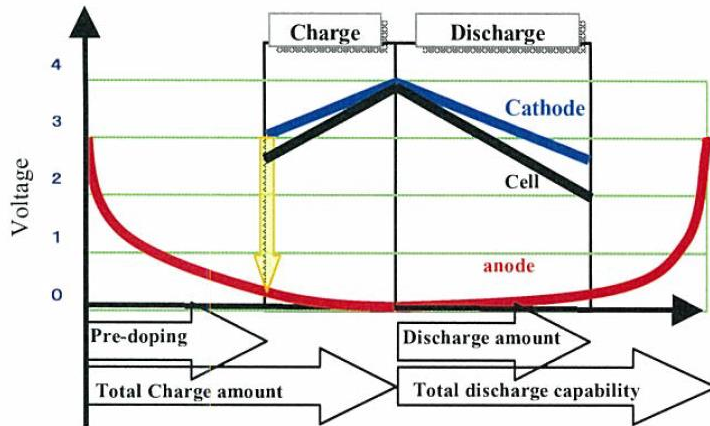
Figure 3.22 - Effects of Lithium pre-doping on charge/discharge behavior [23]
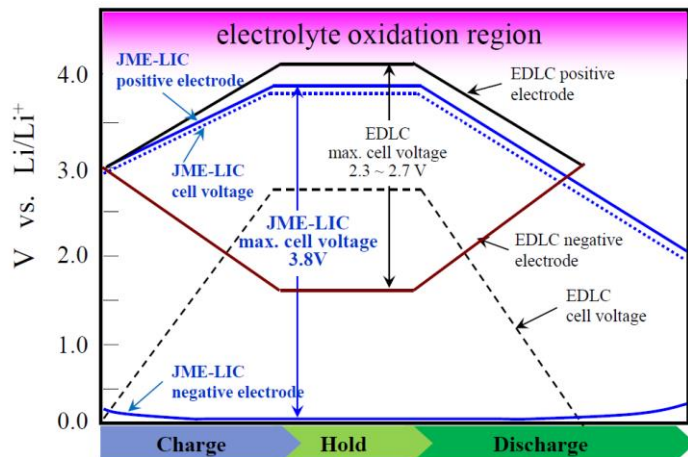
Figure 3.23 – LiC electrode potentials and cell voltages [23]

by charging process of the cell. The potential of anode can be kept low and constant during discharge since the anode capacitance is significantly larger than the one of the cathode. The design of lithium pre-doping is therefore crucial.

The Figure 3.23, portrays the electrode potentials and cell voltages for both LiC and conventional EDLC cell. In the case of this latter, the values of the anode and cathode potentials are the same at first for Li/Li+ potential and change symmetrically during charge and discharge (thus the name symmetric capacitor for EDLC). In the LiC cell, the potential of anode is low with a value close to Li/Li+ and its change during charge and discharge is much smaller than the change in the cathode potential, which, instead, increases during charge and

147

decreases during discharge. Moreover, the lower anode potential of the LiC cell, make it possible a cell voltage from 3.8 to 4.2 V.

Since the polarization of the electrodes are asymmetric, LiC are so commonly defined as **hybrid asymmetric capacitors**.

3.3.2   Features of the LiC

The most significant feature of the LiC cell is its inner capability of increasing the voltage to about 4 V due to the pre-doping process. The cell voltage is as high about 150 % of the one of the EDLC. As regards the cell capacitance, it can be seen substantially as the slope of the charge /discharge curve in Figure 3.23 and it is about equal to the positive electrode potential, which is twice the capacitance of an EDLC cell. With a higher voltage and capacitance than the EDLC, the LiC can be definitely regarded as a power storage device that is capable of providing advantages both of high energy and high power densities.

As a consequence, the Ragone plot (see Figure 3.24), shows that the LiC combines the high specific energy of Lithium ion batteries with the high power density of EDLC. The energy density of a LiC cell is generally 14 Wh/kg, even under a high power density and gradually decreases with increasing discharge rate.

As far as safety concerns with LiC, and they are safer in use than Lithium-ion batteries, because they are chemical reaction-free, heavy metals-free and rare metals-free and there is no danger of explosion. Other remarkable unique characteristics of LiC are good cycle life performance, *high reliability*, zero maintenance, a wide span of typical operating temperatures (ranging from -20 °C to 70 °C), and a *very low self-discharge* (less 5% voltage drop at 25^0C over three months) which could allow energy storage for many years without power input.

On the contrary, if a LiC is completely discharged, it is ruined. The minimum cell voltage can be set between 1.5÷2.2 V depending on the electrode material and electrolyte. So there is the need of control circuitry which actively ensures that all the cells that compose the LiC stack are kept at the same state of charge, through *balancing*, as usually occurs for batteries management system. Moreover LiC suffers considerably at the *low temperatures* due to lower energy ah high current rate, that results in a decreasing in capacitance and an increasing in internal resistance [27]. These last are key factors for designing
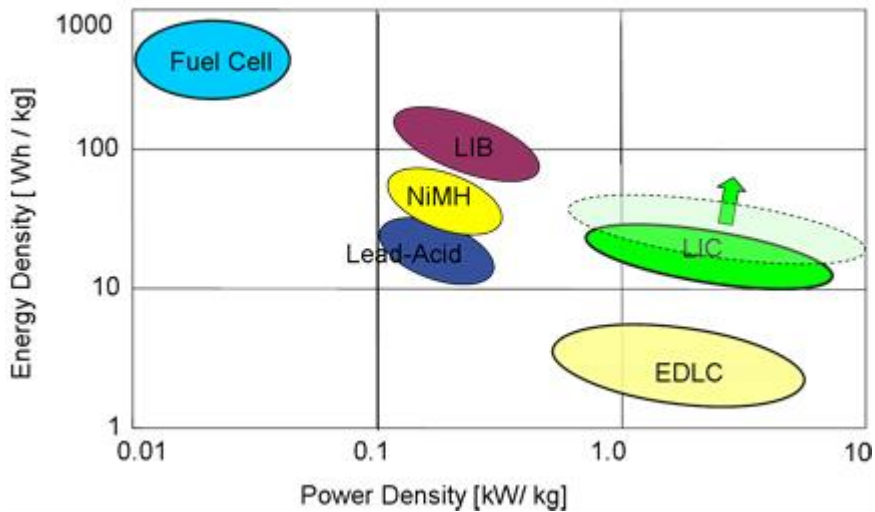
Figure 3.24 - Ragone plot comparing LiC with other storage technologies [26]

cell capacitance, internal resistance and reliability for wider applications of the LiC.

Regarding the applications, LiC are quite suitable for uses which require a high energy density, high power densities and excellent durability. Their potential applications for lithium-ion capacitors are in the fields of wind power generation systems [28], voltage sag compensation [29], photovoltaic power generation [30], spacecraft low orbit systems [31] , uninterruptible power source systems [32], energy recovery systems in industrial machinery [29], and urban transportation systems [33]-[34].

3.3.3   LiC commercial solutions

JM Energy Corp. company began mass production of lithium-ion capacitors and now commercialize *laminate* cells and *prismatic* cells using such LiC technologies

Laminated cells (see Figure 3.25) are contained in an aluminum package and they are thin, lightweight, compact, and excellent in radiation of heat.

Prismatic cell types (see Figure 3.26) have a semi-hard plastic case with large threaded terminals, such as lithium-ion battery packs. They excel in heat radiation efficiency and ease of implementation given their modularity.

149

In the following tables, the main characteristics of a 1100 F laminated cell (CLQ1100S1A see Table 3.4) and a 2300 F prismatic cell type (CPQ2300S see Table 3.5) are reported.

Figure 3.25 – Example of a LiC laminated cell by JM Energy [26]

Rated Voltage	$2.2 \div 3.8$ V
Capacitance	1100 F
DC – E.S.R.	1.2 mΩ
Max. ch./dis. current	200 A
Gravimetric energy density	10 Wh/kg
Volumetric energy density	19 Wh/L
Gravimetric power density	14 kW/kg
Gravimetric power density	27 kW/kg
Dimension (L x W x T)	180 x 126 x 5.5 mm
Weight	145 g

Table 3.4 - Main characteristics of the JM Energy ULTIMO CLQ1100S1A cell [26]

Figure 3.26 – Example of a LiC prismatic cell by JM Energy [26]

Rated Voltage	2.2 ÷ 3.8 V
Capacitance	2300 F
DC – E.S.R.	0.7 mΩ
Max. ch./dis. current	200 A
Gravimetric energy density	8 Wh/kg
Volumetric energy density	15 Wh/L
Gravimetric power density	8 kW/kg
Gravimetric power density	15 kW/kg
Dimension (L x W x T)	150 x 91.5 x 15.5 mm
Weight	369 g

Table 3.5 - Main characteristics of the JM energy ULTIMO CPQ2300S cell [26]

Finally, in the Figure 3.27 is depicted a LiC module composed of 36 ULTIMO CLQ1100S1A series-connected laminated cells. The LiC module, which is at the Transport Laboratory of the Department of Electrical Engineering and Information Technologies (D.I.E.T.I.) of the University Federico II of Naples, has a rated equivalent capacitance of 30.5 F, a rated DC resistance equal to 43.2 mΩ, and an allowable working voltage that varies from 79.2 to 136.8 V. Each cell is equipped with active balancing control circuitry and case package temperature monitoring.

Figure 3.27 – Prototype 30.5 F 136 V laminated LiC module of D.I.E.T.I.

3.3.4   LiC modeling

The LiC is a new technology and its modeling has not yet been deeply analyzed. At present, no exhaustive analysis of LiC behavior exists in the literature, and no equivalent circuit models for the LiC module have been proposed. Moreover, only characterizations and rougly experimental tests of single LiC cells have been carried out so far. Indeed, *Lambert et al.* showed a comparison between EDLC and LiC in an attempt to characterize it by augmenting the proper parameter identification technique for EDLC [35]; *Omar et al.* presented a complex LiC polynomial model whose capacitance value depended on many parameters such as the temperature, current rate, state of charge, and life cycle [33]; whereas, *Manla et al.* attempted to find a relationship between the capacitance and the terminal voltage by using a polynomial interpolant, but no detailed explanation and experimental validation of the module has yet been provided (see Figure 3.28) [36]. Finally, *Smith et al*. conducted some experimental procedure for evaluating the electrochemical performance and thermal behavior on several LiC laminated cells, underlining their self-discharge rates at the various temperatures [25].
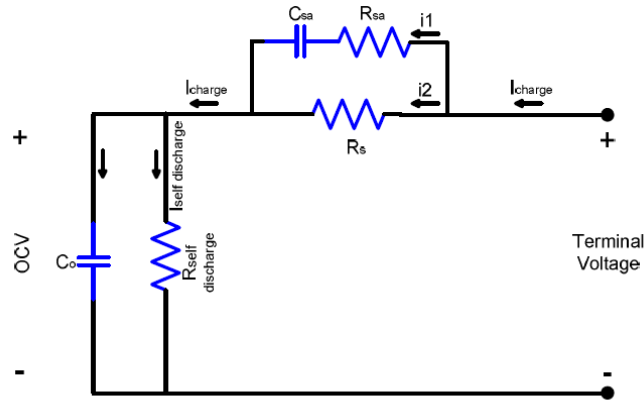
Figure 3.28 – LiC electrical model propose by [36]
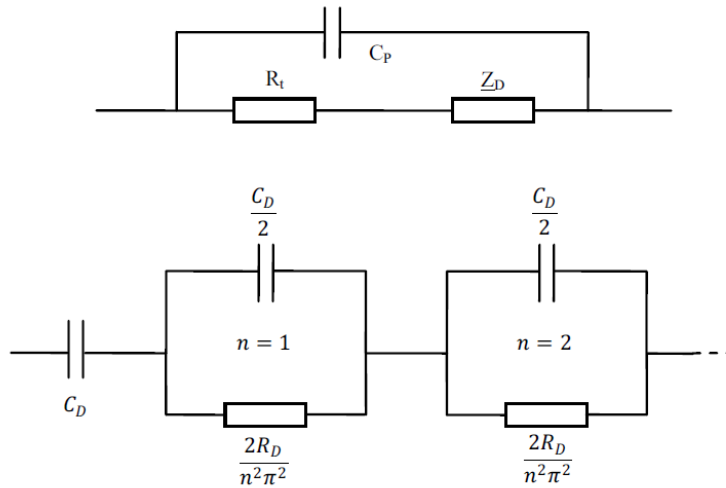
Figure 3.29 – LiC electrical model proposed by [35]

Very recently, *Ciccarelli et al.* in [37], attempt to adapt the model proposed for conventional SC in [19] to these devices. To this aim, many experimental tests have been performed on several cells, and it was verified that the model is useful to represent the behavior of this device [37]. More specifically, the technique developed in [35] to characterize EDLC with an equivalent circuit has been used here with the data acquired from the JM Energy ULTIMO lithium ion capacitor to demonstrate the method used to obtain a discrete component equivalent circuit model for the LiC device. This technique has been augmented to include a method for obtaining a characteristic equation and equivalent circuit model for LiC (see Figure 3.29).
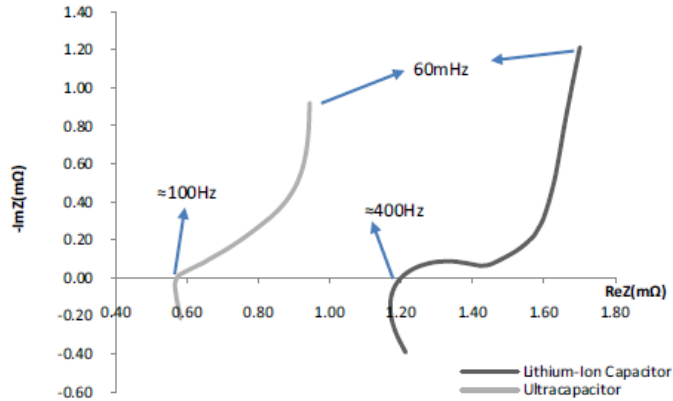
Figure 3.30 - Complex impedance plot comparison at full rated voltage for EDLC and LiC (Frequency range 1.2kHz ÷ 60mHz) by [35]

In fact *Lambert et al.* reported the impedance trace shown in Figure 3.30. It shows the impedance measured for both EDLC and LiC cells at their maximum operating voltage for a frequency range of 1.2kHz to 60mHz. The traces show that the ESR value for the LiC is more than twice the value for the traditional EDLC. As frequency decreases from the real axis intersection the well evident 45° slope of the curve suggest a stable capacitive behavior, whereas at very low frequencies the EDLC approaches a purely capacitive behavior. Regarding the case of the LiC, the 45° slope appears distorted, which suggests that in mid-frequency range the spectrum resembles that of a lithium-ion battery; however the behavior at lower frequency resembles the EDLC more closely. This curve in the spectrum in the high-middle frequency range corresponds to a *series diffusion impedance* generated by the constituent technology of the device. For the purposes of power electronic interface this effectively means a *separate parallel impedance* associated with the energy storage mechanism. Since the imaginary part of the complex impedance of a LiC cell is much higher at low frequency than that of an EDLC and its zero-crossing point is at a comparatively much higher frequency (around 400Hz vs. 100Hz for the EDLC), it can be stated that LiC operate in capacitive region at fundamental frequencies four times higher than the EDLC. However, the high impedance magnitude for high frequencies shows it is more susceptible to terminal voltage fast transients.

In order to achieve a *LiC model* which could be suitable for use with power electronics simulation, a full frequency range model and experimental parameter identification of some LiC cells together their variation with the applied voltage, is described in the next paragraph.

154

3.4 LiC proposed model and experimental validation

In order to build a general model that takes into account the variability of different parameters, it is necessary to collect and highlight the results of tests conducted on the different types of LiC cells. Again, for assessing the frequency behavior of these LiC cells, different tests were carried out using the impedance spectroscopy technique by means of the aforementioned EIS technique.

The two previously mentioned different pairs of LiC cells from JM energy (laminated CLQ1100S1A and prismatic CPQ2300S) have been tested in conjunction with the Department of Electrical Engineering, Polytechnic of Milan, Italy.

The equipment used to realize the frequency analysis consisted of a 100-A booster (VMP3B-100) connected to a potentiostat (SP-150), which were both from Biologic Science Instruments, controlled by a PC via USB with EC-LAB software . In Figure 3.31 there is an image of the arranged test bench.

In order to verify the behavior of the cells to vary the temperature, the tests were carried out in a climate chamber in order to perform the test at different temperatures.

For each cell several tests were carried out at temperatures in the range -30 ÷ +60° C with 10° C step. Furthermore, for each temperature, the test spectroscopy has been performed for different values of the LiC technology polarization voltage (2.2 V - 2.6 V - 3.0 V-3.4 V - 3.8 V).
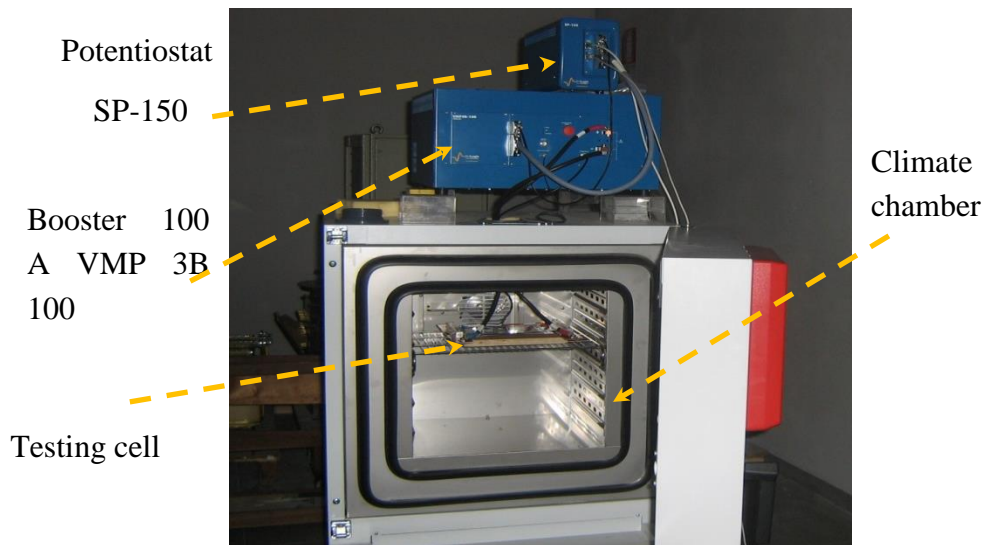
Figure 3.31 - Test bench used for LiC impedance spectroscopy

In particular, for each temperature, two graphs are shown, which correspond to the equivalent resistance and the equivalent capacitance coming from the real and the imaginary part of the cell complex impedance as:

$$\dot{Z}_{eq}\left(\omega,V,T\right)=R_i(T)+\mathrm{j}\omega L+Z_p\left(\omega,V,T\right)$$

$$\begin{cases} R_{eq}=\Re\left\{\dot{Z}_{eq}\right\} \\ C_{eq}=-\dfrac{1}{\omega\Im\mathrm{m}\left\{\dot{Z}_{eq}\right\}} \end{cases} \tag{3.26}$$

where ω indicates the pulsation test, T the room temperature and $\dot{Z}_{eq}$ the complex impedance obtained from the spectroscopy.

Each graph shows the values of the equivalent resistance and capacitance obtained with different polarization voltages. The frequency range is between 10 mHz and 100 Hz not taking into account higher frequencies because immediately after 100 Hz the capacitance is strongly reduced, as it will be evident from the reported results.

3.4.3   1100 F LiC laminated cell test results

As it will be noted from the Figure 3.32 and Figure 3.33 below, both the resistance and the capacitance vary significantly not only in frequency, but also with their polarization voltage and obviously with the temperature. In particular, it seems that the effects of temperature and voltage are somehow related because, as the temperature changes, the voltages to which they exhibit certain behaviors change too.

In order to better assess the cell behavior with both the temperature and voltage variations, the capacitance trends are reported before those of the resistances.

The capacitive behavior shown by this type of cell at room temperature is quite similar to one of a conventional EDLC cell . However, the capacitance is not a monotonic function of the voltage but has a **minimum** at an intermediate voltage in the operation range.

Firstly, the capacitance variation with the voltage shifts its minimum point as the temperature varies . In fact, regarding temperatures values higher than the room temperature (20 °C) the minimum capacitance occurs for a cell voltage equal to 3.0 V (about the half of the operation range for these cells), whereas for lower values of the room temperature, the minimum capacitance shifts going down to 2.6 V and then to 2.2 V.

156
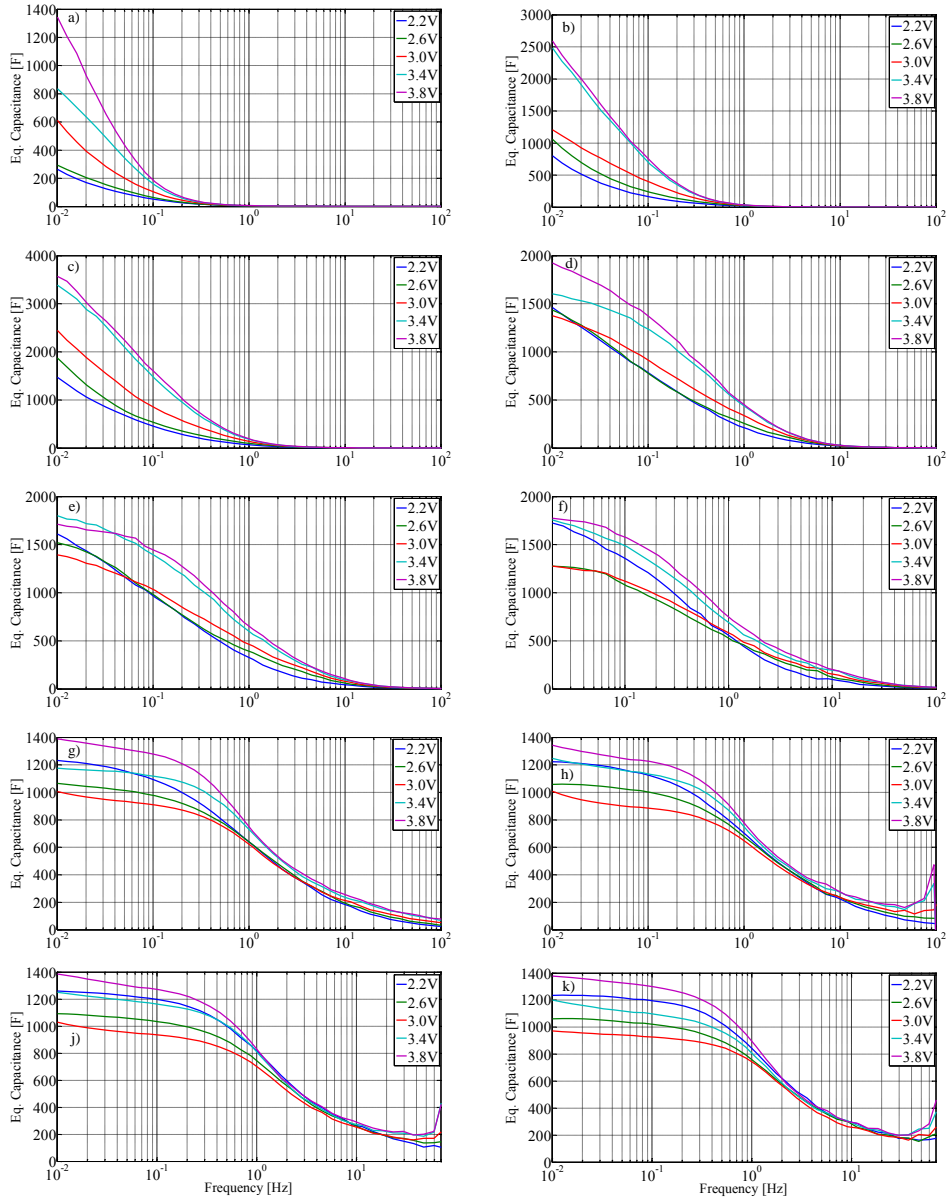
Figure 3.32 – Frequency behavior of the 1100 F laminated LiC cell equivalent capacitance for different polarization voltages and temperatures: a) -30 °C; b) -20 °C; c) -10 °C; d) 0 °C; e) 10 °C; f) 20 °C; g) 30 °C; h) 40 °C; j) 50 °C; k) 60 °C

At very low temperatures the capacitance is an increasing function with the voltage, as it happens for conventional EDLC, while at room temperature the capacitance first decreases and then grows varying with the bias voltage in the operating range. It can be also observed that the capacitance reduction with the frequency is always more highlighted as more the temperature is lowered. The

higher the temperature the better the dynamic behavior of the LiC. This could be explained by taking into account that at high temperature increases the mobility of the electrolyte.
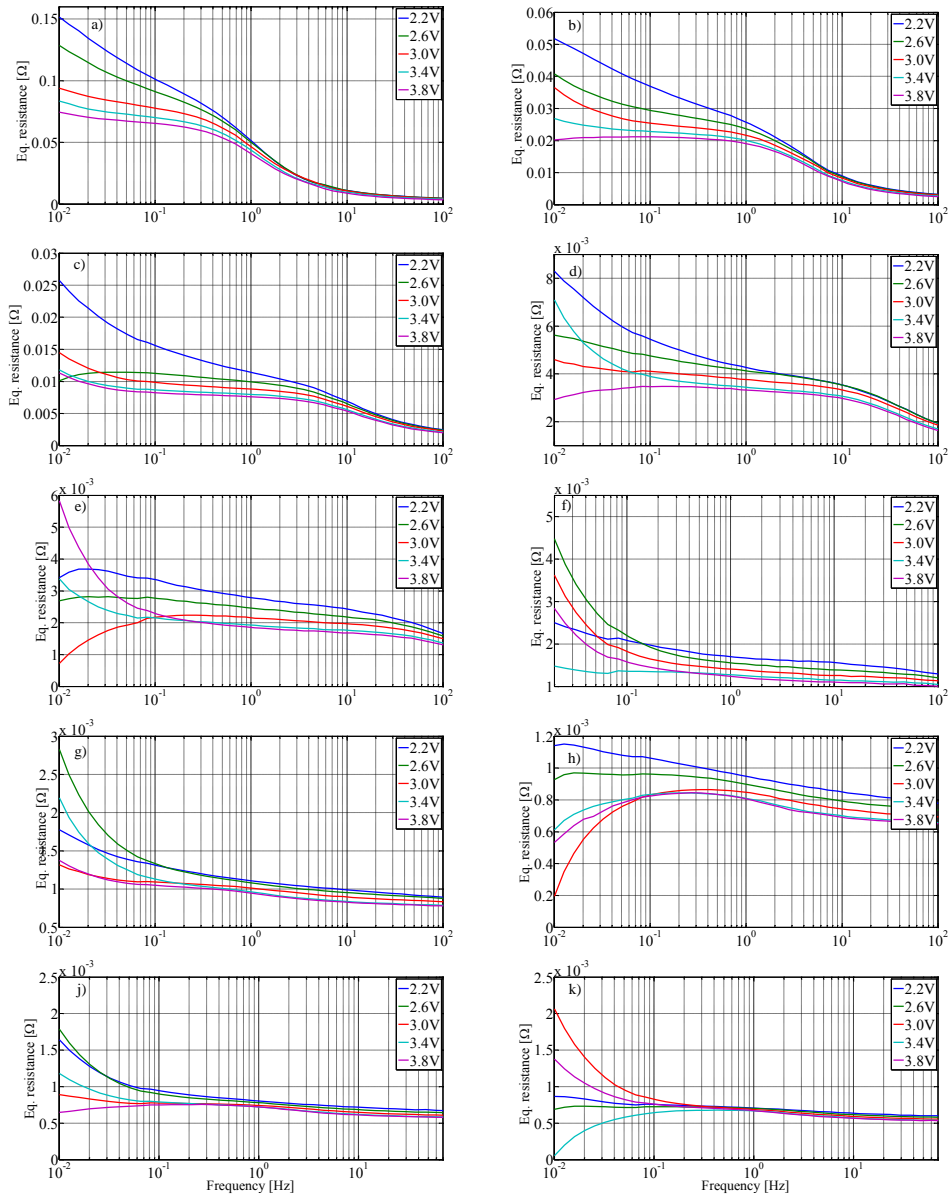
Figure 3.33 - Frequency behavior of the 1100 F laminated LiC cell equivalent resistance for different polarization voltages and temperatures: a) -30 °C; b) -20 °C; c) -10 °C; d) 0 °C; e) 10 °C; f) 20 °C; g) 30 °C; h) 40 °C; j) 50 °C; k) 60 °C

Although the capacitance at low-temperature degrades quickly with the frequency, the same parameter at a very low frequency increases with decreasing temperature until reaching its maximum values around -10° C. At this temperature and at high voltage, the cell shows a capacitance three times higher than the nominal one. By further decreasing the temperature, the capacitance begins to decrease even at very low frequency, to become lower than the nominal one at low voltage and at -30° C.

In the Figure 3.33 below are reported the resistance values obtained in the same tests. On the contrary, with respect to the capacitive behavior, the equivalent resistance shown by this type of cells is quite different from the one shown by standard EDLC. In fact, by not considering the test at the lowest temperature, there is at least one voltage value for which the resistance variation with the frequency is not monotonically decreasing. Indeed it may happen that the minimum resistance at certain voltages and temperatures occurs at very low frequencies. This behavior, which seems totally absent at -30 ° C is very weakened at room temperatures (see the tests at 20 ° C and 30° C) but appears both at higher temperatures and lower temperatures. Of course, this behavior makes it fairly complex modeling of this type of cells as the temperature varies.

Globally, as well as for conventional EDLC, the equivalent resistance decreases with increasing temperature (probably because it increases the mobility of the ions in the electrolytic solution). Moreover, at high frequencies the resistance is a decreasing function of the voltage, whereby at higher bias voltages correspond lower high frequency resistances. This behavior, however, is not true at low frequency. At low frequency, in fact, the voltage value whereby the resistance is maximum varies with the temperature. This contributes to make more complex the modeling of this type of cells at low frequencies.

3.4.4   2300 F LiC prismatic cell test results

The behavior of the prismatic LiC cells differ significantly from the laminated ones. This may be due to the fact that the rigid package does not allow any **volume variation** that occurs in the normal cell operation (it is a phenomenon that also occurs in conventional EDLC). Therefore, the volumetric constraint changes the macroscopic behavior of the cell as will be clear from the analysis of the spectroscopy results that are in the following reported.

By looking at the graphs in Figure 3.34, it can be noted that the capacitance trend in frequency is significantly different from the laminar cells. Indeed, apart from the test at -30° C, the capacitance variation with the frequency has a double hump and is no longer a monotonic function. The double hump is more emphasized in certain voltages rather than others. The voltage for which the effect is more evident varies with the temperature. In particular, the greater the temperature the lower the voltage for which the phenomenon is highlighted. The capacitance at low frequency does not grow at low temperatures as in the case of laminar cells and never exceeds significantly the rated value. In a similar way as it occurs for the laminar cells, the dynamic response of this prismatic cell improves with increasing temperature, and this is evident from the fact that the capacitance decreases with gradually increasing frequency values when the temperature increases. In analogy to what happens for the laminar cells, the capacitance variation with the voltage is a monotonic function only at very low temperature, while, starting from room temperature it shows a minimum at half the interval of the operating voltage (even in this case at 3.0 V).

In the Figure 3.35, the equivalent resistance values with the frequency are reported.

Even in the evolution of resistance is highlighted a similar double hump. In particular, in the minimum capacitance area it can be noted an increase of resistance. This concurrence suggests that the two effects are due to the same phenomenon. For a deeper investigation of this effect, a chemical analysis of the structure should be done. On the contrary, at very low frequency, for any voltage and any temperature, the equivalent resistance tends to increase. However, it can be assumed that the reduction of resistance, which can be noted in the laminated cell, is due to an effect similar to the one which involves the hump in prismatic cells. The effect of the rigid structure may have transferred the hump to higher frequencies. With reference to an analysis up to 10 mHz, this allows to see the increasing resistance values with the decreasing frequency that is not visible (but foreseeable) in the case of laminar cells.
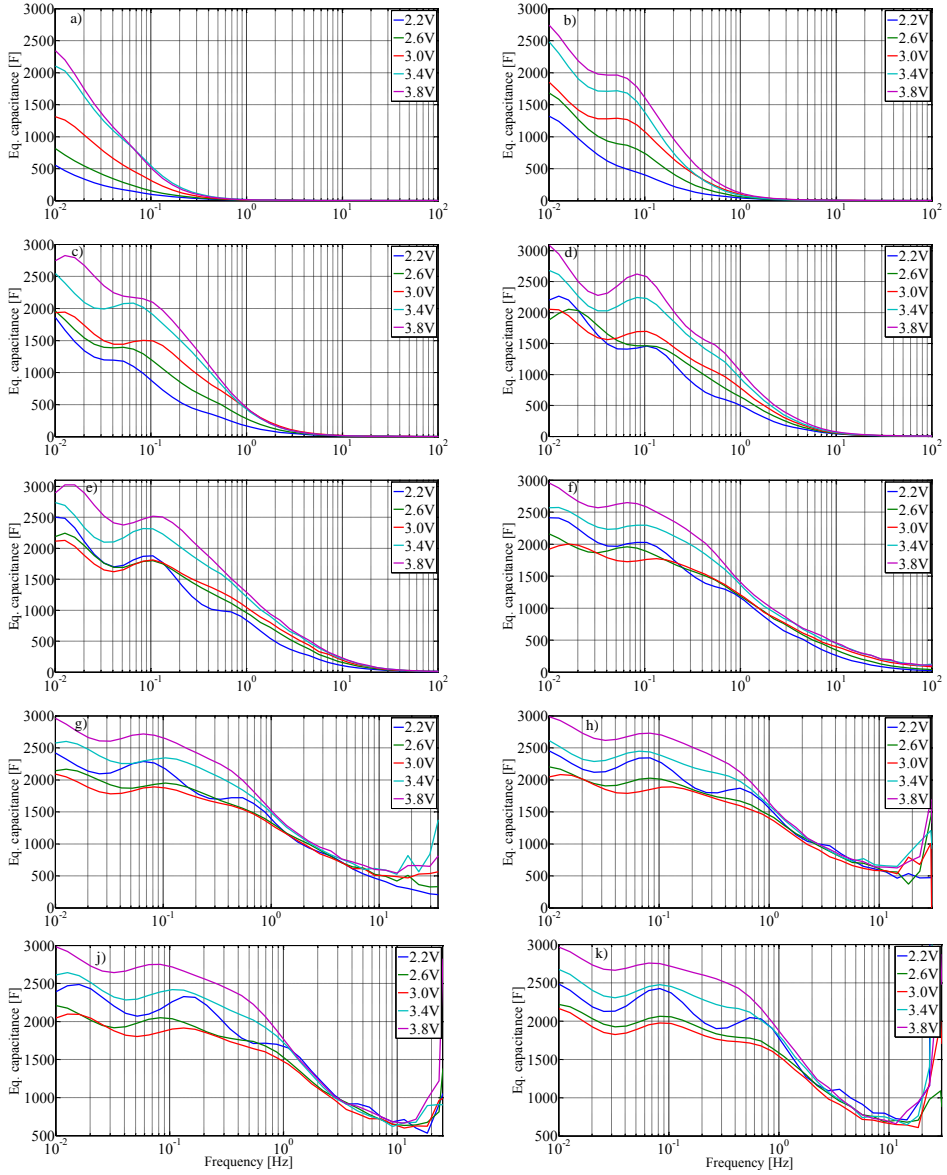
Figure 3.34 - Frequency behavior of the 2300 F prismatic LiC cell equivalent capacitance for different polarization voltages and temperatures: a) -30 °C; b) -20 °C; c) -10 °C; d) 0 °C; e) 10 °C; f) 20 °C; g) 30 °C; h) 40 °C; j) 50 °C; k) 60 °C
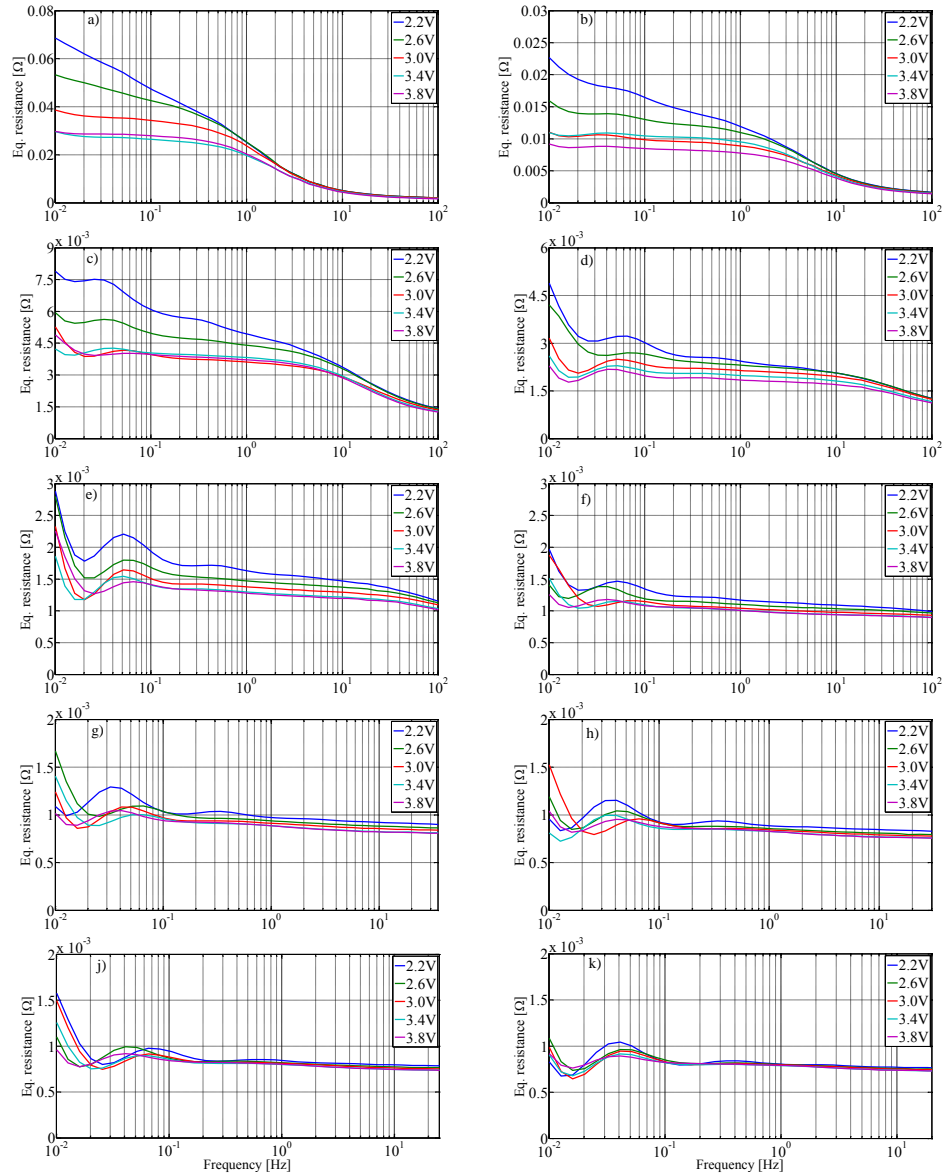
Figure 3.35 - Frequency behavior of the 2300 F prismatic LiC cell equivalent resistance for different polarization voltages and temperatures: a) -30 °C; b) -20 °C; c) -10 °C; d) 0 °C; e) 10 °C; f) 20 °C; g) 30 °C; h) 40 °C; j) 50 °C; k) 60 °C

3.4.5   LiC dynamic model at standard temperature

By looking at the previously reported graphs it is immediate to understand that it is not in general possible to apply the models developed for the traditional EDLC to this novel type of cells. However, if the focus is limited to laminated LiC cells at a temperature close to ambient temperature and therefore the graphs of capacitance and resistance variation at 20 °C and 30 °C are observed, it can be seen, for each polarization voltage, the frequency behavior of the LiC cells is similar to that of a conventional EDLC. Moreover, as was also observed previously, the variability of the capacitance with the voltage does not have a monotonic trend with the same voltage so as it occurs for the EDLC.

From how above said, it can be deduced the possibility of modeling the laminated cells at room temperature by adopting a model very similar to that of Figure 3.18.

It has been then investigated the possibility of representing the dynamic behavior of the laminated LiC cells with the conventional EDLC model. This results feasible just if the analysis is limited to tests at 30 °C, which seem to be more similar to the dynamic responses of a EDLC. Moreover, it can be also carried out an estimation the parameters of the equivalent circuit of Figure 3.18 by analyzing their dependence on voltage.

In particular, it is considered only the **first branch** of the model neglecting self-discharge and recombination phenomena as already depicted in Figure 3.17 - SC circuital model represented by 4 parameters *L*, *Ri*, *C* and τ [18]
.

It has to be outlined that the impedance of the LiC is more complex because the system has multiple kinetic steps. The transfer impedance of the EDLC is due solely to the porous nature of the electrode. Nevertheless, there is diffusion impedance associated with the doped Li-ion electrode.

By keeping in mind the approach showed in paragraph 3.2.5, The equivalent impedance shown by the LiC can be represented by rearranging eq. (3.13), in which the frequency (ω) the temperature (*T*) and applied voltage (*u*) dependence is highlighted:

$$Z_{eq}(\omega,V,T) = R_i(T) + j\omega L_i + \frac{\tau(u,T)\coth\left(\sqrt{j\omega\tau(u,T)}\right)}{C(u,T)\sqrt{j\omega\tau(u,T)}} \cong R_p(\omega,u,T) + \frac{1}{j\omega C_p(\omega,u,T)} \qquad (3.27)$$

The Figure 3.17 shows the discrete representation of Z_P from (3.13), where R_i is the resistance at an infinite frequency, L_i is the leakage inductance, ω is the angular frequency, u is the internal voltage, C is the DC capacitance value, and τ is, dimensionally, a time. The leakage inductance is usually very small and is neglected in the following.

As reported in [19], it is possible to write:

$$\lim_{\omega \to 0} \Re e\{Z_p\} = \lim_{\omega \to 0} R_p = R_i + \sum_{n=1}^{\infty} \frac{2\tau(u)}{n^2 \pi^2 C(u)} = R_i + \frac{\tau(u)}{3C(u)} = R_{dc}$$

$$\lim_{\omega \to \infty} \Re e\{Z_p\} = R_i \qquad (3.28)$$

$$\lim_{\omega \to 0} \Im m\{\omega Z_p\} = -\frac{1}{C(u)}$$

For each polarization voltage, from the EIS, it is possible to obtain the measured real and imaginary part of Z_p versus angular frequency ω. In particular, for each polarization voltage, the parameters C, R_i, and τ of the model have been found. This detailed procedure is highlighted by *Ciccarelli et al*. in [37] and the results is that it is possible to see that C, R_i, and τ are dependent on the polarization voltage. Using the method of least-square minimization, polynomial interpolation functions were found and are depicted in Figure 3.36.

In particular, for both cells, R_i can be approximated by a 3rd degree polynomial. In any case, in the following, a constant value of R_i will be utilized because of its small absolute variation. In contrast, C and τ can be well approximated by a 4th degree polynomial, where the minimum is around 3 V.

$$\begin{cases} R_i(u) = 9.679 \cdot 10^{-5} u^3 - 8.420 \cdot 10^{-4} u^2 + 2.280 \cdot 10^{-3} u - 1.076 \cdot 10^{-3} \\ C(u) = -528.3 u^4 + 6157 u^3 - 26167 u^2 + 48074 u - 31242 \\ \tau(u) = -5.459 \cdot 10^{-2} u^4 + 6.362 u^3 - 26.93 u^2 + 48.90 u - 31.15 \end{cases} \qquad (3.29)$$

After investigating the model for a single cell and identifying its parameters, the limits on the applicability of the model to a stack were investigated. Several tests were performed at the Transport Laboratory of the D.I.E.T.I. of the University Federico II of Naples on the stack of 36 laminated LiC cells previously highlighted in Figure 3.27. Starting from the single cell model, it is possible to build an **aggregate model** for the LiC module, as long as it is right to consider that the cells are perfectly equal and the voltages applied to them are equally divided on the cells.
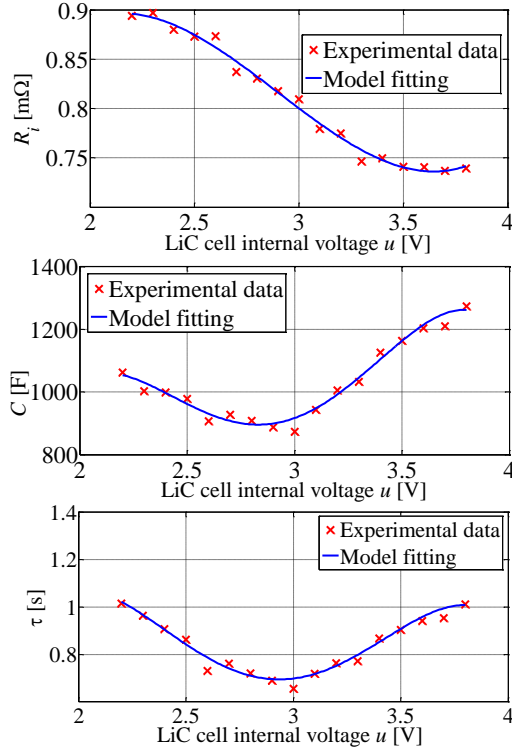
Figure 3.36 - CLQ1100S1A. Model-based fitting (continuous line) and experimental data (marked line)

Because the tests were conducted at a constant current, the variations in R_i with the voltage were assumed to be negligible. Therefore, it was set equal to 0.7 mΩ for all of the cells. By using N to denote the number of series cells constituting the LiC module and assuming that the cells are strictly equal, the mathematical relation for an aggregate model that expresses the variation in the module equivalent capacitance, C_{LiC}, as a function of the polarization voltage, u_{LiC}, is:

$$C_{LiC}(u_{LiC}) = \frac{a_4}{N^5} u_{LiC}^4 + \frac{a_3}{N^4} u_{LiC}^3 + \frac{a_2}{N^3} u_{LiC}^2 + \frac{a_1}{N^2} u_{LiC} + \frac{a_0}{N} \qquad (3.29)$$

where the coefficients a_i are the same as reported in eq. (3.29) for $C(u)$ and obviously N=36.

Therefore, the aggregate model was simulated via Matlab-Simulink for the same conditions as used in the experimental tests with the same charge/discharge rate currents. The agreement between the experimental and simulated data resulted satisfactory for all the current values and is even reported in [37].

165

In conclusion, the results of experiments and numerical simulations demonstrate the value and effectiveness of the proposed model for the laminated LiC cells when they operate at a standard temperature (20÷30 °C). More specifically:

- It has been shown that at temperatures higher than 20 °C, the full frequency range EDLC model can be used with little modifications. In particular, the dependence of the model parameters on the applied voltage cannot be considered linear. Using **polynomial interpolations** of the parameter variations with the voltage, a model suitable to represent the behavior of laminated LiC cells has been found.

- The **applicability** of the model to a module of the same cells was also analyzed. It has been shown that an aggregate model obtained by considering all of the cells to be equal can give good results only for voltages far from the boundary voltages. This could be due to the electronic balancing circuits that act when the voltage is higher than a fixed threshold.

After a comparison with the other relevant research works in the literature, it appears that the [33] showed that the LiC capacitance evolution in function of current rate and state of charge is not linear as is the case of conventional EDLC but has a polynomial evolution, which also parameterizes all in function of the temperature and life cycle. This definitely guarantees that the developed model is more accurate, but on the other hand increases the computational burden for the parameters determination. The work presented in [35] presents two additional parameters, the parallel double layer capacitance C_P with the limiting resistance R_t in series with a diffusion impedance Z_D (see Figure 3.29). Besides the fact that is not shown the parameters dependency on both the voltage and the temperature, in this last work it seems the extra complexity of the LiC cell requires five coefficients − R_i, R_t, C_p, C_D and R_D − which makes parameter extraction more timing consuming. In addition, since the bulk of the equivalent circuit parameters is obtained through a series of mathematical expansion, the model could be quite complex. Finally, the model presented in [36] is simpler and consists of only a RC circuit, this resulting in a computationally less demanding model, despite a non-linear voltage dependent capacitance is used (see Figure 3.28). By comparing this last one with the our proposed model, it can be stated that our approach better models the dynamic behavior of the LiC

166

cells. In any case it is noted that no equivalent circuit models for the LiC module have been proposed in the mentioned papers, this could be explained because the LiC technologies are still under development and the long cycle behavior of these systems is still unknown. This is a challenge which are going to study for a next improvement.

3.4.6　LiC model suitable for transport application and simplified parameter identification

As already mentioned in paragraph 3.2.6, concerning the use of a LiC as an storage system for transport applications, it is not necessary to refer to a high-performance model from the dynamic point of view, so it can be repurposed the simplified model of Figure 3.20 in which it has to replace the subscripts with term "*LiC*". Obviously, on the basis of how widely highlighted in the previous paragraph, the relationship between capacitance and cell voltage will be very different from a linear trend, then the characteristics relations can be in general expressed as:

$$
\begin{cases}
v_{LiC} = u_{LiC} - r_{LiC}\, i_{LiC} \\
i_{LiC} = -\dfrac{d\left[u_{LiC} \cdot C_{LiC}\left(u_{LiC}\right)\right]}{dt}
\end{cases}
\tag{3.30}
$$

at this point it is proposed a simplified procedure for the identification of the parameters of this model LiC for transport applications, which consists in obtaining the r_{LiC} value and the trend $C_{LiC}(u_{LiC})$ of the capacitance as a function of the applied internal voltage by means of constant current charge/discharge tests. In this way procedure the long and laborious analysis EIS is avoided.

Several measurement has been performed at the Transport Laboratory of the Department of Electrical Engineering and Information Technologies of the University Federico II of Naples on the aforementioned laminated LiC module of Figure 3.27 for different constant current rates charge and discharge operations in order to evaluate the effective equivalent capacitance and the DC equivalent internal resistance.

As shown in Figure 3.37, the test bench consisted of a 380-V, 50-Hz three-phase main supply and a diode-unidirectional rectifier, in order to obtain a 550-V DC-bus. An interleaved three-leg full bridge bidirectional DC-DC converter (Sinus Penta 0086-S20), with a rated power of 20 kVA, was employed for
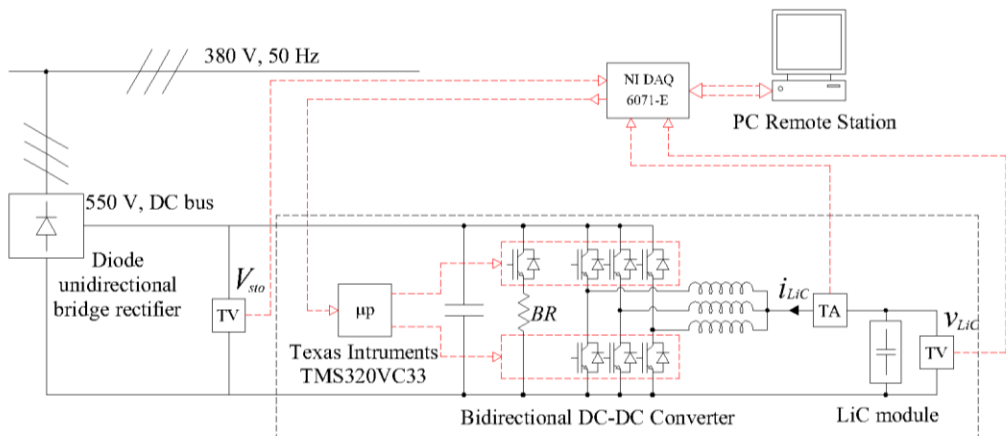
Figure 3.37 - LiC 30.5 F module test setup

charging/discharging the LiC module.

In order to control the charge/discharge phases, an appropriate control algorithm based on LiC power and current loops was implemented in the DSP for managing the DC-DC converter. In this way, it was possible to perform both constant power and constant current tests, by imposing the respective reference values. The DSP is based on a Texas instruments TMS320VC33 chipset, with a sampling time of 400 µs. The control algorithm required the measurements of the LiC module terminal voltage v_{LiC}, the LiC module current i_{LiC}, and the DC-bus voltage V_{sto}. These were instantaneously measured using transducers and digitally acquired via a National Instruments DAQ 6071E under a sampling frequency of 50 kHz to ensure a satisfactory precision. It should be noted that the tests were conducted under a **constant** ambient temperature of about 25 °C.

Firstly, LiC module has been discharged and charged the within different constant current rate (25 A, 50 A, 75 A, 100 A and 135 A) and the relative voltage and current curves have been acquired.

In Figure 3.38 the charging/discharge voltages with reference to the constant current rate of 100 A and 135 A are reported. Afterwards, it has been noted that during constant charge/discharge current values, the behavior of the voltage measured at the module terminals was not linear over the whole allowable working voltage. Furthermore, it has been observed that for time slots below $\Delta t_k = 1s$, the measured voltage can be considered linear and therefore the equivalent capacitance can be considered as good as constant during the above time interval.

168
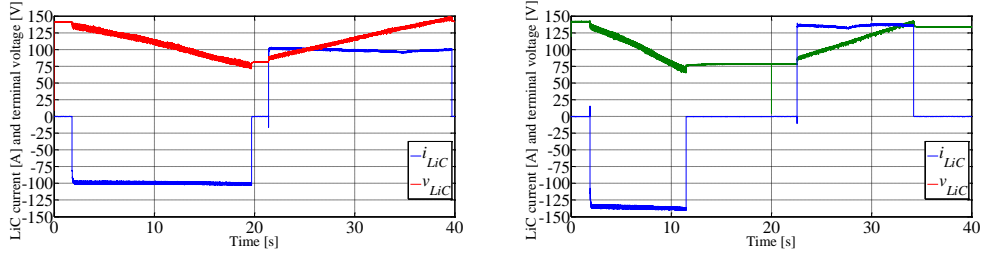
Figure 3.38 - LiC module voltage and current evolution during discharge and charge at 100 A a) and 135 A b)

So the voltage measured has been interpolated every 0.5 s intervals throughout the duration of the charging/discharging phases. The interpolation started a few tens of milliseconds after the initial charge/discharge transient due to the sudden application of the test current has been extinguished. In Figure 3.39 the interpolated measured voltages relating to the different constant current rates are reported with reference to the discharge cycles for sake of clarity.

Therefore the evolution of the LiC module voltage throughout the whole operating voltage range for a fixed charge/discharge current rate is given by the sequence of several interpolating straight lines and the expression of the equivalent LiC module capacitance as a function of the applied internal voltage, has been evaluated as:

$$
\begin{cases}
C_{LiC}\left(u_{LiC}\right) = \dfrac{SoC\left(t\right)}{u_{LiC}\left(t\right)}, \\[2ex]
SoC\left(t\right) = \displaystyle\int_0^t i_{LiC}\,dt + SoC_0, \\[2ex]
SoC_0 = C_{LiC}\left(u_{LiC,0}\right)u_{LiC,0}.
\end{cases}
\tag{3.31}
$$

the eq.(3.31) can be discretized as follows:

$$
C_{LiC}^{(k)} = \frac{\displaystyle\sum_{k=1}^{n} i_{LiC}^{(k)}\Delta t_k + C_{LiC}\left(u_{LiC,0}\right)u_{LiC,0}}{u_{LiC}\left(t_k\right)}
\tag{3.32}
$$

where $\Delta t_k = t_{k+1} - t_k, \quad k = 1,...n$ and $n = \left[\dfrac{T}{\Delta t_k}\right]$.

169
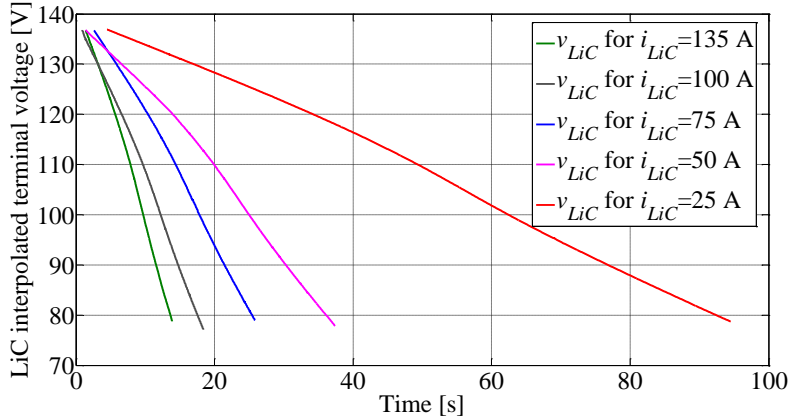
Figure 3.39 - Sequence of the interpolating lines for the LiC module terminal voltage

In the eq. (3.32), $C_{LiC}^{(k)}$ is the equivalent module capacitance value evaluated for the kth interpolating line, $i_{LC}{}^{(k)}$ is the LiC mean current during the time interval Δt_k, $u_{LC}(t_k)$ is the corresponding final voltage value at each interval and $C_{LC}(u_{LC,0})$ is the initial equivalent capacitance, which refers to the initial voltage value $u_{LC,0}(0)$ at $t_k = 0$. The interpolated internal LiC voltage $u_{LC}(t_k)$ has been calculated from the measured voltage $uv_{LC}(t_k)$ augmented or reduced by the rated voltage drop on the DC-ESR, $r_{LC}i_{LC}$ respectively during the discharging and charging phases.

The equivalent module capacitance shown in eq. (3.32) is calculated at each kth interpolating line for the whole operating voltage range and the capacitance – internal voltage behavior with respect to all the current rates is highlighted in Figure 3.40 a) for the several discharging cycles. According to the capacitance evaluated values for all the current rates, the law of capacitance variation is approximated by 5th order polynomial interpolating curve:

$$
\begin{cases}
C_{LiC}\left(u_{LiC}(t)\right) = a_5 z^5 + a_4 z^4 + a_3 z^3 + a_2 z^2 + a_1 z + a_0 \\
z = \dfrac{u_{LiC}(t) - 110}{18} \\
a_5 = -0.042 \\
a_4 = -0.09 \\
a_3 = 0.28 \\
a_2 = 0.48 \\
a_1 = -0.6 \\
a_0 = 30
\end{cases}
\tag{3.33}
$$

170
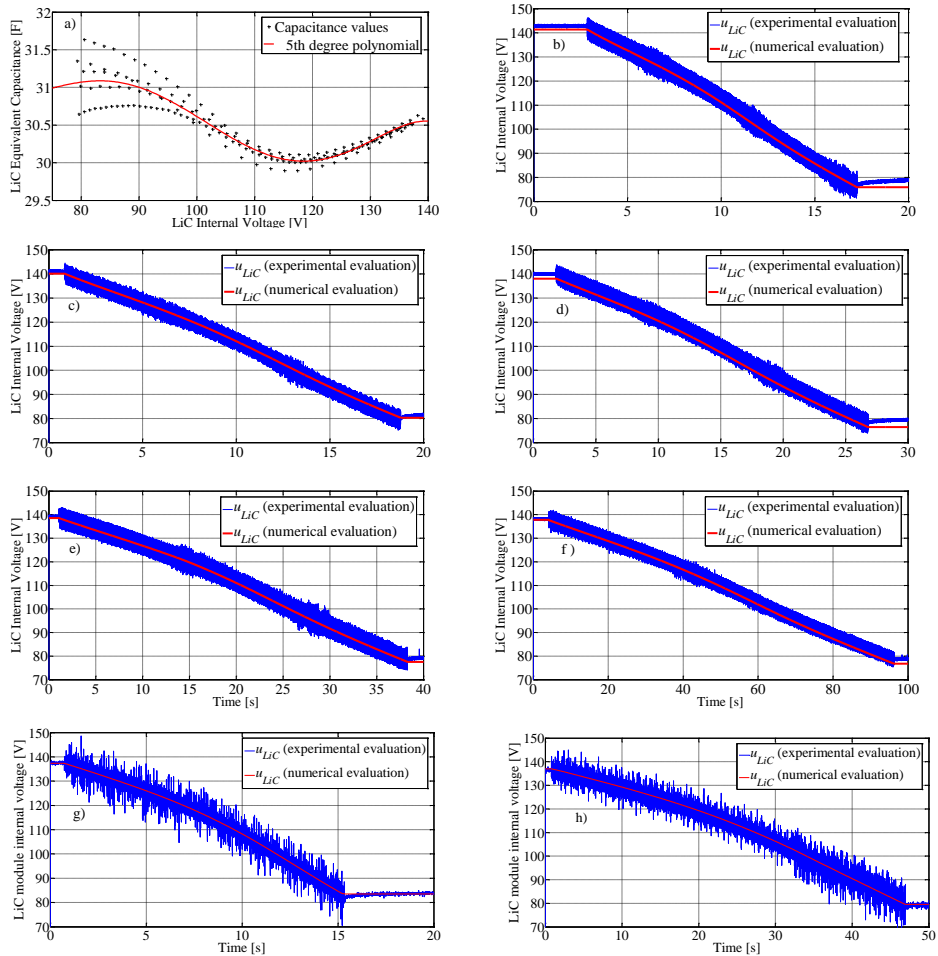
Figure 3.40 - Numerical results of the LiC characterization tests:
a) Equivalent capacitance values for all discharge current tests and corresponding 5th order interpolating polynomial;
b) Experimental and numerical evaluation of LiC module internal voltages at 135 A current discharge;
c) Experimental and numerical evaluation of LiC module internal voltages at 100 A current discharge;
d) Experimental and numerical evaluation of LiC module internal voltages at 75 A current discharge;
e) Experimental and numerical evaluation of LiC module internal voltages at 50 A current discharge;
f) Experimental and numerical evaluation of LiC module internal voltages at 25 A current discharge;
g) Experimental and numerical evaluation of LiC module internal voltages at 12 kW constant power discharge;
h) Experimental and numerical evaluation of LiC module internal voltages at 4 kW constant power discharge

171
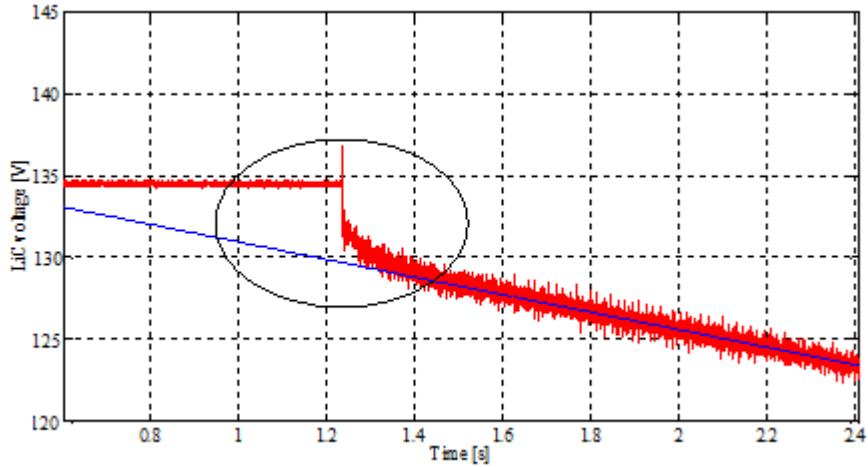
Figure 3.41 – Zoom view of the voltage drop on the ESR

It is clear to see that the variations between the rated capacitance value and the actual value evaluated over the operating voltage limits are constrained within the range [-1.9% 2.1%].

As concerns the DC ESR, its measurement is based on the evaluation of the sudden LiC terminal voltage decrease/increase LiC once the discharge/charge constant currents are applied. By keeping in mind the approach (IEC 62576, [38]), the internal resistance results the ratio between this sudden difference in the terminal voltage just before discharging/charging process begins and the value of the DC current applied to LiC (see Figure 3.41). This has been evaluated for all the discharge/charge test and it returned an average ESR very close to the rated one.

Finally, on the basis of identified capacitance − internal voltage behavior, the mathematical model expressed by eq. (3.33), has been experimentally validated. In particular the model has been simulated via Matlab-Simulink for the same condition of experimental tests with different discharge rate currents. In the Figure 3.40, the agreement between the experimental and simulated internal voltage of LiC module have been reported and it can be noticed the satisfactory overlapping between the numerical evaluation of the internal voltages and the corresponding measured ones for all the current tests.

In conclusion, since good agreement between the experimental and numerical data has been found, this simplified laminated LiC module parameter identification is *quickly* and *ease* for implementation as far as the module are concerned at standard temperature, nevertheless it has been employed a 5th order

172

polynomial instead of a 4th order one as outlined in eq. (3.29). This could be explained by the fact that during the charging of the prototypal module, the circuits for balancing are involved because an action equalizer is more evident for voltages close to the boundary voltages.

Finally, for confirming the goodness and ease in implementation of this fast parameter identification method, it has been validated its application to *traditional EDLC*. In particular, even in the *TrLab* of D.I.E.T.I. was tested a stack of SC formed by two modules by EPCOS of 3.3 F 75 V, see Table 3.6.

Figure 3.42 - Picture of EPCOS 3.3 F 75 V SC modules of D.I.E.T.I.

Part Number	48511A0333Q032
Rated Capacitance (@T_a=25°C)	3.3 [F]
Tolerance of rated capacitance	-10/+30 [%]
Rated/Surge Voltage (@T_a=25°C)	75/88 [V]
Maximum series resistance (@T_a=25°C; 1kHz)	200 [mΩ]
Maximum series resistance (@T_a=25°C; 50mHz)	500 [mΩ]
Stored Energy (@ Rated voltage)	9281 [J]
Specific Energy (@ Rated voltage)	1.6 [Wh/kg]
Specific Energy (@ Rated voltage)	1.4 [Wh/L]
Specific Power (Matched load)	4.4 [kW/kg]
Specific Power (Matched load)	3.7 [kW/L]
Weight	1.6 [kg]
Volume	1.9 [L]
Operating temperature range	-30/+70 [°C]
Lifetime (@T_a=25°C; rated voltage)	90000 [h]
Lifetime (@T_a=25°C; 10 A current)	500000 [cycles]

Table 3.6 - Characteristics of EPCOS 3.3 F 75 V SC modules of D.I.E.T.I
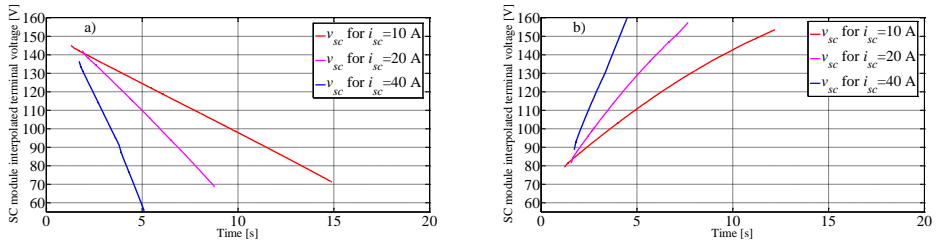
Figure 3.43 - Sequence of the interpolating lines for the SC module terminal voltage: a) discharging test; b) Charging test

Apart from the SC modules, the test bench and the employed procedures are the same of the ones aforementioned for the LiC module. The SC modules have been charged and discharged with different values of constant current (10 A, 20 A, 40 A) and the corresponding terminal voltage, v_{sc}, and current, i_{sc}, curves were acquired.

Subsequently, it was noted that during tests of charge / discharge at constant current, the behavior of the voltage measured at the series module terminals is fairly linear throughout the range of working voltage. This phenomenon is intended to mean that the equivalent capacitance varies little with the applied voltage and this is confirmed by the fact that this change is linear according to eq. (3.24).

In the Figure 3.43 are therefore reported the interpolated measured voltages relating to the different constant current rates with reference both to the discharge and charge cycles and for the next calculations is assumed $\Delta t_k = 1s$.

The relationship capacitance-internal voltage for each value of the test current is shown in Figure 3.44 for different discharge cycles. In accordance with the different values of equivalent capacity evaluated for all test currents, the law of variation of the equivalent capacity is approximated by a linear interpolating as:

$$C_{sc}\left(u_{sc}\left(t\right)\right) = 0.502 \cdot 10^{-3} u_{sc}\left(t\right) + 1.63 \tag{3.34}$$

As concerns r_{sc}, by bearing in mind the approach (IEC 62576, 2009), this was performed for all tests in discharge and charge and equivalent series resistance values for the SC modules have been reported in Table 3.7 . By averaging these values we can say that the ESR of the SC modules is equal to 266 mΩ.

174
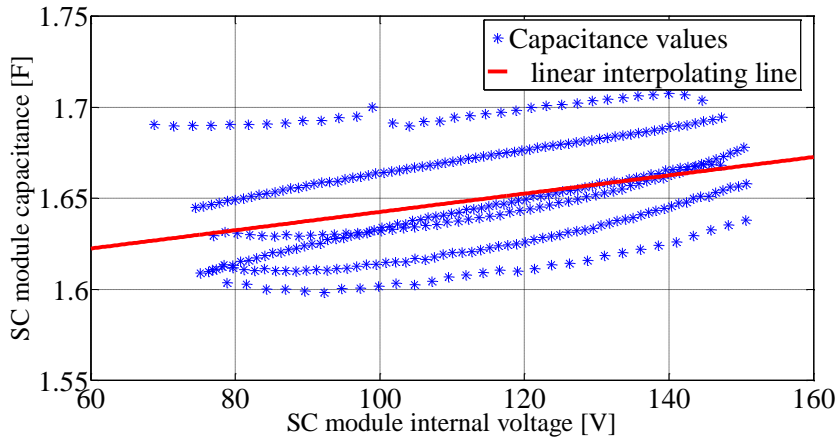
Figure 3.44 - Equivalent capacitance values for all discharge current tests and corresponding interpolating line;

	Measured module ESR r_{sc} (discharge)	Measured module ESR r_{sc} (charge)
10 A const. current	293 mΩ	268 mΩ
20 A const. current	281 mΩ	249 mΩ
40 A const. current	267 mΩ	238 mΩ

Table 3.7 – Measured values for ESR of the SC modules

Lastly, again the mathematical model expressed by eq. (3.34), has been experimentally validated. In particular the model has been simulated via Matlab-Simulink for the same condition of experimental tests with different discharge rate currents. In Figure 3.45 are outlined the trends of the measured voltage resulting from the experimental tests and the SC internal voltage resulting from numerical simulations by adopting the relation (3.34). It is noted the satisfactory agreement between the numerical evaluation of the internal voltage and the corresponding experimental measured SC terminal voltage for both all tests at constant current (Figure 3.45 (a) ... (f)) that for tests requiring a control on the terminal voltage (Figure 3.45 (g) and (h)).
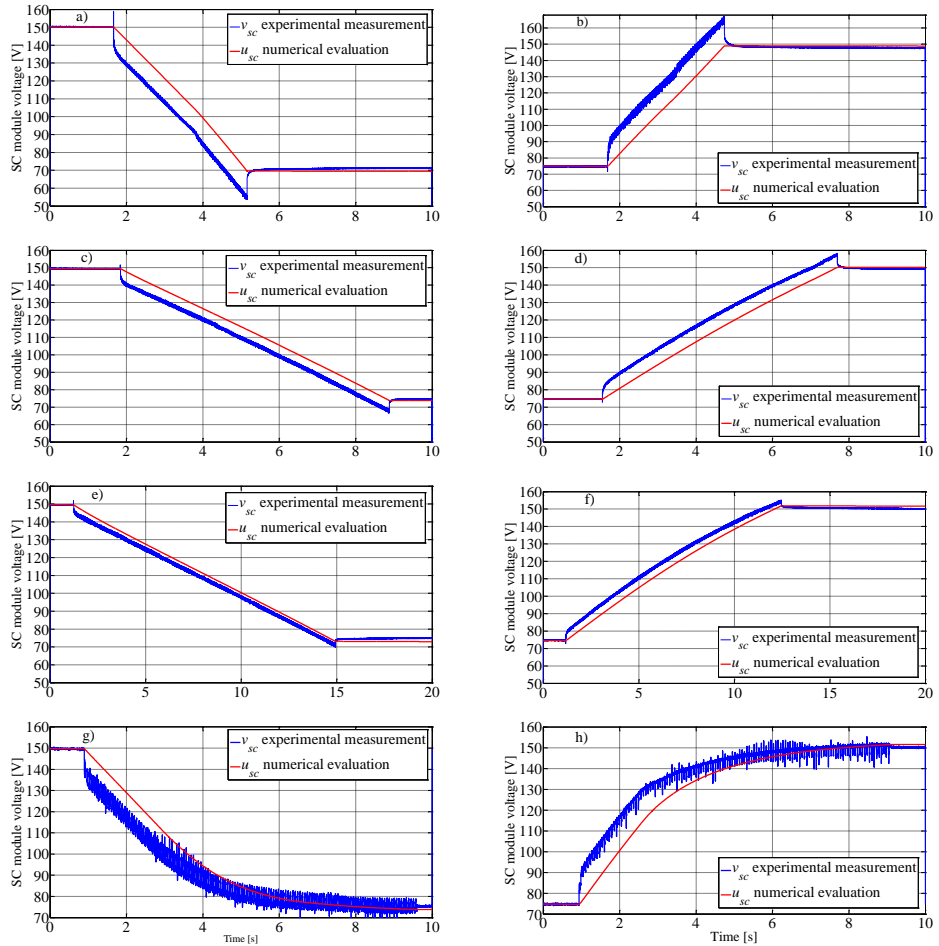
Figure 3.45 - Numerical results of the SC characterization tests:

a) b) Experimental and numerical evaluation of SC module internal voltages at 40 A current discharge and charge;

c) d) Experimental and numerical evaluation of SC module internal voltages at 20 A current discharge and charge;

e) f) Experimental and numerical evaluation of SC module internal voltages at 10 A current discharge and charge;

g) h) Experimental and numerical evaluation of SC module internal voltages for discharge up to reference voltage 75 V and a charge up to reference voltage 150 V

3.5   Chapter 3 references

[1] Conway, B. E.. Electrochemical Supercapacitors – Scientific Fundamentals and Technological Applications. *New York, Kluwer Academic / Plenum Publishers*, 1999.

[2] Miller, J. M.. Ultracapacitor Applications. *The Institution of Engineering and Technology*, UK, 2011.

[3] Musolino, V.. Supercapacitor storage systems: modeling, control strategies, applications and sizing criteria. Ph.D. Thesis in Electrical Engineering, XXVI Cycle, Electrical Department, Polytechnic of Milan, Italy, 2011, supervisor Tironi E.

[4] Kotz, R.; Carlen, M. Principles and applications of electrochemical capacitors. *Electrochimica Acta*, vol. 45 (15-16), May 2000, pp. 2483–2498.

[5] Namisnyk, A. M. A survey of electrochemical supercapacitor technology. Ph.D Thesis in Electrical Engineering, University of Technology, Sydney, Supervisor: Jian Guo Zhu.

[6] Čihak, E.E.T.; Jakopović, E.E.Z. Supercapacitors in power converter DC link: A short overview of design and application issues. *Proc. 34th Int. convention on information and communication technology, electronics and microelectronics MIPRO 2011*, Opatija; Croatia; 23-27 May 2011, pp. 130-135.

[7] Arbizzani, C.; Mastragostino, M.; Meneghello, L. Polymer-based redox supercapacitors: A comparative study. *Electrochimica Acta*, vol. 41 (1), Jan. 1996, pp. 21-26.

[8] Wikipedia the free encyclopedia. Supercapacitors. Available on-line: http:// http://en.wikipedia.org/wiki/Supercapacitor (Accessed 2013).

[9] Maxwell Technologies. BC series ultracapacitors. Available on-line: http://www.maxwell.com/products/ultracapacitors/docs/bcseries_ds_1017105-4.pdf (Accessed 2013).

[10] Rosario, L. C. Power and Energy Management of Multiple Energy Storage Systems in Electric Vehicles. Ph.D Thesis in Electrical Engineering, Department of Aerospace Power & Sensors, Cranfield University, DCMT Shrivenham, UK, June 2007, Supervisor: Patrick Chi Kwong Luk.

[11] Maxwell Technologies. 125 V heavy transportation module. Available on-line: http://www.maxwell.com/products/ultracapacitors/docs/125vmodule_ds_1014696-7.pdf (Accessed 2013).

[12] Devillers, N.; Jemei, S.; Péra, M.; Bienaimé, D.; Gustin, F. Review of characterization methods for supercapacitor modelling. *J Power Sources*, vol. 246, 2014, pp. 596-608.

[13] Spyker, R.L.; Nelms, R.M. Classical equivalent circuit parameters for a double-layer capacitor. *IEEE Transactions on Aerospace and Electronic Systems*, vol. 36 (3 –PART 1), 2000, pp.829-836.

[14] Kurzweil, P.; Frenzel, B. Capacitance characterization methods and ageing behaviour of supercapacitors. *Proc. 15th Int. Seminar on Double Layer Capacitors*, Deerfield Beach, FL., U.S.A., Dec. 5-7, 2005.

[15] Zubieta, L.; Bonert, R. Characterization of double layer capacitors for power electronics applications. *IEEE Trans. on Industry Applications*, vol. 36 (1), Jan./Feb. 2000, pp. 199-205.

[16] Belhachemi, F.; Rael, S.; Davat, B. Physical based model of power electric double-layer supercapacitors. *Proc. 35th IAS Annual Meeting and World Conference on Industrial applications of Electrical Energy*, Rome, Italy, 8-12 Oct. 2000, pp. 3069-3076.

[17] Faranda, R.; Gallina, M.; Son, D.T. A new simplified model of double-layer capacitors. *Proc. Int. Conf. on Clean Electrical Power, ICCEP 2007*; Capri; Italy; 21-23 May 2007, pp. 706-710.

[18] Buller, S.; Karden, E.; Kok, D.; De Doncker, R.W. Modeling the dynamic behavior of supercapacitors using impedance spectroscopy. *IEEE Trans Ind Appl*. , vol. 38 (6), Nov. 2002, pp. 1622-1626.

[19] Musolino, V.; Piegari, L.; Tironi, E. New full-frequency-range supercapacitor model with easy identification procedure. *IEEE Trans Ind Electron*. Vol. 60 (1), 2013, pp.112-120.

[20] Camara, M.B.; Gualous, H.; Dakyo, B. Supercapacitors modeling and integration in transport applications. *Proc. 46th IEEE Industry Applications Society Annual Meeting IAS 2011*, Orlando, FL, U.S.A., 9-13 Oct. 2011.

[21] Rafik, F.; Gualous, H.; Gallay, R.; Crausaz, A.; Berthon, A. Frequency, thermal and voltage supercapacitor characterization and modeling. *J Power Sources*, vol. 165 (2), Mar. 2007, pp. 928-934.

[22] Funaki, T. Evaluating energy storage efficiency by modeling the voltage and temperature dependency in EDLC electrical characteristics. *IEEE Trans. on Power Electronics*, vol. 25 (5), May 2010, pp. 1231-1239.

[23] Marumo, C.; Ando, N.; Taguchi, M. Design and performance of lithium-ion capacitors. *Proc. 3rd Eur. Symp. on Supercapacitors and Applications ESSCAP 2008*, Rome, Italy, 6-7 Nov 2008.

[24] Risa, M.; Yukinori, H.; Masako, I.; Koji, I.; Daisuke, S. Development of high-power lithium-ion capacitor. *NEC Technical Journal*, vol. 5 (4), Dec. 2010, pp. 52-56.

[25] Smith, P.H.; Tran, T.N.; Jiang, T.L.; Chung, J. Lithium-ion capacitors: Electrochemical performance and thermal behavior. *J Power Sources*, vol. 243, 2013, pp. 982-992.

[26] JM Energy Corp. Feature of Lithium-Ion Capacitors. Available on-line: http://www.jmenergy.co.jp/en/product_whats.html (Accessed 2013).

[27] Omar, N.; Al Sakka, M.A., Van Mierlo, J.; Van Den Bossche, P.; Gualous, H. Electric and thermal characterization of advanced hybrid li-ion capacitor rechargeable energy storage system. *Proc. 4th Int. Conf. on Power Engineering, Energy and Electrical Drives POWERENG 2013*, Istanbul, Turkey, 13-17 May 2013, pp. 1574-1580.

[28] Mandic, G.; Nasiri, A.; Ghotbi, E.; Muljadi, E. Lithium-Ion Capacitor Energy Storage Integrated With Variable Speed Wind Turbines for Power Smoothing, *IEEE Journal of Emerging and Selected Topics in Power Electronics*, vol.1 (4), Dec. 2013, pp.287-295.

[29] JM Energy Corp. Lithium-Ion Capacitors Applications. Available on-line: http://www.jmenergy.co.jp/en/product_ex.html (Accessed 2013).

[30] Koyanagi, K.; Hida, Y.; Ito, Y.; Yoshimi, K.; Yokoyama, R.; Inokuchi, M.; Mouri, T.; Eguchi, J. A Smart Photovoltaic Generation System Integrated with Lithium-ion Capacitor Storage. *Proc. 46th Int. Universities' Power Engineering Conf. UPEC 2011*, Soest, Germany, September 5-8, 2011.

[31] Uno, M.; Tanaka, K. Spacecraft electrical power system using lithium-ion capacitors. *IEEE Transaction on Aerospace and Electronic Systems*, vol. 49 (1), Jan. 2013, pp. 175-188.

[32] Porcarelli, D.; Brunelli, D.; Benini, L. Characterization of lithium-ion capacitors for low-power energy neutral wireless sensor networks. *Proc. 9th Int. Conf. on Networked Sensing Systems INSS 2012*, Antwerp, Belgium, June 11-14, 2012.

[33] Omar, N.; Daowd, M.; Hegazy, O.; Al Sakka, M.; Coosemans, T.; Van den Bossche, P.; Van Mierlo, J. Assessment of lithium-ion capacitor for using in battery electric vehicle and hybrid electric vehicle applications. *Electrochimica Acta*, vol. 86, Dec. 2012, pp. 305-315.

[34] Ciccarelli, F.; Del Pizzo, A.; Iannuzzi, D. Improvement of Energy Efficiency in Light Railway Vehicles based on Power Management Control of Wayside Lithium-ion Capacitor Storage. *IEEE Transactions on Power Electronics,* vol. 29 (1), Jan. 2014, pp. 275-286..

[35] Lambert, S. M.; Pickert, V.; Holden, J.; He, X.; Li, W. Comparison of supercapacitor and lithium-ion capacitor technologies for power electronics applications. *Proc. IET Int. Conf. on Power Electron., Machines and Drives PEMD 2010*, Brighton, U.K., April 19-21, 2010.

[36] Manla, E.; Mandic, G.; Nasiri, A. . Testing and modeling of lithium-ion ultracapacitors. *Proc. IEEE Energy Conversion Congress and Exposition: Energy Conversion Innovation for a Clean Energy Future ECCE 2011*, Phoenix, Arizona, U.S.A., September 17-22, 2011, pp. 2957–2962.

[37] Ciccarelli, F.; Barcellona, S.; Iannuzzi, D.; Piegari, L. Modeling and parameter identification of lithium-ion capacitor modules. *IEEE Trans. on Sustainable energy*, early access, 2014.

[38] IEC International Electrotechnical Commission. IEC 62576 - Electric double-layer capacitors for use in hybrid electric vehicles - Test methods for electrical characteristics. 2009.

Chapter 4

Supercapacitor Energy Storage: Modelling and Control strategies

This chapter presents the mathematical model of the entire urban railway drive system (substation, line, vehicle) with the aim of a theoretical analysis of the physical system behavior. In particular, it is briefly presented the simplified *mathematical model* of a feeding station / conversion and the supply lines. It is also described the power model of the electric traction drive load measured at the vehicle pantograph. The electrical power required by the vehicle was determined from the traction diagram of railway vehicle. Finally will be described a comprehensive model of electrical traction network with reference to the case of urban lines of radial distribution network.

Finally two **case study** base configuration are investigated, for the on-board and the stationary ESS installation respectively. With reference to real data of a sample metro line network, a SC ESS *design* methodology is assessed. Ultimately, some energy management **control strategies** are developed.

4.1 Urban Electrified Traction Systems

The urban electrified public transport, employ the low voltage DC systems, generally supplied at 750 V or 1500 V, which are usually the most economic. In this case, the pantograph connects directly the contact line to the power inverters of the train by means of filter capacitors. The average distance between
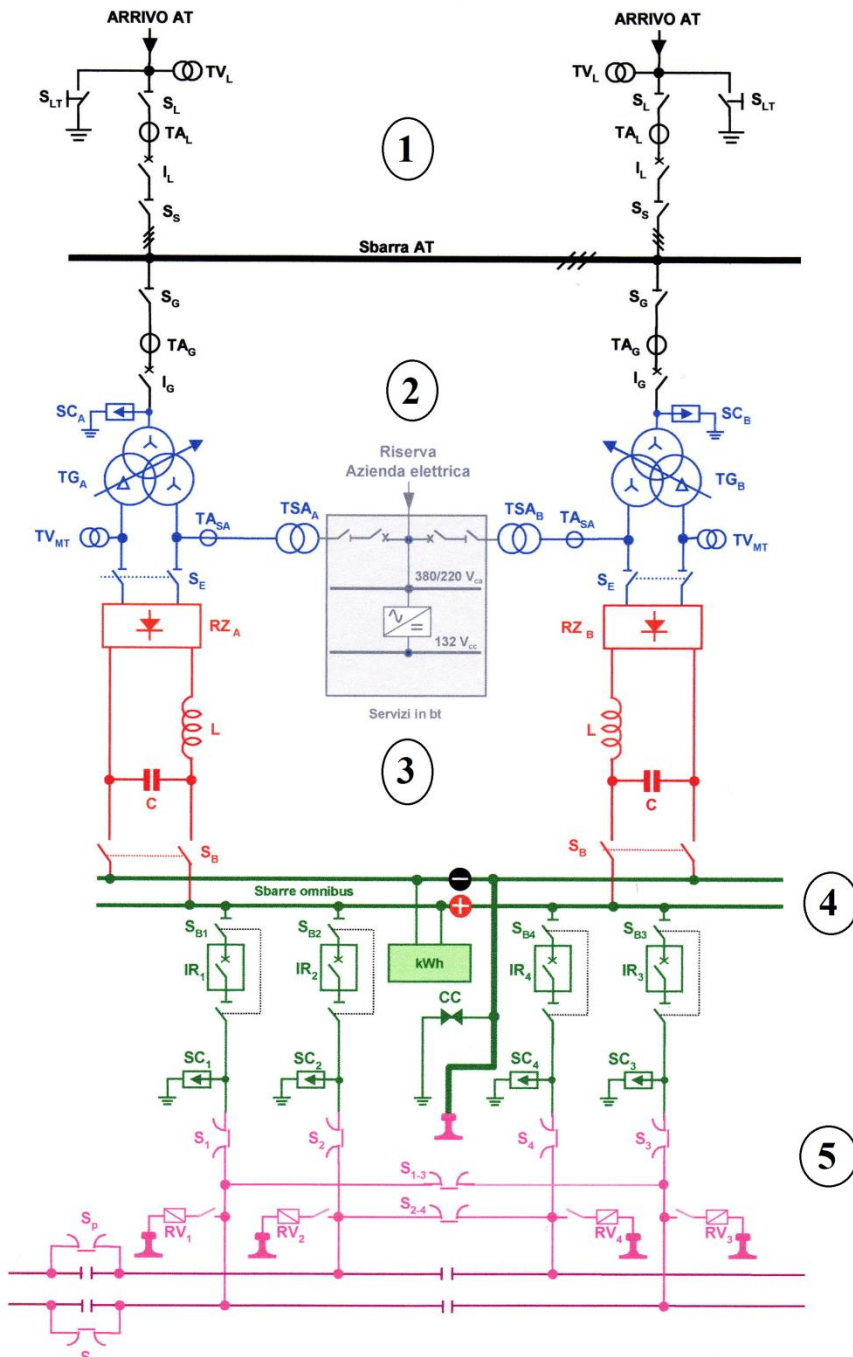
Figure 4.1 - Typical DC Electrical Substation scheme [2]

substations is very limited for example, in a subway at 750 V with heavy traffic, it can be of the order of 1.5 km, with minimum values of 1.3 km.

In general , the electrical substation are distributed along the lines at distances whose value mainly depends on the nominal voltage level as well as the intensity of the traffic. In the system at 3000 V were once adopted distance values between 35 to 45 km and beyond, but the increase of the power consumption in the main lines has led to reduce this distance not more than 20 - 30 km. For networks at 1500 V , the average distance from 6 to 8 km in lines with heavy traffic.

A DC substation derives AC High Voltage energy from one or more supply nodes. Then it converts the voltage to a suitable level for feeding the contact wires.. The feeding voltage of the DC substations can be 10, 20 or 30 kV. A direct-current feeding system features a three-phase bridged silicon rectifier for conversion from alternating to direct current. In order to reduce the harmonics, a modern 12-pulse system rectifier featuring two sets of 6-pulse rectifying circuits is used [1]-[2].

A typical electrical DC substation scheme is represented in Figure 4.1.

Basically, in a DC substation, the following sections are identified:

1. High voltage supply
2. Transformer and Medium voltage supply
3. Converter
4. Protection and Distribution
5. Overhead contact lines

The railway line circuit, constituted by the contact line and the rails, for operating, maintenance and protection reasons, is divided in many branches, to be supplied and separable with circuit breaker and disconnectors. Significant are the branches that can be listed below:

- *sectors*, fed to one or both ends by circuit breakers protections;
- *elementary sections*, separated from the contiguous disconnectors with simple command manual or remote, or with remote-controlled switches, but not for automatic opening.

Each sector fed at both ends or only at one end, must be protected at the supply point by ultrafast circuit breakers.

The two standard configurations of contact lines are listed below.
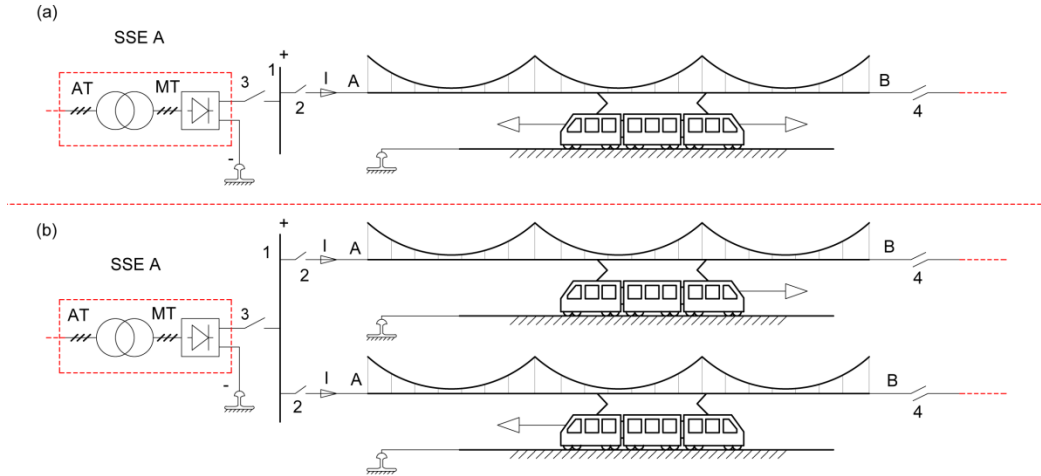
Figure 4.2 - One side supplied DC line: a) Single-track line; b) Double-track line. 1) Positive DC Bus 2) Ultrafast circuit breakers, 3) Circuit breakers of the conversion group; 4) Isolating air space disconnections.
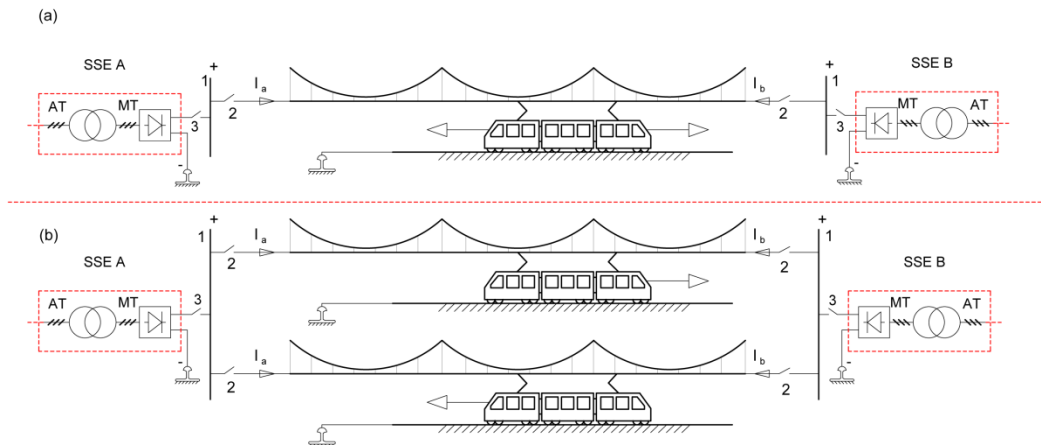
Figure 4.3 - Two side supplied DC line: a) Single-track line; b) Double-track line. 1) Positive DC Bus 2) Ultrafast circuit breakers, 3) Circuit breakers of the conversion group; 4) Isolating air space disconnections.

- Contact lines supplied by electrical substations at **both sides** (see Figure 4.2);
- Contact lines supplied by an electrical substation at **one side** (see Figure 4.3).

In the first situation, the overhead contact lines for going and returning are supplied by DC substations located at both sides of the line. The ends of each line are always considered to have the same voltage value. The maximum

voltage drop is reached when a vehicle is right between two substations. For simplicity, the two substations are supposed to provide always the same voltage output. This configuration is preferred for longer lines and many vehicles.

For latter one, the contact lines for going and returning are supplied by a single DC substation located at one end of the track. The voltage drop follows the vehicle displacement and its maximum is reached at the end of the track (the side not supplied by the substation) when a train is there. This configuration generally is used for contact lines with reduced length and few vehicles.

In the following, the mathematical models of the physical system constituted by the abovementioned supply line – railway vehicle configurations are analyzed.

4.2   Model of the electrical substation and contact wire

As previously mentioned, the electrical substation in urban electrified traction, which are in general supplied by the city power grid, have the task of adjusting the level of the primary voltage three-phase generally supplied in high voltage , to the level of DC voltage required by the network of electric traction, typically 600-750 V up to 1500 V.

Due to the notable power involved, polyphase *rectifier substations*, with silicon diodes connected as *Graetz* bridge are used (see **Errore. L'origine riferimento non è stata trovata.**). The advantages of using silicon diodes are substantially the following: possibility of realizing high power unit with small size, excellent performance , safety of operation, wide operating temperature range. These features facilitate the operation of automatic and remotely controlled substations. However, the traction substations are characterized by strong and overload overvoltage , then the rectifiers must be sized appropriately according to the maximum peak current.

In the Figure 4.4 is depicted the complete equivalent electrical circuit representing the main electrical diode supply substation and the overhead contect line.

As concerns the electrical substation, by keeping in mind the general scheme in Figure 4.1, with L_{sub} and C_{sub} are denoted the inductive and the capacitive rectifier output filters, whereas the resistance R_{sub} takes into account only the voltage drops due to non-ideality of the components [3]-[4]. In fact, because of
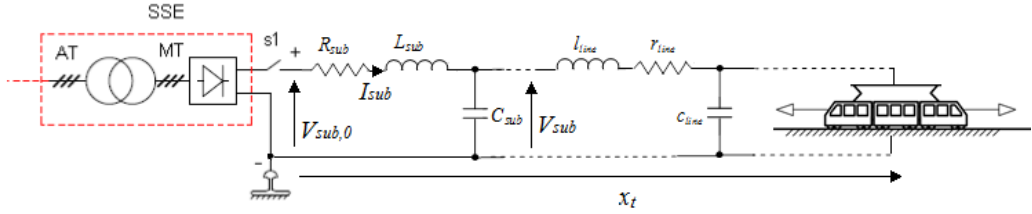
Figure 4.4 – Complete electrical model of the DC traction line

the non-ideality of the semiconductor components, transformer inductances and voltage switching phenomenon, the rectifier output shows a voltage drop which is a function of the current. This voltage drop is taken into account by schematizing it with a fictitious resistance R_{sub} (in the following called *internal substation resistance*):

$$R_{sub} = \frac{3\omega L_S}{\pi} \tag{4.1}$$

in which ω is the output frequency of the rectifier and L_S is the inductance of the main transformer.

However, since we are assuming to be in the continuous steady state power supply and that the time constants of our interest are in the time magnitude order of *seconds*, it can therefore be considered extinct all the inductive and capacitive transient phenomena, characterized by dynamics of the order of *milli seconds*.

Therefore, it is possible to model the power substation by making reference to its *Thevenin* equivalent circuit, as an ideal voltage source, $V_{sub,0}$ in series with the resistance R_{sub}. In addition, because of the unidirectional power flow, it is necessary to insert a diode in series to prevent the reverse current. The no-load substation output value is therefore V_{sub}.

Regarding the model of the contact line, for a complete modeling it should be employed very complex mathematical models using partial differential equations, which lead to an accurate model of the DC traction supply system modelled as a *Multiconductor Transmission Line* [4]. However, the per-unit-length line parameters (r_{line}, l_{line}, c_{line}) referring to a two conductor representation of the traction line uses simplified expressions of the traction line impedance, giving satisfactorily approximation in particular if a low frequency range is considered [5].

Therefore, the equivalent line impedance values, will change as the position of the vehicle on the same line will varies. The total line inductance values and the

186

capacitance to ground and the line to line capacitance values per–length line unit can be evaluated with the dimensional lumped parameters as showed by *Stevenson* in [6]:

$$l_{line} = \left(\frac{1}{2} + 2\ln\left(\frac{D}{r} \right) \right) \times 10^{-7} \quad \left[\frac{H}{m} \right]$$

$$c_{line} = \frac{2\pi\varepsilon_r}{\ln\left(\dfrac{D}{r} \right)} \quad \left[\frac{F}{m} \right] \tag{4.2}$$

$$r_{line} = \rho_{Cu} \frac{1}{\pi r^2} \quad \left[\frac{\Omega}{m} \right]$$

where D is the distance between conductors, and r the radius of the conductors and ρ_{Cu} is the copper resistivity.

By neglecting the fast transient related to inductive and capacitive phenomena for the same reasons as above mentioned, the DC network overhead contact line can be modeled as simple *variable resistance* whose value varies in dependence of the vehicle movement and on their length and their equivalent section.

Below is reported the time-varying electrical equations of the model for the DC urban railway electrical network:

$$\begin{cases} V_{sub} = V_{sub,0} - R_{sub}I_{sub} \\ I_{sub} \geq 0 \\ V_t = V_{sub} - r_{line}x_t I_{sub} \end{cases} \tag{4.3}$$

where x_t is the curvilinear abscissa which expresses the distance of the rail vehicle considered from the zero reference and V_t the voltage at the vehicle's pantograph.

4.3 Model of the vehicle

The study of the dynamics concerning a vehicle for railway traction , implies the knowledge of the schematization and *mechanical equations* that govern its motion on a rail path. In order to accomplish this study, it is necessary to identify, under certain simplifying assumptions, a mathematical model of the physical system under investigation in order to analyze its behavior in the
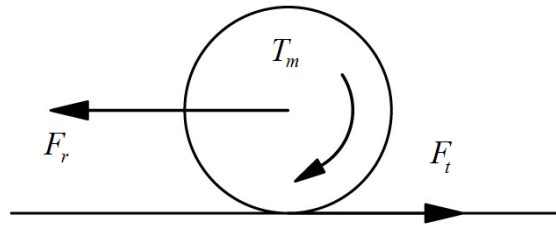
Figure 4.5 - Torques and forces acting on the rail wheel

possible operating conditions. In this section, we highlight the dynamic aspects with particular emphasis on the translating speed of the vehicle (in general of the convoy), on the rotational speed of the drive wheels and the skidding phenomena between wheels and rails. To this aim, the characteristics of the motion of a generic railway vehicle rail and the forces acting on it are described, under the assumption of rigid body [1]-[7].

The base vehicle is comparable in its entirety to a rigid body on which act external forces and, on the other hand , the reaction forces of the rails that are conducted through the wheels - rails contact surfaces; these last, which are the so called adhesion forces, in the last analysis, determine the motion of the vehicle on the rail (see Figure 4.5).

The maximum force that can be transmitted from the wheel-rail kinematic torque depends on the carried load and is expressed through the *adhesion* phenomenon relationship. The motion is then transmitted due to the friction that exists between the wheel and rail, called static friction, which is different and greater than the properly sliding friction. Hence, the transmission of the motion must be done without loss of adhesion, so the following relationship has to be verified:

$$F_t \leq f_a Q \tag{4.4}$$

where, f_a is the coefficient of kinetic friction, Q the weight of the wheel that rests on the rail and F_t is the tractive effort. The grip conditions obviously must also be fulfilled during braking operation otherwise there could be skidding and the wheel tends to break.

4.3.1   Dynamic equation

The motion of any railway vehicle can be described using standard *Newtonian* motion equations. The mathematical model of the vehicle is established easily by imposing rotation and translation balance conditions. They are expressed by the *equations of motion* (4.5), in which is denoted with v_t the vehicle translating speed, with m_t the translating mass of the vehicle, the resultant of all the tractive forces with F_t and the resultant of all motion resistances F_r. In the first of (4.5) is indicated with T_m the moment of the electromagnetic torque furnished by the traction motor, with ω_t the angular speed of the drive wheel, with D_{wh} the diameter of the drive wheel and with Θ_M the polar moment of inertia of the totality of the rotating masses on board the vehicle, which are kinematically connected with the wheels.

$$
\begin{cases}
\Theta_M \dfrac{d\omega_t}{dt} + F_t \dfrac{D_{wh}}{2} - T_m = 0 \\[2mm]
m_t \dfrac{dv_t}{dt} + F_r - F_t = 0 \\[2mm]
v_t = \omega_t \dfrac{D_{wh}}{2} + \sigma
\end{cases}
\tag{4.5}
$$

The system (4.5) takes into account the dynamic evolution of the system both in skidding and in gripping conditions. In the case of perfect adhesion of wheel - rail contact, characterized by $\sigma = 0$ which means that $F_t < f_a Q$, the system of differential algebraic equations (4.5) is reduced, therefore, to a single first-order differential equation, representative of rolling, since the frictional force is uniquely determined as a reaction force:

$$
\begin{cases}
F_t = F_r + m_{t,e} \dfrac{dv_t}{dt} \\[3mm]
\text{where } m_{t,e} = m_t + \displaystyle\sum_d \left(\dfrac{2}{D_{wh}}\right)^2 \Theta_d + \sum_u \left(\dfrac{2\tau}{D_{wh}}\right)^2 \Theta_u
\end{cases}
\tag{4.6}
$$

In the (4.6) with $m_{t,e}$ is denoted the so called *equivalent mass*, which takes into account also the mass of rotating components of the train by converting their rotational inertia to an equivalent mass. In particular, for rotating masses downstream the gearbox such as wheels, disc brakes, axles and so on, the Θ_d-th inertia of the d-th rotating component is taken into account, whereas for masses

upstream the gearbox (rotor of electric motors), the Θ_u-th inertia of the u-th rotating component has to be considered together with the gearbox ratio τ.

The *resistive force* (and therefore the tractive effort needed to follow the speed cycle) acting on the vehicles is calculated by using eq. (4.7):

$$\begin{cases} F_r = F_{roll} + F_{grade} + F_{aero} \\ F_{roll} = f_R m_t g \cos \iota \\ F_{grade} = m_t g \sin \iota \\ F_{aero} = \frac{1}{2} \rho_{air} A_f C_D v_t^2 \end{cases} \qquad (4.7)$$

where F_{roll} is the rolling resistance force, F_{grade} is the force due to the rail path slope, f_R the rolling resistance coefficient, g the gravity acceleration, ι the rail path slope and F_{aero} is the aerodynamic drag force which has been previously described in eq. (1.2). In a more compact form, for the rapid assessment of systematic motion resistance, according to the *Davis* equation (1.1), the resulting motion resistance is:

$$F_r = a + b v_t + c v_t^2 \qquad (4.8)$$

where the constants *a, b* and *c* are available from the train manufacturer.

4.3.2   Electrical traction drive

In order to take into account the overall dynamic behavior of a railway vehicle, it has to be considered how the tractive effort is generated by the on-board electrical drive system. The generation of the traction force applied to the equivalent wheel of the rail vehicle is realized through the implementation of appropriate control laws of the electric motors.

Modern traction drives are supplied by the overhead contact line by means of pantographs. In case of DC lines, the pantograph connects directly the contact line to the power inverters of the train by means of filter capacitors; conversely in case of AC lines the inverter is connected in cascade to an AC-DC rectifier. Figure 4.6 shows the typical electrical drive configuration of a rapid transit train in case of DC lines, equipped with *three-phase asynchronous motors* and *variable voltage variable frequency inverter*. The mathematical model of the electromechanical system "*railway vehicle*" is constituted by the equation of the converter, the electric motor and mechanical equation.
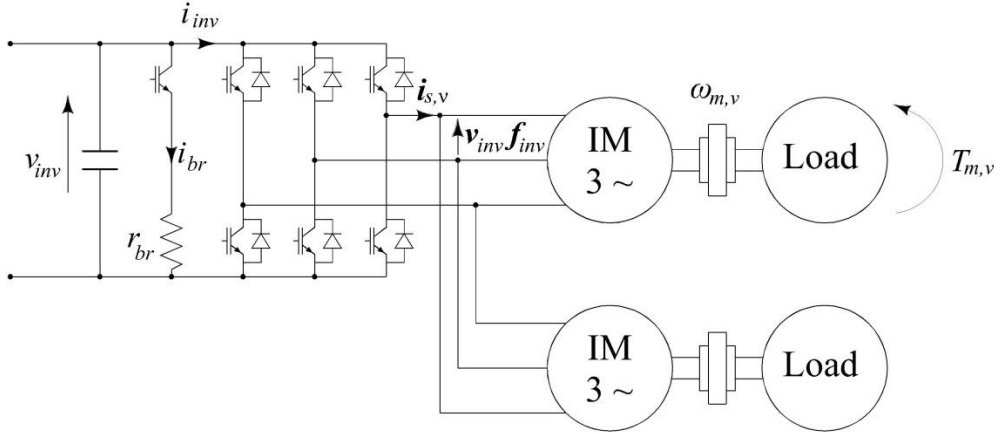
Figure 4.6 - Electrical traction drive configuration

The total traction force F_t is the sum of the torques delivered by the N_m motors of the vehicle. Considering for simplicity that all the motors have the same speed, the following equations can be written [1]:

$$\begin{cases} F_t = \sum_{v=1}^{N_m} \frac{T_{m,v}}{D_{wh}} 2\tau \\ v_t = \frac{D_{wh}\,\omega_{m,v}}{2\tau} \end{cases} \tag{4.9}$$

where τ is the gearbox transmission ratio, $T_{m,v}$, the motor torque of the v-th motor and $\omega_{m,v}$ the angular speed of the v-th motor. Motor torques are related to the currents absorbed by the inverter DC-link by the motor drive equations [8]:

$$\begin{cases} v_{inv}f_{inv,d} = R_s i_{sd,v} + \left(L_s - \frac{L_m^2}{L_r'}\right)\frac{d}{dt}i_{sd,v} + \frac{d}{dt}\varphi_{r,v} - \left(L_s - \frac{L_m^2}{L_r'}\right)\omega\, i_{sq,v}, \\[2mm] v_{inv}f_{inv,q} = R_s i_{sq,v} + \left(L_s - \frac{L_m^2}{L_r'}\right)\frac{d}{dt}i_{sq,v} + \frac{L_m}{L_r'}\omega\,\varphi_{r,v} + \left(L_s - \frac{L_m^2}{L_r'}\right)\omega\, i_{sd,v}, \\[2mm] 0 = \frac{d}{dt}\varphi_{r,v} + \varphi_{r,v}\frac{R_r'}{L_r'} - \frac{R_r'}{L_r'}L_m i_{sd,v}, \\[2mm] 0 = \varphi_{r,v}\left(\omega - p\omega_{m,v}\right) - \frac{R_r'}{L_r'}L_m i_{sq,v}, \\[2mm] T_{m,v} = \frac{3}{2}p\frac{L_m}{L_r'}\varphi_{r,v}i_{sq,v}, \\[2mm] i_{inv} = \frac{3}{2}\sum_{v=1}^{2}\Re e\left\{f_{inv}\breve{i}_{s,v}\right\}. \end{cases} \tag{4.10}$$

191

where

$\varphi_{r,\upsilon}$: rotor flux of the υ-th motor;

i_{inv}: DC-side inverter current;

$i_{sd,\upsilon}$: d-axis symmetrical component of stator current of the υ-th motor;

$i_{sq,\upsilon}$: q-axis symmetrical component of stator current of the υ-th motor;

L_m: self-inductance of induction motor;

L_s: stator phase inductance of the induction motor;

L'_r: rotor phase inductance of the induction motor referred to the stator;

p: number of the pole pair of the induction motor;

R_s: stator phase resistance of the induction motor;

R'_r: rotor phase resistance of the induction motor referred to the stator;

v_{inv}: DC-side input inverter voltage;

$f_{inv}(t)$ is the modulation function of the PWM inverter, which is equal to 0 or 1 at the instant t, depending on the state of the switching and diodes. For simplicity, in the following the inverter is assumed ideal and the modulation function is a continuous time function.

Therefore, the overall model consists of five real differential equations but not linear. Since the mechanical dynamics of a railway vehicle are dominant compared to the dynamics of the individual electric motors and drives, it is possible to particularize the model under quasi - stationary or slowly varying state. This means to consider the electrical equations in the pseudo-sine steady state.

4.3.3   Mechanical characteristic of the railway vehicle

The mechanical characteristic of the rail vehicle is the maximum tractive effort applied to the wheels developed as a function of running speed $F_t= f(v_t)$. It, in fact, defines the *maximum dynamic performance* of railway vehicle and is therefore representative of the boundary in torque-speed regulation domain of the vehicle electrical traction drive. The establishment of this characteristic depends mainly on the number of traction motors, on the kinematic and dynamic performance requirements of the vehicle with respect to the resistances and the planimetric behavior of the rail path (curves and slopes). In the Figure 4.7 a typical mechanical characteristic of a railway vehicle is depicted [1].
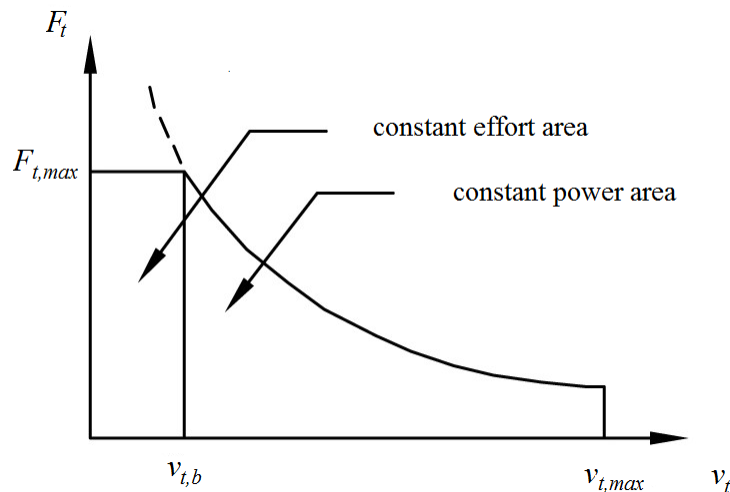
Figure 4.7 - Mechanical characteristic of a railway vehicle

As is evident from Figure 4.7 it is possible to distinguish two major curves that define the border of the regulation domain:

- an upper limit at constant tractive effort determined by the maximum adhesion limit which satisfies the (4.4), for speeds up to the base speed $v_{t,b}$;
- an upper limit at constant power for speed higher than the base speed that base, determined by the power rating of the electrical motors;
- a limit on the maximum speed of the vehicle, $v_{t,max}$.

The *base speed* $v_{t,b}$ is defined as the speed limit beyond which , the increase of speed is not due to an increase of the *supply voltage* of the motors, but rather to a *flux weakening* of the electrical machine. Therefore, the base speed divides the plane $(F_t \, ; \, v_t)$ in two operation zones, an increasing power and a constant power area respectively.

Below is reported a typical traction diagram (Figure 4.8), where four motion stages are clearly distinguishable:

- Phase 1: *acceleration*, is the starting phase, where the speed of the vehicle passes from the value zero to the steady-state value v_r. In a first section up the time instant ta where speeds are still low, the tractive effort is on average constant and the motion resistance is little variable, and then the acceleration can be considered constant . Then there is a section from v_a to v_r where it is practically followed the mechanical characteristic of the motor, with a decreasing in acceleration;

193

- Phase 2: *cruise* at constant speed, is the phase where the motors generally operate at a constant power value;
- Phase 3: *coasting* phase, where are applied only the motion resistances;
- Phase 4: *braking*, in which the vehicle speed decreases from the v_f value.

Once known the traction diagram, assuming to have a traction drive unit capable of giving an equivalent motor torque which allows to achieve the desired performance, it is possible to know the time characteristic of the mechanical power required by multiplying the motor torque and the motor angular speed (see Figure 4.9). This power trend, under the assumptions made, practically coincides with the profile of absorbed power on the supply side scaled appropriately on the basis of the values of the traction chain efficiency (the product of the efficiencies from the wheel to the electric motor and precisely: the mechanical efficiency, η_{mech}, of the gearbox and other mechanical components, the efficiency of the electrical motors, η_{em}, and the efficiency of the traction inverter, η_{inv}).

In particular when the traction drive operates in the traction mode, the absorbed electrical power will be higher than the mechanical output power, causing voltage drop on the overhead contact line; vice versa, during braking mode, the electrical drive operates as a generator and the electric power generated on the supply network side is less than the mechanical braking, leading to a voltage rise.
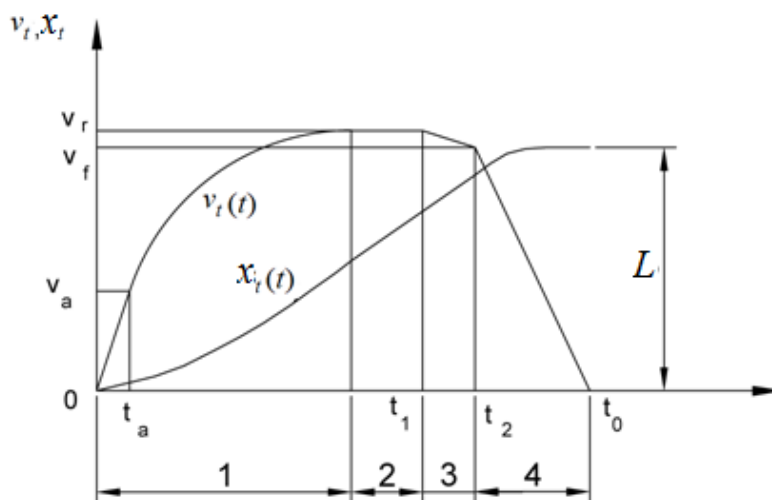
Figure 4.8 - Typical traction diagram of a railway vehicle
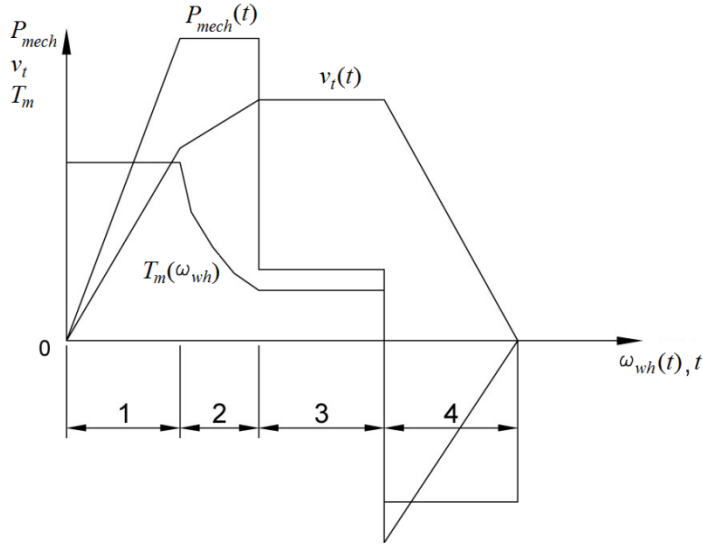
Figure 4.9 - Mechanical characteristic, traction diagram and mechanical power at the wheel during the different motion phases of a railway vehicle

The unexpected voltage fluctuation deteriorates the characteristic of the vehicle. By summarizing, during the phases 1 2 and 3 shown in Figure 4.9, the railway vehicle absorbs electrical power, while during phase 4, it delivers electrical energy to the grid. Ultimately, the rail vehicle is seen, from the supply network, as an electrical load that travels on the basis of the required speed value and the corresponding applied tractive effort. Therefore, it is possible to model the rail vehicle as a power controlled current generator. The vehicle electrical power, P_{inv}, is obtained on the basis of the knowledge of traction diagram of a single motor, i.e. the curve in the plane $(T_{m,v}, \omega_{m,v})$ depicted in Figure 4.9, the rated electrical efficiency, $\eta_{el} = \eta_{em} \, \eta_{inv}$, and rated mechanical efficiency, η_{mech} . So, the *electrical power required* by the train is given by the following relation:

$$P_{inv} = F_t \; v_t \left(\eta_{el} \; \eta_{mech} \right)^{-\text{sgn}(F_t)} \tag{4.11}$$

Obviously, the **current input / output load** will be equal to the ratio between the electrical power (whose trend in time is known) and the voltage at the pantograph (determined by the state of the entire electric power network):

$$i_{inv} = \frac{P_{inv}}{v_{inv}} \tag{4.12}$$

195

4.4   Model of the supercapacitor energy storage system

The SC storage system is the set consisting of a stack of individual SC modules appropriately connected in series and parallel and by a static bidirectional DC-DC converter. The series connection and parallel connection is required in order to obtain the desired values of voltage and current. In urban railway traction applications, where vehicles perform rapid braking and acceleration with typical times range of 5 – 20 s, it is possible in the SC mathematical model to neglect the slow dynamics due to the branches with a time constant of the order of minutes / hours (see section 3.2.6) and then the model is formed by an RC equivalent series circuit whose parameters in general are time-varying. The SC mathematical model is hence given by eq. (3.25) and is there recalled, assuming that it is pre-charged to its maximum allowable voltage $V_{sc,\mathrm{max}}$:

$$\begin{cases} i_{sc} = -\dfrac{d\left[C_{sc}(u_{sc})\cdot u_{sc}\right]}{dt} \\ v_{sc} = u_{sc} - r_{sc}\, i_{sc} \\ u_{sc}(0) = V_{sc,\mathrm{max}} \end{cases} \tag{4.13}$$

The switching power converter is buck-boost type with bidirectional power flow, as depicted in Figure 4.10, and allows SC charge and discharge. This converter is connected to the DC-side of the traction inverter or to the overhead contact line, for on-board or stationary storage installation respectively, which behaves also as a voltage source. This leads to the consideration that the converter is not able to regulate any voltage at its terminals, since both low and high voltage sides behave like voltage sources. Hence, a current-controlled converter has been selected, whose duty-cycle is evaluated on the basis of the reference output current of the converter. With these assumptions, the whole system of SC and current-mode converter can be modeled as an ideal current source with a limited energy, represented by the stored energy into the SC modules. This is true until the converter is capable of boosting SC voltage with a reasonable conversion efficiency, i.e. when the boost ratio is not greater than 3 and there is a residual charge stored into SC.
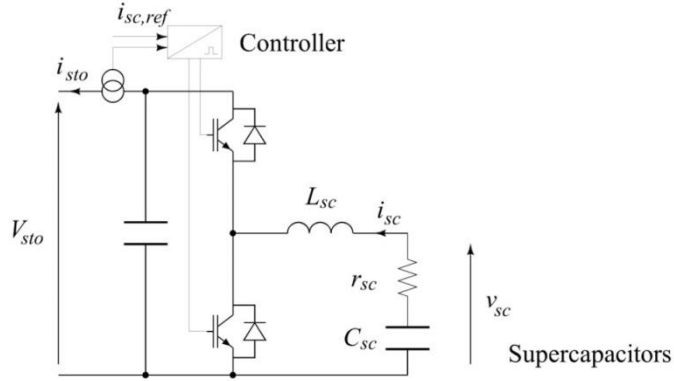
Figure 4.10 - Storage bidirectional DC-DC converter interfaced with the SC module

In this case, by neglecting the switching phenomena on the inductor L_{sc}, the *storage current i_{sto}* is related to SC current by following:

$$i_{sto} = \frac{v_{sc}i_{sc}}{V_{sto}}(\eta_{dcdc})^{\text{sgn}(F_t)} \qquad (4.14)$$

In which V_{sto} is the voltage on the high-side of the DC-DC converter and, η_{dcdc} is the rated efficiency of the DC-DC converter.

4.5 Mathematical model of the physical system for on-board ESS case study

In order to get a **case study**, by considering a radial type underground network, the equivalent electrical simplified scheme for a single railway vehicle equipped with on-board storage is depicted in Figure 4.11. In the evaluation of the equivalent electrical circuit have been neglected all those parameters which take into account electrical fast dynamics (order of *ms*) typically associated with inductive and capacitive transients type. Therefore we consider all the electrical quantities slowly time-varying.

The configuration depicted in Figure 4.11 shows that the SC energy storage unit is installed onboard of the train. Each storage unit is connected to the inverter DC-bus by means of the bidirectional DC-DC converter, for a total amount equal to the number of traction inverters. The overhead contact line is supplied by only one electrical substation, located at the extremity of the line itself.
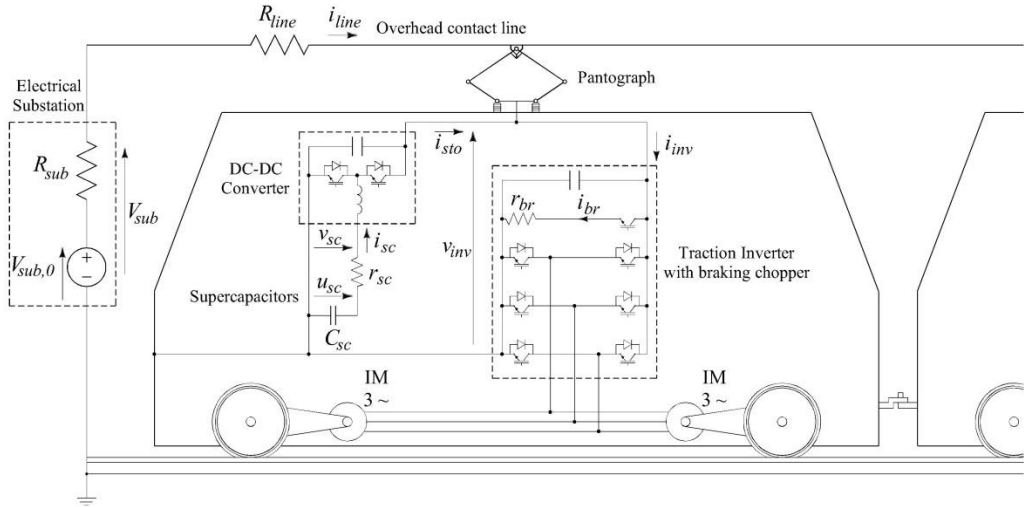
Figure 4.11 - Railway vehicle drive configuration equipped with on-board SC ESS

By applying the *Kirchhoff* laws to the nodes and the electrical path, it is obtained:

$$\begin{cases} i_{line} = i_{inv} - i_{sto} - i_{br} \\ V_{sub} - R_{line}i_{line} = v_{inv} \\ R_{line} = R_0 \dfrac{x_t}{L} \\ i_{br} = \dfrac{v_{inv}}{r_{br}} f_{br} \end{cases} \qquad (4.15)$$

where v_{inv} is the inverter DC-link voltage, i_{inv} the inverter DC-link input current, i_{sto} is the current supplied by the electrical storage device, i_{br} is the current dissipated on the braking resistance, r_{br} is the braking resistance, f_{br} is the switching function of the braking chopper even in this case assumed as a continuous time function, x_t is the position of the train along the track, R_0 is the total resistance of the line and L is the line length.

By arranging the eqs. (4.3), (4.5), (4.6), (4.8), (4.11), (4.13) and (4.15) the overall model of the on-board SC system under investigation is obtained:

$$
\begin{cases}
V_{sub} - R_{line} i_{line} = v_{inv} \\[2mm]
R_{line} = \dfrac{R_0}{L} x_t \\[2mm]
i_{line} = i_{inv} - i_{sto} - \dfrac{v_{inv}}{r_{br}} \\[2mm]
i_{inv} = \dfrac{F_t \; v_t \left(\eta_{em} \, \eta_{inv} \eta_{mech} \right)^{-\mathrm{sgn}(F_t)}}{v_{inv}} \\[2mm]
i_{sto} = \dfrac{v_{sc} i_{sc,ref}}{v_{inv}} \left(\eta_{dcdc} \right)^{\mathrm{sgn}(F_t)} \\[2mm]
u_{sc} = -\displaystyle\int \dfrac{i_{sc,ref}}{C_{sc}\left(u_{sc}\right)} dt \\[2mm]
v_{sc} = u_{sc} - r_{sc} \, i_{sc,ref} \\[2mm]
u_{sc}(0) = V_{sc,\max} \\[2mm]
F_t - F_r = \left(m_t + m_{sc} \right) \dfrac{dv_t}{dt} \\[2mm]
F_r = a + bv_t + cv_t^2 \\[2mm]
\dfrac{dx_t}{dt} = v_t
\end{cases}
\tag{4.16}
$$

It has to be remarked that the addition of the on-board SC stack leads to an increase of the total vehicle translating mass, so in eq. (4.16) it has been taken into account, the total mass of the train as the sum $m_t + m_{sc}$.

Hence, it has been obtained a system of 10 equations in 10 unknown quantities, in which the train translating speed v_t values are known (measured by the encoder of the traction motor). The inputs of the sets (4.16) are the SC current, $i_{sc,ref}$, and the total traction effort, F_t, which are respectively obtained from the control laws of the storage system and the traction drive.

4.6 Mathematical model of urban railway electrical network in case of stationary ESS

A typical urban electrified railway transport system, as previously mentioned, consists of several DC electrical substations distributed in sequence, contact wires, trains and rails.
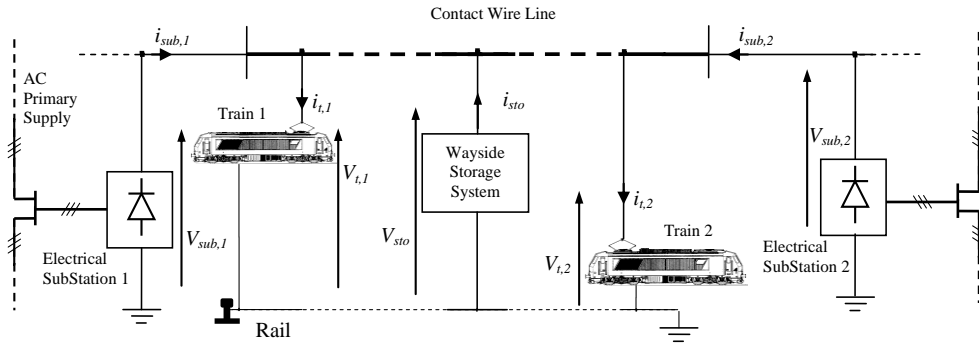
Figure 4.12 - Section of a typical urban railway electrified network equipped with stationary ESS

The most used standard configurations of urban railway electrified contact lines is the two side supplied DC contact line, where the contact lines for going and going back ways are supplied by terminal DC substations (see Figure 4.12). In the practical cases the electrified metro line is constituted by various electric sections separated by line disconnectors, making sure that there is not discontinuity among the feeding substations and then each of them has not a priority supply area but each network-line point is supplied with the contribution of all the substations. Hence, each vehicle is mainly supplied from the nearest substations, while the most far ones do not contribute significantly.

In order to approach to the study of stationary ESS in metro networks, a generalized case study for the urban railway electrified network has been investigated which makes reference to an *electrical section* of a double side supplied DC network with several vehicles that travel in opposite directions. The configuration shows a section of metropolitan line, between three main stops, composed by a main track for both directions with two operating vehicles, whose space driving cycles obviously can never overlap.

In the case examined, the ESS is installed along the urban rail track in an intermediate point between the two substation. More specifically it has to be placed in correspondence of a railroad passenger station, where it might occur in practice the maximum acceleration and braking phases of at most two vehicles circulating in the same feeding line section.

In the following, it is described in more detail the mathematical model of the case investigated. The equivalent network of physical system is depicted in Figure 4.13, where the vehicles, the substations and the storage system have been replaced by current and voltage generators, as previously said.

200
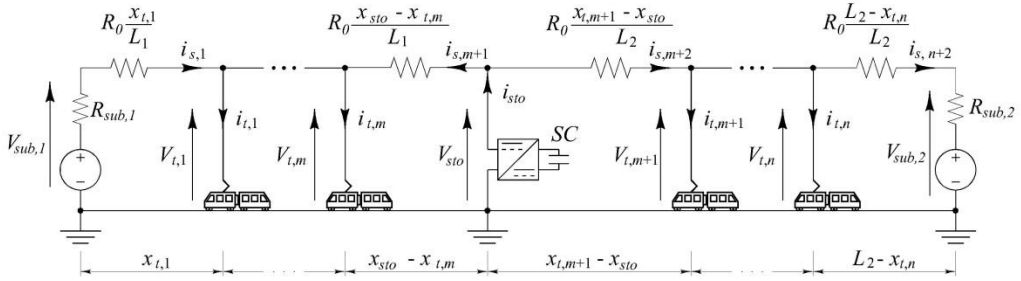
Figure 4.13 - Equivalent circuit of a double side DC contact line with stationary ESS

In order to take into account the substations inductive voltage drop the internal resistances $R_{sub,1}$, $R_{sub,2}$ have been considered, as well as the various line resistances for the line losses. Naturally, the electrical dynamics (time constant around *ms*) correlated to line and substation inductances have been neglected since the model analysis is focused on power flow exchanges among the different sources during the traction cycle of vehicles (*minutes*).

The ESS is placed along the track, in the generic but stationary position x_{sto}. Without loss of generality, it is assumed that at each time instant *m* vehicles are located before the position of the ESS ($x_{t,j} < x_{sto}$, $j = 1,2, ..., m$) while $n - m$ are placed after that ($x_{t,j} > x_{sto}$, $j = m+1, m + 2, ..., n$). The generic *j*-th vehicle is modeled as a time-dependent current source. The value of the current absorbed by the *j*-th vehicle, $i_{t,j}(t)$, depends on the power required in the same time instant and the pantograph voltage, $V_{t,j}(t)$, through the relationship:

$$i_{t,j}\left(t\right) = \frac{P_{t,j}\left(t\right)}{V_{t,j}\left(t\right)} \qquad j = 1,2,...,n \qquad (4.17)$$

where the pantograph voltage is equal to the voltage of the contact line at the point where the vehicle is located at the instant *t* and, as explained before, the powers $P_{t,j}(t)$ of the vehicles are supposed to be known and evaluated as eq. (4.17).

By using the *Kirchhoff's* voltage and current laws, the mathematical model of the urban railway transit with two electrical substation and a stationary ESS is represented by the following set of equations:

$$
\begin{cases}
V_{t,1} = V_{sub,1} - R_0 \dfrac{x_{t,1}}{L_1} i_{s,1} \\[2ex]
V_{t,j} = V_{t,j-1} + \dfrac{R_0}{L_1}\left(x_{t,j} - x_{t,j-1}\right)i_{s,j} & j = 2, 3, ..., m \\[2ex]
V_{sto} = V_{t,m} + \dfrac{R_0}{L_1}\left(x_{sto} - x_{t,m}\right)i_{s,m+1} \\[2ex]
V_{t,m+1} = V_{sto} - \dfrac{R_0}{L_2}\left(x_{t,m+1} - x_{sto}\right)i_{s,m+2} \\[2ex]
V_{t,j-1} = V_{t,j-2} - \dfrac{R_0}{L_2}\left(x_{t,j} - x_{t,j-1}\right)i_{s,j+1} & j = m+2, m+3, ..., n \\[2ex]
V_{t,n} = V_{sub,2} + \dfrac{R_0}{L_2}\left(L_2 - x_{t,n}\right)i_{s,n+2} \\[2ex]
i_{s,j} = i_{t,j} - i_{s,j+1} & j = 1, 2, ..., m \\[1.5ex]
i_{s,m} = i_{s,m+1} - i_{sto} \\[1.5ex]
i_{s,j} = i_{t,j-1} - i_{s,j+1} & j = m+2, m+3, ..., n+1 \\[1.5ex]
i_{t,j} = \dfrac{P_{t,j}}{V_{t,j}} & j = 1, 2, ..., n
\end{cases}
\tag{4.18}
$$

where L_1 and L_2 are the feeding section line length and R_0 is the total line resistance of the same feeding line section. Since $i_{sto} = i_{sto}(t)$, $x_{t,j} = x_{t,j}(t)$ and $i_{t,j} = i_{t,j}(t)$, this is a time-dependent algebraic set of non linear equations in $2n$ unknown quantities. The behaviour of the system is therefore strongly dependent not only on the laws assigned to the movement of the vehicle, but also on the position of the SC ESS and their control, because this last is responsible for the determination of the time-function $i_{sto} = i_{sto}(t)$.

4.7 Mathematical model of the physical system for stationary ESS case study

As already done for the on-board ESS case, for assessing the next development of this study, a **sample case study** for the urban railway network has been investigated which makes reference to an electrical section of a double side supplied network with two vehicles that travel in opposite directions, as briefly depicted in Figure 4.14. Both the railway vehicles can absorb or generate electrical powers depending on their load dynamic behavior. The stationary SC ESS has been placed at the end of the supplied lines, so that to reproduce a
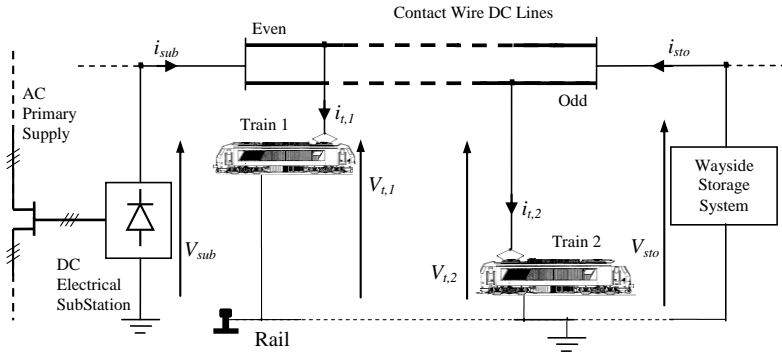
Figure 4.14 - Configuration for a section of a double side DC contact line with stationary ESS

proper electrical section of the line network with operating vehicles. It has to be highlighted that with reference to this placement of SC units, this most suitable position allows the lowest voltage drops for a given value of the energy injected into the line. A sample scheme for the connection of the SC ESS block to the contact line, is shown Figure 4.15.
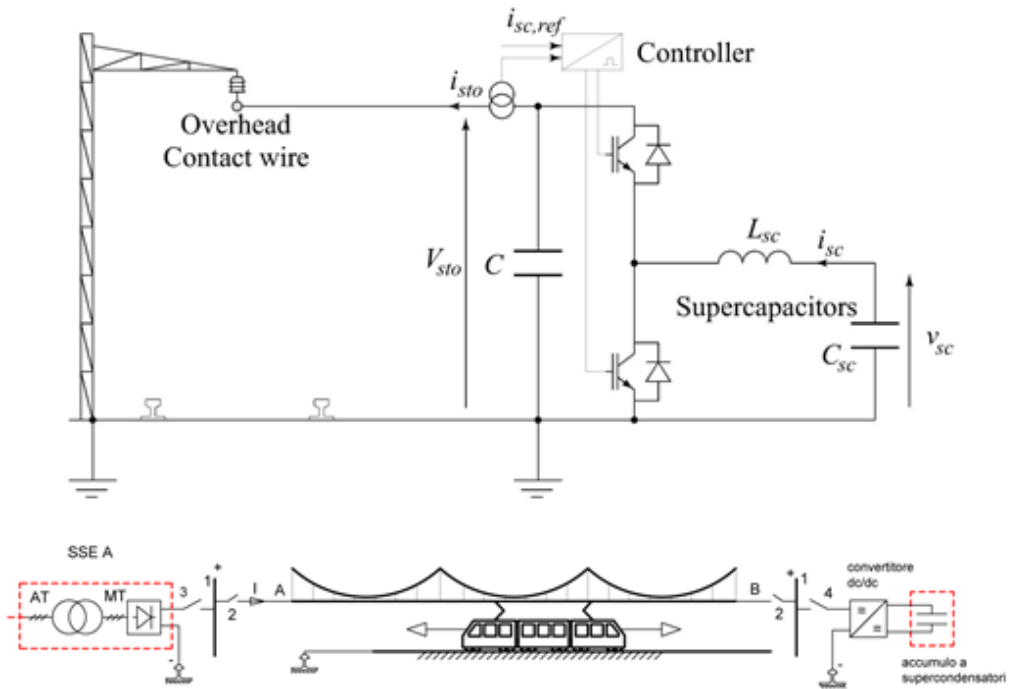
Figure 4.15 - Figure for the connection of stationary SC ESS to the contact line

In the configuration considered for the stationary ESS installation, considered in this study, the trains move along the first track away from the electrical substation. When they arrive at the end of the line, they come back along the second track toward the electrical substation. The two trains can be delayed each other depending on the timetable. However, a cycle is considered complete when both train finish a round-trip.
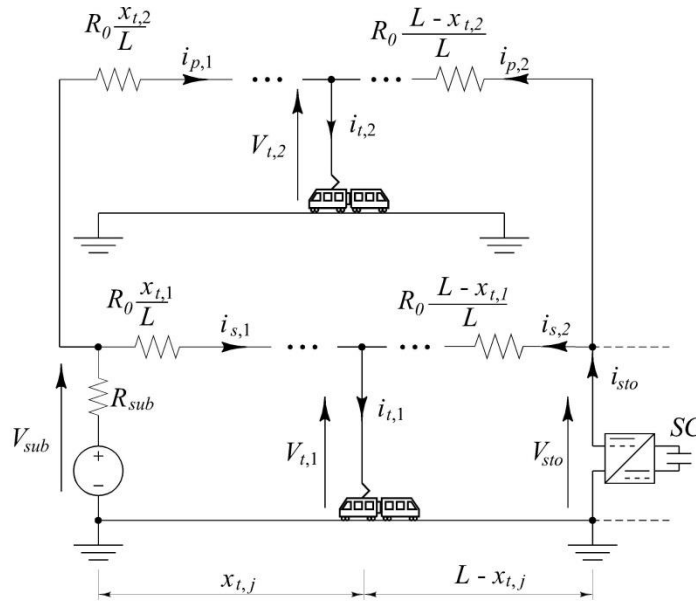
Figure 4.16 - Equivalent circuit of a double side DC contact line with stationary ESS and two operating vehicles

The equivalent electrical simplified scheme for a double track electrical line section with two circulating railway vehicles and equipped with stationary endline ESS, is depicted in Figure 4.16.

In the case of only two trains running on the track, the mathematical model (4.18) presented in the previous paragraph, can be particularized for the double track rail path as follows:

$$
\begin{cases}
V_{sub} - \dfrac{R_0}{L} x_{t,j} i_{r,1} = V_{t,j} & j=1,2 \quad \text{and} \quad r=s,p \\[2mm]
V_{t,j} - \dfrac{R_0}{L}\left(L - x_{t,j}\right) i_{r,2} = V_{sto} & j=1,2 \quad \text{and} \quad r=s,p \\[2mm]
i_{sub} = i_{s,1} + i_{p,1} \\[1mm]
i_{sto} = i_{s,2} + i_{p,2} \\[1mm]
i_{t,1} = i_{s,1} + i_{s,2} \\[1mm]
i_{t,2} = i_{p,1} + i_{p,2} \\[3mm]
i_{t,j} = \dfrac{F_{t,j}\, v_{t,j} \left(\eta_{em}\, \eta_{inv}\, \eta_{mech}\right)^{-\mathrm{sgn}\left(F_{t,j}\right)}}{V_{t,j}} & j=1,2 \\[3mm]
i_{sto} = \dfrac{v_{sc} i_{sc,ref}}{V_{sto}} \left(\eta_{dcdc}\right)^{\mathrm{sgn}\left(i_{sc,ref}\right)} \\[3mm]
u_{sc} = -\displaystyle\int \dfrac{i_{sc,ref}}{C_{sc}(u_{sc})} dt \\[3mm]
v_{sc} = u_{sc} - r_{sc}\, i_{sc,ref} \\[2mm]
u_{sc}(0) = V_{sc,\max}
\end{cases}
\tag{4.19}
$$

In the eq. (4.20) are shown the motion equations for the two vehicles.

$$
\begin{cases}
F_{t,j} - F_{r,j} = m_{t,j}\dfrac{dv_{t,j}}{dt} & j=1,2 \\[3mm]
F_{r,j} = a + b v_{t,j} + c v_{t,j}^2 & j=1,2 \\[3mm]
\dfrac{dx_{t,j}}{dt} = v_{t,j} & j=1,2
\end{cases}
\tag{4.20}
$$

Finally the mathematical model of physical system is represented by the set of electrical and mechanical equations given by (4.19) and (4.20), constituting a set of 16 equations in 16 unknown quantities. The inputs of these sets of equations are the SC reference current, $i_{sc,ref}$, and the total traction force of the *j*-th vehicle, F_t, which are respectively obtained from the control laws of the storage system and the *j*-th traction drive, under the hypothesis that all the vehicles have the same rated electrical and mechanical efficiencies as well as the same friction coefficients of rail-wheel contact and air.

4.8   Characteristic parameters of a real urban railway line

The urban railway electrified network line analyzed is that of the **Rome underground Line B** (see Figure 4.17) [9]. This metro network operates between *Laurentina* and *Rebibbia* stations and it is double track, with 8 substations, 22 passenger stations for a total length of about 18.15 km . It is not considered any gradient or curve . The average length between the line sections fed by two substations streak is about 2.4 km. The average waiting times at all passenger stations are 20 seconds. The maximum operating speed is 80 km/h. All trains are assumed operating under peak-conditions, for example, are generally carries with maximum acceleration and deceleration rates.

Figure 4.18 shows the typical sections of power feeder from a substation to the double overhead contact line. The power substation is fed with a primary supply at 20 kV voltage provided by two primary transformation station of the city grid. The substations are equipped with a diode bridge rectifiers . Each group is protected upstream by three-pole circuit breaker of 800 A rated current.

In the Table 4.1 are summarized the main characteristics of the traction network of this line:

Electrical network line section parameters	Unit	Value
Electrical section average length (*L*)	[km]	2.4
Number of stops	-	22
Contact wire per-length resistance (R_0/L)	[mΩ/km]	27.6
Contact line equivalent cross sectional area	[mm^2]	680
Rail per-length resistance	[mΩ/km]	5.0
Substation power (P_{sub})	[kVA]	3500
Substation internal resistance (R_{sub})	[mΩ]	10
No load rated voltage ($V_{sub,0}$)	[V]	1600
Rated voltage	[V]	1500

Table 4.1 - Main supply line parameters of Rome Underground Line B
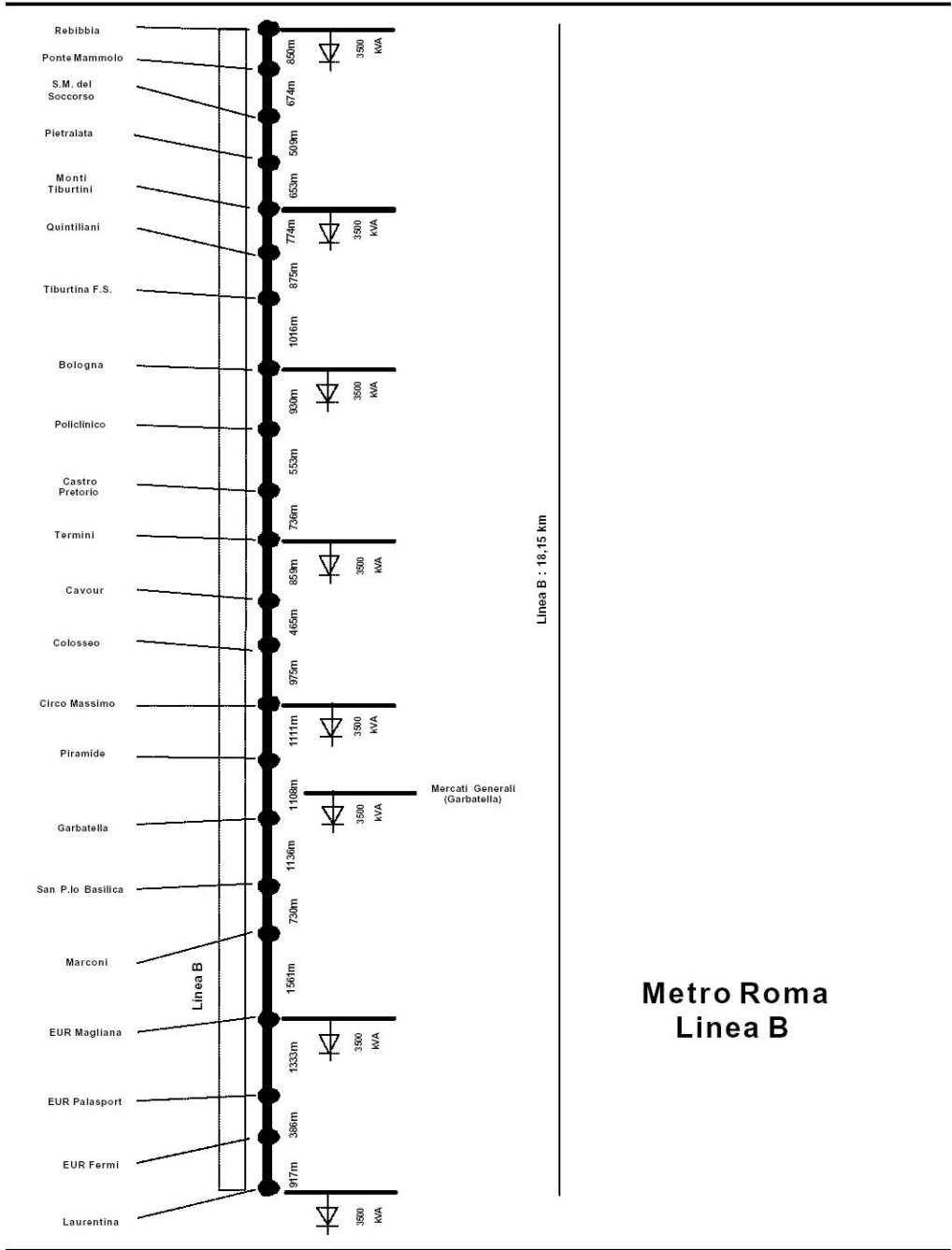
Figure 4.17 - Scheme of passenger station and electrical substation of Rome Underground Line B [9]

207
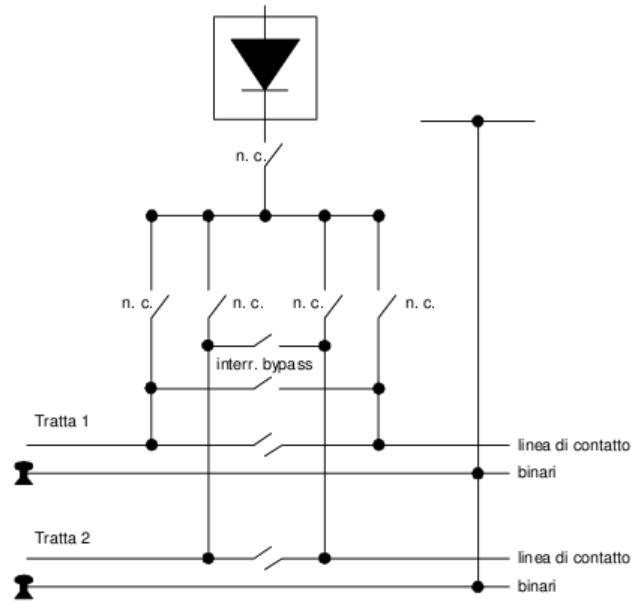
Figure 4.18 - Scheme of typical feeding section of electrical substation of Rome Underground Line B [9]

The operating railway vehicles are the electrical multiple unit train manufactured by *CAF S.A.* (*Construcciones y Auxiliar de Ferrocarriles*) named MB100 (see Figure 4.19). The metro train convoy under investigation is constituted of three railroad carriages, each one having a full load translating mass equal to 92 600 kg which incorporates four electrical traction motors. The power train is arranged with two asynchronous induction motors of 250 kW rated power and operating on the same bogie, supplied by a three phase voltage source inverter. The traction motors are connected via a transmission system placed on the axis and transmit the movement to the wheels by means of a mechanical reducer. The main parameters of the metro train are reported in Table 4.2.

Finally, in the Figure 4.20 and Figure 4.21 are reported the mechanical characteristics and the electrical drive limit currents during traction and braking phases.

208

Figure 4.19 - Picture of MB100 electrical multiple units operating on of Rome Underground Line B

Railway vehicle parameters	Unit	Value
Number of Electrical Traction Unit (N_c)	-	3
Bogie composition	-	B_oB_o
Empty translating mass	[kg]	62 500
Full load translating mass (m_t)	[kg]	92 600
Rated motor power	[kW]	250
Number of motors (N_m)	-	4
Max speed ($v_{t,max}$)	[km/h]	80
Base speed ($v_{t,b}$)	[km/h]	40
Max acceleration/braking rates ($\dot{v}_{t,max}/d$)	[m/s^2]	1.2/1.1
Max tractive effort ($F_{t,max}$)	[kN]	333
Max electrical drive current	[kA]	3.0
Motion resistance (F_r) coefficient a	[kN]	$2.13 + (2.96*10^{-3})\, m_t$
Motion resistance (F_r) coefficient b	[kg/s]	$(0.11*10^{-3})\, m_t$
Motion resistance (F_r) coefficient c	[kg/m]	10.95
Wheel Diameter (D_{wh})	[m]	0.84
Transmission ratio (τ)	-	6 : 1
Rated Electrical efficiency ($\eta_{el} = \eta_{em} \times \eta_{inv}$)	-	0.86
Rated Mechanical efficiency (η_{mech})	-	0.98

Table 4.2 - Main metro train parameters of Rome Underground Line B
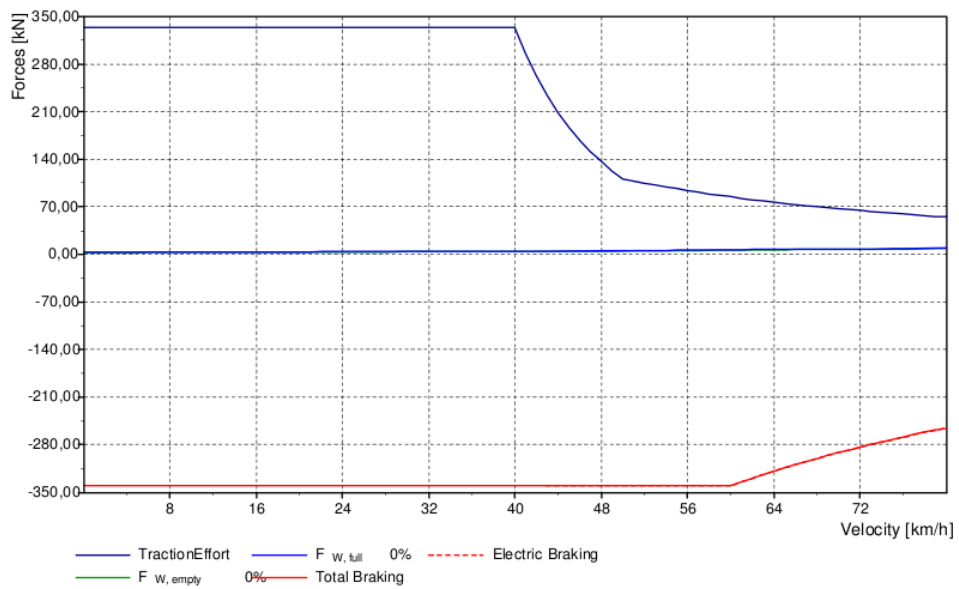
Figure 4.20 - Mechanical characteristics of MB100 electrical multiple units [9]
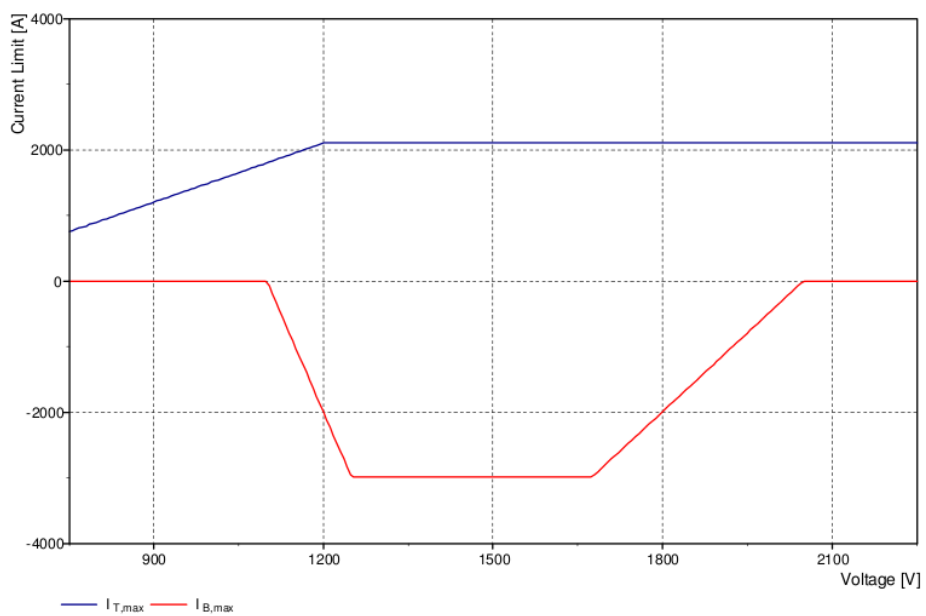
Figure 4.21 - Electrical drive limit currents of MB100 electrical multiple units [9]

4.9   Designing guidelines for the SC unit

The sizing of a SC ESS consists in defining the *storage capacity* in terms of storable energy on the basis of the maximum current, voltage and time required in the charging and discharging processes. The determination of the storage entity allows to define the dimensions and weights of the storage device. Moreover, the sizing consists also in the choice of the size of the DC-DC interfacing converter, in particular the determination of the maximum and minimum input and output voltage levels and the maximum allowable current. Mathematically the sizing procedure consists in the resolution analytical *multivariable constrained problem*. In most cases the functional relationships between the variables of interest, such as the power and the "size" of the system in terms of volumes and weights are not linear, so the mathematical solution of the problem is not reached in a closed analytical form. This imposes the use of procedures for the numerical solution. Traditionally, the sizing is based on "*put and try*" procedures based on past experience. This allows greatly to reduce the domain of possible solutions. Furthermore , the solution of the problem is not uniquely determined since the number of output variables is , in most cases , higher than the number of equations in the system, hence the problem has to be defined in terms of solving an *optimum problem* through the definition of appropriate cost functionals. By summarizing, the mathematical tool and methodological approach that is well suitable to describe a sizing problem is the variational analysis. Therefore, the determination of the optimal size of the storage devices can be carried out by solving a multivariable constrained optimization problem, where the constraints are substantially the technical specifications of individual components as well as the physical laws that ensure compliance with the principles of energy conservation; simultaneously, the objective function takes into account requirements such as the power line losses reduction, the improvement of the voltage profiles and the minimization of the ESS size itself. As already said in Chapter 2 this has been studied by *Ciccarelli, Iannuzzi et al.* in [10-15].

4.9.1   On-board SC ESS sizing

In the case on-board, the crucial goal is the reduction of the energy consumption, and therefore the SC ESS has to be designed accordingly.

As sample case, reference has been made to the traction units illustrated in the previous paragraph. The sizing has to be done taking into account an *energy-based criterion*: the objective function chosen is the maximization of braking energy recovery taking into account the weight constraints. Therefore, it is considered the greatest available energy during the braking phase of the vehicle, on the basis of conversion efficiencies.

The configuration depicted in Figure 4.11 shows that the each storage unit will result connected to the inverter DC-bus by means of the bidirectional DC-DC converter. Therefore, the number of SC ESS units is equal to the number of inverters of the train, i.e. six in the case study considered.

The SC ESS is constituted of several modules of SC in series and in parallel in order to attain the required values of voltage and current. Supposing all the modules identical, the six ESS can be substituted by one equivalent storage device having a total number of modules in series, N, equal to that of each ESS and a total number of modules in parallel, M, equal to the sum of the parallel branches of each ESS.

With reference to a typical traction cycle of a metro train, during braking phases the kinetic energy of the vehicle can be stored in the SC devices, which are recharged up to their initial SoC; afterwards the SC is able to deliver energy together with the main electrical substation in the subsequent acceleration phases and finally the SC are idle during the costing phases. Although the variation of train kinetic energy is the same in acceleration and braking, the electrical energy involved is obviously different due to losses. Therefore, the size of SC referred to acceleration phase is greater than that obtained if reference is made to braking phase. Since the weight increment of the train should be reduced as much as possible, the ESS have been sized referring to the braking phase. The sizing has been referred to the total translating mass and the maximum speed of the train. In the evaluation of the actual energy available, the mean efficiencies of the mechanical transmission, η_{mech}, electric motors, η_{em}, inverter, η_{inv} have been taken into account. On the basis of the estimations provided by the train manufacturer, these efficiencies can be considered equal to $\eta_{mech} = 0.98$, $\eta_{em} = 0.91$ and $\eta_{inv} = 0.95$. The efficiency of SC, η_{sc}, is dependent on the type of DC-DC converter, the modules used and the recharge current. For sizing purposes, the values $\eta_{dcdc} = 0.95$ and $\eta_{sc} = 0.90$ can used prudentially. Therefore, the energy stored in SC can be evaluated as:

$$E_{sc,\max} = \eta_{mech}\,\eta_{em}\,\eta_{inv}\eta_{dcdc}\,\eta_{sc}\,\frac{1}{2}\left(m_t + m_{sc}\right)v_{t,\max}^2 \tag{4.21}$$

Since the SC mass can be considered inversely proportional to the energy stored by SC with a coefficient α, i.e. $m_{sc} = E_{sc}/\alpha$, (4.21) can be rewritten as follows:

$$E_{sc,\max} = \frac{\alpha\,\eta_{mech}\,\eta_{em}\,\eta_{inv}\eta_{dcdc}\,\eta_{sc}\,m_t\,v_{t,\max}^2}{2\alpha - \eta_{mech}\,\eta_{em}\,\eta_{inv}\eta_{dcdc}\,\eta_{sc}\,v_{t,\max}^2} = 14.2\text{ kWh} \tag{4.22}$$

where α is equal to 1.75 Wh/kg using the SC modules of Table 3.2 in par. 3.1.4. The energy given by (4.22) can be stored in 140 modules, taking into account that only 75% of the total energy stored is actually used. Considering that the train is made by three traction unit, each equipped with two traction inverters, the SC can be split in a set of 24 modules in each car with their own DC-DC converter. Although this choice leads to a final sizing of 144 modules instead of 140 strictly necessary, it is possible to locate in each car six identical storage devices. For each set of modules, the DC-DC converter is controlled in order to manage the energy flow between SC and the power train; in particular it works as a buck converter when it charges SC and as a boost converter when discharges SC. In the latter case, the efficiency of the converter is acceptable if the maximum amplification voltage ratio is less than or equal to 3. For a line voltage of 1500 V, the voltage of SC should be greater than 500 V. SC reach their minimum voltage when they can be considered fully discharged, i.e. the voltage of each module is 62.5 V, equal to the half of their rated voltage. Therefore, in each set the module string is made of at least $N = 8$ modules connected in series. Finally, in order to reach the amount of the energy stored, the number of strings of modules connected in parallel is $M = 18$, i.e. three per car. The additional mass of SC in the train is then 8 352 kg, which is 3% of the full load translating mass. However, the SC modules can be placed on the roof of each carriage in the place of the ballast resistor, for a total length of 4.60 m and a width of 1.70 m for each SC set.

It worth to be noted that the energy given by (4.21) is evaluated on the basis of the rated values of the efficiencies. However, the uncertainty in the efficiency measurement affects the evaluation of the energy actually regenerated. Considering that the uncertainty of each efficiency can be estimated as 1-2%, the uncertainty of the product is about 5-10%. Since the efficiencies given by manufacturers are usually optimistic, only a reduction of 10% in the global

efficiency has been considered. Therefore, in the worst case, $E_{sc,max}$ can be reduced down to 12.80 kWh. This energy can be stored in 126 modules, i.e. 21 per carriage. However, since the SC string is always made by 8 modules in series, the final number of modules is still 24 per carriage. In this hypothesis, the storage has a size of 14% greater than that strictly required from an energetic point of view.

The sizing procedure carried out so far is based only on energetic considerations. However, it is also necessary to check if SC recharge current is acceptable for the modules. The maximum power peak to be recovered by the SC is:

$$P_{sc,\max} = (m_t + m_{sc})\, d\, v_{t,\max}\, \eta_{mech}\, \eta_{em}\, \eta_{inv}\, \eta_{dcdc} = 5\,600 \ \text{kW} \qquad (4.23)$$

This power has to flow in SC at the beginning of the braking, i.e. when the modules are fully discharged and SC voltage is the half of the rated one. Therefore, the maximum current flowing in each module is equal to:

$$I_{sc,\max} = \frac{P_{sc,\max}}{M\,N\,\dfrac{V_{m,\max}}{2}} = 622 \ \text{A} \qquad (4.24)$$

where $V_{m,\max} = 125$ V according to Table 3.2. Since the max current of each module is 750 A, the sizing is validated also with reference to SC powers.

4.9.2   Stationary SC ESS sizing

The advantage of the stationary ESS, compared to the case on-board, is the lack of weight and required space constraints together to the possibility of having a simultaneous energy recovery from multiple vehicles.

Unfortunately, due to the upper limits on the line voltage it might not have a total energy recovery for a vehicle that is very far from the ESS installation point just because significant voltage drops occur along the line with consequent increase in losses.

In general, the regenerated current delivered to the network increases with the maximum allowed upper voltage and decreases with the line resistance, the distance between the vehicle and the ESS and the ESS SoC.

Hence, designing the size of the ESS for wayside application results more complex than the previous mentioned on-board case, bearing in mind plus that

the number and positioning of the stationary ESS on the line affects the way the braking energy is distributed among them.

The wayside SC ESS are mainly used *to improve the performance of traction systems* and they have to be properly designed to obtain the expected results. The input data are the characteristics of the electrical substations, the overhead contact line and the trains. The practical application of any design procedure is complicated by the movement of trains, which can only be taken into account statistically, because the distances and currents magnitude carried-on by trains vary in a stochastic manner, together with their distances from the supplying DC sources. A sample procedure is suggested in the following under the assumption that reference is made to traditional vehicles, moving along a traditional line, fed by old contact lines. The suggested procedure is outlined as follows:

1. The trains are placed on the track in fixed positions. The number of the trains and their positions are given by a preliminary probabilistic study on real traffic conditions on the line. These quantities can be obtained for example as the expected values of random variables describing their stochastic behaviour;

2. After an identification of the line voltage drop diagram, this is interpolated by a polynomial approximation in each branch of the electrical line section. This is equivalent to substitute the currents concentrated in trains locations with continuous current distributions. The chosen approximation has to be made using the mean least square method. The simplest analytical approximation is of second order; it means that the voltage drop function are approximated by parabolas;

3. The maximum allowable voltage drop ΔV_{des} is set;

4. The SC units are located in the stations which are as close as possible to the points where parabolas have their minimum;

5. For each SC ESS is selected the value of energy storable;

6. The parabolas evaluated in step 2 are modified by the introduction of SC sized in Step 5;

7. The size of SC could be increased until the voltage drop is lower than ΔV_{des} in any point of the line.

By summarizing, the criterion is based on a polynomial approximation of the load distribution, which would be representative of the best fit for different load configuration. For a fixed configuration of traction network electrified, it is laborious to find analytically the diagrams of the voltage drops along the line and then their interpolation. This problem can be easily overcome if use is made of existing simulation software and resolution of distribution networks. An example of this procedure is given by *Iannuzzi et al*. in [16].

4.10 Supercapacitors ESS control strategies

In the recent relevant literature any publications and advertisements, from both companies and academic researchers, concerning the SC ESS products for using on urban railway transportation systems, present mainly their advantages and their potential benefits. This has been widely discussed in the previous Sections 2.4 and 2.6 for the on-board and the stationary installation, respectively.
In general, they do not mention in detail how to *design*, *control* and *connect* the devices, or which power electronics interface is used to control the power flows with the electrified railway line. More specifically, the control strategies matter has not been completely addressed in a systemic and organic manner.

Many studies deal with the **on-board** SC SoC control of when a train follows an assigned speed profile. Even if these investigations surely can contribute to the development of more efficient railway systems, their global control strategies does not seem to be completely comprehensive, as the calculation of the reference SC voltages are independent from both the motion control and drive control algorithms; moreover the control algorithms of the storage devices do not take into account their actual SoC. This aspect appear to be worked out by *Barrero et al*. [17], where the SC SoC reference is correlated with the kinetic energy of the moving vehicle and the proportional control of the state of charge considers the actual power required by the traction drive, but no actual control implementations are presented. *Grbovic et al.* have presented a control of the DC-bus voltage and the SC voltage and current, based on a cascade control technique for general electrical drive applications [18]. In this paper the references of storage voltage and current have been obtained without taking into account the actual motor torque and drive speed control. The proposition for a similar application in railways has been proposed by *Wang W. et al*. [19] for

increasing DC line voltage during start-up, whereas *Wang D. et al*. [20] propose power distribution control strategy between SC and the main supply based on line current limiters. No particular details regarding how the actual vehicle speed could affect the choice of the current or line voltage references are deepened.

Even for the *stationary* SC ESS application, the most part of papers does not deal in depth with the main problem of the proper evaluation in real-time of the ESS optimal reference in terms of voltage and current on the basis of control strategy adopted. This aspect appear to be worked out by *Barrero et al.* [21-22], where the storage state of charge reference is correlated with the kinetic and potential energies of the moving vehicle and the controller seems to set the reference of the amount of power to be transferred from/to the network according to the current state and the network voltages, via a state selection process; however, the explanation is not deepened because the actual implementation of the control on a power converter is not presented. By keeping in mind the aforementioned DC-bus control proposal discussed in [18], *Kwon et al.* [23] describe the overall operation of wayside ESS to save the regenerative braking energy and to achieve the line voltage regulation in DC transit systems. Although both the controller design and the tracking algorithm are well presented and the test results show good agreement with theoretical analysis, no further details about the DC line voltage reference are given.

A common aspect that should be above all highlighted, however, is that very few controls are *verified* and *validated* by a careful series of *experimental tests*.

In any case, the amount of the regenerative braking energy that SC can store and the methodology to select the most suitable control for an assigned rail vehicle are still open questions. In particular, the limitation of the SC SoC is a critical trade-off between weight and volume of the storage device, the overall system-state of the whole supply network and the power ratings of the interfacing converter.

By summarizing, in the case of on-board ESS installation, in order to manage as efficiently as possible the regenerative braking energy, the SC-based ESS should be discharged at high vehicle speeds for better accepting the braking energy, and fully charged during the vehicle stand-stills for an effective contribution to the

accelerations. It is so clear that the SC SoC have to be therefore controlled according to the vehicle actual kinetic energy. During the pauses or the cruising phases, the SC could be slowly recharged from the main network.

Instead, as concerns the stationary ESS, its performance depends on how the energy flows are managed, by selecting the amount of the power exchanges based on the catenary line voltage, since this last one will result altered. A proper strategy should tend to discharge the ESS when it detect a voltage drop on the catenary network, whereas it has to be sooner ready to catch the braking energy of other vehicles.

In order to fill the gap present in the technical literature by satisfying the control requirements above discussed, in the following three control strategies have been proposed, potentially suitable for both on-board and stationary SC ESS installation:

1) **Speed Tracker Control** (STC) strategy

2) **Line Voltage Tracker Control** (LVTC) strategy

3) **Line Current State Control** (LCSC) strategy

Then, as it will be described in the next chapters, the experimental tests campaign conducted on the laboratory reduced scale electromechanical simulator fully confirm the theoretical performances of the SC controls and allowed to quantify the technical advantages obtained in terms of overall energy saving improvement.

4.10.1   Speed Tracker Control strategy

The *hierarchical* structure of the STC control is deduced from the block diagram depicted in Figure 4.22, where the actual train speed represents the external loop of the control schemes. Three control parts are considered: *Motion Control* (*MC*), *Field Oriented Control* (*FOC*), and SC energy saving *Speed Tracker Control* (*STC*). The MC and FOC set up the traction drive control; they are focused on the train speed and motor torque control respectively. On the contrary the STC is focused on the control of SC SoC in order to maximize the recovery of kinetic energy during the electrical braking [24].

Motion Control

The MC calculates the total vehicle tractive effort reference, $F_{t,ref}$, from the speed measurement, v_t, and its reference, $v_{t,ref}$ that is set by the driver, using a PI controller Reg_ω:

$$F_{t,ref} = k_{I,\omega} \int_0^t (v_{t,ref} - v_t)\, dt + k_{P,\omega}(v_{t,ref} - v_t) \tag{4.25}$$

Field Oriented Control

The FOC calculates the voltage stator references in (d,q) frame for asynchronous traction motors on the basis of actual values of train speed and tractive force.

The reference rotor flux of the motor, $\phi_{r,ref}$, is obtained from the actual train speed by means of the non linear-block, Reg_ϕ. The reference traction force and the reference flux are used to evaluate the q-axis current, $i_{sq,ref}$, and the d-axis reference current, $i_{sd,ref}$, respectively. Finally the stator voltages references are evaluated on the basis of the error of (d,q) currents and EMF voltage block compensation:

$$\begin{cases} v_{sd,ref} = k_{I,d} \int_0^t (i_{sd,ref} - i_{sd})\, dt + k_{P,d}(i_{sd,ref} - i_{sd}) + \hat{e}_{sd} \\[2mm] v_{sq,ref} = k_{I,q} \int_0^t (i_{sq,ref} - i_{sq})\, dt + k_{P,q}(i_{sq,ref} - i_{sq}) + \hat{e}_{sq} \end{cases} \tag{4.26}$$

The stator voltage in (d,q) frame, then, are transformed in (x,y) stationary frame on the basis of the estimation of rotor flux position, $\hat{\psi}_r^s$, in order to get the commands for the inverter [8].

Speed Tracker Control

The main target of the STC is the recovery of the kinetic energy available during train braking and the limitation of the line current during acceleration, by properly taking into account the SC-SoC. It consists of *cascaded* SC voltage and current control. The reference can be determined from the consideration that SC voltage has to be a decreasing function of the **vehicle speed**, which is directly.

219
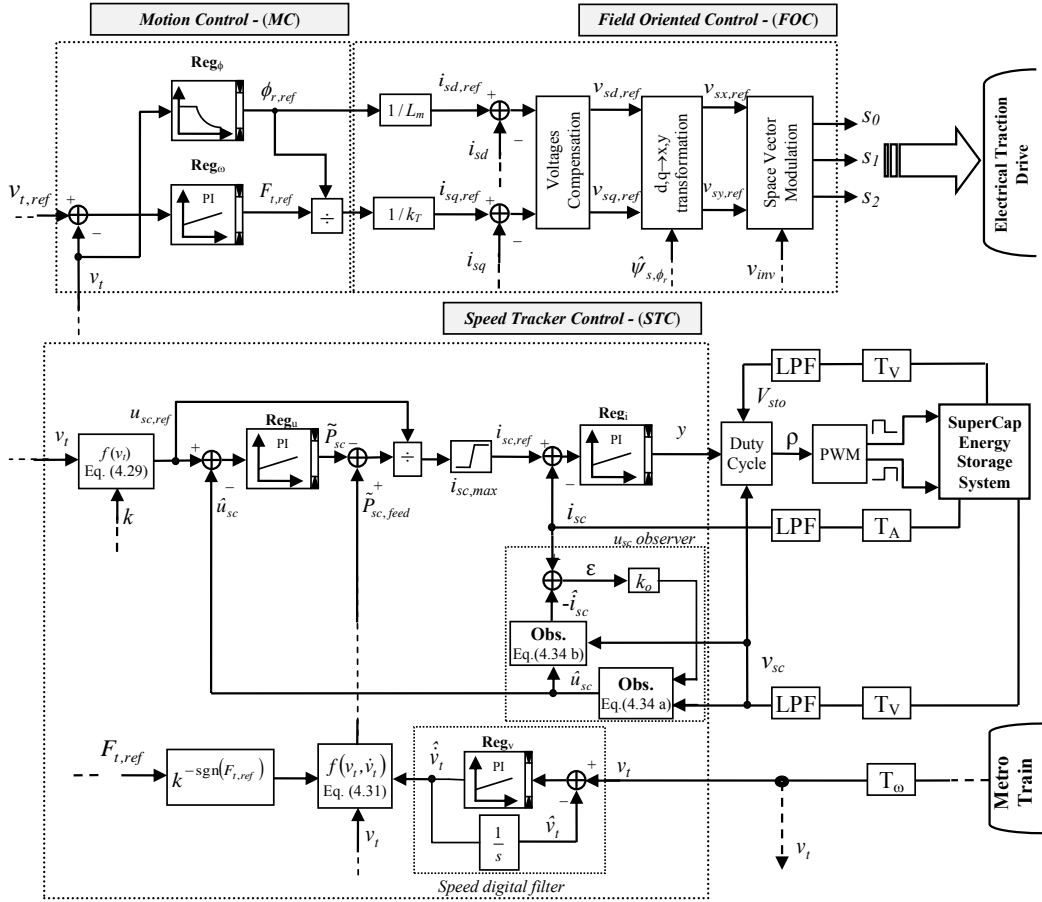
Figure 4.22 - Block diagram of the STC strategy

related to the **kinetic energy** of the moving mass. For a low speed, it is more logical to expect acceleration rather than braking; in addiction, the kinetic energy available at low speed is very low. Therefore a high value of SC voltage, corresponding to an high SoC of SC, has to be set. On the contrary, for higher speed a braking is likely expected and, hence, SC should be at a lower SoC. With respect to the full load vehicle translating mass and by bearing in mind the (4.21), assuming the SC pre-charged at $V_{sc,\max}$, the actual energy stored in the SC can be computed as:

$$E_{sc} = \frac{1}{2} C_{sc} \left(V_{sc,\max}^2 - u_{sc}^2 \right) \tag{4.27}$$

220

where it is considered as a first approximation of the SC constant capacitance model. Since only a part of the kinetic energy can be actually recovered due to friction and electrical losses and by keeping in mind that the maximum energy stored in SC is proportional to their weight by means of the coefficient α (eq. 4.22), the following equation can be written:

$$\frac{1}{2}C_{sc}\left(V_{sc,\max}^2 - u_{sc,ref}^2\right) = \frac{1}{2}k\left(m_t + \frac{E_{sc,\max}}{\alpha}\right)v_t^2 \qquad (4.28)$$

where $V_{sc,\max}$ is the SC rated voltage, $u_{sc,ref}$ is the SC *reference internal voltage* and k is a *constant* taking into account friction and electrical losses dependent on the previously mentioned conversion efficiencies. Solving eq. (4.28) for $u_{sc,ref}$, the reference voltage of SC is given by:

$$u_{sc,ref} = f(v_t) \cong V_{sc,\max}\sqrt{1 - k\frac{\left(m_t + \frac{E_{sc,\max}}{\alpha}\right)v_t^2}{C_{sc}V_{sc,\max}^2}} \qquad (4.29)$$

Equation (4.29) points out that SC reference voltage allows the evaluation of a SC reference feed-forward power term, $\tilde{P}_{sc,feed}$.

From the mathematical model of SC, presented in the previous section, the power output of SC is:

$$P_{sc} = i_{sc}u_{sc} = -C_{sc}u_{sc}\frac{d\,u_{sc}}{dt} \qquad (4.30)$$

Making the time derivative of (4.29) and by substituting it in (4.30), this feed forward reference is equal to:

$$\tilde{P}_{sc,feed} = f\left(v_t, \dot{v}_t\right) = k\,v_t\left(m_t + \frac{E_{sc,\max}}{\alpha}\right)\dot{v}_t \qquad (4.31)$$

The suggested control strategy is depicted by the STC block diagram in Figure 4.22.

The core of the energy saving speed tracker algorithm control is represented by the cascaded SC voltage and current control, as shown in the the same Figure 4.22. In particular, the reference current of the SC modules, $i_{sc,ref}$, is obtained starting from two power contributes: a feed forward term that takes into account the power associated to inertial forces ($\tilde{P}_{sc,feed}$) and a compensating term ($\tilde{P}_{sc}$)

221

referred to the error between actual and reference SC voltage, obtained from (4.29).

The first term, $\tilde{P}_{sc,feed}$, is obtained by (4.31) requiring the knowledge of train speed, its acceleration $\dot{v}_t$ and the sign of the traction effort, $F_{t,ref}$. The train speed v_t is available from the measure of an encoder placed on the motor shaft and the knowledge of the wheel diameter and the transmission ratio. The acceleration has to be estimated from the measured actual train speed. According to Figure 4.22, in fact the actual value of the speed is compared to the speed obtained by integration of the acceleration, $\dot{\hat{v}}_t$, estimated by a 2nd order *digital filter* (DF) with a PI regulator Reg_v, whose integral and proportional constants, $k_{I,v}$ and $k_{P,v}$, have to be selected in order to track the acceleration of the train for rates up to their maximum values.

Instead, the compensating term, $\tilde{P}_{sc}$, takes into account the error in the evaluation of model parameters and it is the output of the PI regulator Reg_u which processes the error between the SC reference internal voltage given by (4.29) and the actual estimated one:

$$\tilde{P}_{sc} = k_{P,u}\,(u_{sc,ref} - \hat{u}_{sc}) + k_{I,u} \int_0^t (u_{sc,ref} - \hat{u}_{sc})\,dt \qquad (4.32)$$

Hence, the actual value of SC reference power, $P_{sc,ref}$, is obtained as the algebraic sum of the two aforementioned terms ($\tilde{P}_{sc,feed} + \tilde{P}_{sc}$). Therefore, the optimal SC reference current set-point, $i_{sc,ref}$, can be finally determined :

$$i_{sc,ref} = \frac{P_{sc,ref}}{u_{sc,ref}} \qquad (4.33)$$

This reference current value has to be properly limited on the basis of the SC module maximum allowable continuous current, $i_{sc,max}$.

In addition, the SC voltage control makes use of the internal voltage of SC, obtained by a proper online estimation of the voltage drop on SC equivalent series resistance. In fact, the actual value of internal SC voltage, u_{sc}, cannot be directly measured due to the presence of the voltage drop in the internal resistance for $i_{sc} \neq 0$. Therefore, an identification procedure has been applied for the estimation of u_{sc} based on a *Luenberger observer* [25]:

$$
\begin{cases}
\dfrac{d\hat{u}_{sc}}{dt} = v_{sc}\dfrac{1}{r_{sc}C_{sc}} - \hat{u}_{sc}\dfrac{1}{r_{sc}C_{sc}} + k_o\left(i_{sc} - \hat{i}_{sc}\right) & \text{a)} \\[3mm]
\hat{i}_{sc} = \dfrac{\hat{u}_{sc} - v_{sc}}{r_{sc}} & \text{b)}
\end{cases}
\qquad (4.34)
$$

where $\hat{u}_{sc}$ and $\hat{i}_{sc}$ are the estimated SC internal voltage and current and k_o is the gain of the observer. Possibly, this observer can be used in turn for the identification of the SC equivalent series resistance variation, $\delta\hat{r}_{sc}$, around its rated value r_{sc}, due, for example, to the changes the ambient temperature:

$$
\begin{cases}
\dfrac{d\hat{u}_{sc}}{dt} = v_{sc}\dfrac{1}{(r_{sc} + \delta\hat{r}_{sc})C_{sc}} - \hat{u}_{sc}\dfrac{1}{(r_{sc} + \delta\hat{r}_{sc})C_{sc}} + k_o(i_{sc} - \hat{i}_{sc}) \\[3mm]
\hat{i}_{sc} = \dfrac{\hat{u}_{sc} - v_{sc}}{r_{sc} + \delta\hat{r}_{sc}} \\[3mm]
\delta\hat{r}_{sc} = k_{P,r}(i_{sc} - \hat{i}_{sc})i_{sc} + k_{I,r}\displaystyle\int(i_{sc} - \hat{i}_{sc})i_{sc}\,dt
\end{cases}
\qquad (4.35)
$$

Finally, the SC reference current is compared to the actual SC current and the error is processed by a PI regulator, Reg_i, and produces as output:

$$
y = k_{P,i}(i_{sc,ref} - i_{sc}) + k_{I,i}\int_0^t (i_{sc,ref} - i_{sc})\,dt
\qquad (4.36)
$$

The output of the current regulator, y, allows the evaluation of the command signal, ρ, with the *Duty-Cycle* block:

$$
\rho = 2\frac{v_{sc} - y}{V_{sto}} - 1
\qquad (4.37)
$$

The signal ρ is intended to be 1 when the upper switch of DC-DC converter is always in ON state and equal to -1 when the lower switch is always in ON state. The signal ρ is finally processed by the pulse wide modulation block (PWM), which compares ρ with a carrier triangular wave. The PWM block produces as output the two TTL signals for the upper and lower switches of DC-DC converter.

If the more accurate SC model presented in par. 3.2.6, eq (3.25), would to be employed for the evaluation of the actual SC reference internal voltage value, it has to be remarked that in this case the actual SC energy has the more complex following form:

$$E_{sc} = \frac{1}{2} C_0 \left(V_{sc,\max}^2 - u_{sc}^2 \right) + \frac{2}{3} C_1 \left(V_{sc,\max}^3 - u_{sc}^3 \right)$$ (4.38)

so, the eq. (4.38) has to be properly rearranged:

$$\frac{1}{2} C_0 \left(V_{sc,\max}^2 - u_{sc,ref}^2 \right) + \frac{2}{3} C_1 \left(V_{sc,\max}^3 - u_{sc,ref}^3 \right) = \frac{1}{2} k \left(m_t + \frac{E_{sc,\max}}{\alpha} \right) v_t^2$$ (4.39)

Equation (4.39) is now a cubic function in $u_{sc,ref}$ whose real solutions have to be calculated. The nature of the coefficients of this equation points out that there is one real and two complex roots in the normal range variation of the coefficients, so that the solution of (4.39) is unique. In fact, in a more compact way, it can be rearranged as:

$$\begin{cases} \gamma_3 u_{sc,ref}^3 + \gamma_2 u_{sc,ref}^2 + \gamma_1 u_{sc,ref} + \gamma_0 = 0 \\ \\ \gamma_0 = \frac{3}{4} \frac{k}{C_1} \left(m_t + \frac{E_{sc,\max}}{\alpha} \right) v_t^2 - \frac{3}{4} \frac{C_0}{C_1} V_{sc,\max}^2 - V_{sc,\max}^3 \\ \gamma_1 = 0 \\ \gamma_2 = \frac{3}{4} \frac{C_0}{C_1} \\ \gamma_3 = 1 \end{cases}$$ (4.40)

The (4.40) has to be solved for $u_{sc,ref}$ by applying the *Cardano*'s method, so the internal SC reference voltage results a function of the train speed $u_{sc,ref} = f(v_t)$.

Ultimately, to conclude the discussion of this control strategy, it is easy to see how it can be extended in the case of stationary SC ESS. In particular the control is mainly based on the knowledge of the actual vehicle speeds and acceleration estimations of all the vehicles that are supplied by the same feeding line sections from which is expected to recover the maximum regenerative braking energy. The control algorithm evaluates SC current and voltage set-points on the basis of an energetic balance between the resulting trains kinetic energies and the LiC stored energy, so the eq (4.28) takes the following form:

$$\frac{1}{2} C_{sc} \left(V_{sc,\max}^2 - u_{sc,ref}^2 \right) = \frac{1}{2} \sum_i^{N_T} k_i \, m_{t,i} v_{t,i}^2$$ (4.41)

In this equation N_T is the number of vehicles that circulate submitted to the same feeding line section and the variables identified by the subscript i refer to the i-th circulating vehicle. In the energetic balance the SC mass is obviously not considered since the ESS is placed wayside.

Then the eqs (4.29) and (4.31) assume the re-arranged form:

$$u_{sc,ref} = f(v_{t,i}) = V_{sc,max} \sqrt{1 - \frac{\sum_{i}^{N_T} k_i \, m_{t,i} \, v_{t,i}^2}{C_{sc} \, V_{sc,max}^2}} \tag{4.42}$$

$$P_{sc,ref} = f(v_{t,i}, \dot{v}_{t,i}) = \sum_{i}^{N_T} k_i \, m_{t,i} \, v_{t,i} \, \dot{v}_{t,i} \tag{4.43}$$

4.10.2 Line Voltage Tracker Control strategy

The target of the Line Voltage Tracker Control (LVTC) is to regulate the **supply voltage** during the motoring/braking operation of the circulating vehicles by properly managing the SC SoC unit used as storage device. The charging/discharging currents are given according to the changes of the supply line voltage, V_{line}. By using this line voltage tracker, the set-point voltage, $V_{line,ref}$, for the discharge/charge of the ESS can be adjusted to smooth the DC line *voltage fluctuations*.

In principle, when the line voltage exceeds a certain voltage level, the SC have to be charged; conversely, when the line voltage is lower than a certain predefined limit, a SC discharge action occurs.

It has to be outlined that with line voltage is intended the voltage of the supply line point where the corresponding ESS unit is installed, so it could be the voltage at the vehicle pantograph, V_t, in case of ESS on-board, or the catenary line point voltage, V_{sto}, where the stationary ESS is placed.

In Figure 4.23 is shown the LVTC block diagram. It consists in triple nested control loops: a double cascaded voltage controls and a final current loop.

The actual line voltage is increased when the input power supplied by the SC is greater than the output power consumed by loads; on the contrary, in the opposite case the line voltage is decreased.

The SC reference voltage, $v_{sc,ref}$ is evaluated from the outer voltage control loop on the line side. In particular, the difference between the line voltage reference
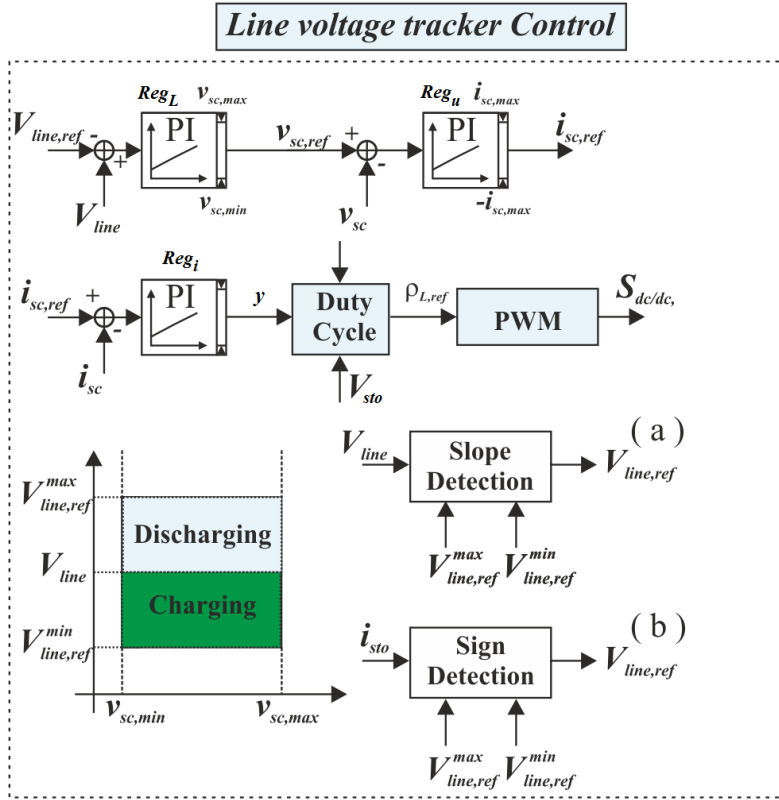
Figure 4.23 – Simplified block diagram of the LVTC strategy

and its actual measured value is sent to the first PI controller Reg_L:

$$v_{sc,ref} = k_{P,L}(V_{line} - V_{line,ref}) + k_{I,L}\int_0^t (V_{line} - V_{line,ref})\,dt \qquad (4.44)$$

Therefore, once known the SC reference voltage, $v_{sc,ref}$, and suitably limited ($v_{sc,min} \div v_{sc,max}$), it is in turn compared with its actual measured value, v_{sc}, and the error is processed by the PI controller Reg_u whose output is the SC set-point reference current, $i_{sc,ref}$ even this appropriately limited in function of the maximum permissible current from the SC units themselves:

$$i_{sc,ref} = k_{P,u}(v_{sc,ref} - v_{sc}) + k_{I,u}\int_0^t (v_{sc,ref} - v_{sc})\,dt \qquad (4.45)$$

Finally, once determined the value of the SC reference current, it is easy to evaluate the command signal ρ of the DCDC converter similar to that expressed by eqs (4.36) and (4.38).

226

The effectiveness of this control strategy is dependent on the choice of the reference line voltage $V_{line,ref}$. A value close to the no-load line voltage, $V_{sub,0}$, would result in a very fast discharge of the SC that could exceed their lower voltage limit; on the contrary, the choice of a reference value much lower than the rated line voltage tends to exploit little the SC making the line unreceptive and favoring the intervention of the braking resistors.

The main idea is to detect line voltage *drops* or *spikes* to decide whether the ESS state should be discharged or charged. In order to achieve conditions of line always *receptive*, it is convenient to assume two values ($V_{line,ref}^{\max} \div V_{line,ref}^{\min}$), depending on the detection of the sign of the current $i_{sto,}$ injected into the line by the converter (calculus performed by the block "*sign detection*" illustrated in the Figure 4.23). This allows to discern between an "equivalent" phase of traction and braking for all vehicles traveling in the same electric power section.

Alternatively , a more elegant way to identify an "equivalent" phase of motion and impose the line voltage reference value, consists in a "*sensorless*" manner, i.e. starting from the actual line voltage and calculating the gradient (block "*slope detection*"). Obviously, this gradient is estimated using a 2nd order derivative digital filter as already made in the previous control.

4.10.3   Line Current State Control strategy

The expected goal of the Line Current State Control (LCST) strategy is the reduction of the power peaks supplied by the catenary, with consequent stabilization of the line voltage. The line current, i_{line} , is maintained *constant*, even when the train accelerates and brakes, due to the SC ESS contribution. They should be capable of supplying an extra power during accelerations and storing the energy available from train braking [26].

The charge and discharge of SC during braking and acceleration are controlled by a catenary current set-point ($i_{line,ref}$) and the boundary of line voltage, keeping the voltage of SC within the lower and upper voltage limits ($v_{sc,min}$ and $v_{sc,max}$).

The main difficulty of this strategy is basically the proper on-line determination of the **line current set-point**. A value too low involves the full SC discharge before the end of the acceleration, with consequent increasing in catenary line current and losses; conversely, a set-point value too high implies an insufficient use of the storing capacity of the SC. The optimal current set-point has to be

determined depending on the SoC of the SC and the amount of energy to be recovered during the braking process.

However, it is very difficult to estimate correctly the amount of energy because it depends strictly on the speed profile of the vehicle.

The second aspect of the control strategy is the regulation of the SC power flows in order to keep constant the line current. It is possible to define on the plane (i_{line}, v_{sc}) the working area of the controller Reg_i, as it is shown in Figure 4.24. Then, the working operations are defined by the lower and upper bounds of the SC voltage, i.e. $v_{sc,min} \leq v_{sc} \leq v_{sc,max}$. Outside this zone SC are disconnected from the catenary supply line.

In particular, these limits define the maximum energy recovered and provided to the line during load cycle. The controller can automatically control the SoC of the SC within the working area, as soon as the actual line current, i_{line}, is lower and greater than the set-point or $v_{sc} < v_{sc,min}$ and $v_{sc} > v_{sc,max}$.. In the range $v_{sc,min} \leq v_{sc} \leq v_{sc,max}$, the control guarantees that SC are not charged over the upper threshold and discharged under the lower threshold.

Therefore one profitable way to implement such a control strategy is the use of a changeover finite state controller.
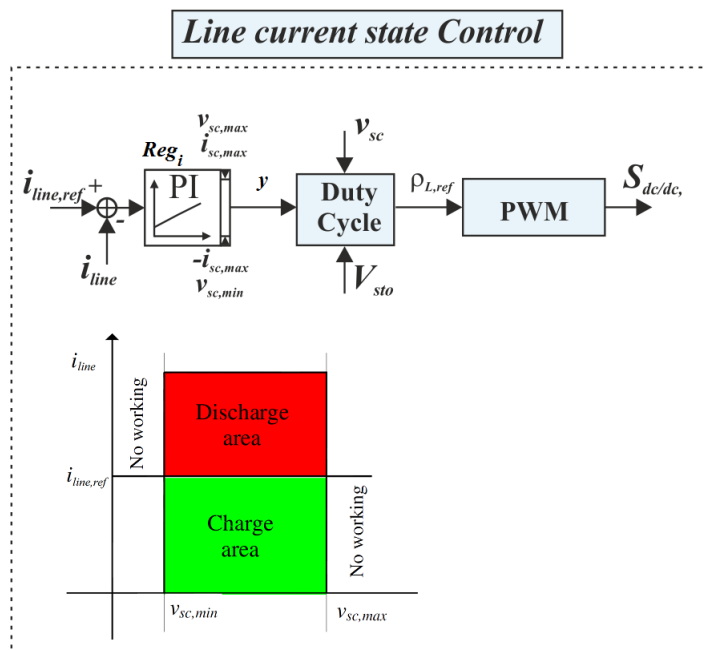
Figure 4.24 - Simplified block diagram of the LCSC strategy

This controller changes its state depending on the actual current supplied by the line and the SC SoC, as depicted in Figure 4.24. Until a transition condition is not verified, the controller keeps staying in the same state.

The first state, named *line current control*, occurs if $v_{sc,min} \leq v_{sc,} \leq v_{sc,max}$ and the line current supplied by the catenary is maintained to the reference value, independently on load current requests and SC supply the extra power required. The reference SoC is obtained as the output y of PI regulator, Reg_{i}, which compares the actual line current and its set-point reference as shown by the first of eq. (4.46). The transitions from the line current control state to the other states, called *SC lower voltage limit* and *SC upper voltage limit*, are related to the operating conditions of SC and occur if SC voltage goes outside the lower and upper bounds, respectively. During these states, the regulator Reg_i saturates its control according to the SC voltage bounds and the SC maximum allowable current and the output y is proportional to $i_{sc,max}$ or $-i_{sc,max}$ depending if the *lower voltage limit* state or the *upper voltage limit* state respectively occurs, as shown in second and third eq. (4.46).

When the controller is in state *idle*, SC are charged and there is no energy consumption on the catenary line, the regulator Reg_i set in off state all switches of DCDC converter, as shown by the last eq. in (4.46).

$$
\begin{cases}
y = k_{P,i} (i_{line,ref} - i_{line}) + k_{I,i} \int_0^t (i_{line,ref} - i_{line})\, dt & \text{if } v_{sc,min} < v_{sc} < v_{sc,max} \\[4mm]
y \propto i_{sc,max} & \text{if} \quad v_{sc} \leq v_{sc,min} \\[4mm]
y \propto -i_{sc,max} & \text{if} \quad v_{sc} \geq v_{sc,max} \\[4mm]
y = 0 & \text{if} \quad v_{sc,min} < v_{sc} < v_{sc,max} \text{ AND } i_{line} \approx 0
\end{cases}
\tag{4.46}
$$

The command signal ρ of the DCDC converter is calculated in a similar way as already done regarding the last controls.

It is clearly evident that the line current set-point defines the charge and discharge areas. In particular, when the line current is greater than the set-point, SC supply the extra power required by the loads and support the catenary. If the duty-cycle of the train is repetitive and SC store the kinetic energy of the train,

the energy supplied in a cycle by the catenary is equal to the losses of the system. Therefore the line current set-point could be defined as the ratio of the total energy lost and the product of the average line voltage and cycle duration.

4.11 Chapter 4 references

[1] Perticaroli, F. Electric Systems for Transportation. (in Italian), *Casa Editrice Ambrosiana*, Milan, Italy, 2001.

[2] Turri, R. Electrical Systems in Transportation. Lesson notes, University of Padova, Italy, 2006.

[3] Mohan, N.; Undeland, T. Power electronics: converters, applications, and design. *Wiley*, India, 2007.

[4] Ferrari, P.; Mariscotti, A.; Pozzobon, P. Reference curves of the pantograph impedance in DC railway systems. *Proc. Int. Symp. on Circuits and Systems IEEE 2000*, Vol. 1, Geneva, Switz., 28-31 May 2000, pp. I 555-I 558.

[5] Bertini, S.; Fracchia, M.; Garbero, M.; Mariscotti, A.; Pierrat, L. Statistical and probabilistic methods applied to dc traction system supply. *Proc. 6th Int. Conf. on Computer Aided Design, Manufacture and Operation in the Railway and Other Advanced Mass Transit Systems*, Lisbon, Portugal, 2-4 Sept. 1998, pp. 501-510.

[6] Stevenson, W. D. Elements of Power System Analysis. 4th Edition. *Mc Graw-Hill book company*, 1982.

[7] Iannuzzi, D.. Theoretical and experimental analysis of the vibrational phenomena in the railway bogies. Ph.D. Thesis in Electrical Engineering, XIV Cycle, Department of Electrical Engineering, Univesity of Naples Federico II, Italy, 2001, supervisor Pagano E.

[8] Del Pizzo, Electrical Drives. (in Italian), Vol.2*, Prize Worthy Praise*, Naples, Italy, 2013.

[9] Steinbauer, J. Metro Roma Linea B: Calcolo di rete con esercizio veicolare simulato. *Siemens technical report*, nr. TS EL EN2/369.003/JS, Sept. 2003.

[10] Iannuzzi, D.; Tricoli, P. Optimal control strategy of onboard supercapacitor storage system for light railway vehicles. *Proc. IEEE Int. Symp. Industrial Electronics ISIE 2010*, Bari, Italy, 4-7 July 2010, pp.280-285.

[11] Ciccarelli, F.; Iannuzzi, D.; Lauria, D. Stationary ultracapacitors storage device for improving energy saving and voltage profile of light transportation networks. *Transportation Research Part C: Emerging Technologies*, vol. 21 (1), Jan. 2012, pp. 321-337.

[12] Battistelli, L.; Ciccarelli, F.; Lauria, D.; Proto, D. Optimal design of DC electrified railway Stationary Storage System. *Proc. 2nd Int. Conf. Clean Electrical Power ICCEP 2009*, Capri, Italy, June 9-11, 2009, pp. 739-745.

[13] Iannuzzi, D.; Lauria, D.; Tricoli, P. Optimal Design of Stationary Supercapacitors Storage Devices for Light Electrical Transportation Systems. *Journal of Optimization and Engineering*, vol. 13 (4), Dec. 2012, pp. 689-704.

[14] Ciccarelli, F.; Clemente, G.; Iannuzzi, D.; Lauria, D. An analytical solution for optimal design of stationary lithium-ion capacitor storage device in light electrical transportation networks. *International Review of Electrical Engineering*, vol. 8 (3), June 2013, pp. 989-999.

[15] Ciccarelli, F.; Iannuzzi. D.; Spina, I. Comparison of Energy Management Control Strategy based on Wayside ESS for LRV application. *Proc. 39th Annual Conference of the IEEE Industrial Electronics Society IECON2013*, Vienna, Austria, 10-14 Nov. 2013, pp. 1548-1554.

[16] Iannuzzi, D.; Pagano, E.; Tricoli, P.. The use of energy storage systems for supporting the voltage needs of urban and suburban railway contact lines. *Energies*, vol. 6 (4), Apr. 2013, pp. 1802-1820.

[17] Barrero, R.; Tackoen, X.; Van Mierlo, J. Energy saving in public transport: enhanced energy storage systems for improved on-board light rail vehicle efficiency, *IEEE Vehicular Tech. Magazine*, vol. 3 (3), Sept. 2008, pp. 26-36.

[18] Grbovic, P.J.; Delarue, P.; Le Moigne, P.; Bartholomeus, P. Modeling and control of the ultracapacitor-based regenerative controlled electric drives. *IEEE Trans. Industrial Electronics*, vol. 58 (8), Aug. 2011, pp. 3471-3484.

[19] Wang, W.; Cheng, M.; Wang, Y.; Zhang, B.; Zhu, Y.; Ding, S.; Chen, W. A Novel Energy Management Strategy of Onboard Supercapacitor for Subway Applications with Permanent Magnet Traction System. *IEEE Trans. Vehicular Technology*, , early access 2014.

[20] Wang, D.; Zhao, K.; Wang, S.; Yang, Z., You, X. Power distribution control strategy of on-board supercapacitor energy storage system of railway vehicle. *Proc. Int. Conf. on Materials for Renewable Energy and Environment ICMREE 2011*, vol. 1, Shanghai, China, 20-22 May 2011, pp. 664-668.

[21] Barrero, R.; Tackoen, X.; Van Mierlo, J. Stationary or onboard energy storage systems for energy consumption reduction in a metro network. *Proc. Inst. Mech. Eng. Pt. F: J Rail Rapid Transit*, vol. 224 (3), Jan. 2010, pp. 207–225.

[22] Barrero, R.; Tackoen, X.; Van Mierlo, J. Improving energy efficiency in public transport: stationary supercapacitor based energy storage systems for a metro-network. *Proc. Vehicle Power Propulsion Conf. VPPC 2008*, Harbin, China, September 3-5, 2008.

[23] Kwon, K.; Lee, E.; Choi, J.; Baek, S. Efficiency improvement of ESS for DC transit system. *Proc. 7th Int. Power Electronics and Motion Control Conf. ECCE Asia IPEMC 2012*, vol. 4, Harbin, China, 2-5 June 2012, pp. 2641-2646.

[24] Ciccarelli, F., Iannuzzi, D.; Tricoli, P. Control of metro-trains equipped with onboard supercapacitors for energy saving and reduction of power peak demand. *Transportation Research Part C: Emerging Technologies*, vol. 24, Oct. 2012, pp. 36-49.

[25] Price, M. G.; Cook, G. Identification/Observation Using an Extended Luenberger Observer. *IEEE Trans. Industrial Electronics*, vol. IE-29 (4), Nov. 1982, pp. 279-287.

[26] Iannuzzi, D., Tricoli, P. Metro trains equipped onboard with supercapacitors: a control technique for energy saving. *Proc. 20th Int. Symp. Power Electron., Elect. Drives, Automation and Motion SPEEDAM 2010*, Pisa, Italy, June 14-16, 2010, pp. 750-756.

Chapter 5

Scale model of urban railway simulator

In order to confirm the effectiveness and the validity of the suggested control strategies, it is need to carry out a wide experimental investigation on large scale. Generally, the management of experimental tests on *real systems* (scale 1:1) is expensive and laborious, like i.e. assembling of sensors on the vehicles and testing the performance during running operations on metro line.

Scale models can give experimental answers which are very useful for testing and simulating operating conditions.

For this reason a *Laboratory reduced-scale mode* has been designed and built-up. This complex experimental platform consists in an *electromechanical simulator* to reproduce the energy flows between typical urban railway vehicle and the related DC supply network. The subsequent realization and development of dedicated Hardware and Software systems, has made this scaled model suitable for *testing* and *validating* control strategies for SC ESS energy management, both in case of on-board and stationary application.

For achieving this aim, it is necessary to guarantee dynamic resemblance between the real system and the scaled simulator.

5.1 Overview on reduced scale models

The study of the systems similarity and the calculation of the proportionality constants between values of the same magnitude in the various similar systems can be carried out comfortably taking into account the size of the variables that is necessary to consider. Of course, similar systems in respect of a particular phenomenon, or group of phenomena, might not be compared to other phenomena and hence it has to be specified the similarity validity. Therefore, it

is possible to consider different similarities according to the phenomena that are examined: *geometric similarity*, if the variables are purely geometric, *kinematic similarity* when they concern phenomena dependent lengths, and *dynamic similarities* if they concern to the times and forces or masses [1].

Due to the fact that similar systems with respect to a given phenomenon are not typically compared to another, it can be easily deduced that the number of similarities, which is possible to establish, decreases as the number of phenomena considered valid increases.

- *Geometric Similarity* - It is characterized by a constant ratio between the homologous lengths and by the constancy of dimensionless quantities (angles) counterparts. For other quantities related to the two similar systems (figures), the proportionality relationships are immediately deducted from the knowledge of their dimensional expressions: e.g if Γ is the size of the symbol length and η is the ratio of similarity between two similar systems (the ratio between the lengths of two homologous similar figures), being Γ^2 the dimensional areas equation, η^2 will be the ratio between the areas of two similar figures.

- *Kinematic Similarity* - The motion of two points P_1 and P_2 can be considered similar when the positions of the two points are related by the vector equation $\rho_2 = \eta \, \rho_1$ (where ρ_2 and ρ_1 are the linking vectors of the two movable points P_1 and P_2 referred to two fixed points O_1 and O_2, respectively, while η is a constant) when the above-mentioned vectors are respectively measured at times t_1 and t_2 are related by $t_2 = t_1 \, \lambda$, where the origins of the two times, usually not coincident, are suitably chose to eliminate a possible additive constant c in second member. From the above equations, it is easy to show that the ratio between the speeds of the two points is expressed by $\eta \, \lambda^{-1}$, and the ratio of the accelerations is $\eta \, \lambda^{-2}$; these relationships are indeed also immediately deductible dimensional equation of the two variables considered, respectively $\Gamma \, \Omega^{-1}$ and $\Gamma \, \Omega^{-2}$ .For systems of points or a continue body, the simile kinematics is assured when the first equations written is applied to all copies of homologous points of the system at all times bound by the second equation. Considering that η and τ are constant for all pairs of points, this condition implies that η is the geometric similarity ratio between the corresponding systems or continues bodies. The similarity between the kinematic motions of two bodies or systems therefore implies the existence of geometrical similarity between the same.

- *Dynamic Similarities* - The dynamic law of similarity (also called mechanical) establishes a proportional relationship between the homologous forces, acting on systems which are similar in geometry and in kinematic. In this case the switch from one system to another (if the lengths, masses and times are respectively multiplied by η, μ and λ), can be obtained as indicated in the equation (5.1).

The equation that governs a phenomenon is valid whatever the measurement system adopted and could be applied for all systems dynamically similar: consequently a phenomenon instead of a system in real size can be studied on a reduced scale model whose mechanical is equivalent to the real system. This experimental method, which in some branches of the technique has gained considerable importance, it has spread after the systematic use made by *Froude* in 1870 in the naval architecture.

During the method application, attention to special conditions has to be paid: in fact, it is possible set only one or two of the three ratio η, μ, λ, because exist the impossibility to reduce in scale some physical quantities that influence the phenomenon of interest.

In a real phenomenon, dependent on several parameters that affect itself, there are different relations between the fundamental units and it is possible to carry out different similarity laws. For example, by considering a systems where acts only inertia forces, if the mechanical, geometric and cinematic similarity are respected, regarding the two systems they have in the relation $\mu\ \eta\ \lambda^{-2}$. Indeed, the inertia forces depend on the accelerations of the systems, the masses of the homologous parts of the systems and on the density of the masses homologous. The first will result in the ratio $\eta\ \lambda^{-2}$, the masses depend on the respective volumes (whose relationship is η^3) and their densities that result in the relationship $\mu\ \eta^{-3}$. In the case that the model is made with the same materials of the real system, it is necessary to take into account that the mechanical similarity used for the construction of the model must satisfy the condition:

$$\mu\eta^{-3}=1 \quad \Rightarrow \mu=\eta^3 \qquad (5.1)$$

In this case, can be chosen arbitrarily only η , λ and the ratio between the masses homologous μ is defined by the values η and λ. Consequently, the derived quantities will vary with specific similarity relations that can be deduced from the equations of size and by eq. (5.1).

5.2 Electromechanical railway simulator

As above mentioned, the realization of a scale model similar to the assigned physical system needed the knowledge of phenomenon which is meant to refer. The phenomenology is that we want to study is the energy behavior of a railway vehicle on an electrified urban railway power line arranged with on-board or stationary Supercapacitor ESS. In particular the aim is to evaluate the energy contribution and improvement that the ESS is able to provide during the acceleration and braking phases of the vehicles. For achieving this target it is has been necessary to realize and tune a scaled **electromechanical** system, where the electrical part had to reproduce the power demand at the pantograph of the vehicle and the mechanical part must reproduce the dynamics of the vehicle during the different operating conditions (acceleration, cruising and braking). This can be simulated by an electric drive whose power supply voltage varies with the position of the vehicle along the feeding line.

In this framework, dynamical aspects have to be evidenced, with particular care to the vehicle speed, rotational speed of the traction wheels taking into account the transmission ratio, the speed of the electrical traction motors, and eventually skidding phenomena. The criteria adopted to scale the system is based on the *dynamic similarity* principle, leading to respect the same dynamic characteristics of the real system (same indicial response). For designing the scale model it is therefore necessary to define the criteria based on the reduction in scale, for guaranteeing dynamic resemblance between the real system and the simulator. The own frequencies belonging to the real system are the same in the scaled model and all the amplitudes of quantities as inertia forces, friction forces, motoring torques and power flows are scaled.

In other words, the reduction criteria is based on the reproduction of the same characteristic eigenvalues [1]-[2].

The parameters and quantities of the simulator, designed according to the above criteria of dynamic resemblance to a real system, are the following:

- each rotating shaft has the same velocity and angular acceleration;
- the linear velocities are in radius relation;
- the inertia, stiffness, and torque are scaled by a factor ε;
- the electrical power of the motor and the kinetic energies are chosen according to the same factor ε;
- there is the same *hertzian* pressure of wheel-rail contact.

From a previous design of the mechanical system this scale factor was chosen equal to $\varepsilon_{mech}= 200$ [1-4].

In order to assess the performance of the entire network electrified system - vehicle - storage system in several cases study, have been played the two configurations as previously described in paragraphs 4.5 and 4.7 for installation on-board of the ESS unit (see Figure 4.11) and stationary ESS placement (see Figure 4.14 or Figure 4.16).

As concerns the supercapacitor storage device it has been used the module with **LiC** technology described and validated in the paragraph 3.3.3, with the further intention of demonstrating the feasibility of the use of this technology for urban railway applications.

The reduced scale simulator has been set up and tuned at the *Transport Laboratory* (*TrLab*) of the *D.I.E.T.I.* of the *University Federico II of Naples.*

The overall block diagrams of the experimental test platforms are shown in Figure 5.1 and Figure 5.2, respectively.

The simulator is mainly composed by an *electrical* and a *mechanical* part. The electrical part reproduces the power supplied from the contact line by the vehicle electric drives (converter + motor) with installed a LiC storage system both **on-board** the vehicle or **wayside**, placed at the end of a one side supplied DC double track line with two operating vehicles. Since it is impossible to reproduce in the laboratory the powers of the real system, we have chosen a scale factor in power ($\varepsilon_{pel} \approx 30$) for the simulation of the power line and the DC traction drives. It is given by the product of the voltage and current scale factor (ε_v and ε_i respectively). The first one is very close to unity ($\varepsilon_v \approx 1.4$), since we assumed that the supply voltage to be used in the simulated network (535 V) differs little from the typical DC supply voltage of urban rail transport systems (750 V). As concerns the current reduction factor, it has been chosen on the basis of the input limit current of typical urban light railway vehicles (300 ÷ 400 A) and the maximum continuous current of the simulated electrical drive, thus resulting $\varepsilon_i \approx 20$.

For the measurement of the interest quantities the simulator has been provided with proper sensors and transducers and a "*dedicated*" data acquisition, processing, and transmission systems.

By summarizing, the experimental test platform is mainly constituted by the following functional parts:

237
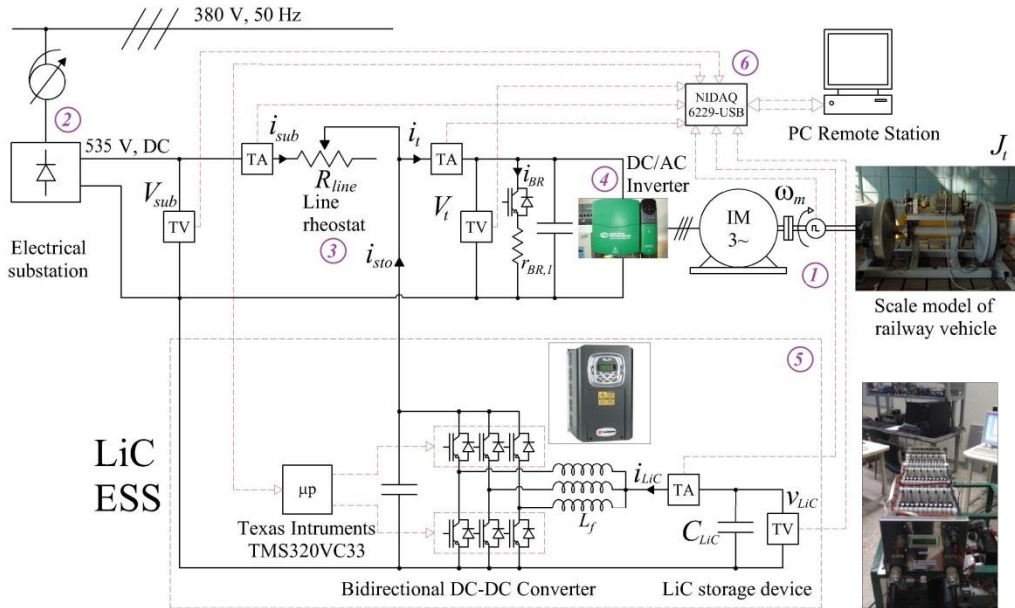
Figure 5.1 – Lab. experimental platform for the on-board ESS case study

1) Mechanical load

2) Electrical substation

3) Line rheostats

4) Electrical drives

5) Lithium-ion capacitor based energy storage system

6) Data acquisition, control and supervisory systems

The following paragraphs will give a brief description of each subsystem.
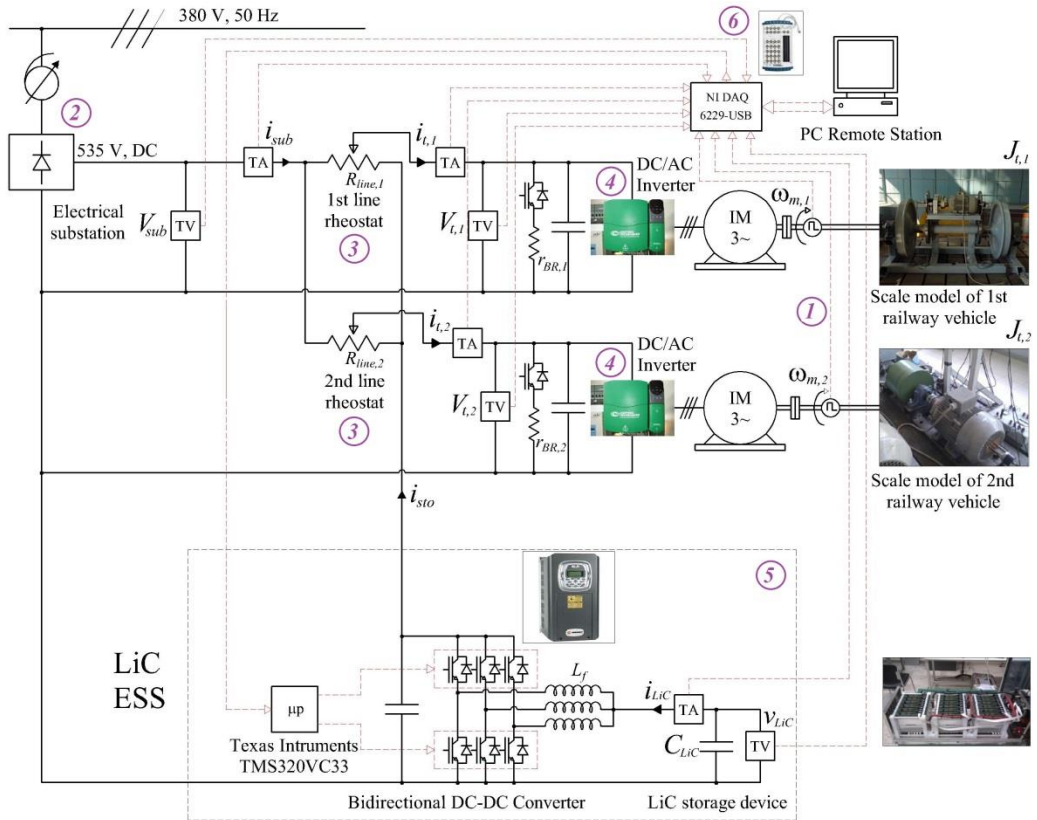
Figure 5.2 - Lab. experimental platform for the stationary ESS case study with two railway vehicles

5.2.1   Mechanical simulator

The mechanical part of the scaled simulator in scale essentially reproduces the mechanical traction load constituted by the railway vehicle and in particular its bogie. In fact, it, reproduces forces and inertia of a typical urban railway vehicle. It is mainly composed of a mechanical transmission unit (asynchronous three-phase motor, gearbox, wheel-set) fixed on a mobile frame and four wheels set on a rigid axle, together with their interconnections by hollow shaft, cardan shaft and couplings.

More specifically, with reference to the frontal view depicted in the Figure 5.3, the homokinetic transmission permits high axial and radial movements, and consists of:

- a motor shaft (1);
- a reduction unit, consisting of 3 gears (3,4,5);
- two coaxial hollow shafts (7,8);

239
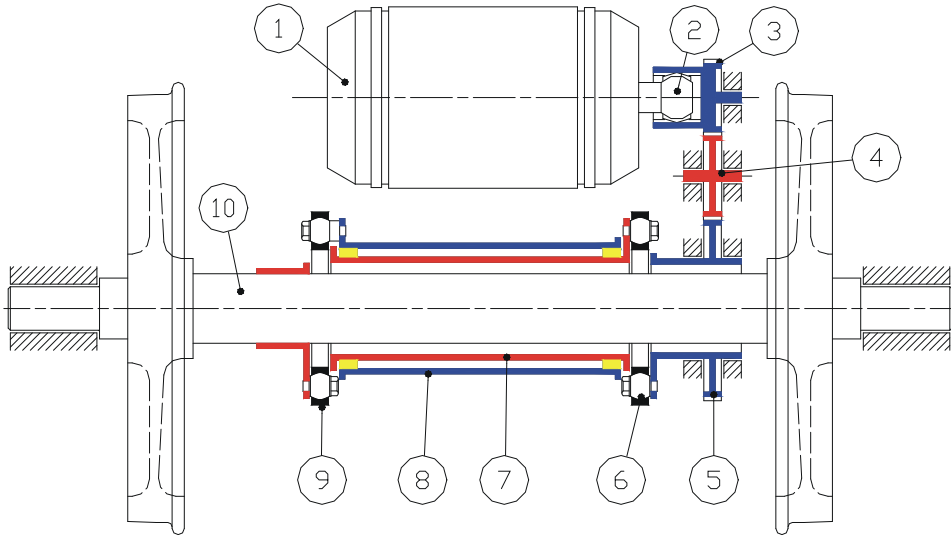
Figure 5.3 – Front view of the mechanical drive simulator

- an axle with wheel set (10);
- a thooted coupling (2);
- two sets of rods (6, 9);
- the second one (9) connects the hollow shafts with axle;
- two elastic spacers.

The spacer allows small angular shifts between the shafts and make the articulation of the dancing ring (see Figure 5.4) kinetically possible with the consequent possibility of reciprocal shifting between the assembly of hollow shafts and axle.

Figure 5.4 – Particular of the dancing ring and the reduction unit
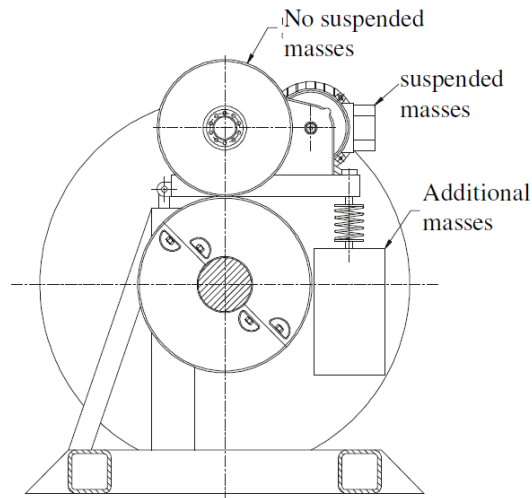
Figure 5.5 - Side view of the mechanical drive simulator

By looking at the side view of the mechanical drive reported in Figure 5.5, it is shown that the transmission and the mobile frame lean on a couple of wheels by means of a wheel-set, which represents a pair of driving wheels of the motoring traction unit. In order to obtain different friction forces between the pairs of contacting wheels, there is an additional mass fixed on the mobile frame. The wheels represent the inertia of translating masses, which is proportionally direct to the mass of the real train. A front picture of the mechanical simulator, located in the *TrLab.*, is reported in Figure 5.6. , whereas its main characteristics are briefly reported in Table 5.1 – Main parameters of the mechanical simulator. It is worth noting that the total inertia of the system, reported to the axis of the drive motor is 3.7 kgm^2. As concerns the reports, the gear ratio of the speed reducer has been taken into account (2.53:1) as well as the ratio adopted between the diameter of the driving wheels and the diameter of the driven wheel (1.29:1), which is necessary in order to increase the rotational speed of the motor up to theoretical 1500 rpm. However, the inertia of the two wheels, which are made in steel, have the most part of equivalent inertia and represent the inertia of translating mass which are directly related to the mass of the real vehicle. Further details on the mechanical simulator can be found in [1-4].

Figure 5.6 – Picture of the complete mechanical simulator

Mechanical simulator parameters	Unit	Value
Rated power of the induction motor	[kW]	5.5
Rated frequency of the induction motor	[Hz]	50
Rated voltage of the induction motor	[V]	400
Rated current of the induction motor	[A]	11.4
Rated speed of the induction motor	[rpm]	1455
Rated power factor	-	0.82
Magnetizing-inductance of induction motor (L_m)	[mH]	128
Stator phase inductance of the induction motor (L_s)	[mH]	5.3
Rotor phase inductance of the induction motor (L'_r)	[mH]	5.3
Stator phase resistance of the induction motor (R_s)	[Ω]	0.91
Rotor phase resistance of the induction motor (R'_r)	[Ω]	0.93
Max motor angular speed ref. to the motor axle ($\omega_{m,max}$)	[rpm]	1500
Equivalent inertia referred to the motor axle (J_t)	[kgm^2]	3.7
Max motor torque (to transmission system) ($T_{m,max}$)	[Nm]	100
Wheel Diameter (D_{wh})	[m]	0.90
Overall transmission ratio (τ)	-	3.26 : 1

Table 5.1 – Main parameters of the mechanical simulator

Figure 5.7 – Mechanical simulator of the 2ⁿᵈ vehicle

Due to the impossibility to reproduce another similar mechanical simulator, the second vehicle has been realized by coupling directly an induction motor and a rotating inertia, as depicted in Figure 5.7. In this case, the inertia rotates at higher speed than the real system. In the Table 5.2 the main characteristics of the mechanical simulator reproducing the 2ⁿᵈ vehicle are summarized.

2ⁿᵈ Vehicle Mechanical simulator parameters	Unit	Value
Rated power of the induction motor	[kW]	7.5
Rated frequency of the induction motor	[Hz]	50
Rated voltage of the induction motor	[V]	380
Rated current of the induction motor	[A]	15.6
Rated speed of the induction motor	[rpm]	1450
Rated power factor	-	0.85
Magnetizing-inductance of induction motor (L_m)	[mH]	105
Stator phase inductance of the induction motor (L_s)	[mH]	4.8
Rotor phase inductance of the induction motor (L'_r)	[mH]	3.9
Stator phase resistance of the induction motor (R_s)	[Ω]	0.72
Rotor phase resistance of the induction motor (R'_r)	[Ω]	0.48
Max motor angular speed ref. to the motor axle ($\omega_{m,2,max}$)	[rpm]	2500
Equivalent inertia referred to the motor axle ($J_{t,2}$)	[kgm²]	0.95
Overall transmission ratio (τ)	-	1

Table 5.2 – Main parameters of the mechanical simulator reproducing the 2ⁿᵈ vehicle

5.2.2 Electrical network simulator

As is evident from Figure 5.1 or Figure 5.2, the electrical substation conversion of the urban electrified line, and therefore the power supply of the catenary, is simulated by a three-phase bridge rectifier unidirectional diode (see Figure 5.8) that converts the fixed alternating 3- phase 380 V 50 Hz mains voltage, to a DC voltage of about 535 V no-load voltage.

The contact between line and pantograph of the vehicle, were simulated through variable resistances with sliding contact, in order to simulate the variations of

Figure 5.8 – Front picture of the bridge rectifier

the track lines resistances according to the vehicles movement.. The variable resistance is formed by two contacts, a fixed one which is connected to the positive terminal of rectifier bridge and the sliding contact at the input of the DC traction inverter DC or to the DC-side of the ESS converter in case of two vehicles.

Obviously this requires an automatic and continuous synchronization between the angular speed of the railway vehicle wheels and the space covered by the train (and then by the cursor).

The rheostat will change its position based on the speed profile imposed to the drive. The cursors are matched with a recirculating ball screw and preloaded, coupled with a brushless servo motor and its drive (see Figure 5.9). The brushless servo motor that moves the cursor on the rheostat requires a pulses sequence as setting the allowance and travel speed.

The synchronization is ensured through an external reference signal to the servo motor proportional to the integral of the speed of the drive wheel . In this way there is a sure correspondence between the position of the simulated vehicle and the position of the sliding contact on the rheostat. For the purposes of determining the power and resistance, is has been necessary to take into account the voltage value at the start line of 535 V and the maximum voltage drop at the end line equal to 30 % of the voltage at the start line. In the Table 5.3 – Main parameters of the simulated supply traction networkthe main parameters of the simulated electrical traction network are reported.

The electrical simulator is completed with the electrical traction drives, which are simulated by Voltage Source DC/AC Inverters manufactured by Control Techniques.

Supply traction network parameters	Unit	Value
Substation input 3-phase AC voltage	[V]	380
Substation bridge diode rectifier: SINUS/T		
Rated substation power	[kW]	22
Substation DC no-load voltage ($V_{sub,0}$)	[V]	535
Substation output filter capacitance	[mF]	0.4
Line resistance range variation (R_{line})	[Ω]	0.1÷10
Max. line rheostat dissipable power	[W]	3100
Rated line rheostat current (i_{BR})	[A]	18

Table 5.3 – Main parameters of the simulated supply traction network
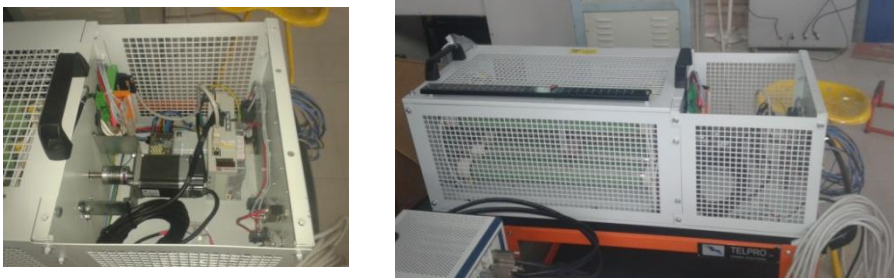
Figure 5.9 – Particular of the servomotor and the line rheostat
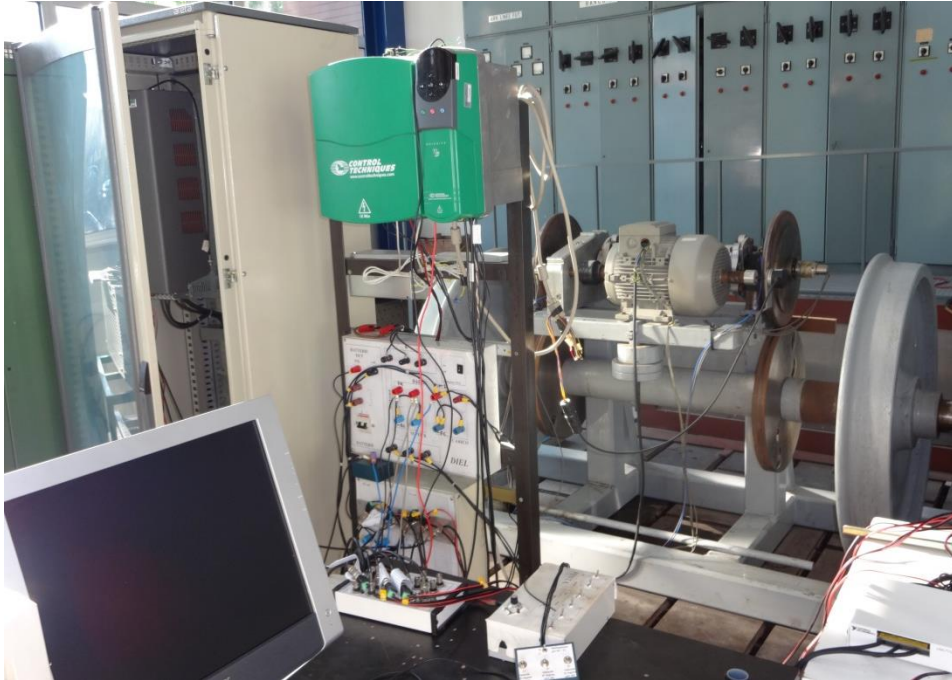
Figure 5.10 – Front side of the DC/AC inverter and the transducer box

Electrical traction drive parameters	Unit	Value
DC/AC inverter: Control Techniques UNI3403		
Rated inverter power	[kW]	22
Input DC voltage range (V_t)	[V]	380÷750
Rated input current	[A]	46
Input DC filter capacitance	[mF]	2.0
1st BR rheostat resistance ($r_{BR,1}$)	[Ω]	11.3
2nd BR rheostat resistance ($r_{BR,2}$)	[Ω]	33.0
1st BR rheostat dissipable power	[W]	3900
2nd BR rheostat dissipable power	[W]	1300

Table 5.4 – Main parameters of the electrical traction drive

The positive terminal of the input capacitive filter of each DC/AC converter is connected to the sliding contact of line resistance. The negative terminal is connected to the common ground of the power substation.

In Figure 5.10 is shown a front view of the DC/AC inverter, which are the same for the two mechanical loads, whereas in Table 5.4 – Main parameters of the electrical traction drive are briefly reported its main parameters.

The drive involves the measurement of the line voltage, and the motor phase currents. Furthermore there is also the measurement of the angular velocity, $\omega_{m,i}$, of the traction motors measured by 2000 pulses/rotation encoders. The inverter is controlled by remote with a closed loop realized on the LiC speed which allows the variation of the motor speed and acceleration, as well as the torque-current limit, obtaining different value of the electrical power absorbed.

In order to limit the increase of the supply line voltage, is placed a shunt resistor (r_{BR}) in parallel to the input capacitive filter of the converter. This shunt resistor acts as a braking rheostat and its can dissipate the excess energy during braking. Finally several voltage and current transducers have been installed since they were necessary to monitor the substation, i_{sub}, and vehicle currents, $i_{t,i}$, as well as the substation, V_{sub}, the vehicle, $V_{t,i}$ or the line voltages, V_{sto}.

5.2.3   SC ESS simulator

Regardless of the configuration expected (on-board or stationary), the Lithium-ion Capacitor Energy Storage, is constituted by the LiC unit stack (see Figure 3.27) interfaced with the electromechanical subsystem by means of an interleaved three-leg full-bridge DCDC converter with a rated power of 20 kVA, manufactured by Elettronica Santerno. The employed realization of the interleaved converter may involve a reduction in volume and weight due to the phase shifting action, especially as fas as the inductors are concerned. The single output phases are merged to three filter inductors, L_f, star-connected. This neutral point is connected to the positive terminal of the LiC module, while the negative terminal LiC ESS is linked to the common ground of the power line. The converter has an input filter DC-link capacitance, which has to be connected to the electrical drive of the mechanical simulator in case of on-board ESS (Figure 5.1), or to the end limit point of the line rheostat, which simulates the ESS stationary installation at the end-line of a double track traction line (Figure 5.2).

The variables that are transduced and measured are the LiC current, i_{LiC}, and the LiC voltage, v_{LiC}, as well as the DCDC converter high side voltage, V_{sto}, and current i_{sto}. This allows to manage proper closed loop control of voltage and current. The Figure 5.11shows a view of the LiC ESS and in Table 5.5 are given its main electrical parameters.

Figure 5.11 – Frontal picture of the interleaved DCDC converter

It has to be strongly remarked that the LiC storage device arrangement is not optimal from an energetic point of view, since the sizing has not been referred to the total rotating inertia and the maximum angular speeds. In fact it has been constrained by the LiC module at our disposal, which has a storable energy greater than the maximum braking energy available from the simulator.

Electrical traction drive parameters	Unit	Value
DC/DC inverter: Elettronica Santerno SINUS PENTA S20-0086		
Rated Converter power	[kVA]	20
Input DC voltage range (V_{sto})	[V]	$360 \div 810$
Input DC filter capacitance	[mF]	10
Max output current ref. to LiC side ($i_{LiC,max}$)	[A]	135
Output filter inductance (L_f)	[mH]	1.0
LiC module rated eq. capacitance (C_{LiC})	[F]	30.5
LiC module rated ESR (r_{LiC})	[mΩ]	43.3
LiC module voltage range ($V_{LiC,min} \div V_{LiC,max}$)	[V]	$80 \div 136$
LiC module storable energy ($E_{LiC,max}$)	[Wh]	52.7

Table 5.5 – Main parameters of the LiC ESS

248

5.2.4 Control and supervisory systems

The real time operation of the entire system by means of the scaled lab simulator involves to control and coordinate the interactions between the various subsystems in a hierarchical manner. To achieve this requirement, it has been provided the use of a **supervisory system** that has the function of generating the reference values of the various subsystems and to synchronize the various events that describe the behavior of the global system. Each subsystem has its own control which generates references for its actuators.

The supervision is devolved to a **central personal computer** through a high-level logical hierarchy implemented in *Matlab* environment, which interrogates the various subsystems and, on the basis of data received from the platform, it processes the reference signals to be applied and the digital signals for applying enable/disable logics such as starting and stopping the drive motor and the control of the LiC storage system.

The control unit is mainly distinguished in two **Digital Signal Processor** (DSP) boards. The first one is used for the implementation of the vector control of the induction traction motor, whereas the second one is dedicated to the power management of LiC storage unit. An example of the integration between the two control systems could be the one already described in Figure 4.22.
The traction control is in turn constituted by control of the motion of the vehicle, called "MC" and the torque control of the motor, called "FOC". Both controls are implemented on the microcontroller of the inverter traction drive. The MC receives as input the value of the measured speeds and the reference ones generated by supervision system. The FOC, instead receives in input the motor phase current, the speed and the torque reference.

Conversely, the control and management system of the LiC ESS is implemented for a part on the central PC supervisory station in the *Matlab* environment and partially on the microcontroller of the DCDC converter SINUS PENTA S20. More specifically, this last one is based on the *Texas Instruments* platform TMS320VC33, that offers up to 4 analog inputs (A/D converters), 4 analog outputs (D/A converters), 4 digital input and 4 digital outputs. The sampling time is 400 μs. This DSP is responsible for the inner current control loop, as it is reported in the control schemes analyzed in section 4.10, for evaluating the command signal ρ for the PWM modulation of the DCDC converter switches. In

fact, it receives as input the value of the LiC reference current, $i_{LiC,ref}$, the actual LiC current, i_{LiC} ,and voltages, v_{LiC} , the high-side DCDC converter voltage, V_{sto} , as well as the LiC current and voltage limits.

Instead, the more external control loops have been implemented in *Matlab* on the supervisor PC, along with other implementations regarding processing of the acquired signals, e.g. the derivative filter for the evaluation of estimated vehicle acceleration, $\dot{\hat{v}}_t$, and the internal LiC voltage, $\hat{u}_{sc}$, identification via *Luenberger* observer.

In order to carry out the overall monitoring and control in real time, acquisition and control systems clearly have to integrate the data acquisition (DAQ) system, which, starting from measurements made by all the transducers of the Lab. Simulator, provides for their time acquisition. For this reason it has been employed a *National Instrument* **data acquisition** (NI-DAQ 6229 USB) board with 16 analog inputs channel and 4 analog output channels. These last ones are the LiC current set-point reference, the speed reference profile for the vehicles and the synchronization signal for the line rheostat. In the fig is reported an assembly view of the NI-DAQ 6229 USB board.

Figure 5.12 – Assembly view of the NI-DAQ 6229 usb DAQ

In the following, the implementation of the control strategies proposed in section 4.10 on the our Lab. scaled electromechanical simulator will be shortly explained.

5.3   Case studies control strategies implementation

In this section is described how the previously mentioned control strategies (see section 4.10) for the LiC ESS energy management, have been implemented in the Laboratory simulator. For sake of brevity we will make reference only to the case of stationary LiC ESS installed at the end-line with two circulating railway vehicles, given that in any way is the case of more general discussion.

5.3.1   Speed Tracker Control strategy implementation

The strategy is oriented to the optimization of the energy saving and the reduction of the overall energy consumption as well as the line voltage drop minimization. Let's keep in mind how said in the section 4.10.1 and the STC scheme depicted in Figure 4.22, by referring to a LiC module instead of a SC one.

Hence, in order to verify and validate the control strategy on the scaled Lab. simulator, the translating physical quantities that appear in eqs. (4.41), (4.42) and (4.43), have been properly scaled and replaced with the corresponding rotating ones, i.e. rotating inertia instead of translating mass, angular speeds instead of translating speeds.

In particular, with reference to the test bench set up in Figure 5.2, eqs. (5.2) and (5.3) shows that the LiC reference internal voltage, $u_{LiC,ref}$, is obtained from the knowledge of the vehicle angular speeds detected at the motor axles, $\omega_{m,i}$, and their related equivalent rotating inertia, $J_{t,i}$,by assuming an equivalent module capacitance equal to its rated value, C_{LiC} for sake of simplicity:

$$\frac{1}{2} C_{LiC} \left(V_{LiC,\max}^2 - u_{LiC,ref}^2 \right) = \frac{1}{2} \sum_i^2 k_i \, J_{t,i} \omega_{m,i}^2 \qquad (5.2)$$

$$u_{LiC,ref} = f\left(\omega_{m,i}\right) = V_{LiC,\max} \sqrt{1 - \frac{\sum_i^2 k_i \, J_{t,i} \omega_{m,i}^2}{C_{LiC} \, V_{LiC,\max}^2}} \qquad (5.3)$$

where all the parameters are given in the previous paragraphs. In particular it has been supposed that the LiC module was pre-charged at $V_{LiC,max} = 136$ V. The coefficient k_i , has been set equal to 1, for the energetic reasons explained in the last part of paragraph. On the basis of eq.(4.43) reported in terms of angular speed and rotating masses, the reference power $P_{LiC,ref}$ is given by:

251

$$P_{LiC,ref} = f\left(\omega_{m,i}, \dot{\hat{\omega}}_{m,i}\right) = \sum_{i}^{2} k_i \, J_{t,i} \, \omega_{m,i} \dot{\hat{\omega}}_{m,i} \qquad (5.4)$$

The traction motors angular speeds, $\omega_{m,i}$, are available by means of the encoders placed on the motors shaft. The angular accelerations, $\dot{\hat{\omega}}_{m,i}$, have been estimated from the measured actual angular motor speeds by the 2nd order digital filter, referring to the regulator Reg_v, shown in Figure 5.2, which is represented by the following transfer function:

$$\dot{\hat{\omega}}_{m,i}(s) = \omega_{m,i} \frac{G(s)}{1 + G(s)H(s)}, \; G(s) = k_{P,v} + \frac{k_{I,v}}{s}, \; H(s) = \frac{1}{s}. \qquad (5.5)$$

The constants $k_{P,v}$ and $k_{I,v}$ have been selected in order to track the acceleration of the traction motors for rates from 6 to 8.7 rad/s^2.

By recalling how said in the previous paragraph, the external voltage control loops has been implemented in *Matlab* on the supervisor PC. The *Matlab* **script** of the program is reported in the Appendix A1. Let's take a brief look to this one.

The *Matlab* **supervision** and **control** program defines the voltage and current references of the LiC module on the basis of the acquisition of variables such as speeds, actual current and voltage of the LiC, current and the input voltage of the traction drives, as described in the algorithm control shown in Figure 5.2. In the first part of the program are defined the acquisition channels of these variables on the NI-DAQ 6229. In particular are defined the sampling frequency of the acquisitions (1000 Hz), the constants of transduction of the quantities of interest, the period in seconds of the entire drive cycle simulated (60 s) and many others system parameters. The sampling time of the control algorithm in this program is 10 ms.

The value of the reference internal voltage, $u_{LiC,ref}$, as described in eq. (5.3), is determined from knowledge of the actual motor speed values, $\omega_{m,i}$. Subsequently is implemented the outer voltage control loop (Reg_u), eq. (4.32), which compares the reference internal LiC voltage, $u_{LiC,ref}$, to the actual estimated one, $\hat{u}_{LiC}$, that comes from the implementation of the *Luenberger* observer (4.34). Therefore, the PI regulator Reg_u has been also implemented and finally the LiC current set-point, $i_{LiC,ref}$, (4.33) is calculated.

This output is made available on an analog output channel after a suitably scaled voltage signal to send as an input to the next LiC current control loop in the DCDC converter of ESS.

The inner **current control loop** LiC ESS program is implemented in the DSP of the DC DC converter and is achieved through a structure of **state machines**, each of one independent by the other. Each state machine has a different function. Some are devoted to the implementation of the converter control (e.g. CONTROL, PWM machines), other to the generation of reference (REF machines), and so on. Below is shown a list of the main state machines of the management software and their main features:

- AIN machine: Conditioning analog input;
- ALR machine: Alarm Management;
- AOU machine: Conditioning of analog output;
- CTR machine: Generation of control signals;
- DGI machine: Digital inputs;
- DGO machine: Digital outputs;
- LED machine: LED Management;
- MIS machine: Measurement of input variables;
- MMI machine: User interface (Keypad)
- MOD machine: MODBUS communication protocol;
- PRT machine: Management of Protection alerts;
- PWM machine: Generations signals of PWM modulation technique;
- REF machine: Generation of reference signals;
- RWM machine: Writing and reading variables in memory.

Each state machine is constituted by a main program, e.g. CTR_Main.c, and several procedures named with the same type of machine that treat and define different data. For example, a procedure of the CTR machine, defines and manages only variables CTR_Var.c and/or parameters CTR_Par.c . Other procedures , however, define the variables and the input parameters CTR_In, which can be used within the machine CTR, and output CTR_Out which may be used by other machines.

Although this structure is very flexible and modular, it imposes a number of variables to allocate in memory not acceptable for a microcontroller. So, a limited number of memory location are used, that through a dynamic management of indirect addressing allows to manage an high number of

variables. In particular, the procedure for each machine uses some local variables and other global, which via macros enabling instruction allows to be used by other machines without using new memory locations. The macro functions are a form of indirect addressing, which allows you to move within the processor's memory without the need of associating a static memory location for any declared.

In the Appendix A2 are reported some scripts in C language of the CONTROL and REF state machines implemented in the processor TI TMS320VC33 of the SINUS PENTA converter. They represent the core of the LiC current control algorithm. The REF machine makes it available to the machine CTR the reference signals generated by the supervision and control system ($i_{LiC,ref}$). In the CTR machine is obviously implemented the PI regulator Reg_i (4.36) and the evaluation of the command signal, ρ (4.37). Moreover, this machine translates these reference signals into control signals for the semiconductor components of the converter, using PWM modulation techniques.

The following Table 5.6, tries to summarize all the control parameters employed as concerns the STC strategy.

Speed Tracker Control parameters	Unit	Value
NI-DAQ sampling time	[ms]	1
External control loop sampling time	[ms]	10
Inner control loop sampling time	[ms]	0.4
LiC module current limit ($i_{LiC,max}$)	[A]	135
LiC module voltage limits ($V_{LiC,min} \div V_{LiC,max}$)	[V]	80 ÷ 136
Observer proportional gain (k_o)	[Ωs^{-1}]	1
Proportional gain digital filter DF ($k_{P,v}$)	[s^{-1}]	15
Integral gain digital filter DF ($k_{I,v}$)	[s^{-2}]	12.5
Proportional const. regulator Reg_u ($k_{P,u}$)	[A]	1400
Integral const. regulator Reg_u ($k_{I,u}$)	[As^{-1}]	15
Proportional const. regulator Reg_i ($k_{P,i}$)	[Ω]	120
Integral const. regulator Reg_i ($k_{I,i}$)	[Ωs^{-1}]	6000

Table 5.6 – Main parameters of the STC strategy

5.3.2 Line Voltage Tracker Control strategy implementation

By keeping in mind how treated in the section 4.11.2, the block diagram LVTC control strategy has been depicted in Figure 4.23.

The LVTC *Matlab* supervision and control program is reported in the Appendix A3 and it is simpler than the STC one, since it is not implemented both the

digital speed filters and the internal LiC voltage identification. The supervision and monitoring script part is substantially the same as used for the STC technique, with the exception for the acquisition of the line voltage at the point where it is installed the LiC ESS. As concerns the LiC voltage control loops, by bearing in mind eqs. (4.44) and (4.45), once assigned the line voltage reference value, $V_{line,ref}$, the LiC voltage, $V_{LiC,min}$ and $V_{LiC,max}$, and current, $i_{LiC,max}$, limits, the corresponding PI regulator (Reg_L) and (Reg_u) have been implemented in *Matlab* code as well as proper limiting and anti wind-up actions. Even in this case this leads to the knowledge of the LiC current reference, $i_{LiC,ref}$, which is sent as input for the DSP of the DCDC converter.

As regards the inner LiC current control loop (Reg_i) it is practically the same as the one implemented for the STC and for the state machines, reference can be made to the Appendix A2.

The Table 5.7, tries to summarize all the control parameters employed as concerns the LVTC strategy.

Line Voltage Tracker Control parameters	Unit	Value
NI-DAQ sampling time	[ms]	1
External control loop sampling time	[ms]	10
Inner control loop sampling time	[ms]	0.4
Line voltage reference set-point ($V_{line,ref}$)	[V]	510
LiC module current limit ($i_{LiC,max}$)	[A]	135
LiC module voltage limits ($V_{LiC,min} \div V_{LiC,max}$)	[V]	$80 \div 136$
Proportional const. regulator Reg_L ($k_{P,L}$)	[-]	100
Integral const. regulator Reg_L ($k_{I,L}$)	[s^{-1}]	1
Proportional const. regulator Reg_u ($k_{P,u}$)	[A]	10
Integral const. regulator Reg_u ($k_{I,u}$)	[As^{-1}]	100
Proportional const. regulator Reg_i ($k_{P,i}$)	[Ω]	100
Integral const. regulator Reg_i ($k_{I,i}$)	[Ωs^{-1}]	5000

Table 5.7 – Main parameters of the LVTC strategy

5.3.3 Line Current State Control strategy implementation

With reference to the section 4.11.3, the block diagram of the LCSC strategy has been depicted in Figure 4.24.

The LCSC *Matlab* supervision and control program script is not reported for sake of brevity, since it consist only of sending the line current reference set-point, $i_{line,ref}$, as input for the DSP of the DCDC converter, whereas the remaining supervisory and monitoring part are the same of the other controls.

Once known the line current actual set-point reference, in the CTR state machine is implemented the changeover finite state controller described by eq. (4.46). In the Appendix A4 is reported the C language script file for the CTR machine of the LCSC strategy, while the corresponding REF machine is the same seen for the previous controls.

The Table 5.8, reports the main control parameters employed as concerns the LCSC strategy.

Line Voltage Tracker Control parameters	Unit	Value
NI-DAQ sampling time	[ms]	1
Inner control loop sampling time	[ms]	0.4
Line current reference set-point ($i_{line,ref}$)	[A]	8
LiC module current limit ($i_{LiC,max}$)	[A]	135
LiC module voltage limits ($V_{LiC,min} \div V_{LiC,max}$)	[V]	$80 \div 136$
Proportional const. regulator Reg_i ($k_{P,i}$)	[Ω]	12.5
Integral const. regulator Reg_i ($k_{I,i}$)	[Ωs^{-1}]	2500

Table 5.8 – Main parameters of the LCSC strategy

5.4 Chapter 5 references

[1] Iannuzzi, D.. Theoretical and experimental analysis of the vibrational phenomena in the railway bogies. Ph.D. Thesis in Electrical Engineering, XIV Cycle, Department of Electrical Engineering, Univesity of Naples Federico II, Italy, 2001, supervisor Pagano E.

[2] Grassia, P.; Iannuzzi, D. A scale model for experimental evaluation of bogie vibrations: Design, manufacture and measurement techniques. *Proc. Int. Conf. on Railway Traction Systems*, Capri, Italy, May 15-17, 2001.

[3] Rizzo, R.; Iannuzzi, D. Simulator for the analysis of vibration phenomena in railway traction drive systems. *Ciencia y Engenharia/ Science and Engineering Journal.*, vol. 12 (1), Jan. 2003, pp. 77-81.

[4] Grassia, P.; Iannuzzi, D.; Migliaccio, M.; Pagano, E. Un simulatore di trasmissione ferroviaria in similitudine dinamica. Ingegneria Ferroviaria, vol. 57 (3), Mar. 2002, pp. 147-156.

Chapter 6

Experimental results and control performance comparison

In this final chapter will be presented the performed extensive experimental test campaign conduced on the Lab. scaled electromechanical simulator for confirming the validity and the effectiveness of the control techniques suggested on typical traction cycles. Moreover it is assessed the behavior of the simulated light transportation network equipped with LiC ESS unit installed on-board of one vehicle or placed wayside with two operating vehicles.

With reference to the two case studies described in par. 4.5 and in par. 4.7, the benefits achieved by the presence of the LiC ESS will be compared with the respective case studies evaluated in the absence of storage unit, which are used as base comparison reference.

Finally an overall comparison among the different control strategies tested for both the on-board and the stationary LiC ESS installation, will be carried out, as well as the energy saving improvement has been highlighted and the energy storage system integration and challenges are addressed.

6.1   Base case study test results for on-board LiC ESS

The test bench configuration is reported in Figure 5.1 , where the LiC ESS is obviously not connected.

The main parameters of the simulated railway vehicle and the supply line under consideration are reported in the previous Table 5.1, Table 5.3 and Table 5.4.

It worth to be noted that the rotating kinematic and mechanical quantities have been properly scaled and replaced with the corresponding translating ones:

$$\begin{cases} v_t = \dfrac{D_{wh}\, \omega_m}{2\tau} \\[2ex] \dot{v}_t = \dfrac{D_{wh}\, \dot{\omega}_m}{2\tau} \\[2ex] F_t = \dfrac{T_m\, 2\tau}{D_{wh}} \\[2ex] x_t = \displaystyle\int_T v_t dt \end{cases} \qquad (6.1)$$

where τ is the overall transmission ratio, D_{wh} the rail wheel diameter, T_m the induction motor torque ω_m, the angular speed of motor axle and $\dot{\omega}_m$ the estimated acceleration of the motor axle.

The speed cycle considered for experimental tests is shown in Figure 6.1 a) and lasts $T=60$ s. The simulated vehicle starts from standstill, accelerates up to $v_t=$ 65 km/h (corresponding to a motor speed $\omega_m=1250$ rpm), cruises for about eleven seconds and brakes for sixteen seconds until it stops. The whole cycle has been simulated for one stop for a total covered distance of 570 m (see Figure 6.1 c)). During the starting phase ($\Delta t \cong 24$ s), the reference speed has been set to $v_{t,ref} = 65$ km/h and the vehicle linearly accelerates (see Figure 6.1 b)) with a maximum traction effort set to $F_{t,max}= 340$ N (corresponding to a motor torque $T_{m,max} = 47$ Nm), as shown in Figure 6.1 d).
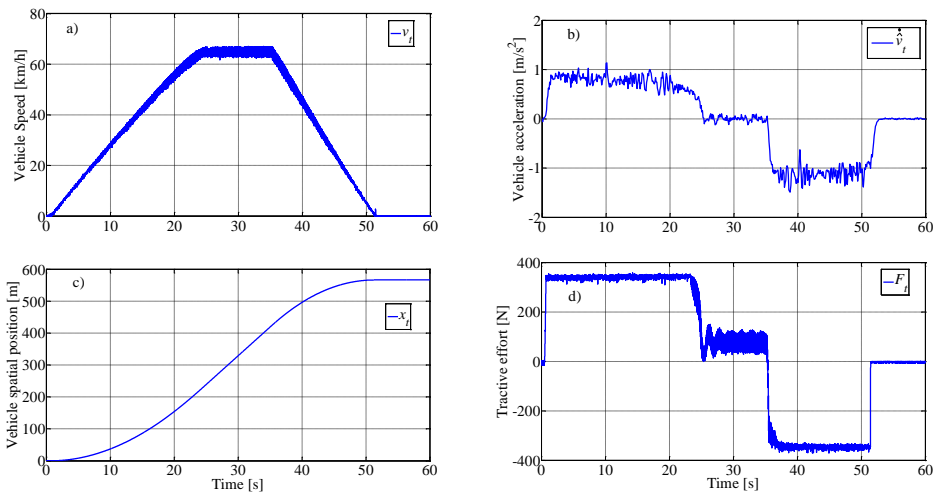
Figure 6.1 – On-board base case experimental results: a) Vehicle speed; b) Vehicle estimated acceleration; c) Total distance covered by the vehicle; d) Vehicle traction effort
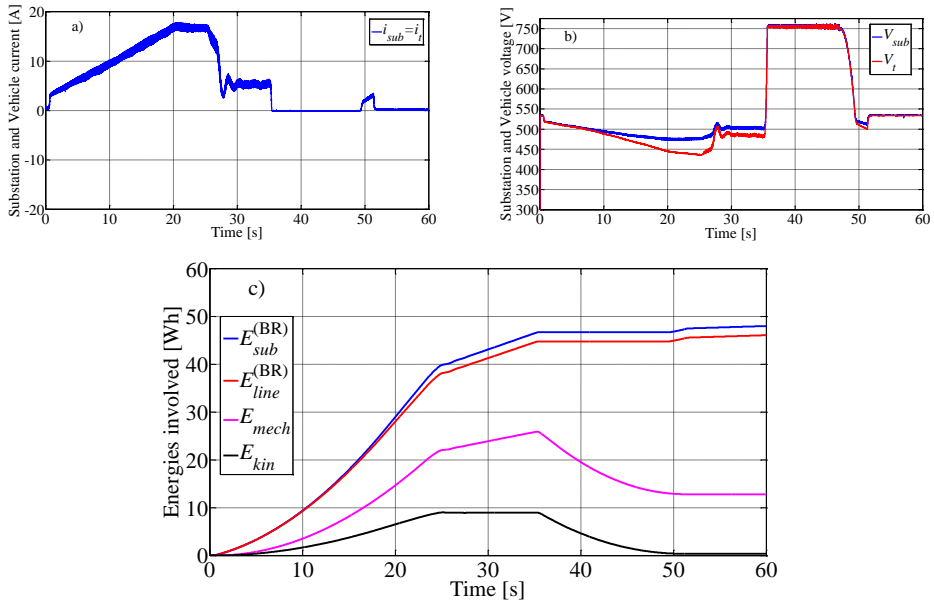
Figure 6.2 - On-board base case experimental results: a) Line and vehicle currents; b) Substation and vehicle voltages; c) Energies involved with dissipative braking

The higher the simulated vehicle speed, the higher is the mechanical power delivered to its wheels and, hence, the higher the current amplitude of the traction inverter. Since the ESS control is not active, the line current i_{sub} is equal to the vehicle current i_t, as shown in Figure 6.2 a), and increase up to the peak value $i_{sub,peak}^{(BR)} = 17$ A and the vehicle voltage, V_t, drops from 535 V to 460 V, therefore having a maximum voltage drop of $\Delta V_{t,max}^{(BR)} = 75$ V that occurs at $t = 24$ s (see Figure 6.2 b)). In the same time instant, the substation output voltage V_{sub} is equal to 494 V.

Then the steady-state speed is reached, the vehicle current drops to $i_t = 5.4$ A and the vehicle voltage increases up to $V_t = 492$ V. Both the line and vehicle current present several oscillation due to mechanical torque vibrations. After the cruise, the speed reference is set to zero and the vehicle brakes with a constant effort equal to $F_t = -348$ N; the speed linearly decreases until the vehicle stops. During the braking, the kinetic energy of the train is converted into electrical energy by the electrical traction drive. During the braking operation, since the AC/DC diode rectifier is unidirectional, the energy coming from the drive charges its DC-link capacitor, involving the increase of the vehicle voltage depicted in Figure 6.2 b).

259

Energy [Wh]	Acceleration (at t=24.8 s)	Cruise (at t=35.4 s)	Braking (at t=51.5 s)	Cycle
$E_{sub}^{(BR)}$	39.8	6.90	0.90	**47.8**
$E_{line}^{(BR)}$	38.1	6.68	0.82	**45.6**
E_{mech}	22.0	3.83	-13.0	**12.8**
E_{kin}	8.94	0.00	-8.94	**0.00**
E_{LiC}	-	-	-	**-**
$E_{loss}^{(BR)}$	17.8	3.07	14.1	**35.0**

Table 6.1 - Cycle energy and losses evaluation in experimental tests for the on-board case base without LiC ESS

$$
\begin{cases}
E_{sub}^{(BR)} = \int_T V_{sub} i_{sub} dt \\[2mm]
E_{line}^{(BR)} = \int_T \left(V_{sub} i_{sub} - R_{line} i_{sub}^2 \right) dt \\[2mm]
E_{mech} = \int_T T_m \omega_m dt \\[2mm]
E_{kin} = \int_T J_t \frac{d\omega_m}{dt} \omega_m dt \\[2mm]
E_{loss}^{(BR)} = E_{sub}^{(BR)} - \left(E_{mech} \right) \mathrm{sgn} \left(T_m \right)
\end{cases}
\tag{6.2}
$$

When the braking rheostat of the traction inverter is switched on, the vehicle voltage is limited to 750 V (dissipative braking).

The Figure 6.2 c) depicts the energies involved during the traction cycle, where as the table reports their numerical values. In particular, $E_{sub,}$ denotes the energy spuppled by the electrical substation, $E_{line,}$ evaluates the energy supplied by the catenary line, $E_{mech,}$ is the vehicle mechanical energy and E_{kin} is its kinetic energy. The total system losses $E_{loss,}$ are evaluated as the difference between the total input energy and the energy available at the vehicle's wheel. These losses collect the overall electrical and mechanical losses, (i.e. energy lost on the line resistance, friction losses etc…). However, by keeping in mind the Figure 5.1, the eq. (6.2) shows how the aforementioned energies have been evaluated, in

which the superscript "BR" refers to the energy values evaluated for this dissipative case base.

The energy diagrams depicted in Figure 6.2 c) are also summarized in Table 6.1. In the case of no ESS on-board, at the end of acceleration, the total input energy is $E_{sub}^{(BR)}$ = 39.8 Wh, whose 1.7 Wh are lost on the contact line. The delivered mechanical energy is E_{mech} = 22 Wh, whose E_{kin} = 8.94 Wh are stored as kinetic energy of the vehicle. The total losses are computed in 17.8 Wh. During cruising, the kinetic energy is constant. The energy supplied by the substation is equal to 6.9 Wh and covers the mechanical and electrical energy losses, equal to 3.07 Wh. At the end of braking, the train stops and the input energy is equal to 13.9 Wh, whose 13.0 Wh is the mechanical energy available by the vehicle and 0.90 Wh is supplied by the line. The total energy losses in this phase is 14.1 Wh that has been partially dissipated on the brakig rheostat $r_{BR,1.}$

At the end of the operating cycle, the total input energy is $E_{sub}^{(BR)}$ = 47.8 Wh, whereas the total losses results $E_{loss}^{(BR)}$ = 35.0 Wh. These values are taken as reference values for the further comparative analysis.

6.2 Base case study test results for stationary LiC ESS

The test bench configuration is reported in Figure 5.2, where the LiC ESS is again not connected. The quantities under investigation are the same of the previous case by making reference to the *j*-th subscript, which can be *1* or *2* for values belonging to the 1st ot the 2nd simulated railway vehicle.

The main parameters of the simulated railway vehicles and the related double track DC railway network under consideration are reported in the previous Table 5.1, Table 5.2, Table 5.3 and Table 5.4.

By bearing in mind eqs. (6.1), the speed cycles (see Figure 6.3 a)) simulated for the two vehicles are obviously mirrored and made up of one way running cycle. The operating cycle lasts again *T*= 60 s and 1st vehicle repeats the same cycle simulated for the previous case. Instead, the 2nd vehicle runs in the opposite direction with an imposed starting time displacement of 13 s, its operating speed cycle starts from standstill at *t*= 13 s, accelerates up to $v_{t,2}$= 62.5 km/h (corresponding to a motor speed $\omega_{m,2}$ = 1500 rpm), has a coasting phase of about 22 s and finally it stops at *t*= 55 s with resulting 10 s braking.
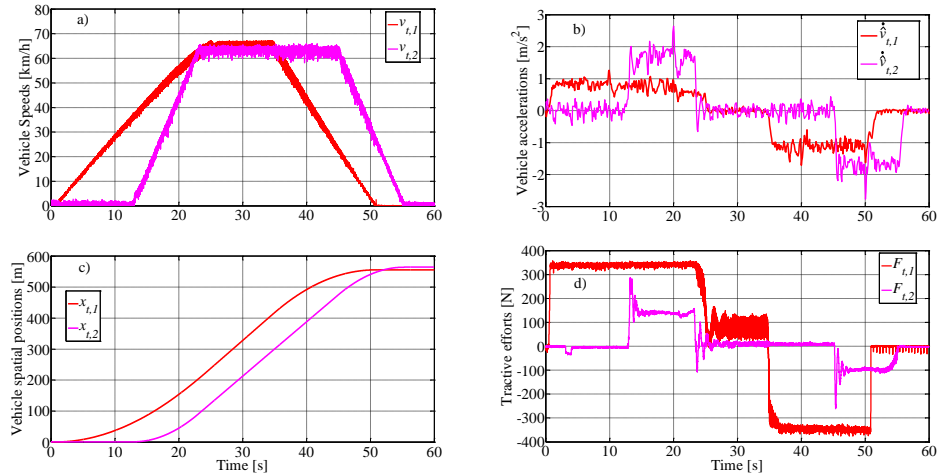
Figure 6.3 – Stationary base case experimental results: a) Vehicle speeds; b) Vehicle estimated accelerations; c) Total distance covered by the vehicles; d) Vehicle traction efforts

Its travelled spatial distance is 570 m. (see Figure 6.3 c)).

As clearly depicted in Figure 6.3 a), during the accelerations (see Figure 6.3 b)) the tration effort of the 2nd vehicle is set constant and equal about to $F_{t,2}=$ 140 N (corresponding to a motor torque $T_{m,2}=$ 20.2 Nm), whereas in the cruise phases this value is equal to about $F_{t,2}=$ 10 N ($T_{m,2}=$ 1.45 Nm). When the braking phases begin, the resulting braking effort is approximately equal to $F_{t,2}=$ -102 N ($T_{m,2}=$ -14.7 Nm).

In each cycle, the load current linearly increases during the acceleration, as well-known in variable speed drives and the peak current is obviously dependent on the maximum speed required. The line current i_{sub} is equal to the sum of the vehicle currents $i_{t,1} + i_{t,2}$, as shown in Figure 6.4 a), and increase up to the peak value $i_{sub,peak}^{(BR)}=$26.6 A when the current of the 2nd vehicle peaks ($i_{t,2}=$ 10 A) at $t=$ 23.3 s. During the overlapped cruise pheses of the two veichles the substation currnet is set consant and qual to $i_{sub}=$ 6.0 A, showing the compensating action of the regenerating currents.

The Figure 6.4 b), which displays the substation voltage, V_{sub}, the voltages at the pantograph of both the vehicles $V_{t,1}$ and $V_{t,2}$, and the endline voltage $V_{endline}$. The 2nd vehile voltage drop reaches its maximum value $\Delta V_{t,max}^{(BR)}=$115 V at $t=$ 23.3 s, whereas, in the same time instant, the substation output voltage V_{sub} is equal to $V_{sub}=$ 434 V and the endline voltage results $V_{endlinee}=$494 V.
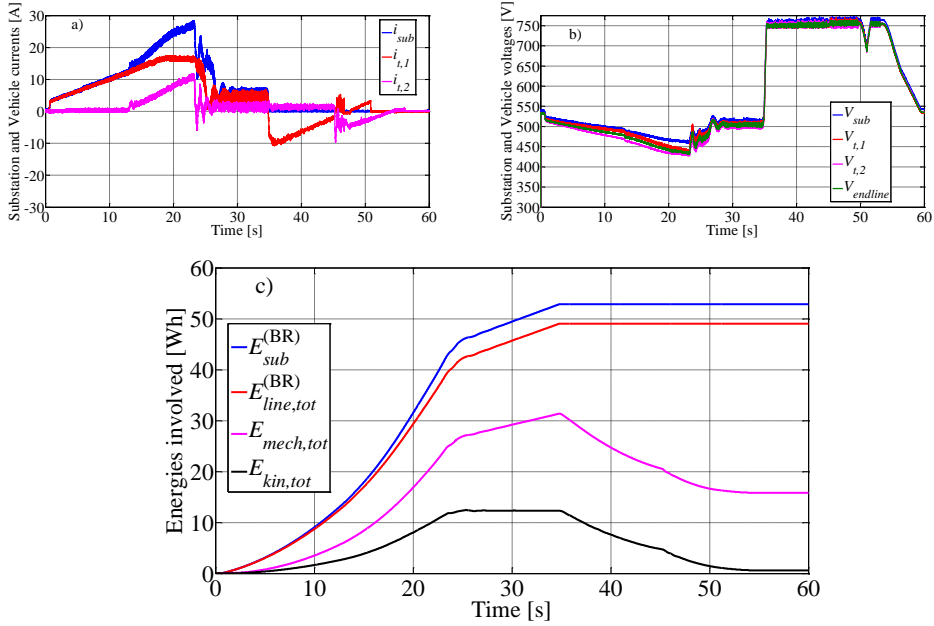
Figure 6.4 - Stationary base case experimental results: a) Line and vehicle currents; b) Substation, vehicles and endline voltages; c) Energies involved with dissipative braking

Furthermore, also the surge voltage during the braking results limited to 750 V because the regenerated energy is dissipated on the braking rheostat.

The Figure 6.4 c) finally show the energies involved,which are defined as reported in eq. (6.3) and summarized in Table 6.2.

$$
\begin{cases}
E_{sub}^{(BR)} = \int_T V_{sub} i_{sub} dt \\[2ex]
E_{line,tot}^{(BR)} = \int_T \left(V_{sub} i_{sub} - \frac{(V_{sub} - V_{t,1})^2}{R_{line,11}} - \frac{(V_{sub} - V_{t,2})^2}{R_{line,21}} - \frac{(V_{endline} - V_{t,1})^2}{R_{line,12}} - \frac{(V_{endline} - V_{t,2})^2}{R_{line,22}} \right) dt \\[2ex]
E_{mech,tot} = \int_T \left(T_{m,1}\omega_{m,1} + T_{m,2}\omega_{m,2} \right) dt \\[2ex]
E_{kin,tot} = \int_T \left[J_{t,1}\frac{d\omega_{m,1}}{dt}\omega_{m,1} + J_{t,2}\frac{d\omega_{m,2}}{dt}\omega_{m,2} \right] dt \\[2ex]
E_{loss}^{(BR)} = E_{sub}^{(BR)} - \left(E_{mech,tot} \right)\mathrm{sgn}\left(T_{m,1} + T_{m,2} \right)
\end{cases}
\tag{6.3}
$$

With reference to the speed cycles, in the case of regenerative braking, at the end of 1st vehicle acceleration ($t= 24.7$ s), the total input energy is $E_{sub}^{(BR)} =$ 45.4 Wh. The delivered global mechanical energy ($E_{mech,tot}$) is 26.6 Wh, whose

263

Energy [Wh]	Acceleration (at t=24.7 s)	Cruise (at t=34.7 s)	Braking (at t=55.3 s)	Cycle
$E_{sub}^{(BR)}$	45.4	7.40	0.10	**52.9**
$E_{line,tot}^{(BR)}$	41.8	7.20	0.00	**49.0**
$E_{mech,tot}$	26.6	4.70	-15.5	**15.8**
$E_{kin,tot}$	12.3	0.00	-12.3	**0.00**
E_{LiC}	-	-	-	**-**
$E_{loss}^{(BR)}$	18.8	2.70	15.6	**37.1**

Table 6.2 - Cycle energy and losses evaluation in experimental tests for the stationary case base without LiC ESS

12.3 Wh are stored as kinetic energy of the vehicles ($E_{kin,tot}$). The total losses are computed in $E_{loss}^{(BR)}$ = 18.8 Wh. At the end of the last braking (t= 55.3 s), both the vehicles stop and the input energy is equal to 15.6 Wh, whose 15.5 Wh is the global mechanical energy available by the vehicles and 0.10 Wh is supplied by the electrical substation. The total energy losses in this phase is 15.6 Wh and has been partially dissipated on the braking rheostats $r_{BR,1}$ and $r_{BR,2}$. From Figure 6.4 c), it is evident that the global electrical energy consumption in case of dissipative braking is 52.9 Wh. These values are taken as reference values for the further comparative analysis.

6.3 Case study test results for on-board LiC ESS with STC strategy

The test bench configuration is reported in Figure 5.1. The main parameters of the simulated railway vehicle and the supply line under consideration are reported in the previous Table 5.1, Table 5.3, Table 5.4 and Table 5.5.

The STC strategy has been implemented on the basis of how said in the par. 5.3.1 with reference to one simulated vehicle and the main control parameters are reported in the Table 5.6.

The performed tests evaluate the contribution of LiC during accelerations of the vehicle and their recovering capability during braking operations by implementing the STC strategy.
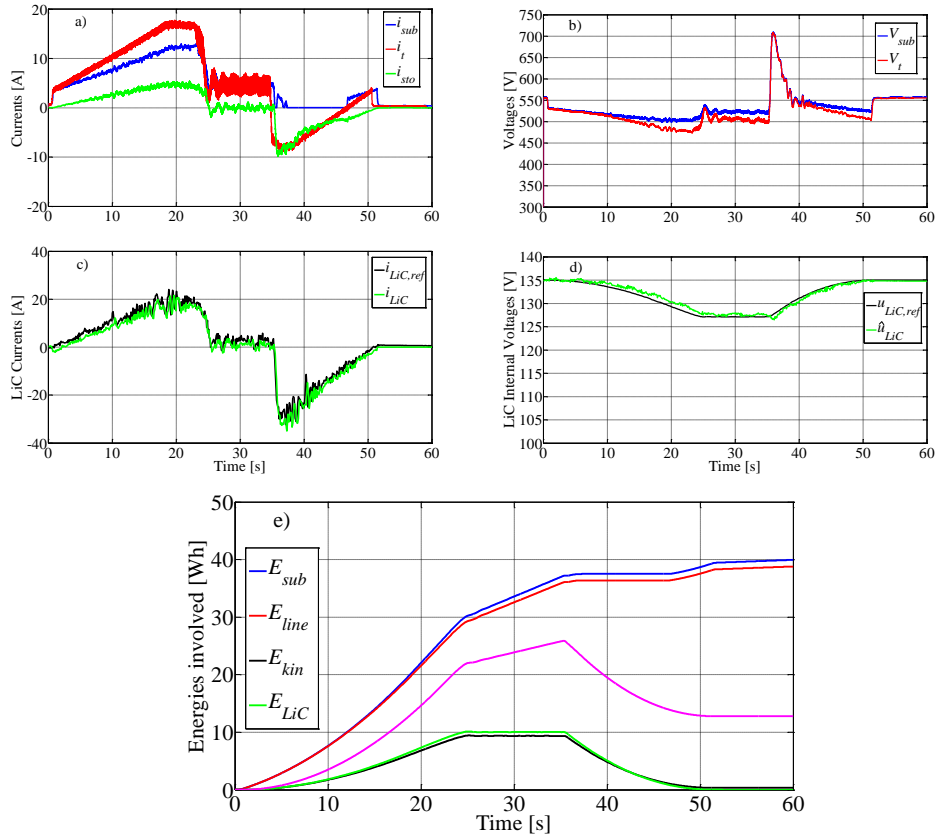
Figure 6.5 - On-board LiC ESS with STC strategy case study experimental results: a) Line, vehicle and storage currents; b) Substation and vehicle voltages; c) LiC actual current and its reference; d) LiC internal estimated voltage and its reference; e) Energies involved in the traction cycle

The speed cycle of the vehicle, as well as the mechanical quantities and the vehicle current, are the same of the ones simulated in the par. 6.1 and are depicted in the Figure 6.1 and Figure 6.2 a).

The LiC are pre-charged to $V_{LiC,max}$= 135 V. The behavior of the traction drive equipped with LiC is evident from the compared analysis of Figure 6.5 a) and Figure 6.5 c). In particular, this last one shows that LiC reference current, $i_{LiC,ref}$, change in sign according to vehicle acceleration. In fact, actual LiC current, , $i_{LiC,ref}$ reaches its maximum of 19.5 A at the maximum speed and falls to zero at the end of the acceleration. During the braking, a similar behavior can be observed with the opposite current sign whose maximum results -33.6 A. The LiC current is reflected in the current supplied by the substation and that drawn by the dc-bus of the traction vehicle, i_t, shown in Figure 6.5 a). The "peak

shaving" action due to the contribution of LiC is highlighted by the diagram of the substation current, i_{sub}, that in correspondence of $t=$ 24 s, presents a peak equal to $i_{sub,peak}=$ 12.4 A, significantly smoothed respect to one of the vehicle current, which is obviously the same as for the case of dissipative braking ($i_{sub,peak}^{(BR)}=$17 A), with consequent current peak reduction by 27.1 %.

The Figure 6.5 d) shows how LiC speed tracker control is capable of tracking quickly the LiC reference internal voltage, $u_{LiC,ref}$, calculated according to the actual vehicle speed eq. (5.3). In agreement with the suggested control strategy, LiC reach the minimum voltage of 127 V when the simulated vehicle travels at the maximum speed.

During the braking, the kinetic energy is converted into electrical energy by the electrical traction drive, as it can be seen since i_t is negative. In this phase, the LiC ESS stores the electrical energy available and is recharged to its initial SoC value since the LiC internal voltage reference is directly related to the actual vehicle kinetic energy E_{kin}, as it is evident from Figure 6.5 e). This effect can be also highlighted in Figure 6.5 d) by the increasing of LiC voltage when the braking starts.

As it is evident from the figure, the agreement between estimated ($\hat{u}_{LiC}$) and reference LiC voltage is very good for all the cycle, confirming the effectiveness of the STC proposed.

The impact of the ESS on the simulated railway DC electrified line is shown in Figure 6.5 b). The voltage drop on the line, which occurs at $t=$ 24 s, is significantly reduced ($\Delta V_{t,\max}=$52 V respect to the no-load substation voltage $V_{sub,0}=$ 535 V) by the presence of LiC for the whole duration of the acceleration. Moreover, also the surge voltage during the braking is strongly reduced because the regenerated energy is stored in LiC.

The previous comments are supported by the diagram of the energies involved in the experimental test, reported in Figure 6.5 e) and summarized in Table 6.3.

It has to be remarked that the energies evaluated by eq. (6.2) have to be re-defined due to the presence of the on-board storage unit, which stores an energy denoted with E_{LiC} (6.4).

$$
\begin{cases}
E_{sub} = \displaystyle\int_T V_{sub} i_{sub} dt \\[3ex]
E_{line} = \displaystyle\int_T \left(V_{sub} i_{sub} - R_{line} i_{sub}^2 \right) dt \\[3ex]
E_{mech} = \displaystyle\int_T T_m \omega_m dt \\[3ex]
E_{kin} = \displaystyle\int_T J_t \frac{d\omega_m}{dt} \omega_m dt \\[3ex]
E_{LiC} = \displaystyle\int_T \hat{u}_{LiC} i_{LiC} dt \\[3ex]
E_{loss} = E_{sub} - \left(E_{mech} \right) \operatorname{sgn}\left(T_m \right) + \left(E_{LiC} \right) \operatorname{sgn}\left(T_m \right)
\end{cases}
\tag{6.4}
$$

The mechanical and kinetic energies are the same as the base case seen in par. 6.1. With reference to the acceleration phase, the total input energy is 40.26 Wh, whose 9.96 Wh have been supplied by LiC and 30.3 Wh by the supply substation. and are equal to is 23.8 Wh. The total losses are computed in 18.3 Wh. During the cruise phase, the kinetic energy and the energy stored in LiC are both constant and the energy supplied by the substation is equal to 7.2 Wh, which covers the line losses and the mechanical energy delivered to the vehicle, equal to 0.50 Wh and 3.83 Wh respectively.

At the end of the regenerative braking, the vehicle stops and the input energy is equal to 15.4 Wh, whose 13.0 Wh is the mechanical energy available by the vehicle and 2.40 Wh is supplied by the substation.

Energy [Wh]	Acceleration (at t=24.8 s)	Cruise (at t=35.4 s)	Braking (at t=51.5 s)	Cycle
E_{sub}	30.3	7.20	2.40	**39.9**
E_{line}	29.3	6.80	2.20	**38.3**
E_{mech}	22.0	3.83	-13.0	**12.8**
E_{kin}	8.94	0.00	-8.94	**0.00**
E_{LiC}	9.96	0.00	-9.96	**0.00**
E_{loss}	18.3	3.37	5.44	**27.1**

Table 6.3 - Cycle energy and losses evaluation in experimental tests for the on-board LiC ESS case study with STC strategy

The energy actually stored in the LiC is equal to 9.96 Wh which implies that they are re-charged up to their starting voltage. The total energy losses in this phase is 5.44 Wh. At the end of the operating cycle, the total input energy is E_{sub} = 39.9 Wh, whereas the total losses results E_{loss} = 27.1 Wh and it is evident that the comparison with the corresponding dissipative case (par. 6.1) shows that the total energy losses are decreased with consequent energy saving of about 16.5 %.

It is worth to be noted that the design of the simulator and the storage device has not been optimized for this specific traction cycle. Therefore, the energy saved can be further improved in a real system when the design of each device is oriented on the basis of the specific application.

6.4   Case study test results for stationary LiC ESS with STC strategy

The test bench configuration is reported in Figure 5.2. The main parameters of the simulated railway vehicle and the supply line under consideration are reported in the previous Table 5.1, Table 5.2, Table 5.3, Table 5.4 and Table 5.5. The stationary STC strategy has been implemented on the basis of how said in the par. 5.3.1 and the main control parameters are reported in the Table 5.6.

The speed cycle of the vehicles, as well as the mechanical quantities and the vehicle currents, are the same of the ones simulated in the par. 6.2 and are depicted in the Figure 6.3 and Figure 6.4 a).

The improvement due to the installation of stationary LiC ESS for the whole simulated transit system is evident from Figure 6.6 a), , in which is reported the sum $i_{t,1}$+ $i_{t,2}$ of both the vehicle currents, for simplicity of analysis. The LiC module is even pre-charged to 135 V, as portrayed in Figure 6.6 d). With reference to the time instant t= 23.3 s, where the sum of the vehicles current reaches its peak value of $i_{sub,peak}^{(BR)}$ =26.6 A, the storage current, i_{sto}, increases up to about 8.1 A, limiting the peak of line current, i_{sub}, to the value $i_{sub,peak}$= 18.5 A.. The "peak shaving" action provided by the LiC ESS is therefore evident in the same time, since the presence of LiC storage reduces the substation current peak of 30.4 %. During the braking phases, the kinetic energies are converted into
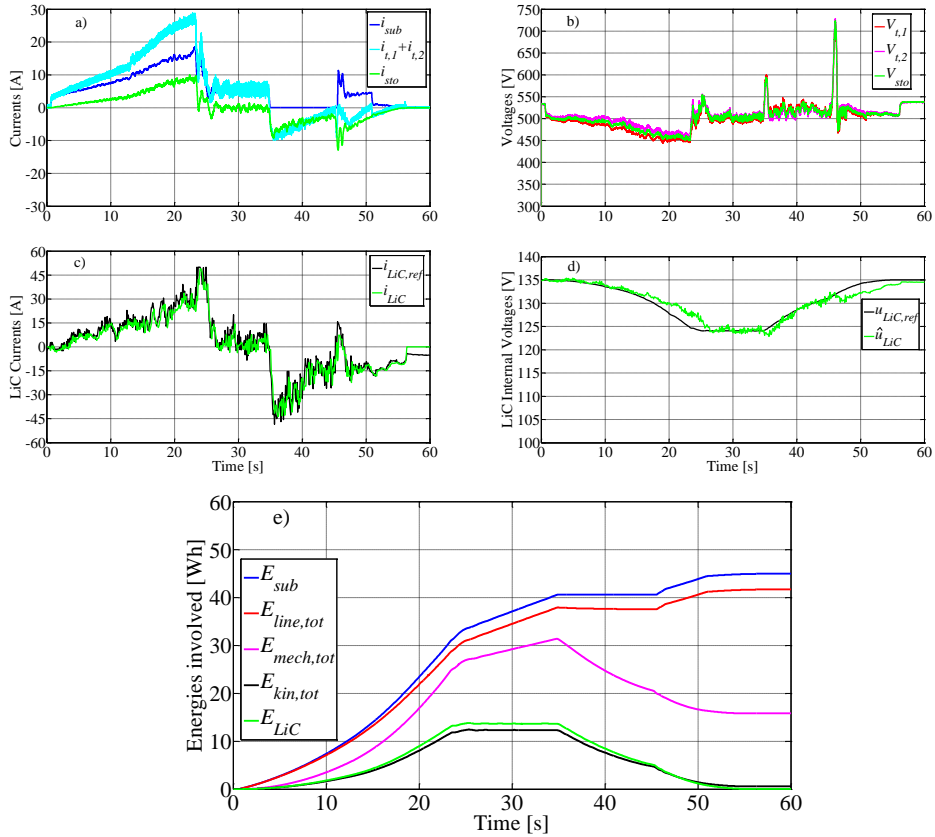
Figure 6.6 - Stationary LiC ESS with STC strategy case study experimental results: a) Substation, vehicles and storage currents; b) Substation, vehicles and storage voltages; c) LiC actual current and its reference; d) LiC internal estimated voltage and its reference; e) Energies involved in the traction cycles

electrical energy by the electrical traction drives, as it can be seen as long as $i_{t,1} + i_{t,2}$ is negative; more specifically the maximum regenerated vehicle current occurs when the 1st vehicle begin to brake ($t= 34.7$ s). In this time i_{sto} reaches the maximum regenerating current equal to about 9.80 A.

The line voltage drops smoothing action carried out by the stationary LiC ESS, is clearly highlighted in Figure 6.6 b), which displays the line voltages of both the vehicles $V_{t,1}$ and $V_{t,2}$, as well as the storage voltage V_{sto}, at the line point where the ESS is placed. The impact of the storage system on the main electrical substation is shown by the decreasing of the 1st line voltage drop ($\Delta V_{t,\max}$ =79 V at $t= 23.3$ s) compared to the case of total dissipative electrical braking on the ballast resistor, where the same line voltage drop reached about 21.5 % of the line no-load voltage ($V_{sub,0}$= 535 V). Furthermore, also the overvoltage during

269

the braking phases is excellently reduced because the regenerated energy is stored in the ESS.

The Figure 6.6 c) shows the LiC equivalent module current, i_{LiC} , which during the acceleration phases reaches its peak value (48 A). Instead, Figure 6.6 d) reports the LiC module internal voltage reference, $u_{LiC,ref}$, and the corresponding estimated value, $\hat{u}_{LiC}$, evaluated on the basis of (5.3). As it is evident from the figure, the stationary STC strategy leads to a good agreement between estimated and reference internal LiC voltage for all the cycle. According to this proposed control strategy, the LiC device reach the minimum voltage of 123 V when the vehicle travel at the maximum speeds. Moreover the control of the DC-DC converter discharges LiC and is capable of maintaining the SoC between the voltage rated value ($V_{LiC,max}$= 135 V) and the actual one, tracking the actual speeds of the vehicles.

The set-point current, $i_{LiC,ref}$ increases faster when the set-point speed is higher, because more power is needed for the vehicles acceleration. This means that the contribution of LiC is linked to the power requirements of the mechanical drives, limiting effectively the power drawn by the power supply. The previous statement is supported by the diagram of the energies involved in the experimental test, reported in Figure 6.6 c) and summarized in Table 6.4.

It has to be remarked that the energies evaluated by eq. (6.3) have to be re-defined (6.5) due to the presence of the stationary storage unit.

$$
\begin{cases}
E_{sub} = \int_T V_{sub} i_{sub} dt \\[2mm]
E_{line,tot} = \int_T \left(V_{sub} i_{sub} - \dfrac{(V_{sub} - V_{t,1})^2}{R_{line,11}} - \dfrac{(V_{sub} - V_{t,2})^2}{R_{line,21}} - \dfrac{(V_{sto} - V_{t,1})^2}{R_{line,12}} - \dfrac{(V_{sto} - V_{t,2})^2}{R_{line,22}} \right) dt \\[2mm]
E_{mech,tot} = \int_T \left(T_{m,1} \omega_{m,1} + T_{m,2} \omega_{m,2} \right) dt \\[2mm]
E_{kin,tot} = \int_T \left[J_{t,1} \dfrac{d\omega_{m,1}}{dt} \omega_{m,1} + J_{t,2} \dfrac{d\omega_{m,2}}{dt} \omega_{m,2} \right] dt \\[2mm]
E_{LiC} = \int_T \hat{u}_{LiC} i_{LiC} dt \\[2mm]
E_{loss}^{(BR)} = E_{sub}^{(BR)} - \left(E_{mech,tot} \right) \operatorname{sgn}\left(T_{m,1} + T_{m,2} \right) + \left(E_{LiC} \right) \operatorname{sgn}\left(T_{m,1} + T_{m,2} \right)
\end{cases} \tag{6.5}
$$

Energy [Wh]	Acceleration (at $t=24.7$ s)	Cruise (at $t=34.7$ s)	Braking (at $t=55.3$ s)	Cycle
E_{sub}	33.3	7.30	4.40	**45.0**
$E_{line,tot}$	30.7	7.10	3.80	**41.7**
$E_{mech,tot}$	26.6	4.70	-15.5	**15.8**
$E_{kin,tot}$	12.3	0.00	-12.3	**0.00**
E_{LiC}	13.4	0.00	-13.4	**0.00**
E_{loss}	20.1	2.60	6.50	**29.2**

Table 6.4 - Cycle energy and losses evaluation in experimental tests for the stationary LiC ESS case study with STC strategy

With reference to the speed cycles, in the case of regenerative braking, at the end of 1st vehicle acceleration ($t=$ 24.7 s), the total input energy is 46.7 Wh, whose 13.4 Wh have been supplied by LiC (E_{LiC}) and 33.3 Wh by the electrical substation (E_{sub}). The delivered global mechanical energy ($E_{mech,tot}$) is 26.6 Wh, whose 12.3 Wh are stored as global kinetic energy of the vehicles ($E_{kin,tot}$). The total losses are computed in 20.1 Wh. At the end of the 2nd vehicle braking phase ($t=$ 55.3 s), both the vehicles stop and the input energy is equal to 19.9 Wh, whose 15.5 Wh is the global mechanical energy available by the vehicles and 4.40 Wh is supplied by the electrical substation. The energy actually stored in the LiC module is equal to 13.4 Wh which implies that they are re-charged up to their starting voltage. The total energy losses in this phase is 6.50 Wh. From Figure 6.6 e), it is evident that the global electrical energy consumption in case of stationary LiC ESS is 45.0 Wh and the comparison with the corrensponding case base in par. 6.2 shows that the total energy losses are decreased with consequent energy saving of about 14.9 %.

6.5 Case study test results for on-board LiC ESS with LVTC strategy

The test bench configuration is reported in Figure 5.1. The main parameters of the simulated railway vehicle and the supply line under consideration are reported in the previous Table 5.1, Table 5.3, Table 5.4 and Table 5.5.
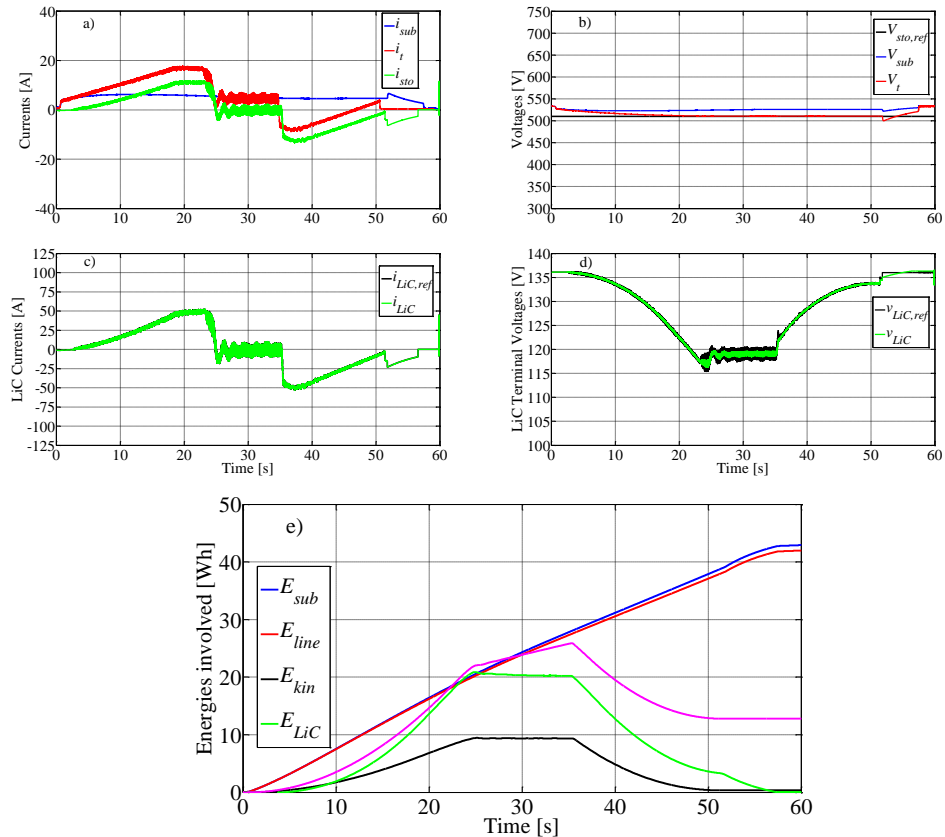
Figure 6.7 - On-board LiC ESS with LVTC strategy case study experimental results assuming $V_{sto,ref}$ = 510 V: a) Line, vehicle and storage currents; b) Substation, vehicle and storage reference voltages; c) LiC actual current and its reference; d) LiC voltage and its reference; e) Energies involved in the traction cycle

The on-board LVTC strategy has been implemented on the basis of how said in the par. 5.3.2 with reference to one simulated vehicle and the main control parameters are reported in the Table 5.7.

Since the ESS in installed on-board, the line voltage reference $V_{line,ref}$ becomes the storage voltage reference $V_{sto,ref}$. The actual storage voltage V_{sto} is in turn equal to the vehicle voltage at the pantograph V_t. Essentially, when the vehicle voltage rises, the LVTC is designed to bring it to the reference value $V_{sto,ref}$ by storing the energy in the ESS. Converserly, when V_t drops below the reference value, the control swithches the LiC ESS to support the line voltage.

By setting $V_{sto,ref}$ = **510 V**, the LVTC behaviour is well described in the Figure 6.7 a) and Figure 6.7 b). During the accelerating phase, the line voltage is well regulated by the discharging operation of the LiC (see Figure 6.7 d)) and

272
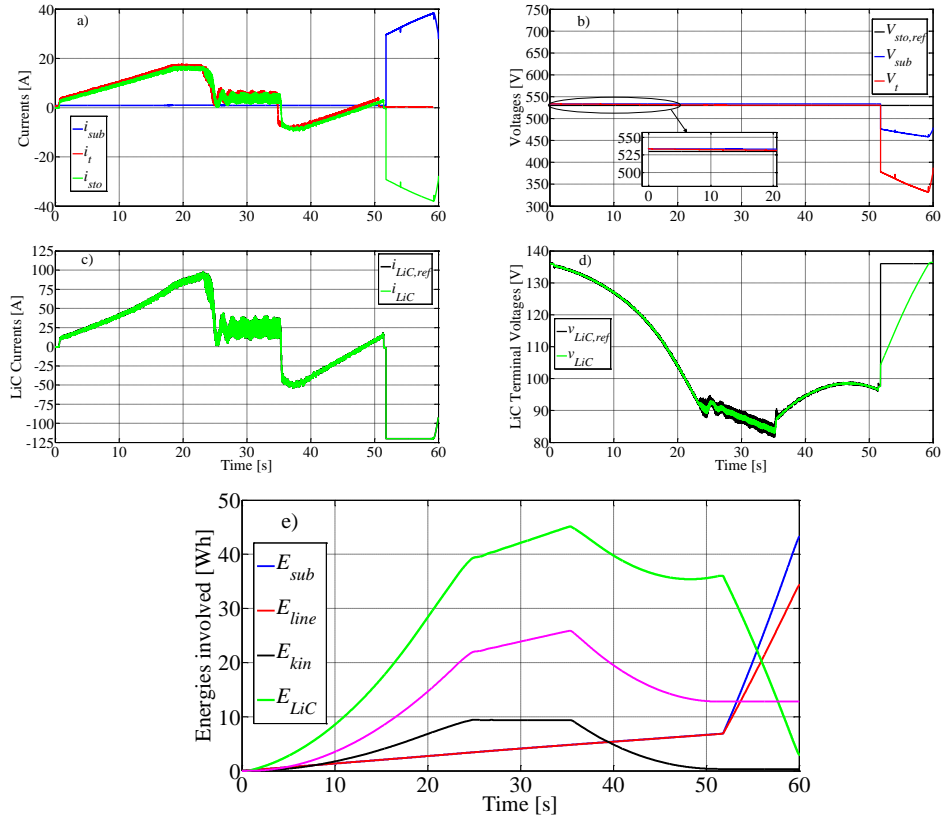
Figure 6.8 - On-board LiC ESS with LVTC strategy case study experimental results assuming $V_{sto,ref}$ = 530 V: a) Line, vehicle and storage currents; b) Substation, vehicle and storage reference voltages; c) LiC actual current and its reference; d) LiC voltage and its reference; e) Energies involved in the traction cycle

the maximum voltage drop on the line, which occurs at t= 52 s, is strongly reduced ($\Delta V_{t,max}$ =36 V respect to the no-load substation voltage $V_{sub,0}$ = 535 V), thus enhancing the acceleration characteristics. When the vehicle is cruising, the LiC ESS results in stand-by mode.

This maximum voltage drop is, however, not linked to vehicle operation, but rather is due to the LiC charge at maximum current limit, $i_{LiC,max}$ (see Figure 6.7 c)) in order to return the ESS to its initial SoC for correctly performing the further energy comparisons. This is due to the fact that for this control strategy, the actual LiC SoC is not related to the actual vehicle kinetic energy.

The same performance can be obtained during the braking phase (t= 36 ÷ 52 s) and the line voltage is regulated by the charging operation of the LiC, avoiding the intervention of the braking rheostat, without any line overvoltage.
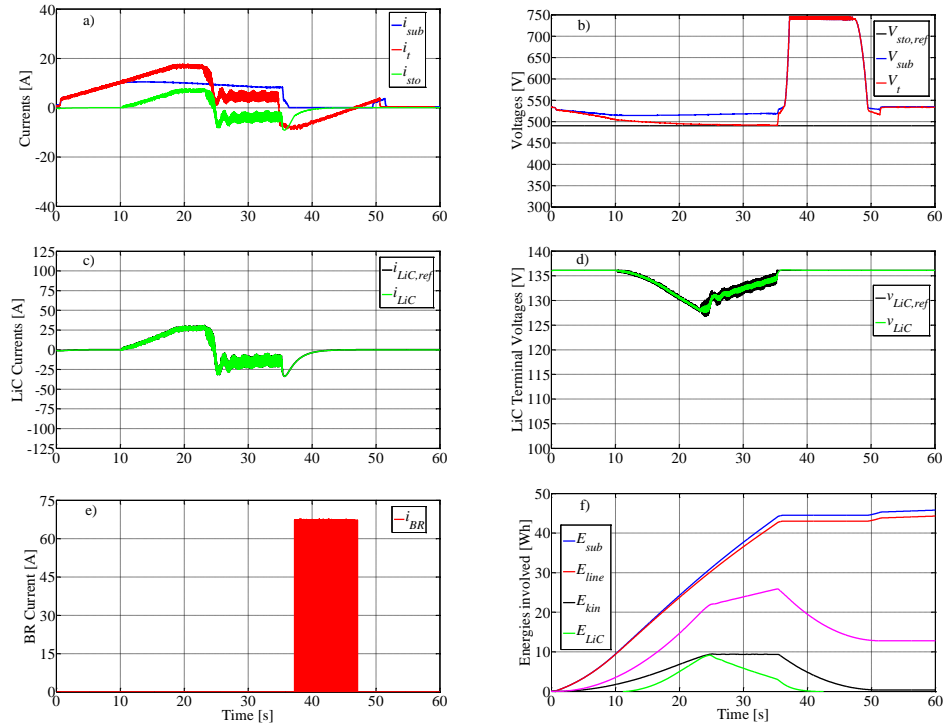
Figure 6.9 - On-board LiC ESS with LVTC strategy case study experimental results assuming $V_{sto,ref}$ = 490 V: a) Line, vehicle and storage currents; b) Substation, vehicle and storage reference voltages; c) LiC actual current and its reference; d) LiC voltage and its reference; e) Current in the braking rheostat; f) Energies involved in the traction cycle

Besides, the vehicle line voltage regulation has improving effects also on the line current, i_{sub}, (see Figure 6.7 a)) which presents a peak equal to $i_{sub,peak}$= 6.6 A occurring at t= 52 s, significantly smoothed respect to one of the vehicle current (17 A).

The behaviour of the LiC measured values, v_{LiC}, (see Figure 6.7 d)) respect to its reference, $v_{LiC,ref}$, shows that the inner LiC voltage control loop represented by the PI controller Reg_u in the eq. (4.45) works good tracking satisfactorily the LiC voltage reference.

Finally in the Figure 6.7 e) are portrayed the energies involved (6.4) during the traction cycle, by bearing in mind that the LiC stored energy, E_{LiC} , has been evaluated by using the LiC measured voltage, v_{LiC}, instead of the internal one. The same energy contributions are also summarized in the Table 6.5 together with their values computed with respect to other reference values of $V_{sto,ref}$ as it will be explained later.

Energy [Wh]		Acceleration (at $t=24.8$ s)	Cruise (at $t=35.4$ s)	Braking (at $t=51.5$ s)	Cycle
E_{sub}	$V_{sto,ref}=530$ V	3.40	1.40	2.05	**43.3**
	$V_{sto,ref}=510$ V	20.5	7.40	10.7	**42.9**
	$V_{sto,ref}=490$ V	31.2	13.0	1.10	**45.7**
E_{line}	$V_{sto,ref}=530$ V	3.40	1.40	2.05	**34.3**
	$V_{sto,ref}=510$ V	20.2	7.20	10.3	**41.0**
	$V_{sto,ref}=490$ V	30.4	12.3	1.10	**44.3**
E_{mech}		22.0	3.83	-13.0	**12.8**
E_{kin}		8.94	0.00	-8.94	**0.00**
E_{LiC}	$V_{sto,ref}=530$ V	39.4	5.70	-9.10	**2.60**
	$V_{sto,ref}=510$ V	20.9	-0.70	-16.8	**0.00**
	$V_{sto,ref}=490$ V	9.11	-6.18	-2.93	**0.00**
E_{loss}	$V_{sto,ref}=530$ V	20.8	3.27	5.95	**33.1**
	$V_{sto,ref}=510$ V	19.4	2.87	6.90	**30.1**
	$V_{sto,ref}=490$ V	18.3	2.99	11.2	**32.9**

Table 6.5 - Cycle energy and losses evaluation in experimental tests for the on-board LiC ESS case study with LVTC strategy according to several values of $V_{sto,ref}$

It is evident that the total consumed energy profiles during the cycle is $E_{sub} = 42.9$ Wh, whereas the total losses result in $E_{sub} = 30.1$ Wh. By comparing to the base case of par. 6.1, the 10.2 % energy is saved.

The Figure 6.8 display the same quantities previously analyzed, by selecting $V_{sto,ref} = 530$ V. It is immediate to see that by choosing the line voltage reference close to $V_{sub,0}$, the LiC is discharged almost completely (up to $v_{LiC}= 83$ V), keeping V_{sto} near to the value of about 530 V until the vehicle stops. As soon as the vehicle is idle, since the energy recovered during braking was not sufficient to bring the LiC at the initial SoC, it had been necessary a constant charging at the maximum allowable current. For this reason both the maximum voltage drop and the the supply current peak, occurs for $t = 59$ s and they are $\Delta V_{t,\max}=202$ V and $i_{sub,peak}= 38.2$ A respectively. Consequently, the choice $V_{sto,ref} = 530$ V gives higher total energy supplied by the substation and more total losses, which are equal to $E_{sub}= 43.3$ Wh and $E_{loss}= 33.1$ Wh, as reported in the Table 6.5.

A different behavior occurs if it is set a lower line voltage reference, i.e. $V_{sto,ref}$ = **490 V**. In fact, by looking at the Figure 6.9, according to this choice the LiC discharges less (up to v_{LiC}= 128 V) and reaches it is initial SoC before completion of the braking phase, which involves the intervention of the braking rheostat for t= 37.2 s (see Figure 6.9 e)). However, apart from the consequent surge voltage, the line voltage results close to the reference value, and reaches the maximum voltage drop $\Delta V_{t,\max}$ =44 V at t= 35.4 s. Instead, the substation current peak occurs at t= 10.4 s and is equal to $i_{sub,peak}$= 10.4 A. By keeping in mind again the Table 6.5, in this case we have the highest value of total energy spent during the cycle (E_{sub}= 45.7 Wh).

6.6 Case study test results for stationary LiC ESS with LVTC strategy

The test bench configuration is reported in Figure 5.2. The main parameters of the simulated railway vehicle and the supply line under consideration are reported in the previous Table 5.1, Table 5.2, Table 5.3, Table 5.4 and Table 5.5. The stationary LVTC strategy has been implemented on the basis of how said in the par. 5.3.2 and the main control parameters are reported in the Table 5.7.

The LiC ESS placed at the end of the double track electrified line ($V_{line,ref}$ = $V_{sto,ref}$), tends to act as a line voltage stabilizer, by discharging when the system voltage falls below the specified reference value, or by absorbing the energy regenerated by braking vehicles which leads to a rise in the line voltage. The limited fluctuations of the line voltage can extend the existing vehicle mechanical performances and enhance the maximum traction motor torque ability at the same speed.

By selecting $V_{sto,ref}$ = **510 V**, the LVTC line voltage regulation action is highlighted in the Figure 6.7 a) and Figure 6.7 b). The storage voltage, V_{sto}, in fact always remains close to its reference value even when occurs the simultaneous acceleration by two simulated vehicles. When V_{sto} falls below the reference value, the LiC ESS starts discharge (see Figure 6.7 d)) and the LVTC stabilization action is shown by the decreasing of the 1st line voltage drop ($\Delta V_{t,\max}$ =63 V at t= 23.3 s respect to the no-load substation voltage $V_{sub,0}$ = 535 V) with consequent reduction of the substation current peak at the same time
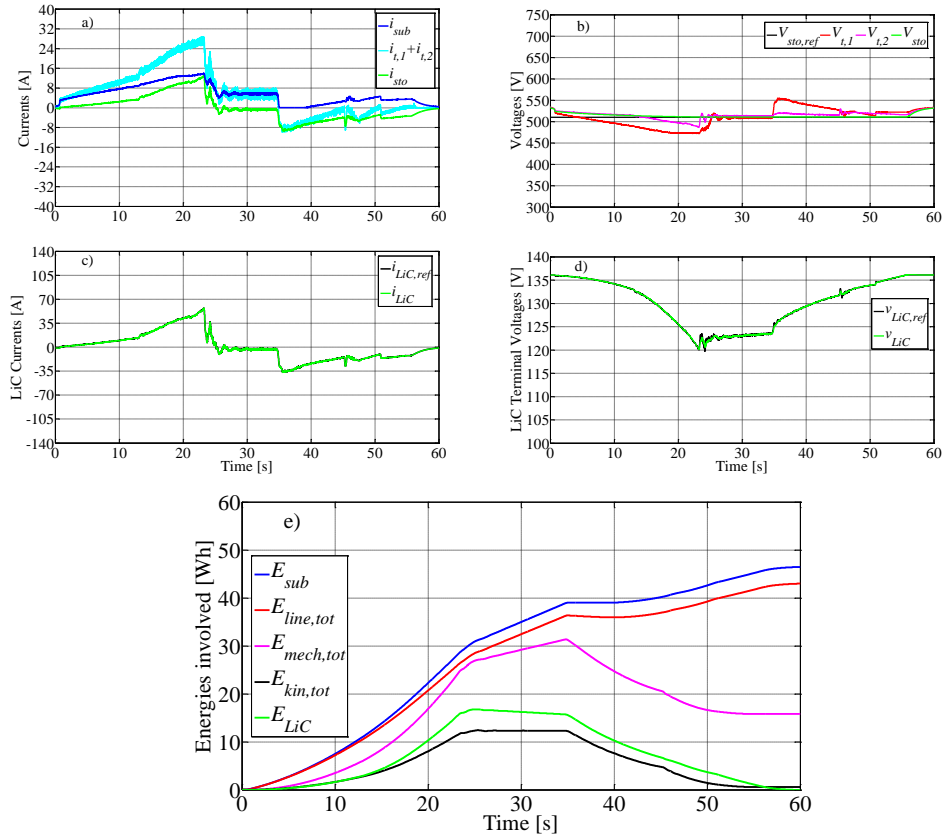
Figure 6.10 - Stationary LiC ESS with with LVTC strategy case study experimental results assuming $V_{sto,ref}$ = 510 V: a) Substation, vehicles and storage currents; b) Substation, vehicles, actual storage and its reference voltages; c) LiC actual current and its reference; d) LiC voltage and its reference; e) Energies involved in the traction cycles

instant resulting equal to $i_{sub,peak}$= 13.9 A.

As soon as the simultaneous accelerating by the two vehicles comes to an end, the line voltages begin to rise and the ESS is recharged, either from the substation or by the regenerating vehicles, without any intervention of the braking rheostat. By looking at figure and table the energy supplied by the substation is reduced significantly (E_{sub} = 46.8 Wh) respect to the case base without ESS ($E_{sub}^{(BR)}$ = 47.8 Wh).
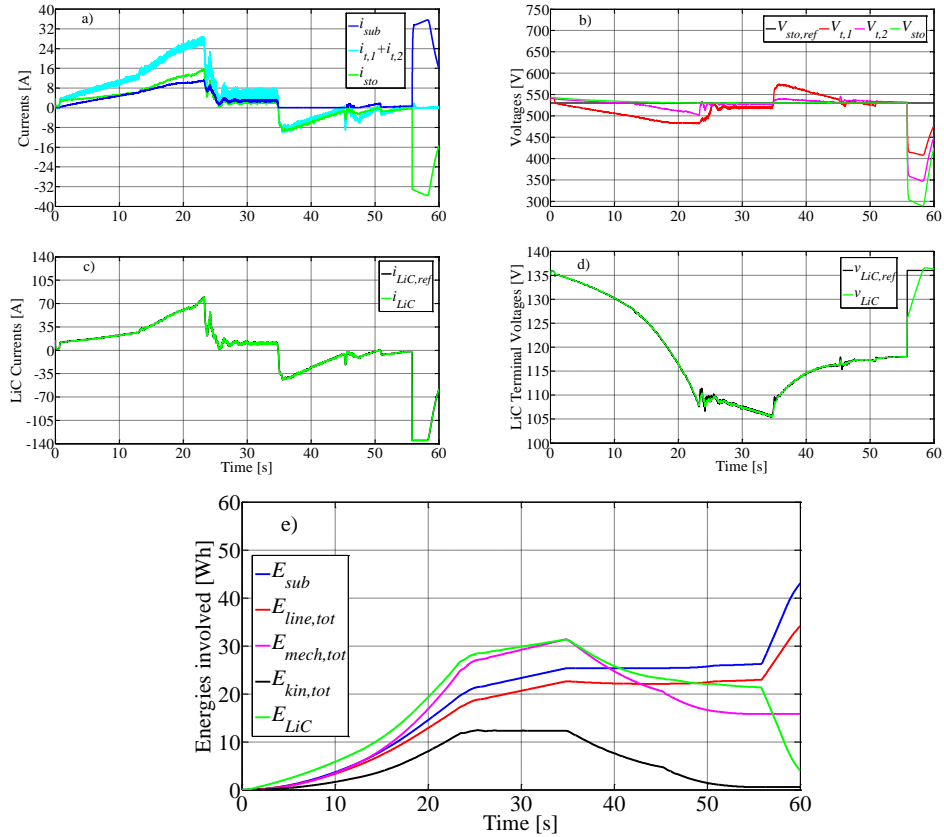
Figure 6.11 - Stationary LiC ESS with with LVTC strategy case study experimental results assuming $V_{sto,ref}$ = 530 V: a) Substation, vehicles and storage currents; b) Substation, vehicles, actual storage and its reference voltages; c) LiC actual current and its reference; d) LiC voltage and its reference; e) Energies involved in the traction cycles

The Figure 6.11 and Figure 6.12 display the test results and the same quantities previously analyzed, by selecting $V_{sto,ref}$ = **530** V and $V_{sto,ref}$ = **490** V, respectively. The results show how the choice of the reference value affects the performance of LVTC. A reference value close to the line no-load voltage (535 V) leads to an additional LiC quick charging phase delivered by the main substation with a consequent increase in system losses. A reference value too low makes the supply line "less receptive" thus implying the turn-on of the braking rheostats.
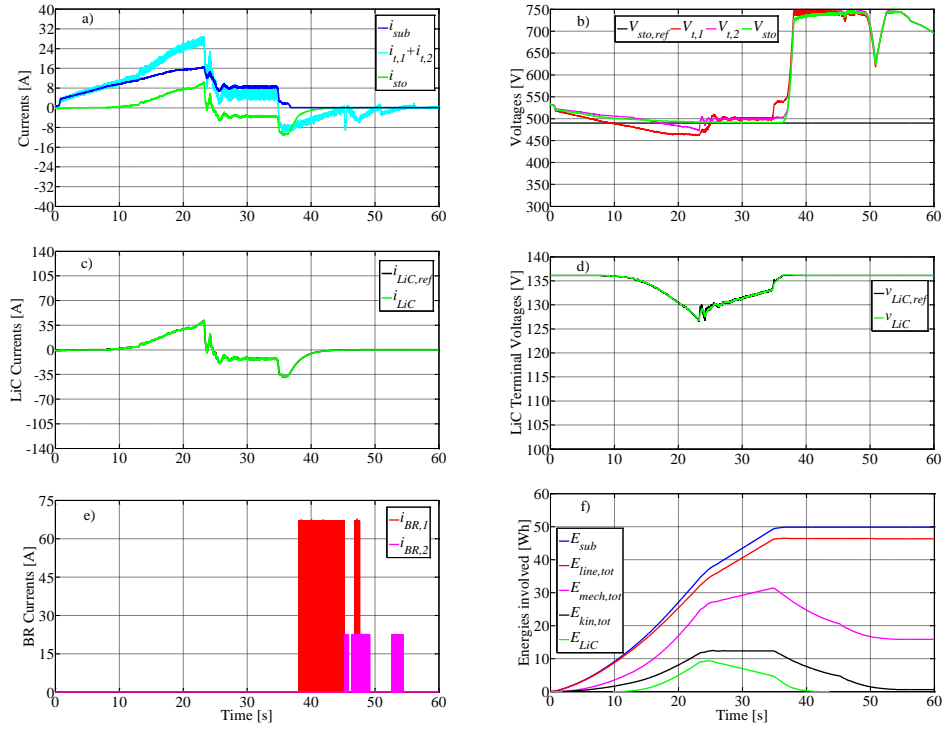
Figure 6.12 - Stationary LiC ESS with with LVTC strategy case study experimental results assuming $V_{sto,ref}$ = 490 V: a) Substation, vehicles and storage currents; b) Substation, vehicles, actual storage and its reference voltages; c) LiC actual current and its reference; d) LiC voltage and its reference; e) Currents in the braking rheostats; f) Energies involved in the traction cycles

Energy [Wh]		Acceleration (at t=24.7 s)	Cruise (at t=34.7 s)	Braking (at t=55.3 s)	Cycle
E_{sub}	$V_{sto,ref}$ = 530 V	21.1	4.20	0.90	**43.0**
	$V_{sto,ref}$ **= 510 V**	30.6	8.30	6.40	**46.8**
	$V_{sto,ref}$ = 490 V	37.1	12.1	0.60	**49.8**
$E_{line,tot}$	$V_{sto,ref}$ = 530 V	18.5	4.10	0.30	**34.1**
	$V_{sto,ref}$ **= 510 V**	28.3	8.00	4.90	**43.0**
	$V_{sto,ref}$ = 490 V	34.5	11.6	0.20	**46.3**
$E_{mech,tot}$		26.6	4.70	-15.5	**15.8**
$E_{kin,tot}$		12.3	0.00	-12.3	**0.00**
E_{LiC}	$V_{sto,ref}$ = 530 V	28.2	3.10	-9.90	**3.90**
	$V_{sto,ref}$ **= 510 V**	16.7	-1.00	-14.7	**0.00**
	$V_{sto,ref}$ = 490 V	9.30	-4.70	-4.60	**0.00**
E_{loss}	$V_{sto,ref}$ = 530 V	22.7	2.60	6.50	**31.1**
	$V_{sto,ref}$ **= 510 V**	20.7	2.60	7.20	**31.0**
	$V_{sto,ref}$ = 490 V	19.8	2.70	11.5	**34.0**

Table 6.6 - Cycle energy and losses evaluation in experimental tests for the stationary LiC ESS case study with LVTC strategy according to several values of $V_{sto,ref}$

6.7 Case study test results for on-board LiC ESS with LCSC strategy

The test bench configuration is reported in Figure 5.1. The main parameters of the simulated railway vehicle and the supply line under consideration are reported in the Table 5.1, Table 5.3, Table 5.4 and Table 5.5.

The LCSC strategy has been implemented on the basis of how said in the par. 5.3.3 with reference to one simulated vehicle and the main control parameters are reported in the Table 5.8..

The test results are reported in the Figure 6.13. The reference line current is set to $i_{sub,ref}$ = 5.25 A. From Figure 6.13 d) the LiC are pre-charged to a voltage equal to 135 V, which has been set as $V_{LiC,max}$.
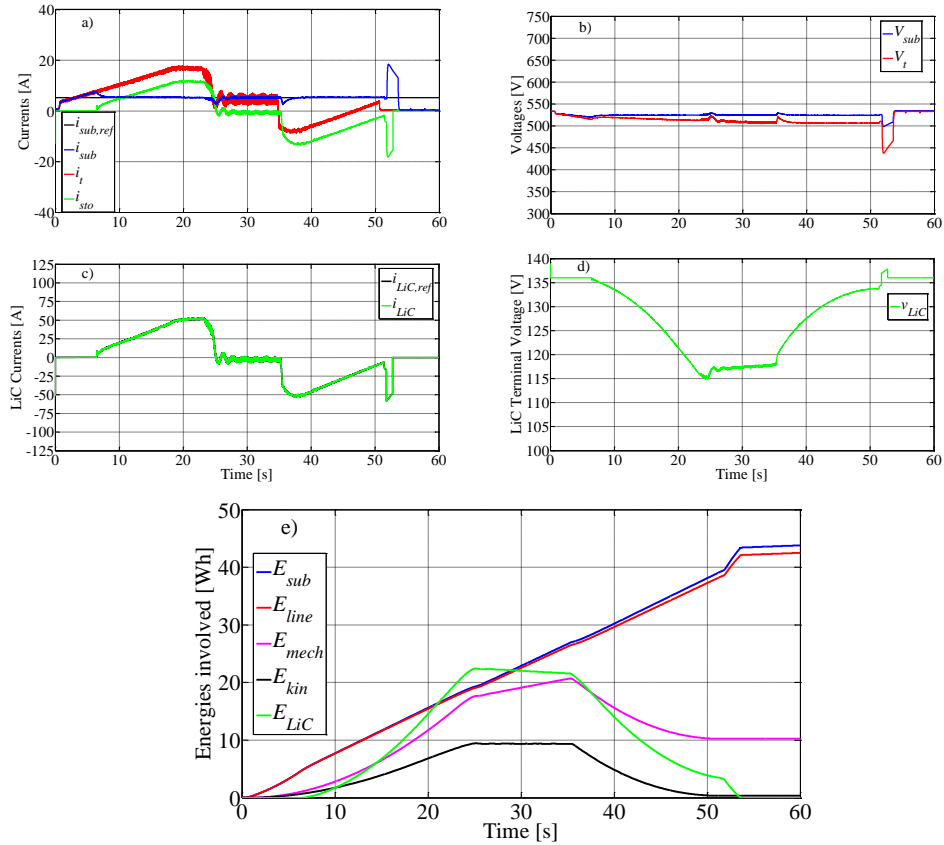
Figure 6.13 - On-board LiC ESS with LCSC strategy case study experimental results assuming $i_{sub,ref}$ = 5.25 A: a) Actual line current, line current set-point, vehicle and storage currents; b) Substation and vehicle voltages; c) LiC actual current and its reference; d) LiC actual voltage; e) Energies involved in the traction cycle

During the starting of the vehicle, the LiC discharge themselves and the voltage decreases from 135 V to 115 V for

t= 24.3 s. The average line current i_{sub} and vehicle voltage V_t, are held respectively constant to about 5 A and 510 V (see Figure 6.13 a) and b)). The recharge of LiC starts when the steady-state speed is reached (t= 24.7 s) and continues also during the regenerative braking. In fact the load current becomes negative (peak of −8.2 A) for about 11.9 seconds and the LiC voltage increases quickly reaching again their initial state of 135 V by taking also advantage of a supply line charging from time instant t= 51.7 s, which is automatically stopped when $v_{LiC} = V_{LiC,max}$. It can be noticed that the slope of voltage v_{LiC}, during the braking, is much higher than that during steady-state conditions. This is due to
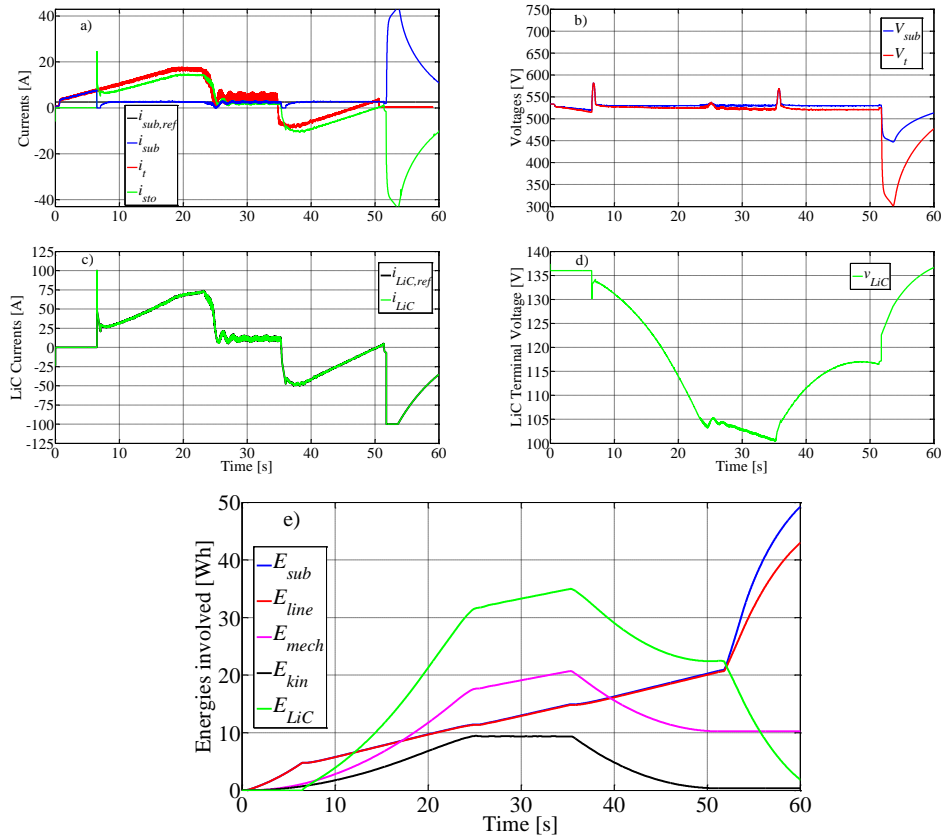
Figure 6.14 - On-board LiC ESS with LCSC strategy case study experimental results assuming $i_{sub,ref}$ = 2.5 A: a) Actual line current, line current set-point, vehicle and storage currents; b) Substation and vehicle voltages; c) LiC actual current and its reference; d) LiC actual voltage; e) Energies involved in the traction cycle

the fact that LiC is recharged both from the line and from the kinetic energy of the simulated vehicle.

The on-board LCSC is capable of holding constant the average line current to 5 A for the entire duration of the cycle also if the vehicle current, i_t, is greater or smaller than the reference value, as shown by Figure 6.13 a). The peak value $i_{sub,peak}$= 18.7 A that occurs at t= 51.7 s, a bit higher respect to that of the vehicle current (17 A).

Moreover, the line current regulation has improving effects also on the line voltage, (see Figure 6.13 b)) which presents only a drop equal to 97 V (respect to the no-load substation voltage $V_{sub,0}$ = 535 V) due to the quick LiC recharge, hence not linked to the vehicle operation. In addition, during the braking, the surge voltages of the line are avoided.
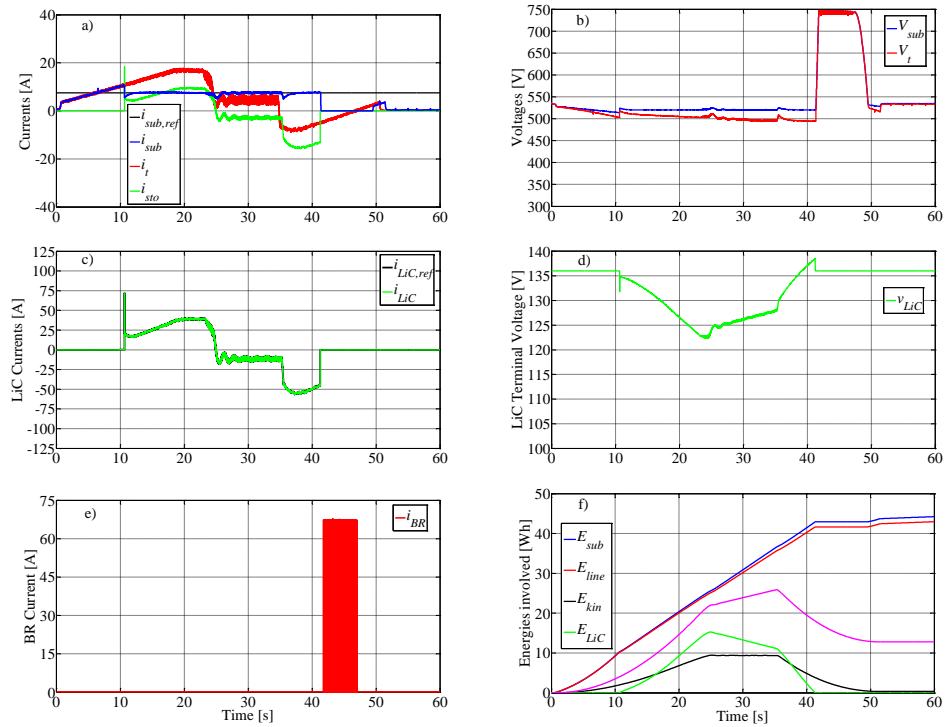
Figure 6.15 - On-board LiC ESS with LCSC strategy case study experimental results assuming $i_{sub,ref}$ = 7.5 A: a) Actual line current, line current set-point, vehicle and storage currents; b) Substation and vehicle voltages; c) LiC actual current and its reference; d) LiC actual voltage; e) Current in the braking rheostat; f) Energies involved in the traction cycle

In Figure 6.13 e) and Table 6.7 are finally shown the energies involved. The energy supplied by the substation increases linearly, since V_{sub} is constant and i_{sub} is almost constant. This means that the instantaneous power supplied by the substation is considerably reduced because the peak is supplied by LiC ESS. At the end of acceleration (t= 24.7 s), the total input energy is 41.7 Wh, whose 22.4 Wh have been supplied by LiC (E_{LiC}) and 19.3 Wh by the substation (E_{sub}). The mechanical and electrical energy losses in this phase are respectively 13 Wh and 6.7 Wh. At the end of coasting (t= 35.4 s), the energy supplied by the main supply is equal to 7.7 Wh and covers the mechanical and electrical energy losses. At the end of braking (t= 51.7 s), the vehicle stops and the input energy is equal to 24.5 Wh, whose 9.0 Wh is the kinetic energy of the mechanical load and 12.5 Wh is supplied by the substation. Therefore at the end of the cycle the total energy supplied by the main supply is 43.8 Wh.

The speed cycle has been repeated with a reference line current of 2.5 A and the results have been plotted in Figure 6.14. In such a case, the set point is too low for the speed cycle considered because the LiC discharge themselves up to $v_{LiC} = 100$ V at the end of acceleration. When the vehicle brakes, the control switch and the line current is controlled again to the set-point of 2.5 A up to the time instant $t = 51.7$ s from which the LiC are recharged by the line.

On the contrary, by setting a reference line current of 7.5 A (see Figure 6.15) the actual current follows quite fine its reference as long as the LiC it reaches its initial SoC ($t = 41.2$ s). Since the LiC discharges less on equal traction cycles, from this time instant, the remaining braking energy has to be dissipated on the braking rheostat.

Energy [Wh]		Acceleration (at t=24.8 s)	Cruise (at t=35.4 s)	Braking (at t=51.5 s)	Cycle
E_{sub}	$i_{sub,ref}$ = **5.25 A**	19.3	7.70	12.5	**43.8**
	$i_{sub,ref}$ = 7.5 A	25.6	11.1	7.00	**44.2**
	$i_{sub,ref}$ = 2.5 A	11.4	3.60	5.90	**49.2**
E_{line}	$i_{sub,ref}$ = **5.25 A**	19.0	7.50	12.1	**42.5**
	$i_{sub,ref}$ = 7.5 A	25.1	10.6	6.80	**43.0**
	$i_{sub,ref}$ = 2.5 A	11.3	3.50	5.90	**42.9**
E_{mech}		22.0	3.83	-13.0	**12.8**
E_{kin}		8.94	0.00	-8.94	**0.00**
E_{LiC}	$i_{sub,ref}$ = **5.25 A**	22.4	-0.90	-18.3	**0.00**
	$i_{sub,ref}$ = 7.5 A	15.3	-4.30	-11.0	**0.00**
	$i_{sub,ref}$ = 2.5 A	31.5	3.50	-12.6	**1.80**
E_{loss}	$i_{sub,ref}$ = **5.25 A**	19.7	2.97	7.20	**31.0**
	$i_{sub,ref}$ = 7.5 A	18.9	2.97	9.00	**31.4**
	$i_{sub,ref}$ = 2.5 A	20.9	3.27	6.30	**34.6**

Table 6.7 - Cycle energy and losses evaluation in experimental tests for the on-board LiC ESS case study with LCSC strategy according to several values of $i_{sub,ref}$

6.8 Case study test results for stationary LiC ESS with LCSC strategy

The test bench configuration is reported in Figure 5.2. The main parameters of the simulated railway vehicle and the supply line under consideration are reported in the previous Table 5.1, Table 5.2, Table 5.3, Table 5.4 and Table 5.5. The stationary LCSC strategy has been implemented on the basis of how said in the par. 5.3.3 and the main control parameters are reported in the Table 5.8.

The same conclusion of how said in the previous par. 6.7 can be stated by selecting several values of the substation current reference $i_{sub,ref}$ (8 A, 5 A, 10 A respectively).
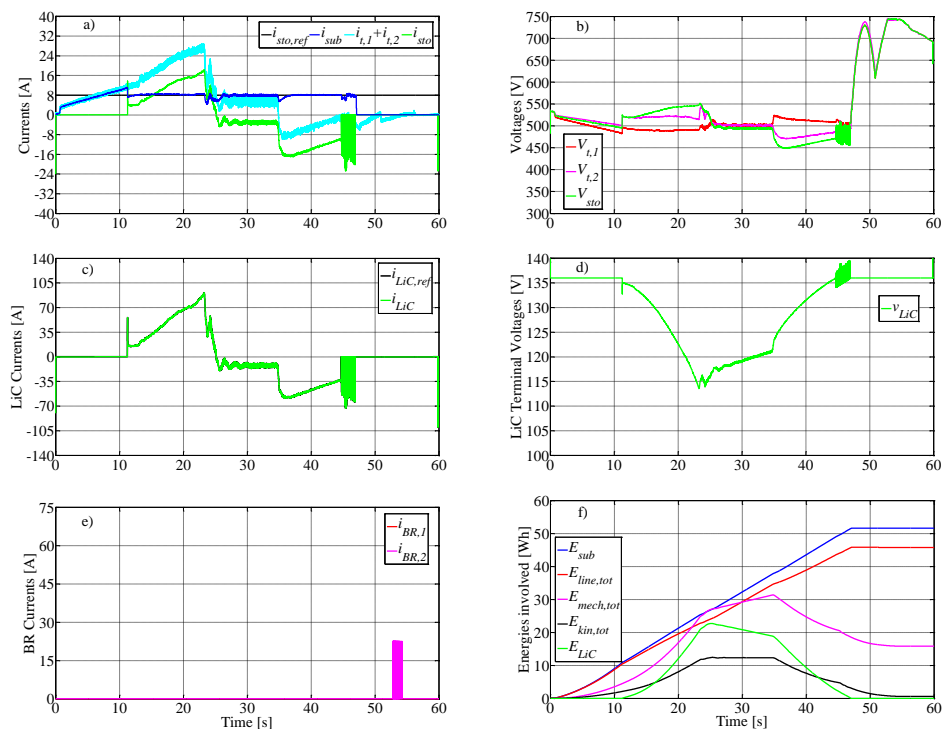
Figure 6.16 – Stationary LiC ESS with LCSC strategy case study experimental results assuming $i_{sub,ref}$ = 8.0 A: a) Actual substation current, substation current set-point, vehicle and storage currents; b) Substation and vehicles voltages; c) LiC actual current and its reference; d) LiC actual voltage; e) Currents in the braking rheostats; f) Energies involved in the traction cycles
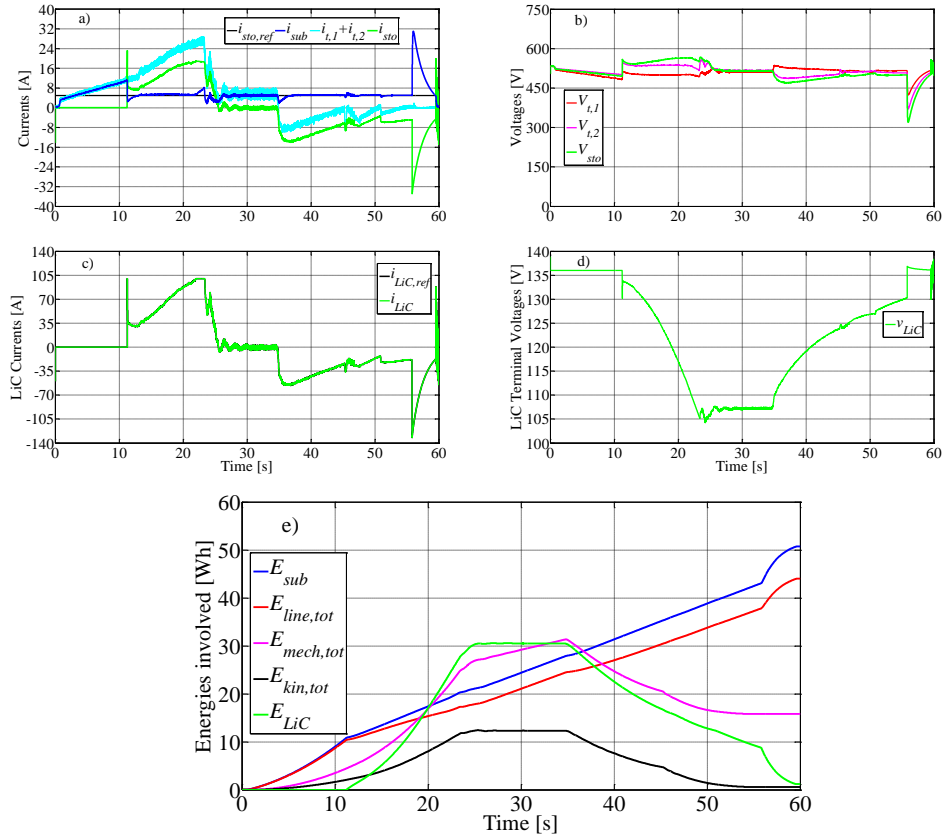
Figure 6.17 - Stationary LiC ESS with LCSC strategy case study experimental results assuming $i_{sub,ref}$ = 5.0 A: a) Actual substation current, substation current set-point, vehicle and storage currents; b) Substation and vehicles voltages; c) LiC actual current and its reference; d) LiC actual voltage; f) Energies involved in the traction cycles

The result is that by implementing the LCSC strategy for the stationary ESS case, the choice of the substation current reference is made even more complicated by the time displacement between the two vehicles which strongly affects the instantaneous supply current absorptions i_{sub}.
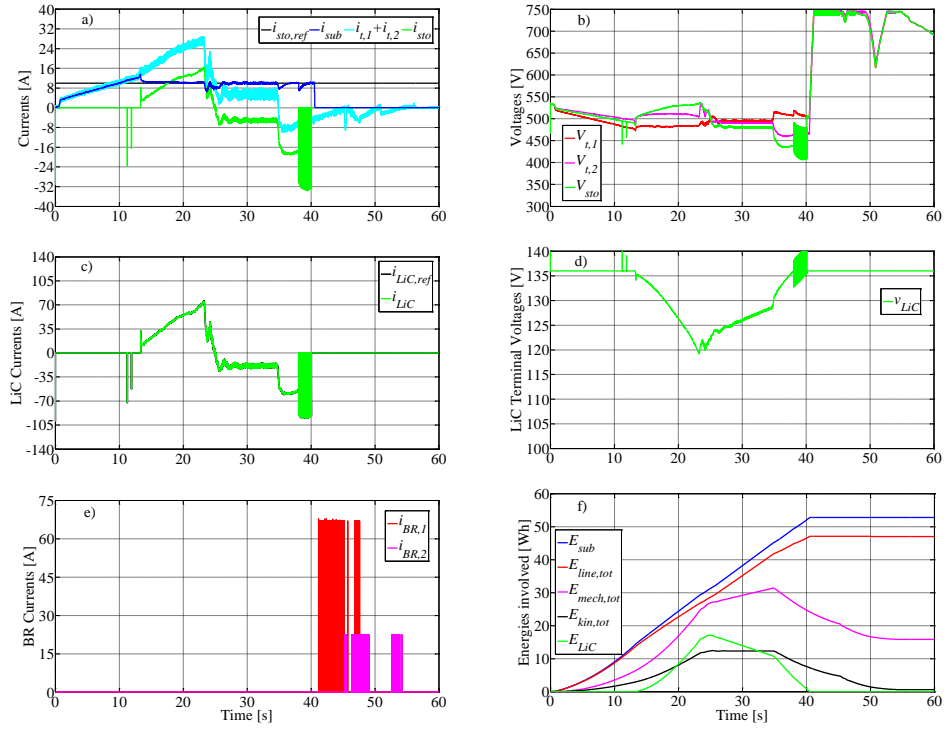
Figure 6.18 - Stationary LiC ESS with LCSC strategy case study experimental results assuming $i_{sub,ref}$ = 10.0 A: a) Actual substation current, substation current set-point, vehicle and storage currents; b) Substation and vehicles voltages; c) LiC actual current and its reference; d) LiC actual voltage; e) Currents in the braking rheostats; f) Energies involved in the traction cycles

Energy [Wh]		Acceleration (at t=24.7 s)	Cruise (at t=34.7 s)	Braking (at t=55.3 s)	Cycle
E_{sub}	$i_{sub,ref}$ = **8 A**	26.6	11.2	13.8	**51.6**
	$i_{sub,ref}$ = 10 A	31.0	14.0	7.80	**52.8**
	$i_{sub,ref}$ = 5 A	21.0	6.90	14.8	**50.8**
$E_{line,tot}$	$i_{sub,ref}$ = **8 A**	23.8	10.8	11.2	**45.8**
	$i_{sub,ref}$ = 10 A	28.4	13.2	5.40	**47.0**
	$i_{sub,ref}$ = 5 A	17.8	6.70	12.9	**44.0**
$E_{mech,tot}$		26.6	4.70	-15.5	**15.8**
$E_{kin,tot}$		12.3	0.00	-12.3	**0.00**
E_{LiC}	$i_{sub,ref}$ = **8 A**	22.6	-3.80	-18.8	**0.00**
	$i_{sub,ref}$ = 10 A	17.0	-6.20	10.8	**0.00**
	$i_{sub,ref}$ = 5 A	30.1	0.40	-21.3	**1.10**
E_{loss}	$i_{sub,ref}$ = **8 A**	22.6	2.70	10.5	**35.8**
	$i_{sub,ref}$ = 10 A	21.4	3.10	12.5	**37.0**
	$i_{sub,ref}$ = 5 A	24.5	2.60	9.00	**36.1**

Table 6.8 - Cycle energy and losses evaluation in experimental tests for the stationary LiC ESS case study with LCSC strategy according to several values of $i_{sub,ref}$

6.9 Control strategies comparison and performance evaluation

In order to better assess the differences and characteristics of the tested control strategies and also for remarking the benefit of installing the LiC storage by evaluating the system performances in terms of energy efficiency improvement and voltage drops compensation, some specific **performance indexes** have been defined. They make reference to all the cases before analysed, without and with the LiC ESS:

Energy saving, $es_\%$, which gives in percent the difference among the substation energy consumption during the traction cycle with and without the LiC device:

$$es_{\%} = \left(1 - \frac{E_{sub}}{E_{sub}^{(BR)}}\right) \cdot 100 \qquad (6.6)$$

Max Voltage drop, $\Delta V_{t,max\%}$ evaluates in percent the maximum voltage drop at the vehicle's pantograph, giving the rate about how much is maximum voltage drop, $\Delta V_{t,max}$, respect to the no-load rated line voltage ($V_{sub,0} = 535$ V):

$$\Delta V_{t,max\%} = \left(1 - \frac{V_{t,min}}{V_{sub,0}}\right) \cdot 100 \qquad (6.7)$$

vhere $V_{t,min}$ is the minimum value of the line voltage ($V_{t,min} = V_{sub,0} - \Delta V_{t,max}$).

Substation peak current reduction, $r_{isub,peak\%}$, refers to the reduction degree of the substation peak current, $i_{sub,peak}$ due to the presence of the ESS compared to its absence:

$$r_{isub,peak\%} = \left(1 - \frac{i_{sub,peak}}{i_{sub,peak}^{(BR)}}\right) \cdot 100 \qquad (6.8)$$

where $i_{sub,peak}^{(BR)}$ is the value of the substation peak current when the ESS is not present.

In the following, some consideration on the $es_{\%}$ index are given.

With reference to one circulating vehicle, the analytical expression of the energy saving has been evaluated on the basis of the energetic efficiencies calculated during the three different motion phases (1-acceleration , 2-cruising, 3-braking), taking into account the control strategy adopted and by assuming that the supply energy E_{sub} cannot come back into the electrical primary network (6.9). In particular the exchanged storage energy has to be constrained between the limits highlighet in the second eq. of (6.9).

The term β is the share coefficient of recoverable energy in braking (6.10)

The superscript 1, 2 and 3 on the several energetic quantities, refer to the respective motion phases, as clearly depicted on the scheme of energy flows in the Figure 2.13. The term η_t is the energetic efficiency of the vehicle evaluated as the product of the several energetic efficiencies $\eta_t = \eta_{mech}\eta_{em}\eta_{inv}$, whereas the storage energetic efficiencies $\eta_{sto} = \eta_{dcdc}\eta_{LiC}$ and E_{run} is the energy required at the wheels to overcome running resistances.

$$\begin{cases} E_{sub} \geq 0 \quad \forall t \\ E_{kin}^{(3)}\eta_t^{(3)} - \dfrac{E_{run}^{(3)}}{\eta_t^{(3)}} \leq E_{LiC} \leq \dfrac{E_{kin}^{(1)} + E_{run}^{(1)}}{\eta_t^{(1)}\eta_{sto}^{(1)}} \\ E_{LiC}^{(1)} = E_{LiC}^{(3)} \end{cases} \qquad (6.9)$$

$$\begin{cases} \beta = \dfrac{E_{LiC}}{E_{kin}\eta_t^{(3)}\eta_{sto}^{(3)}} \\ E_{BR} = (1\text{-}\beta)E_{kin}\eta_t^{(3)} \end{cases} \qquad (6.10)$$

With reference to a single vehicle, the eq. (6.6) becomes:

$$es_\% = 1 - \frac{E_{LiC}\left[\dfrac{1}{\eta_{sto}^{(3)}} - \eta_{sto}^{(1)}\right] + E_{kin}^{(1)}\left[\dfrac{1}{\eta_t^{(1)}} - \beta\eta_t^{(3)}\right] + \dfrac{E_{run}^{(1)}}{\eta_t^{(1)}} + \dfrac{E_{run}^{(2)}}{\eta_t^{(2)}} + \dfrac{E_{run}^{(3)}}{\eta_t^{(3)}}}{\dfrac{E_{kin}^{(1)} + E_{run}^{(1)}}{\eta_t^{(1)}} + \dfrac{E_{run}^{(2)}}{\eta_t^{(2)}}} \qquad (6.11)$$
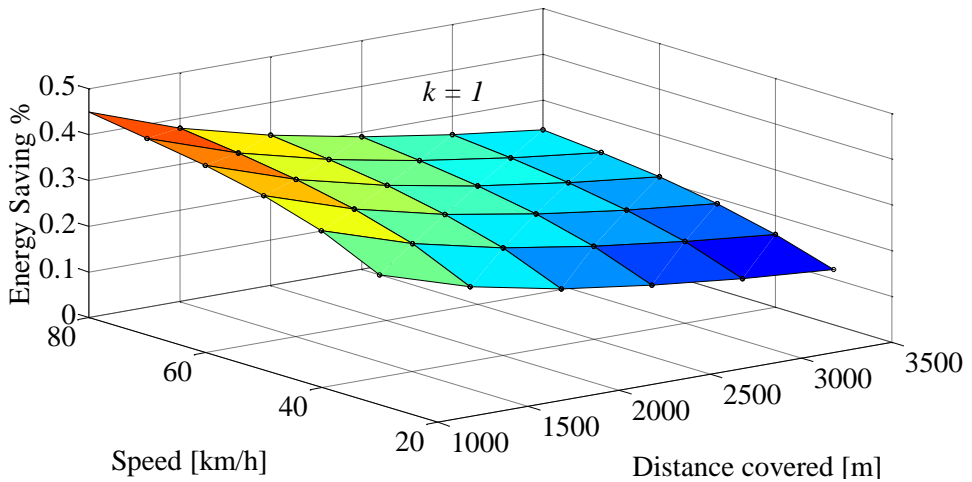
Figure 6.19 – Trend of energy saving in function of the maximum vehicle speed and the total distance covered, with β=1

The energy saving expression points out that it a function of:
- Efficiencies of the subsystems during each motion phases
- The needed storable energy (size) E_{LiC}
- The regenerative braking energy share coefficient β

In practical case, once designed the storage size, it mainly depends on:

- The adopted control strategy
- The rail track characteristics and in general on the motion resistances, E_{run};
- Maximum required performance, acceleration and deceleration rates;
- Total distance covered;
- Max operating speed.

By way of example, the Figure 6.19 shows the trend of the energy saving in function of the maximum cruise speed and different total distance covered, assuming $\beta = 1$. As concerns the data for the simulated vehicle, reference was made to the vehicle presented in Sec. 4.8.

6.9.1   Comparison for on-board ESS installation

The Table 6.9 shows the defined indexes by comparing all the aforementioned test results (Par. 6.1, 6.3, 6.5 and 6.7), whereas the Figure 6.20 displays a bar chart with the same indexes values evaluated by making reference only to $V_{sto,ref}$ = 510 V and $i_{sub,ref}$ = 5.25 A, for sake of brevity.

Index	No LiC onboard (case base)	LiC on-board STC	LiC on-board LVTC			LiC on-board LCSC		
			$V_{sto,ref}$ 530V	$V_{sto,ref}$ 510V	$V_{sto,ref}$ 490V	$i_{sub,ref}$ 2.5 A	$i_{sub,ref}$ 5.25A	$i_{sub,ref}$ 8.0 A
$es_\%$	-*	**16.5**	9.41	**10.2**	4.39	-2.93	**8.37**	7.53
$\Delta V_{t,max\%}$	**13.8****	**9.91**	37.7	**6.73**	8.22	43.1	**18.1**	7.66
$r_{isub,peak\%}$	-***	**27.1**	-125	**60.8**	38.2	-158	-108	38.2

*Base value for the comparison $E_{sub}^{(BR)}$ =**47.8** Wh

** Base value for the comparison $\Delta V_{t,max}^{(BR)}$ =**75.0** V with $V_{t,0} = V_{sub,0}$ = 535 V

*** Base value for the comparison $i_{sub,peak}^{(BR)}$ =**17.0** A

Table 6.9 – Performance indexes evaluation for on-board LiC ESS

As it is clearly highlighted, on equal traction cycles, the on-board STC strategy assures the highest value of $es_\%$ (**16.5** %). This is mainly obtained thanks to the capability of the STC technique to make null the energy wasted in the on-board braking rheostat. This is not a surprise, since the actual energy stored in the LiC , E_{LiC}, is instantly related to the actual kinetic energy of the vehicle, E_{kin} . The STC strategy also gives satisfactory results with regard to maximum line voltage drop, $\Delta V_{t,max\%}$, and substation peak current reduction, $r_{isub,peak\%}$, which corresponds to the **9.91** % of $V_{sub,0}$, (53 V) and the **27.1** % of $i_{sub,peak}^{(BR)}$, (12.4 A).

As concerns the LVTC strategy, this gives better results in terms of voltage drop and substation current peak reduction, provided that the line reference value $V_{sto,ref}$ is set not close to the value $V_{sub,0}$. In fact by selecting $V_{sto,ref} = 530$ V, this implies unacceptable values of $\Delta V_{t,max\%}$ (37.7 % of $V_{sub,0}$) and $i_{sub,peak}$ (38.2 A), due to the quick recharge of the LiC ESS at the end of the traction cycle. However, in the other cases, the benefits due to the line voltage regulation action by means of LVTC are evident, but in any case this control get worse results in terms of $es_\%$ with respect to the STC.

Finally, as concerns the LCSC strategy, as many times said, it is strongly dependent on the selection of $i_{sub,ref}$. In fact only by choosing this value equal to the average vehicle current plus the current due to the line losses ($i_{sub,ref} = 5.25$ A), the index results are reasonable, but still lower than the performance offered by STC strategy.

By summing up, **Speed Tracker Control** strategy, in addition to its inner ability to integrate perfectly with the traction control, represents the natural way to relate the actual LiC SoC to the vehicle's kinetic energy, giving satisfactory results as regards the application of on-board LiC ESS.
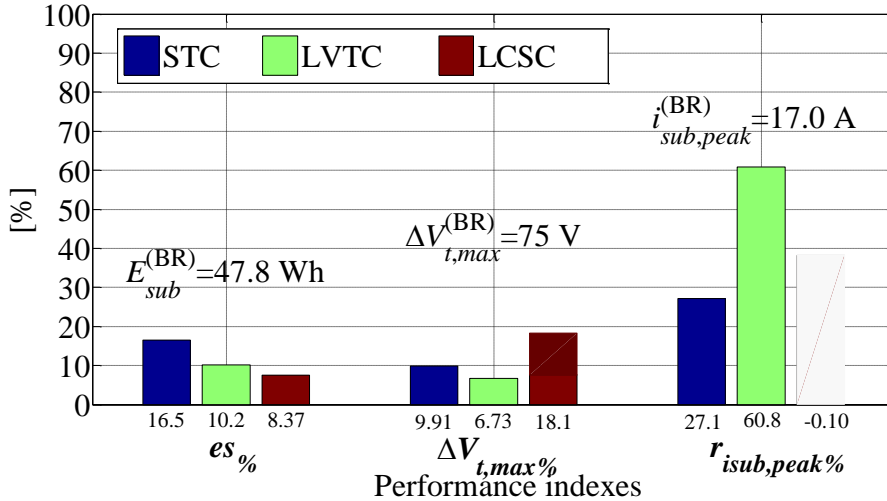
Figure 6.20 – Performance indexes bar chart for on-board LiC ESS

6.9.2   Comparison for stationary ESS installation

The Table 6.10 shows the defined indexes by comparing all the aforementioned test results (Par. 6.2, 6.4, 6.6 and 6.8), whereas the Figure 6.21 displays a bar chart with the same indexes values evaluated by making reference only to $V_{sto,ref}$ = 510 V and $i_{sub,ref}$ = 5.25 A, for sake of brevity.

Even for the application on the ground, the control technique STC gives good overall performance results, for the same reasons before explained. In fact, it guarrantees a lower total input energy spent, since $es_\% = $ **14.9** %), by limiting the maximum line voltage drop, $\Delta V_{t,max\%}$, which occurs on the 1st rail track, to the **14.8** % of $V_{sub,0}$, (79 V) with consequent reduction of the substation current peak , $r_{isub,peak\%}$, to the **30.4** % of $i_{sub,peak}^{(BR)}$, (18.5 A).

Satisfactory values of the $es_\%$ are also obtained with the strategy LVTC ($es_\% = $ **11.5** %), as far as $V_{sto,ref}$ = 510 V is selected, which in addition offers the best performance as regards the reduction of the maximum voltage drop ($\Delta V_{t,max\%} = $ **11.8** % of $V_{sub,0}$) and the current peak limitation ($r_{isub,peak\%} = $ **47.7** % of $i_{sub,peak}^{(BR)}$).

If the line voltage reference value is lower ($V_{sto,ref}$ = 490 V), the overall performance in terms of energy saving decreases ($es_\% = $ 5.86 %), because the rheostats turn on.

293

Index	No LiC stationary (case base)	LiC stationary STC	LiC stationary LVTC			LiC stationary LCSC		
			$V_{sto,ref}$ 530V	$V_{sto,ref}$ **510V**	$V_{sto,ref}$ 490V	$i_{sub,ref}$ 5.0 A	$i_{sub,ref}$ **8.0 A**	$i_{sub,ref}$ 10.0A
$es_\%$	-*	14.9	18.7	11.5	5.86	3.97	2.46	0.19
$\Delta V_{t,max\%}$	**21.5****[(2)]	14.8 [(1)]	35.1[(2)]	11.8[(1)]	13.5[(1)]	30.6[(2)]	9.91[(1)]	13.8[(2)]
$r_{isub,peak\%}$	-***	30.4	-33.8	47.7	38.0	-16.5	57.9	48.5

*Base value for the comparison $E_{sub}^{(BR)}=$**52.9** Wh

** Base value for the comparison $\Delta V_{t,max}^{(BR)}=$**115** V with $V_{t,0}=V_{sub,0}=535$ V

*** Base value for the comparison $i_{sub,peak}^{(BR)}=$**26.6** A

[(1)] Occurring on track 1
[(2)] Occurring on track 2

Table 6.10 - Performance indexes evaluation for stationary LiC ESS

On the contrary, by setting $V_{sto,ref}=530$ V although the energy saving results higher than the STC case ($es_\% = 18.7$ %), the LVTC get the worst line voltage drop ($\Delta V_{t,max\%} = 35.1$ % of $V_{sub,0}$) and the substation current peak result even higher than the case of no LiC ESS installed ($i_{sub,peak} = 35.6$ A).
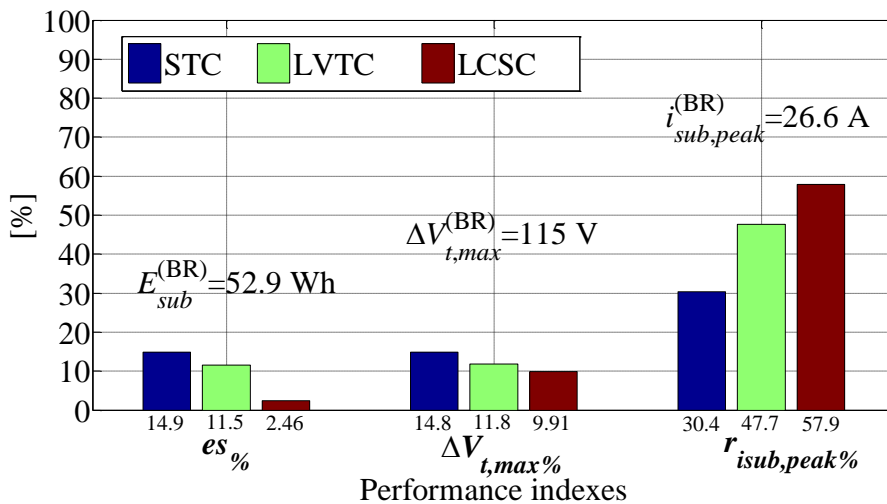
Figure 6.21 - Performance indexes bar chart for stationary LiC ESS

Thus, the stationary LCSC strategy offers poor performances in any case, since it gives values of $es_\%$ less than 4%.

After an overall comparison, even in the case of stationary ESS installation, the choice of the optimal ESS control strategy is made on STC. Although the results show good potentiality, the main limits of this strategy is due to the knowledge in real-time of the actual vehicle speeds.

This last consideration justifies and makes preferable the use of the **Line Voltage Tracker Control** strategy for the correct energy management of stationary ESS.

Conclusions

The thesis presents the uses and applications of energy storage devices employed in urban electrified railways, including both metro trains, light rail vehicles and trams.

Energy storage devices are essentially able to store regenerative braking energy for later releasing it to support vehicles acceleration or the main electrical substations in the neighbourhoods. They can actually improve energy efficiency and support the performance of urban electrified railways.

After a comprehensive overview of the currently available technologies for recovery and management of braking energy in urban rail, also pointing out the current commercially proven solutions, it has been identified the Supercapacitor storage technology as the most suitable that matches the performance requirements of the urban rail traction.

Besides, among the newly emerging technologies, Lithium-ion Capacitors are very interesting because they present a specific power comparable with that of conventional SC and a specific energy about double. Therefore, it has been presented a model suitable to represent the behavior of LiC cells at temperatures higher than 20 °C, by proving its goodness by means of experimental tests.

the applicability of the model to a stack of cells was also analyzed.

The core of the thesis is the proposal of some control strategies potentially suitable for both on-board and stationary ESS installation in order to manage as efficiently as possible the regenerative braking energy.

The methodology proposed for the assessment of the achievable performances offered by these implemented controls has been the execution of wide experimental investigation on a Laboratory reduced scale model of urban railway network. In fact, it proved to be a powerful tool for testing and validating control strategies of energy management of LiC-based ESS in on-board and stationary installations.

Finally, a performance indexes comparison has given an assessment on the effective energy saving achievable by the implementation of the proposed control strategies, pointing out the efficiency enhancement by energy saving, voltage regulation, power compensation and infrastructure power loss reduction. In particular the verified *Speed Tracker Control* strategy for LiC on-board

installation is able to reach an overall energy saving up to 16.5 %, while regarding the stationary applications, by using *Line Voltage Tracker Control* based strategy, values of energy saving up to 12 % may be obtained.

However, the energy saved in experimental tests by the electromechanical simulator can be further improved when a system optimized design, based on the specific application, is carried out for a real system. For this reason, to better confirm the validity and the effectiveness of the proposed controls in all the cases considered, a next study improvement could be the performing of a campaign of experimental tests on real systems (scale 1:1).

Appendix A1

Matlab script of the supervisory program for STC strategy

```matlab
%%% file name: chopper_LiC_stationary_2car_STC_niusb.m %%%
clc
clear all
close all

duration=60; % Acquisition time [s]

Jt   = 3.7;   %%%Total Inertia of the 1st vehicle;
Jt_2 = 0.95; %%%Inerzia del 2^ veicolo;
Cuc = 30.5;   %%%LiC eq. capacitance
ruc = 0.0012*36 + 0.03; %%%LiC ESR
vuc_max = 135.0; %%% LiC max voltage

k = 1.0;   %losses factor vehicle 1
k2 = 1.0; %losses factor vehicle 2
i_limite = 135;

kp = 12.5*1.2*0.7*135; %%% Proportional constant Reg u
ki = 15;%0.5*0.7*6.525; %%% Integral constant Reg u
                        %RICORDA con kp_i=120 (Modbus 2348) e ki_i=6000 (modbus
2350)
k_obs1 = 1; %%gain observer u_lic_est
puc_int = 0;

%%%NI-DAQ initialization%%%
%%%Analog inputs
ingressi = analoginput('nidaq','dev1');

addchannel(ingressi,0,'tensionescaps');%%%%%% morsetto(7,8) del sinus penta
addchannel(ingressi,1,'corrente_linea');
addchannel(ingressi,2,'corrente_carico');
addchannel(ingressi,3,'tensione_carico');   %%% tensione (al pantografo) a monte
dell'inverter
addchannel(ingressi,4,'velocita');   %%% velocità in rpm
addchannel(ingressi,5,'coppia');
addchannel(ingressi,6,'corr_uc');%%%%%% morsetto(5,6) del sinus penta
addchannel(ingressi,7,'tensione_linea'); %%% tensione di sottostazione
addchannel(ingressi,16,'velocita_2');
addchannel(ingressi,17,'coppia_2');
addchannel(ingressi,18,'corrente_carico_2');
addchannel(ingressi,19,'tensione_carico_2');

Tc = 1/10;
RateAttuale = 1000; %DAQ sampling frequency

set(ingressi,'SampleRate',RateAttuale);
set(ingressi,'SamplesPerTrigger',duration*RateAttuale)

%%%%%%%%%CHANNEL SETTINGS%%%%%%%%%%%%%%%%%%
ingressi.tensionescaps.sensorrange = [-10 10];
ingressi.tensionescaps.unitsrange  = [-1000 1000];
```

```matlab
ingressi.tensionescaps.inputrange  = [-10 10];

ingressi.corrente_linea.sensorrange  = [-10 10];
ingressi.corrente_linea.unitsrange   = [-100 100];
ingressi.corrente_linea.inputrange   = [-10 10];

ingressi.corrente_carico.sensorrange   = [-10 10];
ingressi.corrente_carico.unitsrange    = [-100 100];
ingressi.corrente_carico.inputrange    = [-10 10];

ingressi.tensione_carico.sensorrange   = [-10 10];
ingressi.tensione_carico.unitsrange    = [-1000 1000];
ingressi.tensione_carico.inputrange    = [-10 10];

ingressi.velocita.sensorrange   = [-10 10];
ingressi.velocita.unitsrange    = [-1500 1500];
ingressi.velocita.inputrange    = [-10 10];

ingressi.coppia.sensorrange   = [-10 10];
ingressi.coppia.unitsrange    = [-250 250];
ingressi.coppia.inputrange    = [-10 10];

ingressi.corr_uc.sensorrange   = [-10 10];
ingressi.corr_uc.unitsrange    = [-200 200];
ingressi.corr_uc.inputrange    = [-10 10];

ingressi.tensione_linea.sensorrange   = [-10 10];
ingressi.tensione_linea.unitsrange    = [-1000 1000];
ingressi.tensione_linea.inputrange    = [-10 10];

ingressi.velocita_2.sensorrange   = [-10 10];
ingressi.velocita_2.unitsrange    = [-60*60/2 60*60/2];
ingressi.velocita_2.inputrange    = [-10 10];

ingressi.coppia_2.sensorrange   = [-10 10];
ingressi.coppia_2.unitsrange    = [-200 200];
ingressi.coppia_2.inputrange    = [-10 10];

ingressi.corrente_carico_2.sensorrange   = [-10 10];
ingressi.corrente_carico_2.unitsrange    = [-137 137];
ingressi.corrente_carico_2.inputrange    = [-10 10];

ingressi.tensione_carico_2.sensorrange   = [-10 10];
ingressi.tensione_carico_2.unitsrange    = [-837 837];
ingressi.tensione_carico_2.inputrange    = [-10 10];

%%%Analog outputs
uscite = analogoutput('nidaq','dev1');
addchannel(uscite,0,{'chopper'});%%%%%% riferimento corrente sc morsetto(2,1)
del sinus penta
addchannel(uscite,1,{'Load1_Speed_ref'});
addchannel(uscite,2,{'Load2_Speed_ref'});

set(uscite,'SampleRate', RateAttuale);

uscite.chopper.OutputRange = [-10 10];
uscite.chopper.unitsrange = [-300 300]; %%Per trasformare il segnale di uscita
in single-ended

uscite.Load1_Speed_ref.OutputRange = [-10 10];
uscite.Load1_Speed_ref.unitsrange = [-1500 1500]; %%Velocita max inverter
impostata a 1500 rpm

uscite.Load2_Speed_ref.OutputRange = [-10 10];
```

299

```matlab
uscite.Load2_Speed_ref.unitsrange = [-60 60]; %%Velocita max inverter 2
impostata a 1500 rpm
%%%END NI-DAQ Initialization

%%%Set Offset misure
off_v_uc      = 0.07560073260074;
off_i_linea   = 0.21163858363860;
off_i_l       = 0.20539926739927;
off_v_l       = 0.06456654456656;
off_vel       = 3.08542124542158;
off_coppia    = 0.12547008547010;
off_i_uc      = 0.02334554334554;
off_v_linea   = 0.29346764346772;
off_vel_2     = 1.01186446886427;
off_coppia_2  = 0.15595115995120;
off_i_l_2     = 0.139073740508068;
off_v_l_2     = 0.712829910327122;

f = figure;
set(f,'doublebuffer','on') %Reduce plot flicker

%%%%START real-time acquisition
start(ingressi)

i = 1;
w = 1;
tc = 1;
Ts = 0.1;
%%%%Parametri filtro velocità e accelerazione
G = 1; %VECCHIO FILTRO G = 1.497;
tau_v = 0.15;
tau_a = 0.125;
%%%%

kdurata = duration*Tc;

t = 0;
for j = 1:kdurata
    x = [];
    y_iuc = [];
    y_pot = [];
    y_vuc = [];
    y_vref = [];
    y_i_linea = [];
    y_i_carico = [];
    y_v_carico = [];
    y_i_carico_2 = [];
    y_v_carico_2 = [];

    stampe_2; %%%Real-time plot acquired data

    while ingressi.SamplesAcquired < j*ingressi.SamplesPerTrigger/kdurata
        while ingressi.SamplesAcquired < RateAttuale*i*Tc
        end

        %%%%%%%%%%%%%%%%%%%%%%%%%%%%%%%%%%%%%
        %%% Speed profiles of the 1st vehicle in rpm
        vel1_ref(1:(100)) = 1225;
        vel1_ref((100 + 1):(345)) = 1225;
        vel1_ref((345 + 1):(6*100)) = 0;

        %%% Speed profiles of the 2nd vehicle in rpm
        vel2_ref(1:(125)) = 0;
        vel2_ref((125 + 1):(449)) = 2*1500/60;%2*1200/75;
        vel2_ref((450 + 1):(6*100)) = 0;
```

300

```matlab
        %%%%%%%%%%%%%%%%%%%%%%%%%%%%%%%%%%%%
        data = peekdata(ingressi, RateAttuale*Tc);

        y_vel_2(i)= (mean(data(:,5)) - off_vel)*pi/30;
        y_vel_22(i)= (mean(data(:,9)) - off_vel_2)*pi/30;

        if i <= tc
            %Initial conditions for the speed filter
            velf(1)=0;
            acc2(1)=0;
            accf(1)=0;

            velf2(1)=0;
            acc22(1)=0;
            accf2(1)=0;
        else
            %Actual speed filter
            velf(i)=(G*y_vel_2(i) + (tau_v/Ts)*velf(i-1))/(1+tau_v/Ts);
            velf2(i)=(G*y_vel_22(i) + (tau_v/Ts)*velf2(i-1))/(1+tau_v/Ts);

            %calcolo accelerazione 1 come rapporto incrementale
            acc2(i)=(velf(i)-velf(i-tc))/Ts;
            %filtra l'accelerazione 1
            accf(i)=(G*acc2(i) + (tau_a/Ts)*accf(i-1))/(1+tau_a/Ts);

            %calcolo accelerazione 2 come rapporto incrementale
            acc22(i)=(velf2(i)-velf2(i-tc))/Ts;
            %filtra l'accelerazione 2
            accf2(i)=(G*acc22(i) + (tau_a/Ts)*accf2(i-1))/(1+tau_a/Ts);
        end

        %%%%% INTERNAL LIC VOLTAGE LUENBERGER OBSERVER %%%%%
        v_uc(i) = mean(data(:,1)) - off_v_uc;
        i_uc(i) = mean(data(:,7)) - off_i_uc;

        if i == 1
            u_uc_est(i) = v_uc(i);
            i_uc_est(i) = i_uc(i);
        else
            i_uc_est(i) = (u_uc_est(i) - v_uc(i))/ruc;
        end
        u_uc_est(i+1) = u_uc_est(i) + Ts*(1/(ruc*Cuc)*(v_uc(i) - u_uc_est(i)) +
k_obs1*(i_uc(i) - i_uc_est(i)));

        %%%%%%%%%%%%%%%%%%%%%%%%%%%%%%%%%%%%%%%%%%%%%%%%%%%%%%
        %%%% EVALUATION of u_lic_ref %%%

        u_uc_ref(i) = sqrt(vuc_max^2 -
((k*Jt*velf(i)^2)+(k2*Jt_2*velf2(i)^2))/Cuc);

        %%%% PI regulator Reg u for EVALUATION of P_lic_ref %%%%
        puc_int = puc_int + ki*(u_uc_ref(i) - u_uc_est(i))*Ts;
        puc_ref(i) = kp*(u_uc_ref(i) - u_uc_est(i)) + puc_int;

        %%%% EVALUATION of i_lic_ref %%%%%
        out(i) = ((puc_ref(i) -
(k*Jt*velf(i)*accf(i))+(k2*Jt_2*velf2(i)*accf2(i)))/u_uc_est(i)) + 150.9;

        %%%%Antiwindup action on i_lic_ref
        if (out(i)>i_limite + 150.9)
            out(i) = i_limite + 150.9;
            puc_int = puc_int - ki*(u_uc_ref(i) - u_uc_est(i))*Ts;
        elseif (out(i)<-i_limite + 150.9)
            out(i) = -i_limite + 150.9;
```

301

```matlab
                puc_int = puc_int - ki*(u_uc_ref(i) - u_uc_est(i))*Ts;
            end

            ref(1:100)= -(out(i) - 150.9);
            iuc_ref(i) = mean(ref);
            b(1:100)= u_uc_ref(i);
            %putsample(uscite,out(i));
            putsample(uscite,[out(i),vel1_ref(i),vel2_ref(i)]); %%%%Send the LiC
current set-point to the DCDC Converter%%%

            x1=((w-1)*RateAttuale*Tc):(RateAttuale*Tc*w-1);
            x=[x x1];
            y_iuc = [y_iuc;data(:,7) - off_i_uc];
            y_pot = [y_pot ;ref'];
            y_vuc = [y_vuc ;data(:,1) -  off_v_uc];
            y_vref = [y_vref ;b.'];
            y_i_linea = [y_i_linea ;data(:,2) -  off_i_linea];
            y_i_carico = [y_i_carico ;data(:,3) -  off_i_l];
            y_v_carico = [y_v_carico ;data(:,4) - off_v_l];
            y_i_carico_2 = [y_i_carico_2 ;data(:,11) - off_i_l_2];
            y_v_carico_2 = [y_v_carico_2 ;data(:,12) - off_v_l_2];

            set(iuc,'ydata',y_iuc);
            set(rif,'ydata',y_pot);
            set(vuc,'ydata',y_vuc);
            set(vref,'ydata',y_vref);
            set(ilinea,'ydata',y_i_linea);
            set(icarico,'ydata',y_i_carico);
            set(vcarico,'ydata',y_v_carico);
            set(icarico2,'ydata',y_i_carico_2);
            set(vcarico2,'ydata',y_v_carico_2);

            set(iuc,'xdata',x);
            set(rif,'xdata',x);
            set(vuc,'xdata',x);
            set(vref,'xdata',x);
            set(ilinea,'xdata',x);
            set(icarico,'xdata',x);
            set(vcarico,'xdata',x);
            set(icarico2,'xdata',x);
            set(vcarico2,'xdata',x);

            drawnow
            t = t+1;
            w = w + 1;
            i = i + 1;
        end
        w = 1;
    end

    %wait until the acquisition is not ended
    while strcmp(ingressi.Running,'On')
    end
    while strcmp(uscite.Running,'On')
    end
    %%%STOP Real-time acquisition

    %%%POST Acquisition data processing and plotting
    t = 0:1/RateAttuale:(duration-1/RateAttuale);
    ts = linspace(0,duration,length(v_uc));

    output = getdata(ingressi);

    %v_uc = output(:,1)-offv_c;
    i_linea = output(:,2) - off_i_linea;
```

302

```
i_l = output(:,3) - off_i_l;
v_l = output(:,4) - off_v_l;
vel = output(:,5) - off_vel;
coppia = output(:,6) - off_coppia;
v_linea = output(:,8) - off_v_linea;

vel_2 = output(:,9) - off_vel_2;
coppia_2 = output(:,10) - off_coppia_2;
i_l_2 = output(:,11) - off_i_l_2;
v_l_2 = output(:,12) - off_v_l_2;

i_sto = i_linea - i_l - i_l_2;
v_uc = filtrov(v_uc);
v_l = filtrov(v_l);
vel = filtrov(vel);
vel_2 = filtrov(vel_2);
coppia = filtrov(coppia);
coppia_2 = filtrov(coppia_2);
v_linea = filtrov(v_linea);
v_l_2 = filtrov(v_l_2);

delete (ingressi)
clear ingressi
delete (uscite)
clear uscite

P_sub = v_linea.*i_linea;
P_l = v_l.*i_l;
P_m = coppia.*vel*pi/30;
P_l_2 = v_l_2.*i_l_2;
P_m_2 = coppia_2.*vel_2*pi/30;
%P_sto = v_sto.*i_sto;
P_uc = u_uc_est.*iuc;

E_sub = cumsum(P_sub*0.001)/3600;
E_l_2 = cumsum(P_l_2*0.001)/3600;
E_l = cumsum(P_l*0.001)/3600;
E_m = cumsum(P_m*0.001)/3600;
E_m_2 = cumsum(P_m_2*0.001)/3600;
%E_sto = cumsum(P_sto*0.001)/3600;
%E_uc = cumsum(P_uc*0.1)/3600;
E_uc = 0.5*Cuc*(vuc_max^2 - u_uc_est(1:end-1).^2)/3600;
E_kin = 0.5*Jt*((velf(1:end)).^2)/3600;
E_kin_2 = 0.5*Jt_2*((velf2(1:end)).^2)/3600;

close all

figure(1)
plot(t,i_linea),title('Corrente linea')
grid

figure(2)
plot(ts,v_uc,ts,u_uc_est(1:end-1)),title('Tensioni SC misurata e interna
stimata')
hold on
plot(ts,u_uc_ref,'k')
grid
hold off

figure(3)
plot(t,i_l),title('Corrente carico')
%xlabel('Time [s]'),ylabel('Load Current [A]'))
hold on
plot(t,i_l_2,'r'),title('Corrente carico')
hold off
```

303

```
grid

figure(4)
plot(t,v_linea,t,v_l,'r'),title('Tensioni di linea e carico')
hold on
plot(t,v_l_2,'c'),title('Tensioni di carico e linea')
hold off
grid

figure(5)
plot(t,vel),title('Velocità')
hold on
plot(ts,velf*30/pi,'r')
hold on
plot(ts,y_vel_2*30/pi,'g')
grid
hold off

figure(6)
plot(t,coppia),title('Coppia')
grid

figure(7)
plot(ts,i_uc),title('Corrente Scap misurata e riferimento')
hold on
plot(ts,i_uc_est,'r')
hold on
plot(ts,iuc_ref,'k')
grid
hold off

figure(8)
plot(t,E_sub,'k',t,E_l,'r',t,E_l_2,'c',t,(E_m),'m',t,(E_m_2),'b',ts,(E_kin+E_kin
_2),'y',ts,E_uc,'g'),title('Energie')
grid

figure(9)
plot(t,vel_2),title('Velocità 2')
hold on
plot(ts,velf2*30/pi,'r')
hold on
plot(ts,y_vel_2*30/pi,'g')
grid
hold off

figure(10)
plot(t,coppia_2),title('Coppia 2')
grid
```

Appendix A2

C programming script of the REF and CTR state machines for STC strategy

REF machine (REF_Mn.c)

```
/*=============================================================================*/
/* Department of Electrical Engineering  -  University on Naples Federico II                */
/* Group of Converters, Electrical Machines and Drives                                     */
/* Via Claudio, 21, Naples, Italy                                                          */
/*_____*/
/* SCHEDA          : "FPC"  ES789                                                          */
/* SOFTWARE PER        : DSP Texas TMS320VC33                                              */
/* AMBIENTE di PROGETTO  : Texas Code Composer Ver. 4.10.36 c                              */
/* COMPILATORE       : idem                                                                */
/* ASSEMBLATORE       : idem                                                               */
/* LINKER           : idem                                                                 */
/*_____*/
/* AUTHOR          : Flavio Ciccarelli, Diego Iannuzzi, Pietro Tricoli                     */
/* VERSION          : Beta                                                                 */
/* Last Revision Date   : 2012                                                             */
/*_____*/
/*                                                                                         */
/*  REF machine Main file: this machine scales and filter analog inputs                    */
/*_____*/
/*                                                                                         */
/* Modified:                                                                               */
/*=============================================================================*/

#pragma CODE_SECTION(REF_v_SlowMain,"fuori")
#pragma CODE_SECTION(REF_v_SetDefault,"fuori")
#pragma CODE_SECTION(REF_v_Init,"fuori")

#include "User_Ker.h"
#include "..\REF\REF_Out.h"
#include "..\REF\REF_In.h"
#include "..\REF\REF_Var.c"
#include "..\REF\REF_Func.c"

void REF_v_SetDefault(void)
/*_____*/
{
REF_u_sqwave_flag = 1;
REF_f_out = 0.0f;
REF_b_reset_rmp = DEF_TRUE;
```

```
  REF_f_i_nom_dc = 0.0f;
}


void REF_v_Init(void)
/*_____*/
{
 REF_u_sq_wave_time = 0;
 REF_f_sq_wave_period_ms = 50.0f;   //semiperiodo in ms
}


void REF_v_UpdateCfgDpdPar(float f_i_nom_rms)
/*_____*/
{
 REF_f_i_nom_dc = 0.9*f_i_nom_rms;
}


void REF_v_Main(float volatile t_sample)
/*_____*/
{
 float f_rate_coe;

 /*REF_f_dc_curr_in = 3.0* REF_M_f_Get_Pure_In1()* (REF_f_i_nom_dc *0.45)*0.1; // 0.1 = 1/10.0V si assume che
la AIN dia 0:10V*/
 REF_f_dc_curr_in = 300.0f * (REF_M_f_Get_Pure_In1()*0.1 - 0.5f);
          // ^          La massima corrente disponibile per Ramo nel controllo DC/DC = 0.5 *Inom rms
          // |
          // - Qui il Set-Point si intende per l'inverter completo : Somma dei 3 rami
 REF_f_dc_curr_in=(REF_M_b_Rev_IsOn())?(-REF_f_dc_curr_in):(REF_f_dc_curr_in);
 if (REF_M_b_Test_On() == DEF_TRUE)
  {

REF_v_Square_WaveGenerator(&REF_u_sq_wave_time,&REF_f_out,REF_f_sq_wave_period_ms,REF_f_dc_curr_in,
-REF_f_dc_curr_in,&REF_u_sqwave_flag);
  }
 else
  {
  REF_u_sqwave_flag  = 1;
  REF_u_sq_wave_time = TR0_M_u_Get_1ms_Time();  /* Get actual time          */
  if(REF_b_reset_rmp == DEF_FALSE)
   {

  f_rate_coe  = MTH_f_CmptRateLimit_Coeff(10000.0f,t_sample);
  MTH_v_RateLimiter(&REF_f_out,f_rate_coe,REF_f_dc_curr_in);
   }
   else
   {
   REF_f_out = 0.0f;
   }
  }

//REF_f_dc_curr_out =  (REF_M_b_Rev_IsOn())?(-REF_f_out):(REF_f_out);
 REF_f_dc_curr_out =   REF_f_out;
 REF_f_bat_curr_out_c =  0.8*REF_f_out;
 REF_f_bat_curr_out_sc = 1.2*REF_f_out; //Alg.Alter //
```

306

CTR machine (CTR_Mn.c)

```
/*=============================================================================*/
/* Department of Electrical Engineering  -  University on Naples Federico II                    */
/* Group of Converters, Electrical Machines and Drives                                          */
/* Via Caludio, 21, Naples, Italy                                                               */
/*_____*/
/* SCHEDA          : "FPC"  ES789                                                               */
/* SOFTWARE PER      : DSP Texas TMS320VC33                                                     */
/* AMBIENTE di PROGETTO  : Texas Code Composer Ver. 4.10.36 c                                   */
/* COMPILATORE       : idem                                                                     */
/* ASSEMBLATORE      : idem                                                                     */
/* LINKER          : idem                                                                       */
/*_____*/
/* AUTHOR          : Flavio Ciccarelli, Diego Iannuzzi, Pietro Tricoli                          */
/* VERSION          : Beta                                                                      */
/* Last Revision Date  : 2012                                                                   */
/*_____*/
/*                                                                                              */
/*  System manager and Control Algorithm  SW Machine                                            */
/*_____*/
/*                                                                                              */
/* Modified:                                                                                    */
/*=============================================================================*/

#pragma CODE_SECTION(CTR_v_SlowMain,"fuori")         // QUESTA CAUSA Errore del Linker : PC Relative
Overflow
#pragma CODE_SECTION(CTR_v_CtrlReset,"fuori")        // Usare far : QUESTA CAUSA Errore del Linker : PC
Relative Overflow
#pragma CODE_SECTION(CTR_v_StartingReset,"fuori")    // Usare far : QUESTA CAUSA Errore del Linker : PC
Relative Overflow
#pragma CODE_SECTION(CTR_v_SetDefault,"fuori")       // QUESTA CAUSA Errore del Linker : PC Relative
Overflow
#pragma CODE_SECTION(CTR_v_Init,"fuori")         // QUESTA CAUSA Errore del Linker : PC Relative Overflow
#pragma CODE_SECTION(CTR_v_Bg_Main,"fuori")
#pragma CODE_SECTION(CTR_v_UpdateCfgDpdPar,"fuori")
#pragma CODE_SECTION(CTR_v_LimDinPar,"fuori")

#include "User_Ker.h"
#include "..\CTR\CTR_Out.h"
#include "..\CTR\CTR_In.h"
#include "..\CTR\CTR_Var.c"
#include "..\..\User\RWM_Usr.h"
void CTR_v_Main_MAS(void);
inline void CTR_v_Debug(void);
far void CTR_v_CtrlReset();
far void CTR_v_StartingReset(void);
void CTR_v_Bg_Main(void);

#include "..\CTR\CTR_Func.c"

far void CTR_v_CtrlReset()
/*_____*
/
```

```
/* This function resets the variables used by the Control Algorithm                          */
/*_____*
/
{
//--- NOTA : questi in realtà sono i RO della macchina PWM !!
//CTR_f_pwma_ro_r      = 0.0f;
//CTR_f_pwma_ro_s      = 0.0f;
//CTR_f_pwma_ro_t      = 0.0f;
CTR_f_pwmb_ro_u      = 0.0f;
CTR_f_pwmb_ro_v      = 0.0f;
CTR_f_pwmb_ro_w      = 0.0f;

//CTR_f_dcdc_ro_r = 0.0f;
//CTR_f_dcdc_ro_s = 0.0f;
//CTR_f_dcdc_ro_t = 0.0f;

CTR_f_sq_wave_out    = 0.0f;
CTR_b_force_dtcmp    = DEF_FALSE;
CTR_b_disab_dtcmp    = DEF_FALSE;
CTR_f_idc_regstat_s  = 0.0f;
}


far void CTR_v_StartingReset(void)
/*_____*/
{
UIN i;

CTR_v_CtrlReset();
CTR_u_time           = 0            ;/* Reset Actual time                          */
CTR_u_state          = 0            ;
CTR_u_sq_wave_time   = 0            ;
CTR_f_vr             = 0.0          ;/* Phase 'R' voltage (three-phase stator reference)      [V] */
CTR_f_vs             = 0.0          ;/* Phase 'S' voltage (three-phase stator reference)      [V] */
CTR_f_vt             = 0.0          ;/* Phase 'T' voltage (three-phase stator reference)      [V] */
CTR_f_vbus_f         = 560.0        ;
//CTR_u_newperiodcarrier  = 1000     ;/*1kHz*/
}


void CTR_v_SetDefault(void)
/*_____*/
/* Software Machine Initialization after a Reset                            */
/*_____*/
{
/*### STATES and FLAGS INITIALIZATIONS ###################################################*/
CTR_u_cmd            = CTR_U_CMD_NONE; /* Reset the external command to this machine       */
CTR_u_ctrl_on        = DEF_FALSE;    /* Disable the Control (it will wait a Start Command)     */
CTR_u_status         = CTR_U_ST_RESET; /* Init the State Machine                        */
CTR_M_v_Stop_All_Pwm();              /* Stop all PWM                              */
CTR_M_v_Dsg_SetFixed_Zero();         /* The 7 Segment Display will show a "rolling" segment    */
/*#### VARIABLES INITIALIZATION #########################################################*/
CTR_v_StartingReset() ;
}
```

308

```
void CTR_v_Init(float volatile t_sample)
/*_____*/
{
 CTR_f_vout          = 0.0;
 CTR_f_tsample       = t_sample;
 CTR_f_always_zero   = 0.0f;
 CTR_b_force_dtcmp   = DEF_FALSE;
 CTR_b_disab_dtcmp   = DEF_FALSE;
 CTR_f_vsup_min      = 80.0;
 CTR_f_vsup_max      = 136.0;
 CTR_f_isup_err_sc   = 0.0;
 CTR_f_isup_err      = 0.0;
 CTR_f_vdc_sp_s      = 55.0f;
 CTR_f_integ         = 0.0;
 CTR_u_state         = 0;
 CTR_v_Bg_Main();
}

void CTR_v_Main_1(float volatile t_sample)
/*_____*/
/* This function is executed at each FAST Interrupt, after the IPI update and before IPO update        */
/*_____*/
{

 float f_rx,f_ry,f_rz;
 float f_Vdc;
 float f_ierr;
 float f_inv_v2half;
 float f_v1;
 float f_aux;
 float f_sat;
 float f_vbat;
 float f_duty;
 float f_vsup_max;
 float f_vsup_min;
 const float f_ktrasdut_v = 100.0f;//25/1.20f;
 const float f_ktrasdut_i = 20.0f;//10.0f

 /*------------------------------------------------------------------------*/
 f_aux          = CTR_i_Get_FcarrierMax_Mot();

 // f_aux          = 2500;
 f_aux          = (1.0f/f_aux)*1.0e6f;
 CTR_u_newperiodcarrier = (UIN)f_aux; // Periodo Fisico del singolo Ramo IGBT = 3*Ts Motorola

 CTR_f_tsample       = t_sample;
 CTR_v_Main_MAS();
 CTR_u_Pwm_SetNewPeriod(CTR_u_newperiodcarrier) ;

 /*------------------------------------------------------------------------*/

 CTR_f_vdc  = CTR_M_f_Get_Vdc();                     /* Get the actual DC BUS Voltage , Vdc value */
 CTR_f_vdc_riportata = (CTR_f_vdc - 400.0f)*0.1f+5.0f;
 CTR_f_vsup  = f_ktrasdut_v*CTR_M_f_Get_vsup();              //Alg.Alt. //
```

309

```
CTR_f_Get_Isup_Mean = f_ktrasdut_i*CTR_M_f_Get_Isup_Mean();
CTR_f_isup   =  3.0f*CTR_M_f_Get_Idc_Mean();
// CTR_f_isup_ref = CTR_M_f_isup_ref();

CTR_f_vbus_f = ((CTR_f_vdc-CTR_f_vbus_f)*0.1f) +CTR_f_vbus_f;   /* <--ingresso molto filtrato OCCHIO */

/*--- Check: Is The Control Enabled and No alarm is active ? -------------------------------------------*/

/******* Gestione carrier variabile*************/
 // -------- Algoritmo Alternativo ------- //
if((CTR_u_ctrl_on==DEF_TRUE)&&(ALR_M_b_NoAlarms())&&(CTR_f_vdc < 800.0f))
{
 CTR_f_ramo = 0.0f;
 CTR_M_v_Release_Rmp();

 f_sat = (CTR_f_vdc/CTR_f_out_inductance)*100.0;

 f_inv_v2half = 2.0/CTR_f_vdc;

 //--------- Inner LiC current loop CTR-------//
 CTR_f_isup_ref = CTR_M_f_isup_ref();

 if((CTR_f_vsup > CTR_f_vsup_max))
 {
  CTR_u_status = CTR_U_ST_WAIT_UP;              /* Next status = WAIT_UP   */
 }
 if((CTR_f_vsup < CTR_f_vsup_min))
 {
  CTR_u_status  = CTR_U_ST_WAIT_DOWN;          /* Next status = WAIT_DOWN */
 }

 /*CTR_f_isup = CTR_M_f_Get_isup_mean();*/
 CTR_f_isup_err  = CTR_f_isup_ref - CTR_f_isup;
 CTR_f_vs        = MTH_f_PI_Reg_AWU_blk(CTR_f_isup_err,CTR_f_i_kp, CTR_f_i_ki,CTR_f_tsample,
                          -f_sat,f_sat, &CTR_f_idc_regstat_s, DEF_FALSE);

 f_sat = (CTR_f_vdc/CTR_f_out_inductance)*100.0;

 CTR_f_vr = CTR_f_vs;
 CTR_f_vt = CTR_f_vs;
 CTR_f_dcdc_ro_r = ((CTR_f_vr*CTR_f_out_inductance) + CTR_f_vsup)*f_inv_v2half - 1.0;
 CTR_f_dcdc_ro_r = MTH_f_SatMinMaxF(CTR_f_dcdc_ro_r,-1.0,1.0);
 CTR_f_dcdc_ro_s = CTR_f_dcdc_ro_t = CTR_f_dcdc_ro_r;

CTR_M_v_PwmDutyCiclesCompute(1.0,CTR_f_dcdc_ro_r,CTR_f_dcdc_ro_s,CTR_f_dcdc_ro_t,&CTR_f_pwma_ro_r
,&CTR_f_pwma_ro_s,&CTR_f_pwma_ro_t);

 //--- Saturazione delle uscite -------------------------------------------------------------------------------
 CTR_f_pwma_ro_r  = MTH_f_SatMinMaxF(CTR_f_pwma_ro_r,-1.0,1.0);
 CTR_f_pwma_ro_s  = MTH_f_SatMinMaxF(CTR_f_pwma_ro_s,-1.0,1.0);
 CTR_f_pwma_ro_t  = MTH_f_SatMinMaxF(CTR_f_pwma_ro_t,-1.0,1.0);

 f_rx = CTR_f_pwma_ro_r; // Campioniamo qua prima della distorsione dovuta alla centratura dei ro
 f_ry = CTR_f_pwma_ro_s; // Campioniamo qua prima della distorsione dovuta alla centratura dei ro
```

310

```
      f_rz = CTR_f_pwma_ro_t;  // Campioniamo qua prima della distorsione dovuta alla centratura dei ro


   //---- We Set PWM B equal to PWM A -------------------------------------------------------------------------
   /* CTR_f_pwmb_ro_u =  CTR_f_pwma_ro_r;
    CTR_f_pwmb_ro_v =  CTR_f_pwma_ro_s;
    CTR_f_pwmb_ro_w =  CTR_f_pwma_ro_t;

   /*_____Just for a Test we set 'B' PWM duties equal to 'A' PWM ones_____*/
   /*
CTR_v_PwmDutyCiclesCompute(CTR_M_f_Get_Vdc(),CTR_f_vr,CTR_f_vs,CTR_f_vt,&CTR_f_pwmb_ro_u,&CTR
_f_pwmb_ro_v,&CTR_f_pwmb_ro_w);
   */
    CTR_v_Cmpt_Vout_Dc(&CTR_f_vout,CTR_M_f_Get_Vdc(),f_rx,f_ry,f_rz,CTR_f_tsample)  ;
    CTR_f_potenza  = CTR_f_vout * CTR_M_f_Get_Idc_Mean() * 3.0;

    CTR_f_ir       = CTR_M_f_Get_Ir()    ;
    CTR_f_is       = CTR_M_f_Get_Is()    ;
    CTR_f_it       = CTR_M_f_Get_It()    ;
   }
  else   /*....Else, if the control is disabled or an alarm is active : _____*/
   {
    CTR_f_ramo = 4.0f;
    CTR_f_ir          = 0.0f;
    CTR_f_is          = 0.0f;
    CTR_f_it          = 0.0f;
    CTR_f_potenza      = 0.0f;
    CTR_f_vout         = 0.0f;
    CTR_M_v_Reset_Rmp();

    if(CTR_u_resetalr==DEF_TRUE)
     {
     CTR_f_ramo = 5.0f;
     CTR_v_ResetConvertitoreFault();
     }
    else
     {
     CTR_f_ramo = 6.0f;
     CTR_M_v_Stop_All_Pwm();        /*  Stop IGBT switching  (switch all IGBT off)                 */
     }
    CTR_v_CtrlReset();          /*  Reset Control Variables                        */
   }
  }
void CTR_v_Main_2(void)
/*_____*/
/* This function is executed at each FAST Interrupt, after the IPO update                      */
/*_____*/
  {
  }


void CTR_v_SlowMain(void)
/*_____*/
/* This function is executed at each SLOW Interrupt, after the IPI (slow) update and before IPO (slow)update*/
/* it implements a simple State Machine that manage the V/F control of a motor.                  */
/* Here we assume that the user commands starts and stop writing directly CTR_u_cmd via MODBUS        */
```

311

```
/*_____*/
{
}

void CTR_v_Main_MAS(void)
/*_____*/
/* This function is executed at each SLOW Interrupt, after the IPI (slow) update and before IPO (slow)update*/
/* it implements a simple State Machine that manage the V/F control of a motor.                        */
/* Here we assume that the user commands starts and stop writing directly CTR_u_cmd via MODBUS          */
/*_____*/
{
 if(ALR_M_b_AnyAlarm()&& (CTR_u_status != CTR_U_ST_RESET))                    /* If an alarm is active....
*/
  {
   CTR_u_status = CTR_U_ST_ALRM;     /* Next status = ALARM                                */
  }

  /*----- State Machine Implementation ----------------------------------------------------------*/
  switch(CTR_u_status)
  {
   case CTR_U_ST_RESET :                /*<<<<<<< STARTING status after a reset or a power-on         */
    if(ALR_M_b_NoAlarms())
    {
     CTR_M_v_Dsg_SetFixed_Zero();          // Deve rimanere qui, perchè ci può essere ancora allarme.....
     CTR_u_status  = CTR_U_ST_STOP;        /* Next Status = Precharging                       */
    }
    CTR_M_v_Reset_Rmp() ;
    break;

   case CTR_U_ST_STOP :                /*<<<<<<<< STOP status: ready to start, we wait a command      */
    CTR_M_v_Reset_Rmp() ;
    CTR_M_v_Mis_OffsetMeas();
    CTR_M_v_Dsg_SetFixed_Zero();
    CTR_u_ctrl_on = DEF_FALSE;            /* Disable the Control                            */
//  CTR_u_newperiodcarrier  = 1000;        /*1kHz*/
    if((CTR_M_b_StartInput_IsOn())&&(CTR_M_b_MeasuresAreOk()) &&(CTR_b_Activity_Enabled()))
    {
     CTR_M_v_Mis_OffsetSample();
     CTR_v_StartingReset();
     CTR_v_SetCmdConvertitore_ON();          /* Enable PWM switching on side 'A'                */
     CTR_u_status      = CTR_U_ST_RUN;      /* Next status = RUN                        */
     CTR_u_check_pwm_time = TR0_M_u_Get_1ms_Time();
     CTR_b_check_pwm    = DEF_FALSE;
    }
    break;

   case CTR_U_ST_RUN  :               /*<<<<<<< RUN status: the inverter is switching and the control is On    */
    CTR_M_v_Dsg_SetRollMode();          /* The 7 Segment Display will show a "rolling" segment          */
    if(CTR_M_b_StartInput_IsOff() || (CTR_b_Activity_Enabled()==DEF_FALSE))
    {
     CTR_v_SetCmdConvertitore_OFF();        /* Disable PWM switching on side 'A'               */
     CTR_u_status = CTR_U_ST_STOP;          /* Next status = STOP                        */
    }
    else
```

312

```
     {
      CTR_M_v_Release_Rmp();
      if(CTR_M_b_Dgi_Not_Enabled())
      {
       CTR_b_check_pwm      = DEF_FALSE;
       CTR_u_check_pwm_time  = TR0_M_u_Get_1ms_Time();
      }
      else
      {
       if((TR0_u_Elapsed_1ms(CTR_u_check_pwm_time) > 5) || (CTR_b_check_pwm==DEF_TRUE))
       {
        CTR_b_check_pwm      = DEF_TRUE;
        CTR_u_check_pwm_time  = TR0_M_u_Get_1ms_Time();
        if(CTR_M_b_PWMA_Not_Enabled())
        {
         ALR_M_v_SetAlrm(ALR_U_CODE_PWMA_NOT_PWONA); /* Cause a proper alarm                          */
        }
       }
      }
     }
     break;

    case CTR_U_ST_WAIT_UP :                    /*<<<<<<<< WAIT status: the inverter is switching and the control is On
*/
     CTR_M_v_Dsg_SetRollMode();          /* The 7 Segment Display will show a "rolling" segment              */
     if(CTR_M_b_StartInput_IsOff() || (CTR_b_Activity_Enabled()==DEF_FALSE))
     {
      CTR_v_SetCmdConvertitore_OFF();         /* Disable PWM switching on side 'A'              */
      CTR_u_status = CTR_U_ST_STOP;           /* Next status = STOP                         */
     }
     else
     {
      if(CTR_f_vsup < CTR_f_vsup_max)
             {
             CTR_M_v_Mis_OffsetSample();
             //CTR_v_StartingReset();
             CTR_v_SetCmdConvertitore_ON();             /* Enable PWM switching on side 'A'              */
             CTR_u_status       = CTR_U_ST_RUN;        /* Next status = RUN                          */
             CTR_u_check_pwm_time = TR0_M_u_Get_1ms_Time();
             CTR_b_check_pwm      = DEF_FALSE;
             }
     }
     break;

    case CTR_U_ST_WAIT_DOWN  :                    /*<<<<<<<< WAIT status: the inverter is switching and the control is
On     */
     CTR_M_v_Dsg_SetRollMode();          /* The 7 Segment Display will show a "rolling" segment              */
     if(CTR_M_b_StartInput_IsOff() || (CTR_b_Activity_Enabled()==DEF_FALSE))
     {
      CTR_v_SetCmdConvertitore_OFF();         /* Disable PWM switching on side 'A'              */
      CTR_u_status = CTR_U_ST_STOP;           /* Next status = STOP                         */
     }
     else
     {
```

313

```
   if(CTR_f_vsup < CTR_f_vsup_min)
          {
          CTR_M_v_Mis_OffsetSample();
   //     CTR_v_StartingReset();
          CTR_v_SetCmdConvertitore_ON();          /* Enable PWM switching on side 'A'                */
          CTR_u_status      = CTR_U_ST_RUN;       /* Next status = RUN                    */
          CTR_u_check_pwm_time = TR0_M_u_Get_1ms_Time();
          CTR_b_check_pwm    = DEF_FALSE;
          }
    }
    break;

   default:
   CTR_M_v_Reset_Rmp() ;
   CTR_u_status = CTR_U_ST_ALRM;          /*<<<<<<<  ALARM status                          */
   CTR_M_v_Mis_OffsetMeas();
   CTR_b_check_pwm     = DEF_FALSE;
   break;
   }

  if(CTR_u_status ==CTR_U_ST_ALRM)
  {
  CTR_M_v_Reset_Rmp() ;
//CTR_u_newperiodcarrier = 1250;      // Con 1250 abbiamo 400us di esecuzione FAST
  CTR_v_SetCmdConvertitore_OFF();          /* Disable PWM switching on side 'A'              */
  if(CTR_u_resetalr==DEF_TRUE)
   {
   CTR_v_ResetConvertitoreFault();
   CTR_u_status  = CTR_U_ST_RESET;
   }
  }
 CTR_u_ctrl_on = (CTR_u_status==CTR_U_ST_RUN);
}


void CTR_v_Bg_Main(void)
/*_____*/
/*_____*/
{
 float f_aux,f_aux1,f_aux2,f_pnom,f_taurot,f_delta;

 //LIMITAZIONE DINAMICA DEI PARAMETRI FUNZIONE DELLA I nominale motore
 CTR_v_LimDinPar();
 CTR_f_out_inductance       = (float)(RWM_M_u_FalseInts_2_Uin_Conv(CTR_i_outinductance))*0.00001f;  // unità
da 10 micro Henry
```

314

Appendix A3

Matlab script of the supervisory program for LVTC strategy

```
%%% file name: chopper_LiC_stationary_2car_LVTC_niusb.m %%%
clc
clear all
close all

duration=60; % Acquisition time

vuc_max = 135.0; %%% LiC max voltage
vuc_min = 80;    %%% LiC min voltage

k = 1.0;  %losses factor vehicle 1
k2 = 1.0; %losses factor vehicle 2
i_limite = 135;  %%% DCDC converter max output current
v_line_ref = 510;        %%% Vline ref value
kp_l = 12.5*1.2*0.7*135; %%% Proportional constant Reg L
ki_l = 15;               %%% Integral constant Reg L
v_uc_int = 0;

kp_u = 12.5*1.2*0.7*135; %%% Proportional constant Reg u
ki_u = 15;               %%% Integral constant Reg u
i_uc_int=0;


%%%NI-DAQ initialization%%%
%%%Analog inputs
ingressi = analoginput('nidaq','dev1');

addchannel(ingressi,0,'tensionescaps');%%%%%% morsetto(7,8) del sinus penta
addchannel(ingressi,1,'corrente_linea');
addchannel(ingressi,2,'corrente_carico');
addchannel(ingressi,3,'tensione_carico');  %%% tensione (al pantografo) a monte
dell'inverter
addchannel(ingressi,4,'velocita');   %%% velocità in rpm
addchannel(ingressi,5,'coppia');
addchannel(ingressi,6,'corr_uc');%%%%%% morsetto(5,6) del sinus penta
addchannel(ingressi,7,'tensione_linea'); %%% tensione di sottostazione
addchannel(ingressi,16,'velocita_2');
addchannel(ingressi,17,'coppia_2');
addchannel(ingressi,18,'corrente_carico_2');
addchannel(ingressi,19,'tensione_carico_2');
addchannel(ingressi,20,'tensione_storage');

Tc = 1/10;
RateAttuale = 1000; %DAQ sampling frequency

set(ingressi,'SampleRate',RateAttuale);
set(ingressi,'SamplesPerTrigger',duration*RateAttuale)

%%%%%%%%%CHANNEL SETTINGS%%%%%%%%%%%%%%%%%%
```

```matlab
ingressi.tensionescaps.sensorrange = [-10 10];
ingressi.tensionescaps.unitsrange  = [-1000 1000];
ingressi.tensionescaps.inputrange  = [-10 10];

ingressi.corrente_linea.sensorrange = [-10 10];
ingressi.corrente_linea.unitsrange  = [-100 100];
ingressi.corrente_linea.inputrange  = [-10 10];

ingressi.corrente_carico.sensorrange    = [-10 10];
ingressi.corrente_carico.unitsrange     = [-100 100];
ingressi.corrente_carico.inputrange     = [-10 10];

ingressi.tensione_carico.sensorrange       = [-10 10];
ingressi.tensione_carico.unitsrange        = [-1000 1000];
ingressi.tensione_carico.inputrange        = [-10 10];

ingressi.velocita.sensorrange     = [-10 10];
ingressi.velocita.unitsrange      = [-1500 1500];
ingressi.velocita.inputrange      = [-10 10];

ingressi.coppia.sensorrange     = [-10 10];
ingressi.coppia.unitsrange      = [-250 250];
ingressi.coppia.inputrange      = [-10 10];

ingressi.corr_uc.sensorrange    = [-10 10];
ingressi.corr_uc.unitsrange     = [-200 200];
ingressi.corr_uc.inputrange     = [-10 10];

ingressi.tensione_linea.sensorrange      = [-10 10];
ingressi.tensione_linea.unitsrange       = [-1000 1000];
ingressi.tensione_linea.inputrange       = [-10 10];

ingressi.velocita_2.sensorrange     = [-10 10];
ingressi.velocita_2.unitsrange      = [-60*60/2 60*60/2];
ingressi.velocita_2.inputrange      = [-10 10];

ingressi.coppia_2.sensorrange     = [-10 10];
ingressi.coppia_2.unitsrange      = [-200 200];
ingressi.coppia_2.inputrange      = [-10 10];

ingressi.corrente_carico_2.sensorrange   = [-10 10];
ingressi.corrente_carico_2.unitsrange    = [-137 137];
ingressi.corrente_carico_2.inputrange    = [-10 10];

ingressi.tensione_carico_2.sensorrange      = [-10 10];
ingressi.tensione_carico_2.unitsrange       = [-837 837];
ingressi.tensione_carico_2.inputrange       = [-10 10];

ingressi.tensione_storage.sensorrange       = [-10 10];
ingressi.tensione_storage.unitsrange        = [-837 837];
ingressi.tensione_storage.inputrange        = [-10 10];

%%%Analog outputs
uscite = analogoutput('nidaq','dev1');
addchannel(uscite,0,{'chopper'});%%%%%% riferimento corrente sc morsetto(2,1)
del sinus penta
addchannel(uscite,1,{'Load1_Speed_ref'});
addchannel(uscite,2,{'Load2_Speed_ref'});

set(uscite,'SampleRate', RateAttuale);

uscite.chopper.OutputRange = [-10 10];
uscite.chopper.unitsrange = [-300 300]; %%Per trasformare il segnale di uscita
in single-ended
```

316

```matlab
uscite.Load1_Speed_ref.OutputRange = [-10 10];
uscite.Load1_Speed_ref.unitsrange = [-1500 1500]; %%Velocita max inverter
impostata a 1500 rpm

uscite.Load2_Speed_ref.OutputRange = [-10 10];
uscite.Load2_Speed_ref.unitsrange = [-60 60]; %%Velocita max inverter 2
impostata a 1500 rpm
%%%END NI-DAQ Initialization

%%%Set Offset misure
off_v_uc      = 0.07560073260074;
off_i_linea   = 0.21163858363860;
off_i_l       = 0.20539926739927;
off_v_l       = 0.06456654456656;
off_vel       = 3.08542124542158;
off_coppia    = 0.12547008547010;
off_i_uc      = 0.02334554334554;
off_v_linea   = 0.29346764346772;
off_vel_2     = 1.01186446886427;
off_coppia_2 = 0.15595115995120;
off_i_l_2     = 0.139073740508068;
off_v_l_2     = 0.712829910327122;

f = figure;
set(f,'doublebuffer','on') %Reduce plot flicker

%%%%START real-time acquisition
start(ingressi)

i = 1;
w = 1;
tc = 1;

kdurata = duration*Tc;

t = 0;
for j = 1:kdurata
    x = [];
    y_iuc = [];
    y_pot = [];
    y_vuc = [];
    y_vref = [];
    y_i_linea = [];
    y_i_carico = [];
    y_v_carico = [];
    y_i_carico_2 = [];
    y_v_carico_2 = [];

    stampe_2; %%%Real-time plot acquired data

    while ingressi.SamplesAcquired < j*ingressi.SamplesPerTrigger/kdurata
        while ingressi.SamplesAcquired < RateAttuale*i*Tc
        end

        %%%%%%%%%%%%%%%%%%%%%%%%%%%%%%%%%%%
        %%% Speed profiles of the 1st vehicle in rpm
        vel1_ref(1:(100)) = 1225;
        vel1_ref((100 + 1):(345)) = 1225;
        vel1_ref((345 + 1):(6*100)) = 0;

        %%% Speed profiles of the 2nd vehicle in rpm
        vel2_ref(1:(125)) = 0;
        vel2_ref((125 + 1):(449)) = 2*1500/60;%2*1200/75;
        vel2_ref((450 + 1):(6*100)) = 0;
        %%%%%%%%%%%%%%%%%%%%%%%%%%%%%%%%%%%%%
```

317

```
        data = peekdata(ingressi, RateAttuale*Tc);

        %%%%% EVALUATION of v_lic_ref by means of PI regulator Reg L %%%%%
        v_uc(i) = mean(data(:,1)) - off_v_uc;

        v_uc_int = v_uc_int + ki_l*(y_v_sto(i) - v_line_ref)*Ts;
        v_uc_ref(i) = kp_l*(y_v_sto(i) - v_line_ref) + v_uc_int;

        %%%%Antiwindup action on v_lic_ref
        if (v_uc_ref(i)>vuc_max)
            v_uc_ref(i) = 0.95*vuc_max;
            v_uc_int = v_uc_int - ki_l*(y_v_sto(i) - v_line_ref)*Ts;
        elseif (v_uc_ref(i)<vuc_min)
            v_uc_ref(i) = 1.05*vuc_min;
            v_uc_int = v_uc_int - ki_l*(y_v_sto(i) - v_line_ref)*Ts;
        end

        %%%%%%%%%%%%%%%%%%%%%%%%%%%%%%%%%%%%%%%%%%%%%%%%%%%%%
        %%%% EVALUATION OF i_lic_ref by means of PI regulator Reg u %%%%
        i_uc(i) = mean(data(:,7)) - off_i_uc;

        i_uc_int = i_uc_int + ki_u*(v_uc_ref(i) - y_vuc(i))*Ts;
        out(i) = (kp_u*(v_uc_ref(i) - y_vuc(i)) + i_uc_int) + 150.9;

        %%%%Antiwindup action on i_lic_ref
        if (out(i)>i_limite + 150.9)
            out(i) = i_limite + 150.9;
            i_uc_int = i_uc_int - ki_u*(v_uc_ref(i) - y_vuc(i))*Ts;
        elseif (out(i)<-i_limite + 150.9)
            out(i) = -i_limite + 150.9;
            i_uc_int = i_uc_int - ki_u*(v_uc_ref(i) - y_vuc(i))*Ts;
        end

        ref(1:100)= -(out(i) - 150.9); % i_lic_ref %corrente uc di riferimento;
        iuc_ref(i) = mean(ref);
        b(1:100)= u_uc_ref(i);
        %putsample(uscite,out(i));
        putsample(uscite,[out(i),vel1_ref(i),vel2_ref(i)]); %%%%Send the LiC
current set-point to the DCDC Converter%%%

        x1=((w-1)*RateAttuale*Tc):(RateAttuale*Tc*w-1);
        x=[x x1];
        y_iuc = [y_iuc;data(:,7) - off_i_uc];
        y_pot = [y_pot ;ref'];
        y_vuc = [y_vuc ;data(:,1) - off_v_uc];
        y_vref = [y_vref ;b.'];
        y_i_linea = [y_i_linea ;data(:,2) - off_i_linea];
        y_i_carico = [y_i_carico ;data(:,3) - off_i_l];
        y_v_carico = [y_v_carico ;data(:,4) - off_v_l];
        y_i_carico_2 = [y_i_carico_2 ;data(:,11) - off_i_l_2];
        y_v_carico_2 = [y_v_carico_2 ;data(:,12) - off_v_l_2];

        set(iuc,'ydata',y_iuc);
        set(rif,'ydata',y_pot);
        set(vuc,'ydata',y_vuc);
        set(vref,'ydata',y_vref);
        set(ilinea,'ydata',y_i_linea);
        set(icarico,'ydata',y_i_carico);
        set(vcarico,'ydata',y_v_carico);
        set(icarico2,'ydata',y_i_carico_2);
        set(vcarico2,'ydata',y_v_carico_2);

        set(iuc,'xdata',x);
        set(rif,'xdata',x);
```

```matlab
        set(vuc,'xdata',x);
        set(vref,'xdata',x);
        set(ilinea,'xdata',x);
        set(icarico,'xdata',x);
        set(vcarico,'xdata',x);
        set(icarico2,'xdata',x);
        set(vcarico2,'xdata',x);

        drawnow
        t = t+1;
        w = w + 1;
        i = i + 1;
    end
    w = 1;
end

%wait until the acquisition is not ended
while strcmp(ingressi.Running,'On')
end
while strcmp(uscite.Running,'On')
end
%%%STOP Real-time acquisition

%%%POST Acquisition data processing and plotting
t = 0:1/RateAttuale:(duration-1/RateAttuale);
ts = linspace(0,duration,length(v_uc));

output = getdata(ingressi);

%v_uc = output(:,1)-offv_c;
i_linea = output(:,2) - off_i_linea;
i_l = output(:,3) - off_i_l;
v_l = output(:,4) - off_v_l;
vel = output(:,5) - off_vel;
coppia = output(:,6) - off_coppia;
v_linea = output(:,8) - off_v_linea;

vel_2 = output(:,9) - off_vel_2;
coppia_2 = output(:,10) - off_coppia_2;
i_l_2 = output(:,11) - off_i_l_2;
v_l_2 = output(:,12) - off_v_l_2;

i_sto = i_linea - i_l - i_l_2;
v_uc = filtrov(v_uc);
v_l = filtrov(v_l);
vel = filtrov(vel);
vel_2 = filtrov(vel_2);
coppia = filtrov(coppia);
coppia_2 = filtrov(coppia_2);
v_linea = filtrov(v_linea);
v_l_2 = filtrov(v_l_2);

delete (ingressi)
clear ingressi
delete (uscite)
clear uscite

P_sub = v_linea.*i_linea;
P_l = v_l.*i_l;
P_m = coppia.*vel*pi/30;
P_l_2 = v_l_2.*i_l_2;
P_m_2 = coppia_2.*vel_2*pi/30;
P_uc = u_uc_est.*iuc;

E_sub = cumsum(P_sub*0.001)/3600;
```

319

```
E_l_2 = cumsum(P_l_2*0.001)/3600;
E_l = cumsum(P_l*0.001)/3600;
E_m = cumsum(P_m*0.001)/3600;
E_m_2 = cumsum(P_m_2*0.001)/3600;
E_uc = 0.5*Cuc*(vuc_max^2 - v_uc.^2)/3600;
E_kin = 0.5*Jt*((vel).^2)/3600;
E_kin_2 = 0.5*Jt_2*((vel_2).^2)/3600;

close all

figure(1)
plot(t,i_linea),title('Corrente linea')
grid

figure(2)
plot(ts,v_uc,ts,u_uc_est(1:end-1)),title('Tensioni SC misurata e interna
stimata')
hold on
plot(ts,u_uc_ref,'k')
grid
hold off

figure(3)
plot(t,i_l),title('Corrente carico')
hold on
plot(t,i_l_2,'r'),title('Corrente carico_2')
hold off
grid

figure(4)
plot(t,v_linea,t,v_l,'r'),title('Tensioni di linea e carico')
hold on
plot(t,v_l_2,'c'),title('Tensioni di carico e linea')
hold off
grid

figure(5)
plot(t,vel),title('Velocità')
grid

figure(6)
plot(t,coppia),title('Coppia')
grid

figure(7)
plot(ts,i_uc),title('Corrente Scap misurata e riferimento')
hold on
plot(ts,iuc_ref,'k')
grid

figure(8)
plot(t,E_sub,'k',t,E_l,'r',t,E_l_2,'c',t,(E_m),'m',t,(E_m_2),'b',ts,(E_kin+E_kin
_2),'y',ts,E_uc,'g'),title('Energie')
grid

figure(9)
plot(t,vel_2),title('Velocità 2')
grid

figure(10)
plot(t,coppia_2),title('Coppia 2')
grid
```

320

Appendix A4

C programming script of the CTR state machines for LCSC strategy

```
/*==============================================================================*/
/* Department of Electrical Engineering  -  University on Naples Federico II                    */
/* Group of Converters, Electrical Machines and Drives                                          */
/* Via Caludio, 21, Naples, Italy                                                               */
/*_____*/
/* SCHEDA            : "FPC"  ES789                                                             */
/* SOFTWARE PER       : DSP Texas TMS320VC33                                                    */
/* AMBIENTE di PROGETTO : Texas Code Composer Ver. 4.10.36 c                                    */
/* COMPILATORE        : idem                                                                    */
/* ASSEMBLATORE       : idem                                                                    */
/* LINKER          : idem                                                                       */
/*_____*/
/* AUTHOR            : Flavio Ciccarelli, Diego Iannuzzi, Pietro Tricoli                        */
/* VERSION           : Beta                                                                     */
/* Last Revision Date  : 2012                                                                   */
/*_____*/
/*                                                                                              */
/*  System manager and Control Algorithm  SW Machine                                            */
/*_____*/
/*                                                                                              */
/* Modified:                                                                                    */
/*==============================================================================*/
#pragma CODE_SECTION(CTR_v_SlowMain,"fuori")        // QUESTA CAUSA Errore del Linker : PC Relative
Overflow
#pragma CODE_SECTION(CTR_v_CtrlReset,"fuori")       // Usare far : QUESTA CAUSA Errore del Linker : PC
Relative Overflow
#pragma CODE_SECTION(CTR_v_StartingReset,"fuori")   // Usare far : QUESTA CAUSA Errore del Linker : PC
Relative Overflow
#pragma CODE_SECTION(CTR_v_SetDefault,"fuori")      // QUESTA CAUSA Errore del Linker : PC Relative
Overflow
#pragma CODE_SECTION(CTR_v_Init,"fuori")            // QUESTA CAUSA Errore del Linker : PC Relative Overflow
#pragma CODE_SECTION(CTR_v_Bg_Main,"fuori")
#pragma CODE_SECTION(CTR_v_UpdateCfgDpdPar,"fuori")
#pragma CODE_SECTION(CTR_v_LimDinPar,"fuori")

#include "User_Ker.h"
#include "..\CTR\CTR_Out.h"
#include "..\CTR\CTR_In.h"
#include "..\CTR\CTR_Var.c"
#include "..\..\User\RWM_Usr.h"
```

```c
void CTR_v_Main_MAS(void);
inline void CTR_v_Debug(void);
far void CTR_v_CtrlReset();
far void CTR_v_StartingReset(void);
void CTR_v_Bg_Main(void);

#include "..\CTR\CTR_Func.c"

far void CTR_v_CtrlReset()
/*_____*/
/* This function resets the variables used by the Control Algorithm            */
/*_____*/
{
//--- NOTA : questi in realtà sono i RO della macchina PWM !!
//CTR_f_pwma_ro_r     = 0.0f;
//CTR_f_pwma_ro_s     = 0.0f;
//CTR_f_pwma_ro_t     = 0.0f;
CTR_f_pwmb_ro_u     = 0.0f;
CTR_f_pwmb_ro_v     = 0.0f;
CTR_f_pwmb_ro_w     = 0.0f;

//CTR_f_dcdc_ro_r = 0.0f;
//CTR_f_dcdc_ro_s = 0.0f;
//CTR_f_dcdc_ro_t = 0.0f;

CTR_f_sq_wave_out   = 0.0f;
CTR_b_force_dtcmp   = DEF_FALSE;
CTR_b_disab_dtcmp   = DEF_FALSE;
CTR_f_idc_regstat_s = 0.0f;
}

far void CTR_v_StartingReset(void)
/*_____*/
{
UIN i;

CTR_v_CtrlReset();
CTR_u_time          = 0          ;/* Reset Actual time                        */
CTR_u_state         = 0          ;
CTR_u_sq_wave_time  = 0          ;
CTR_f_vr            = 0.0        ;/* Phase 'R' voltage (three-phase stator reference)   [V] */
CTR_f_vs            = 0.0        ;/* Phase 'S' voltage (three-phase stator reference)   [V] */
CTR_f_vt            = 0.0        ;/* Phase 'T' voltage (three-phase stator reference)   [V] */
CTR_f_vbus_f        = 560.0      ;
//CTR_u_newperiodcarrier = 1000   ;/*1kHz*/
}

void CTR_v_SetDefault(void)
/*_____*/
/* Software Machine Initialization after a Reset                    */
/*_____*/
{
```

322

```
/*###                    STATES              and              FLAGS              INITIALIZATIONS
################################################################*/
CTR_u_cmd            = CTR_U_CMD_NONE; /* Reset the external command to this machine        */
CTR_u_ctrl_on        = DEF_FALSE;     /* Disable the Control (it will wait a Start Command)     */
CTR_u_status         = CTR_U_ST_RESET; /* Init the State Machine                          */
CTR_M_v_Stop_All_Pwm();               /* Stop all PWM                                */
CTR_M_v_Dsg_SetFixed_Zero();          /* The 7 Segment Display will show a "rolling" segment    */
/*####                              VARIABLES                              INITIALISATION
##########################################################################*/
CTR_v_StartingReset() ;
}

void CTR_v_Init(float volatile t_sample)
/*_____*/
{
CTR_f_vout           = 0.0;
CTR_f_tsample        = t_sample;
CTR_f_always_zero    = 0.0f;
CTR_b_force_dtcmp    = DEF_FALSE;
CTR_b_disab_dtcmp    = DEF_FALSE;
CTR_f_vsup_min       = 80.0;
CTR_f_vsup_max       = 136.00;
CTR_f_ibat_err_sc    = 0.0;
CTR_f_ibat_err       = 0.0;
CTR_f_vdc_sp_s       = 55.0f;
CTR_f_integ          = 0.0;
CTR_u_state          = 0;
CTR_v_Bg_Main();
}

void CTR_v_Main_1(float volatile t_sample)
/*_____*/
/* This function is executed at each FAST Interrupt, after the IPI update and before IPO update        */
/*_____*/
{

float f_rx,f_ry,f_rz;
float f_Vdc;
float f_ierr;
float f_inv_v2half;
float f_v1;
float f_aux;
float f_sat;
float f_vbat;
float f_duty;
// float f_vsup_max;
// float f_vsup_min;
float f_ktrasdut_v = 100.0f;//25/1.20f;
float f_ktrasdut_i = 10.0f;

/*-----------------------------------------------------------------------*/
f_aux            = CTR_i_Get_FcarrierMax_Mot();

// f_aux           = 2500;
```

323

```
f_aux            = (1.0f/f_aux)*1.0e6f;
CTR_u_newperiodcarrier = (UIN)f_aux;    // Periodo Fisico del singolo Ramo IGBT = 3*Ts Motorola

CTR_f_tsample     = t_sample;
CTR_v_Main_MAS();
CTR_u_Pwm_SetNewPeriod(CTR_u_newperiodcarrier) ;

/*--------------------------------------------------------------------------*/

CTR_f_vdc    = CTR_M_f_Get_Vdc();                    /* Get the actual DC BUS Voltage , Vdc value */
CTR_f_vdc_riportata = (CTR_f_vdc - 400.0f)*0.1f+5.0f;
CTR_f_vsup   = f_ktrasdut_v*CTR_M_f_Get_vsup();          //Alg.Alt. //
CTR_f_Get_Ibat_Mean = f_ktrasdut_i*CTR_M_f_Get_Ibat_Mean();
CTR_f_isup   = 3.0f*CTR_M_f_Get_Idc_Mean();
// CTR_f_ibat_ref = CTR_M_f_ibat_ref();

CTR_f_vbus_f = ((CTR_f_vdc-CTR_f_vbus_f)*0.1f) +CTR_f_vbus_f;    /* <--ingresso molto filtrato OCCHIO */

/*--- Check: Is The Control Enabled and No alarm is active ? -------------------------------------------*/

/******* Gestione carrier variabile**************/
 // -------- Algoritmo Alternativo ------- //
if((CTR_u_ctrl_on==DEF_TRUE)&&(ALR_M_b_NoAlarms()))&&(CTR_f_vdc < 800.0f))
{
 CTR_f_ramo = 0.0f;
 CTR_M_v_Release_Rmp();

 f_sat = (CTR_f_vdc/CTR_f_out_inductance)*100.0;
  f_inv_v2half = 2.0/CTR_f_vdc;
 CTR_f_ibat_ref = CTR_M_f_ibat_ref();

 /* Changeover finite state line current control */

 if((CTR_f_vsup > CTR_f_vsup_max)&&(CTR_f_Get_Ibat_Mean < CTR_f_ibat_ref))
 {
  CTR_u_status = CTR_U_ST_WAIT_UP;              /* Next status = WAIT_UP   */
 }
 if((CTR_f_vsup < CTR_f_vsup_min)&&(CTR_f_Get_Ibat_Mean > CTR_f_ibat_ref))
 {
  CTR_u_status  = CTR_U_ST_WAIT_DOWN;           /* Next status = WAIT_DOWN */
 }

 CTR_f_ibat_err   = CTR_f_ibat_ref - CTR_f_Get_Ibat_Mean;

/*CTR_f_ibat_err   = CTR_f_ibat_ref - CTR_f_isup;*/
 CTR_f_vs       = MTH_f_PI_Reg_AWU_blk(CTR_f_ibat_err,CTR_f_i_kp, CTR_f_i_ki,CTR_f_tsample,
                           -f_sat,f_sat, &CTR_f_idc_regstat_s, DEF_FALSE);

 f_sat = (CTR_f_vdc/CTR_f_out_inductance)*100.0;

   //--- Calcolo dei 3 regolatori PI di corrente sulle 3 fasi ---------------------------------------------
 CTR_f_vr = CTR_f_vs;
 CTR_f_vt = CTR_f_vs;
 CTR_f_dcdc_ro_r  = ((CTR_f_vr*CTR_f_out_inductance) + CTR_f_vsup)*f_inv_v2half - 1.0;
```

324

```
CTR_f_dcdc_ro_r = MTH_f_SatMinMaxF(CTR_f_dcdc_ro_r,-1.0,1.0);
CTR_f_dcdc_ro_s = CTR_f_dcdc_ro_t = CTR_f_dcdc_ro_r;

CTR_M_v_PwmDutyCiclesCompute(1.0,CTR_f_dcdc_ro_r,CTR_f_dcdc_ro_s,CTR_f_dcdc_ro_t,&CTR_f_pwma_ro_r
,&CTR_f_pwma_ro_s,&CTR_f_pwma_ro_t);

 //--- Saturazione delle uscite -----------------------------------------------------------------
 CTR_f_pwma_ro_r = MTH_f_SatMinMaxF(CTR_f_pwma_ro_r,-1.0,1.0);
 CTR_f_pwma_ro_s = MTH_f_SatMinMaxF(CTR_f_pwma_ro_s,-1.0,1.0);
 CTR_f_pwma_ro_t = MTH_f_SatMinMaxF(CTR_f_pwma_ro_t,-1.0,1.0);

 f_rx = CTR_f_pwma_ro_r; // Campioniamo qua prima della distorsione dovuta alla centratura dei ro
 f_ry = CTR_f_pwma_ro_s; // Campioniamo qua prima della distorsione dovuta alla centratura dei ro
 f_rz = CTR_f_pwma_ro_t; // Campioniamo qua prima della distorsione dovuta alla centratura dei ro

 //---- We Set PWM B equal to PWM A ---------------------------------------------------------------
 /* CTR_f_pwmb_ro_u = CTR_f_pwma_ro_r;
 CTR_f_pwmb_ro_v = CTR_f_pwma_ro_s;
 CTR_f_pwmb_ro_w = CTR_f_pwma_ro_t;

 /*_____Just for a Test we set 'B' PWM duties equal to 'A' PWM ones_____*/
 /*
CTR_v_PwmDutyCiclesCompute(CTR_M_f_Get_Vdc(),CTR_f_vr,CTR_f_vs,CTR_f_vt,&CTR_f_pwmb_ro_u,&CTR
_f_pwmb_ro_v,&CTR_f_pwmb_ro_w);
 */
 CTR_v_Cmpt_Vout_Dc(&CTR_f_vout,CTR_M_f_Get_Vdc(),f_rx,f_ry,f_rz,CTR_f_tsample)  ;
 CTR_f_potenza = CTR_f_vout * CTR_M_f_Get_Idc_Mean() * 3.0;

 CTR_f_ir     = CTR_M_f_Get_Ir()   ;
 CTR_f_is     = CTR_M_f_Get_Is()   ;
 CTR_f_it     = CTR_M_f_Get_It()   ;
 }
 else   /*....Else, if the control is disabled or an alarm is active : _____*/
 {
  CTR_f_ramo = 4.0f;
  CTR_f_ir          = 0.0f;
  CTR_f_is          = 0.0f;
  CTR_f_it          = 0.0f;
  CTR_f_potenza     = 0.0f;
  CTR_f_vout        = 0.0f;
  CTR_M_v_Reset_Rmp();

  if(CTR_u_resetalr==DEF_TRUE)
  {
  CTR_f_ramo = 5.0f;
  CTR_v_ResetConvertitoreFault();
  }
  else
  {
  CTR_f_ramo = 6.0f;
  CTR_M_v_Stop_All_Pwm();        /* Stop IGBT switching  (switch all IGBT off)              */
  }
  CTR_v_CtrlReset();             /* Reset Control Variables                          */
 }
```

325

```c
}
void CTR_v_Main_2(void)
/*_____*/
/* This function is executed at each FAST Interrupt, after the IPO update                    */
/*_____*/
{
}
void CTR_v_SlowMain(void)
/*_____*/
/* This function is executed at each SLOW Interrupt, after the IPI (slow) update and before IPO (slow)update*/
/* it implements a simple State Machine that manage the V/F control of a motor.              */
/* Here we assume that the user commands starts and stop writing directly CTR_u_cmd via MODBUS   */
/*_____*/
{
}
void CTR_v_Main_MAS(void)
/*_____*/
/* This function is executed at each SLOW Interrupt, after the IPI (slow) update and before IPO (slow)update*/
/* it implements a simple State Machine that manage the V/F control of a motor.              */
/* Here we assume that the user commands starts and stop writing directly CTR_u_cmd via MODBUS   */
/*_____*/
{
  if(ALR_M_b_AnyAlarm()&& (CTR_u_status != CTR_U_ST_RESET))                    /* If an alarm is active....
*/
  {
    CTR_u_status = CTR_U_ST_ALRM;     /* Next status = ALARM                        */
  }

  /*----- State Machine Implementation ----------------------------------------------------------*/
  switch(CTR_u_status)
  {
  case CTR_U_ST_RESET :                    /*<<<<<< STARTING status after a reset or a power-on           */
    if(ALR_M_b_NoAlarms())
    {
      CTR_M_v_Dsg_SetFixed_Zero();         // Deve rimanere qui, perchè ci può essere ancora allarme.....
      CTR_u_status  = CTR_U_ST_STOP;         /* Next Status = Precharging                    */
    }
    CTR_M_v_Reset_Rmp() ;
    break;

  case CTR_U_ST_STOP :                     /*<<<<<<< STOP status: ready to start, we wait a command        */
    CTR_M_v_Reset_Rmp() ;
    CTR_M_v_Mis_OffsetMeas();
    CTR_M_v_Dsg_SetFixed_Zero();
    CTR_u_ctrl_on = DEF_FALSE;            /* Disable the Control                        */
//  CTR_u_newperiodcarrier  = 1000;      /*1kHz*/
    if((CTR_M_b_StartInput_IsOn())&&(CTR_M_b_MeasuresAreOk()) &&(CTR_b_Activity_Enabled()))
    {
      CTR_M_v_Mis_OffsetSample();
      CTR_v_StartingReset();
      CTR_v_SetCmdConvertitore_ON();          /* Enable PWM switching on side 'A'                */
      CTR_u_status       = CTR_U_ST_RUN;         /* Next status = RUN                        */
      CTR_u_check_pwm_time = TR0_M_u_Get_1ms_Time();
      CTR_b_check_pwm     = DEF_FALSE;
```

326

```c
   }
   break;

  case CTR_U_ST_RUN   :             /*<<<<<<< RUN status: the inverter is switching and the control is On     */
   CTR_M_v_Dsg_SetRollMode();       /* The 7 Segment Display will show a "rolling" segment                    */
   if(CTR_M_b_StartInput_IsOff() || (CTR_b_Activity_Enabled()==DEF_FALSE))
   {
    CTR_v_SetCmdConvertitore_OFF();       /* Disable PWM switching on side 'A'                          */
    CTR_u_status  = CTR_U_ST_STOP;        /* Next status = STOP                          */
   }
   else
   {
    CTR_M_v_Release_Rmp();
    if(CTR_M_b_Dgi_Not_Enabled())
    {
     CTR_b_check_pwm      = DEF_FALSE;
     CTR_u_check_pwm_time = TR0_M_u_Get_1ms_Time();
    }
    else
    {
     if((TR0_u_Elapsed_1ms(CTR_u_check_pwm_time) > 5) || (CTR_b_check_pwm==DEF_TRUE))
     {
      CTR_b_check_pwm      = DEF_TRUE;
      CTR_u_check_pwm_time = TR0_M_u_Get_1ms_Time();
      if(CTR_M_b_PWMA_Not_Enabled())
      {
       ALR_M_v_SetAlrm(ALR_U_CODE_PWMA_NOT_PWONA); /* Cause a proper alarm                          */
      }
     }
    }
   }
   break;

  case CTR_U_ST_WAIT_UP :               /*<<<<<<< WAIT status: the inverter is switching and the control is On
*/
   CTR_M_v_Dsg_SetRollMode();       /* The 7 Segment Display will show a "rolling" segment                    */
   if(CTR_M_b_StartInput_IsOff() || (CTR_b_Activity_Enabled()==DEF_FALSE))
   {
    CTR_v_SetCmdConvertitore_OFF();       /* Disable PWM switching on side 'A'                          */
    CTR_u_status = CTR_U_ST_STOP;         /* Next status = STOP                          */
   }
   else
   {
    if(CTR_f_vsup < CTR_f_vsup_max)
         {
         CTR_M_v_Mis_OffsetSample();
         //CTR_v_StartingReset();
         CTR_v_SetCmdConvertitore_ON();          /* Enable PWM switching on side 'A'                          */
         CTR_u_status       = CTR_U_ST_RUN;      /* Next status = RUN                          */
         CTR_u_check_pwm_time = TR0_M_u_Get_1ms_Time();
         CTR_b_check_pwm     = DEF_FALSE;
         }
   }
   break;
```

327

```c
   case CTR_U_ST_WAIT_DOWN   :                    /*<<<<<<<< WAIT status: the inverter is switching and the control is
On     */
  CTR_M_v_Dsg_SetRollMode();        /* The 7 Segment Display will show a "rolling" segment              */
  if(CTR_M_b_StartInput_IsOff() || (CTR_b_Activity_Enabled()==DEF_FALSE))
  {
  CTR_v_SetCmdConvertitore_OFF();        /* Disable PWM switching on side 'A'                */
  CTR_u_status  = CTR_U_ST_STOP;         /* Next status = STOP                        */
  }
  else
  {
  if(CTR_f_vsup < CTR_f_vsup_min)
        {
        CTR_M_v_Mis_OffsetSample();
  //      CTR_v_StartingReset();
        CTR_v_SetCmdConvertitore_ON();          /* Enable PWM switching on side 'A'               */
        CTR_u_status      = CTR_U_ST_RUN;      /* Next status = RUN                     */
        CTR_u_check_pwm_time = TR0_M_u_Get_1ms_Time();
        CTR_b_check_pwm     = DEF_FALSE;
        }
  }
  break;
  default:
  CTR_M_v_Reset_Rmp() ;
  CTR_u_status = CTR_U_ST_ALRM;         /*<<<<<<<  ALARM status                            */
  CTR_M_v_Mis_OffsetMeas();
  CTR_b_check_pwm     = DEF_FALSE;
  break;
  }

 if(CTR_u_status ==CTR_U_ST_ALRM)
 {
 CTR_M_v_Reset_Rmp() ;
//CTR_u_newperiodcarrier = 1250;      // Con 1250 abbiamo 400us di esecuzione FAST
 CTR_v_SetCmdConvertitore_OFF();        /* Disable PWM switching on side 'A'                */
 if(CTR_u_resetalr==DEF_TRUE)
 {
 CTR_v_ResetConvertitoreFault();
 CTR_u_status  = CTR_U_ST_RESET;
 }
 }
 CTR_u_ctrl_on = (CTR_u_status==CTR_U_ST_RUN);
}

void CTR_v_Bg_Main(void)
/*_____*/
/*_____*/
{
 float f_aux,f_aux1,f_aux2,f_pnom,f_taurot,f_delta;

 //LIMITAZIONE DINAMICA DEI PARAMETRI FUNZIONE DELLA I nominale motore
 CTR_v_LimDinPar();
 CTR_f_out_inductance       = (float)(RWM_M_u_FalseInts_2_Uin_Conv(CTR_i_outinductance))*0.00001f;  // unità
da 10 micro Henry
```

328

Acknowledgements